

Abstract

Experimental study and control of mesoscopic effects inside complex nanophotonic structures

Raktim Sarma

2017

Complex nanophotonic structures refer to composite photonic materials with refractive index that varies on length scales comparable to the optical wavelength. One such example which has a high level of structural complexity and wide prevalence in our daily life is the random medium. Light propagation in a random medium is greatly different from homogeneous medium due to multiple scattering of the light. Interference of the multiply scattered optical waves inside a random medium can lead to many fascinating mesoscopic effects such as localization, non-local intensity correlations and creation of open and closed channels. These effects, besides being of fundamental interest, are being extensively studied for practical applications ranging from random lasers, light harvesting, biomedical imaging to sensing. This thesis presents studies of direct probing as well as manipulation of such mesoscopic effects inside an on-chip random medium.

In the first part of this thesis, we present experimental results of direct probing of mesoscopic effects such as renormalization of the diffusion coefficient and non-local intensity correlations inside a random medium. The random medium studied is a two dimensional silicon waveguide with randomly positioned air holes as scatterers and reflecting photonic crystal sidewalls. Along with demonstrating spatial dependence of the diffusion coefficient, we also show experimentally the buildup of long-range intensity correlations as light propagates inside the random waveguide.

In the second part, we demonstrate a simple and effective approach of using geometry to tailor the above mentioned mesoscopic effects. We show experimentally that in a single random waveguide of varying cross-section, the diffusion coefficient changes spatially in two dimensions due to localization effects and this can lead to modification of the wave diffusion. We further demonstrate that by designing the shape of the random waveguide, the long-range spatial intensity correlation for light propagating inside the waveguide can be efficiently and deterministically modified. In addition to these effects, we also investigate numerically and experimentally the effect of geometry on the transmission and reflection eigenchannels of random media. We show that transmission eigenchannels which have universal structures in conventional random waveguides can be modified using the waveguide geometry. In particular geometries, perfect reflection channels are created, and their large penetration depth into the medium as well as the complete return of probe light to the input end would greatly benefit sensing and imaging applications. In addition, evanescent channels may be converted to propagating channels by modifying the geometry of the random waveguide. Since the transmission eigenchannels determine the energy concentrated inside a random medium, our approach of using geometry opens the door to control efficiently the energy density inside random media without requiring any modification of the intrinsic disorder.

A growing field of research related to random media is coherent control of light transport using adaptive wavefront shaping techniques. Previous studies have shown focusing, reduced reflection and enhanced transmission through a random medium by shaping the input wavefront. A major constraint that limits the efficiency of such experiments is incomplete control of the input. In the third part of this thesis, we implement the adaptive wavefront shaping technique to our on-chip random structures and with a careful design of the coupling waveguide achieve a complete control

of the input. Using adaptive wavefront shaping, we demonstrate an unprecedented enhancement and control of the transmission and energy density inside the random nanostructures. In addition, using wavefront shaping we also demonstrate coherent control of light transport in random waveguides with inhomogeneous scattering and loss. These results demonstrate the possibility of controlling light matter interactions in a random media in an on-chip platform.

Finally, we study numerically the effect of rotation on resonances of dielectric microcavities. Unlike random media, dielectric microcavities have a spatially homogeneous refractive index profile. However, in a rotating frame, the effective refractive index of the resonant modes can become a function of rotation speed which can lead to modification of the resonances of the cavity. We develop a Finite Difference Time Domain simulation algorithm to study dielectric structures in a rotating frame. Using the simulation algorithm, we study in detail the rotation induced changes of resonances of microcavities of different shapes with open boundaries and demonstrate that compared to resonant frequency, other properties of the resonances such as quality factors and farfield intensity can be more sensitive to rotation.

**Experimental study and control of
mesoscopic effects inside complex
nanophotonic structures**

A Dissertation
Presented to the Faculty of the Graduate School
of
Yale University
in Candidacy for the Degree of
Doctor of Philosophy

by
Raktim Sarma

Dissertation Director: Professor Hui Cao

May 2017

ProQuest Number: 10632559

All rights reserved

INFORMATION TO ALL USERS

The quality of this reproduction is dependent upon the quality of the copy submitted.

In the unlikely event that the author did not send a complete manuscript and there are missing pages, these will be noted. Also, if material had to be removed, a note will indicate the deletion.



ProQuest 10632559

Published by ProQuest LLC (2017). Copyright of the Dissertation is held by the Author.

All rights reserved.

This work is protected against unauthorized copying under Title 17, United States Code
Microform Edition © ProQuest LLC.

ProQuest LLC.
789 East Eisenhower Parkway
P.O. Box 1346
Ann Arbor, MI 48106 – 1346

Copyright © 2017 by Raktim Sarma

All rights reserved.

Contents

LIST OF FIGURES. v

ACKNOWLEDGEMENTS. xxxv

1 INTRODUCTION 1

1.1 Light Transport in Random Media 1

1.1.1 Renormalization of diffusion coefficient 5

1.1.2 Intensity correlations in speckle patterns 7

1.1.3 Open and closed channels in random media 11

1.2 Rotating Dielectric Microcavities 13

2 EXPERIMENTAL DEMONSTRATION OF POSITION DEPENDENT
DIFFUSION IN DISORDERED WAVEGUIDES 22

2.1 Introduction 22

2.2 Two dimensional disordered waveguides 24

2.3 Experimental demonstration of PDD 27

2.3.1 PDD in disordered waveguides of different widths 29

2.3.2 PDD in disordered waveguides of different scattering strengths 31

2.3.3 PDD in disordered waveguides of different lengths 33

3	DIRECT PROBING OF LONG-RANGE INTENSITY CORRELATION INSIDE A RANDOM WAVEGUIDE.	37
3.1	Introduction	37
3.2	2D random nanostructures	39
3.3	Theory of long-range intensity correlation	42
3.4	Comparison of experimental results and theory	45
4	CONTROL OF LIGHT DIFFUSION INSIDE A RANDOM WAVEGUIDE USING GEOMETRY	52
4.1	Introduction	52
4.2	2D disordered waveguide and experimental setup	55
4.3	Numerical simulation of position dependent diffusion	57
4.4	Comparison of experimental results and numerical simulation	60
5	USING GEOMETRY TO MANIPULATE LONG-RANGE CORRELATION OF LIGHT INSIDE RANDOM MEDIA	65
5.1	Introduction	65
5.2	Numerical simulations	67
5.3	Experimental results and comparison to numerical simulations	72
5.4	Discussion	77
6	CONTROL OF MESOSCOPIC TRANSPORT BY MODIFYING TRANSMISSION CHANNELS USING GEOMETRY	85
6.1	Introduction	85
6.2	Quasi-two-dimensional random waveguide	88
6.3	Linear tapering of waveguide width	90

6.4	Effect of Absorption	99
6.5	Intensity decay inside random media	101
6.6	Non-monotonic variation of waveguide cross-section	103
6.7	Discussion	107
7	CONTROL OF ENERGY DENSITY INSIDE DISORDERED MEDIUM BY COUPLING TO OPEN OR CLOSED CHANNELS USING ADAPTIVE WAVEFRONT SHAPING	115
7.1	Introduction	115
7.2	Design of the coupling waveguide and the disordered nanostructures .	117
7.3	Wavefront shaping experiment	119
7.4	Experimental results and comparison to numerical simulations	122
8	CONTROL OF LIGHT TRANSPORT INSIDE A RANDOM MEDIUM WITH INHOMOGENEOUS SCATTERING AND LOSS	132
8.1	Introduction	132
8.2	2D random waveguide with inhomogeneous scattering and loss	134
8.3	Experimental setup and results	136
8.4	Numerical simulations	137
9	FINITE DIFFERENCE TIME DOMAIN ALGORITHM FOR RO- TATING DIELECTRIC STRUCTURES	142
9.1	Introduction	142
9.2	FDTD algorithm for rotating frame	144
9.3	Sagnac effect in a microdisk cavity	148
9.4	Validation of the FDTD algorithm	149

9.5	Discussion	151
10	ROTATION INDUCED CHANGES IN OPTICAL RESONANCES OF DIELECTRIC MICROCAVITIES	156
10.1	Introduction	156
10.2	Rotation induced changes in Q factor of resonances of a circular mi- crocavity	158
10.3	Elliptical cavities	161
10.4	Rotating optical microcavities with broken chiral symmetry	167
10.4.1	Simple analytical model of a rotating chiral cavity to calculate Sagnac effect	168
10.4.2	Resonant modes in a non-rotating chiral cavity	170
10.4.3	Effect of rotation on the emission patterns of chiral microcav- ities and comparison of its sensitivity to Sagnac effect	173
10.4.4	Tuning of cavity shape to maximize sensitivity	176
10.4.5	Scaling of rotation-induced relative change in output intensity with cavity size and effect of refractive index	178
10.4.6	Absolute change in output intensity by rotation	182
11	CONCLUSIONS	189

List of Figures

1.1	Side-view scanning electron microscope (SEM) image of a fabricated two dimensional random waveguide.	3
1.2	Weak localization effect. Constructive interference of the waves from the reversed loops increases the energy density at the original position and decreases the net flux through the random medium.	6
1.3	Typical output speckle pattern of laser light transmitted through a diffusive medium	8
1.4	Subset of paths that contribute to the correlations in the speckle pattern. a and b correspond to input and output channels respectively and the reversed arrow signifies the time-reversed path. (a) Independent scattering paths contribute to C_1 . (b) One crossing of scattering paths lead to long-range correlations C_2 . Its magnitude is on the order of $1/g$. (c) Two crossing of scattering paths inside the random medium lead to infinite range correlations C_3 . Since it requires two crossings, therefore the magnitude is on the order of $1/g^2$	10
1.5	Spatial profile (cross section averaged intensity $I(z)$) of maximum transmission channel of a diffusive waveguide of $W = 5.1 \mu\text{m}$ and $L = 10.2 \mu\text{m}$. The dimensionless conductance is $g = 3$. The inset shows the 2D intensity distribution of the maximum transmission channel.	12

1.6	Electric field distribution of a resonant mode in a circular disk with open (a) and closed boundaries (b).	14
2.1	Side-view scanning electron microscope (SEM) image of a fabricated quasi-2D disordered photonic waveguide. The two sidewalls of the waveguide consist of triangular lattices of air holes (lattice constant 440 nm, hole radius 154 nm). They possess a 2D photonic bandgap and behave like reflecting walls for light incident from all angles in the waveguide.	25
2.2	(a) A schematic of the experimental setup. A lensed fiber couples the light to the structure and another 50× objective lens (NA = 0.42) collects the light scattered by the air holes out of the waveguide plane and projects onto a camera. (b) Optical image of the intensity of light scattered out-of-plane from the disordered waveguide. The wavelength of the probe light is 1505 nm.	28
2.3	(a) Schematic of the sample layout showing the ridge waveguides coupling the probe light from the edge of the wafer to the random waveguides with photonic crystal sidewalls (b) Layout of the fabricated structures studied experimentally.	28

- 2.4 (a) Experimentally measured light intensity $I(z)$ inside random waveguides of different width W and constant length $L=80 \mu\text{m}$ (blue solid lines). The curves are vertically shifted for a clear view. $\ell=2.2 \mu\text{m}$ and $\xi_a=30 \mu\text{m}$ are found by fitting the $W=60 \mu\text{m}$ sample with the self-consistent theory of localization (red dashed line). With these parameters, the self-consistent theory of localization predicts $I(z)$ for other samples of $W=40 \mu\text{m}$, $20 \mu\text{m}$, $10 \mu\text{m}$, $5 \mu\text{m}$ (red solid curves), which agrees well with the experimental data. (b) Position-dependent diffusion coefficients for the five samples in (a). 30
- 2.5 (a) Experimentally measured light intensity $I(z)$ inside random waveguides of different width W and constant length $L=80 \mu\text{m}$ in the deep saturation regime $\xi_a \ll L$ (blue solid lines). The curves are vertically offset for a clear view. $\ell = 1.0 \mu\text{m}$ and $\xi_a = 13 \mu\text{m}$ are found by fitting the $W=60 \mu\text{m}$ sample with the self-consistent theory of localization (red dashed line). These values are then used to predict $I(z)$ for other samples $W=40 \mu\text{m}$, $20 \mu\text{m}$, $10 \mu\text{m}$, $5 \mu\text{m}$ (red solid curves), which is in good agreement with the experimental data with no fitting parameters except the vertical intensity scale. (b) Diffusion coefficients $D(z)$ for all samples in (a) are saturated in the region $\xi_{a0} < z < L - \xi_a$ 32
- 2.6 (a) Experimentally measured $I(z)$ of two waveguides with the same width $W=5 \mu\text{m}$ but different length, $L=80 \mu\text{m}$, $160 \mu\text{m}$ (blue solid curves). Red solid curves represent the prediction of the self-consistent theory of localization using the same values of ℓ and ξ_a as in Fig. 2.3(a). (b) Diffusion coefficients $D(z)$ for the two samples in (a), showing the saturation of D inside the longer sample $L=160 \mu\text{m}$ 34

- 3.1 Top-view scanning electron microscope (SEM) image of a quasi-2D disordered photonic waveguide. Light is injected from the left end of the empty waveguide and incident onto the random array of air holes. The waveguide wall is made of a triangle lattice of air holes which forms a 2D photonic bandgap to confine light inside the waveguide. 40
- 3.2 (a) A schematic of the optical measurement setup. One objective lens (NA = 0.4) couples the light from a tunable laser source to the waveguide, and another objective lens (50 \times , NA = 0.42) collects the light scattered by the air holes out of the waveguide plane and images onto a camera. (b) An optical image of the intensity of scattered light from the disordered waveguide. The wavelength of the probe light is 1510 nm. The intensity distribution exhibits short-range fluctuations. z_1 and z_2 represent the axial positions of two cross-sections inside the disordered waveguide. 41
- 3.3 Long-range intensity correlation $\tilde{C}(z_1, z_2)$ in a disordered waveguide of $L = 80 \mu\text{m}$, $W = 60 \mu\text{m}$, $\xi_a = 30 \mu\text{m}$, $\ell = 2.2 \mu\text{m}$. z_1 is varied between 0 and L while z_2 is fixed at L or $L/2$. Solid circles are experimental data and solid lines represent the theoretical predictions. The dashed line corresponds to the background taken outside the waveguide. The inset shows $\tilde{C}(z_1, z_2)$ for $\Delta z = z_2 - z_1 = 10 \mu\text{m}$ and $z_2 = L, L/2, L/4$. Solid circles are experimental data and solid line represents the theoretical prediction. For a fixed Δz , $\tilde{C}(z_1, z_2)$ increases when moving deeper into the sample. 46

- 3.4 Long-range intensity correlation $\tilde{C}(z_1, z_2)$ for two waveguides with the same length $L = 80 \mu\text{m}$ and the degree of disorder ($k\ell = 26$) but different widths $W=60 \mu\text{m}$ and $W = 10 \mu\text{m}$. z_1 is moved from 0 to L and z_2 is set at L . Solid circles are experimental data and solid lines represent the theoretical predictions. The dashed line corresponds to the background taken outside the waveguide. The six-times reduction of the waveguide width results in a six-fold increase in the magnitude of intensity correlation. 47
- 3.5 Normalized variance of the cross-section integrated intensity $I(z)$, $\text{var}[I(z)]/\langle I(z) \rangle^2$, for two waveguides with the same length $L = 80 \mu\text{m}$ and degree of disorder ($k\ell = 26$) but different widths $W = 60 \mu\text{m}$ and $W = 10 \mu\text{m}$. z is changed from 0 to L . The solid circles are experimental data and solid lines represent the theoretical predictions. The dashed line corresponds to the background taken outside the waveguide. The six-times reduction of the waveguide width results in a six-fold increase in the magnitude of intensity fluctuations. . . . 48
- 4.1 Top-view scanning electron microscope (SEM) image of a quasi-2D disordered photonic waveguide. Light is injected from the left end of the waveguide and incident onto the random array of air holes. The waveguide wall is made of a triangle lattice of air holes which forms a 2D photonic bandgap to confine light inside the waveguide. The width of the random waveguide is changed gradually from $40 \mu\text{m}$ to $5 \mu\text{m}$ through a tapered region. 54

4.2	(a) A schematic of the experimental setup. A lensed fiber couples the light to the structure and another $50\times$ objective lens ($\text{NA} = 0.42$) collects the light scattered by the air holes out of the waveguide plane and projects onto a camera. (b) Optical image of the intensity of light scattered out-of-plane from the disordered waveguide. The wavelength of the probe light is 1505 nm.	56
4.3	(a) Calculated return probability in the disordered waveguide shown in Fig. 4.1. $\ell = 2.9\mu\text{m}$, and $\xi_a = 35\mu\text{m}$. (b) 2D renormalized position dependent diffusion coefficient $D(y, z)/D_0$ for the same structure as in (a). (c) Intensity distribution $I(y, z)/I_0$ inside the random structure obtained from $D(y, z)/D_0$ in (b).	59
4.4	(a) Comparison of the measured cross-section integrated intensity $I_t(z)$ of the entire structure (solid blue line) to numerical calculations based on self-consistent theory (dashed red line). The inset plots the measured $I_t(\tilde{z})$ for both the wider(dashed line) and narrower (solid line) sections of the waveguide on top of each other. $\tilde{z} = z/L_1$ for the wide section, and $\tilde{z} = (z - (L_1 + 10))/L_2$ for the narrow section. In the inset, for both cases, $I_t(\tilde{z})$ is normalized to 1 to demonstrate the clear difference in the exponential decay rate (slope).(b) Measured cross-section averaged intensity $I_r(z)$ (solid blue line) in comparison with the results of self consistent theory (dashed red line). The vertical dotted lines in (a,b) marks the starting point and the end point of the tapered region.	61

5.1 Calculated spatial long-range intensity correlation for the constant-width and two types of tapered 2D random waveguides. The waveguide length $L = 80 \mu\text{m}$, the transport mean free path $\ell = 2.2 \mu\text{m}$, and the diffusive absorption length $\xi_a = 26 \mu\text{m}$. The waveguide in (a,d) has a constant width $W = 10 \mu\text{m}$; in (b,e) $W(z)$ increases linearly from $10 \mu\text{m}$ to $60 \mu\text{m}$, while in (c,f) $W(z)$ decreases linearly from $60 \mu\text{m}$ to $10 \mu\text{m}$. (a-c) show spatial distribution of the magnitude of long-range correlation function, $C_2(\mathbf{r}; \mathbf{r})$ for three geometries. (d-f) show long-range correlation function $C_2(z_1; z_2)$ of cross-section averaged intensity for the same geometries. The maximum value is normalized to 1 for comparison. The differences in these plots reveal that the waveguide geometry has a significant impact on the magnitude and range of C_2 69

5.2 Comparison of calculated long-range correlation in six waveguides with different degrees of taper: two with constant widths of $10 \mu\text{m}$ (solid black line) and $60 \mu\text{m}$ (dash-dotted magenta line); two with width linearly increasing from $10 \mu\text{m}$ (thick dashed blue line) or $20 \mu\text{m}$ (thin dashed blue line) to $60 \mu\text{m}$; and two with width linearly decreasing from $60 \mu\text{m}$ to $10 \mu\text{m}$ (thick dotted red line) or $20 \mu\text{m}$ (thin dotted red line). Other parameters are the same as in Fig. 5.1. Both $C_2(z; z)$ (a) and $C_2(z; L)$ (b) clearly demonstrate that while the functional form of long-range correlation is universal for uniform waveguides, it is strongly modified in the tapered ones. 70

- 5.3 Comparison of calculated long-range correlation function $C_2(z; z)$ for the cross-section averaged intensity inside passive diffusive waveguides (solid line) with same scattering strength as Fig. 5.1 to the prediction of the effective conductance model (dashed line). (a) The waveguide has constant width $W = 60 \mu\text{m}$. (b) The waveguide width increases linearly from $10 \mu\text{m}$ to $60 \mu\text{m}$. (c) The waveguide width decreases linearly from $60 \mu\text{m}$ to $10 \mu\text{m}$. All three waveguides have the same length $L = 80 \mu\text{m}$. The effective conductance model fails to predict $C_2(z; z)$ inside all three waveguides. 72
- 5.4 (a) Top-view scanning electron microscope (SEM) image of a quasi-2D disordered waveguide with $W = 60 \mu\text{m}$ and $L = 80 \mu\text{m}$. The waveguide wall is made of a triangle lattice of air holes which forms a 2D photonic bandgap to confine light inside the waveguide. (b) An optical image of the intensity of scattered light from the disordered waveguide shown in (a). The wavelength of the probe light is 1500 nm. The white boxes mark two cross-sections at depths z_1 and z_2 in the disordered waveguide. (c,d) Fitting of experimental data to extract scattering and dissipation parameters. The solid blue line in (c) represents the experimentally measured ensemble and cross-section averaged intensity inside the waveguides shown in (a). The solid blue circles in (d) are the measured $C(z, z)$ for the cross-section averaged intensity in the waveguide shown in (a). The dashed red lines in (c) and (d) are obtained by numerical calculation with parameters $\xi_a = 26 \mu\text{m}$ and $\ell = 2.2 \mu\text{m}$, which have the best fit to the experimental data. 75

5.5 Experimental measurement of long-range intensity correlation inside the tapered waveguides. (a,b) Top-view SEM images of fabricated quasi-2D disordered waveguides with linearly increasing (a) or decreasing (b) width. The width of waveguide in (a) increases from $10 \mu\text{m}$ to $60 \mu\text{m}$, and in (b) it is opposite. Both have the same length $L = 80 \mu\text{m}$. Magnified SEM images show the air holes distributed randomly in the tapered section of the waveguide and the triangle lattice of air holes in the reflecting sidewalls. (c) Measured long-range correlation function for the cross-section-averaged intensity $C(z, L)$ inside the tapered waveguides shown in (a) and (b). The blue circles (green squares) represent experimental data for the waveguides with increasing (decreasing) width, and the dashed lines are theoretical results. . 76

- 5.6 Long-range correlation in a quasi-2D disordered waveguide whose width varies non-monotonically. (a) Top-view SEM image showing the waveguide width W increases linearly from $10 \mu\text{m}$ at $z = 0$ to $60 \mu\text{m}$ at $z = 40 \mu\text{m}$ and then reduces linearly down to $10 \mu\text{m}$ at $z = 80 \mu\text{m}$. Other structural parameters are the same as the waveguides in Fig. 5.5. (b) An optical image of the intensity of scattered light from the disordered waveguide. The wavelength of the probe light is 1510 nm . (c) Long-range correlation function $C(z, L)$ for the cross-section averaged intensities at z and L in the waveguide shown in (a). $C(z, L)$ displays a sharp change in the growth rate before and after z passes $L/2$. (d) Long-range correlation function for the cross-section averaged intensities at z and $L/2$ in the waveguide shown in (a). $C(z, L/2)$ increases monotonically in the first half of the waveguide and decreases slightly in the second half. In (c, d), solid circles represent experimental data and the dashed curves are obtained by numerical calculation. 78
- 5.7 Numerical simulation of focusing of light inside a diffusive waveguide by shaping the input wavefront. The light intensity at the focal spot, $\mathbf{r} = (0, z)$, is normalized to 1. Black dashed curve (solid red curve) represents the background intensity I_b vs. depth z inside a random waveguide of width tapered linearly from $10 \mu\text{m}$ ($60 \mu\text{m}$) to $60 \mu\text{m}$ ($10 \mu\text{m}$). Both waveguides have the same length $L = 80 \mu\text{m}$, and they are identical to the ones shown in Fig. 5.1. $I_b(z)$ follows the spatial variation of C_2 , as shown in Fig. 5.2. in both waveguides. 80

6.1	Quasi-two-dimensional random waveguides of different geometry. (a,b)	
	Top-view SEM images of fabricated quasi-2D disordered waveguides	
	with linearly increasing (a) or decreasing (b) width. The width of	
	waveguide in (a) increases from $W_1 = 10 \mu\text{m}$ to $W_2 = 60 \mu\text{m}$, and in	
	(b) it is opposite. Both have the same length $L = 80 \mu\text{m}$. Magnified	
	SEM images show the air holes distributed randomly in the tapered	
	section of the waveguide and the triangle lattice of air holes in the	
	reflecting sidewalls. (c) An optical image of the intensity of scattered	
	light from the disordered waveguide. The wavelength of the probe	
	light is 1500 nm.	89

6.3 Transmission eigenchannels in tapered waveguide of decreasing width.

(a) Comparison of cross-section-averaged intensity, $I_v(z)$, of the maximum transmission channel ($m = 1$) in two waveguides with different tapering angles and a constant-width waveguide. All waveguides have the same length $L = 20 \mu\text{m}$. The constant-width waveguide has $W_1 = W_2 = 10.2 \mu\text{m}$ (blue dotted line). The two tapered waveguides have $W_1 = 10.2 \mu\text{m}$ and $W_1/W_2 = 2$ (red dashed line), 4 (green solid line). The $I_v(z)$ curves are offset along the y axis for clarity. The intensity peak shifts from the waveguide center ($W_1/W_2 = 1$) towards the output end ($W_1/W_2 > 1$), and the shift is larger for higher tapering angle (larger W_1/W_2). (b) Cross-section-averaged intensity, $I_v(z)$, of a perfect reflection channel for the same tapered waveguides as in (a). The blue dotted line corresponds to tapering of $W_1/W_2 = 2$ and green dashed line corresponds to $W_1/W_2 = 4$. $I_v(z)$ of a high reflection channel of the constant-width waveguide (blue solid line) is added for comparison. The insets show the spatial distribution of electric field intensity for the high reflection channel of the constant-width waveguide and the perfect reflection channel of the tapered waveguide with $W_1/W_2 = 2$. The perfect reflection channel in a tapered waveguide exhibits slower intensity decay inside the random medium (followed by a sharp drop near the rear end) and thus can penetrate much deeper into the turbid medium than the high reflection channel in the constant-width waveguide. The penetration length increases with the tapering angle. 94

6.4 Effect of absorption on the maximum transmission eigenchannel and energy flux decay in the constant-width and tapered waveguides. (a) Comparison of the cross-section-averaged intensity, $I_c(z)$, of the maximum transmission channel in a constant-width ($W = 5.1 \mu\text{m}$, $L = 20 \mu\text{m}$) disordered waveguide with (dashed line) and without (solid line) absorption. In the absorbing waveguide, $L/\xi_a = 3$. Absorption modifies the spatial profile of the maximum transmission channel. (b) Comparison of spatial decay of energy flux $J(z)$ in random waveguides with constant widths $W = 5.1 \mu\text{m}$ (blue solid line) and $W = 10.2 \mu\text{m}$ (dashed magenta line), increasing width of $W_1 = 5.1 \mu\text{m}$, $W_2 = 10.2 \mu\text{m}$ (green dotted line) and decreasing width of $W_1 = 10.2 \mu\text{m}$ and $W_2 = 5.1 \mu\text{m}$ (red dashed line). For all waveguides, $L = 20 \mu\text{m}$, $L/\xi_a = 3$ and $J(z)$ is normalized to 1 at $z = 0$. While the flux decay length remains the same for the two rectangle waveguides of different widths, it is lengthened in the expanding waveguide and shortened in the contracting waveguide. 100

6.5 Experimentally measured intensity decays inside disordered waveguides in comparison to numerically calculated spatial profiles of the maximum transmission eigenchannels. (a) Experimentally measured cross-section-averaged intensity $I_v(z)$ inside quasi-2D waveguides of constant width $W = 60 \mu\text{m}$ (solid blue line), increasing width with $W_1 = 10 \mu\text{m}$, $W_2 = 60 \mu\text{m}$ (dotted green line), and decreasing width with $W_1 = 60 \mu\text{m}$, $W_2 = 10 \mu\text{m}$ (dashed red line). All the waveguides have $L = 80 \mu\text{m}$ and $L/\xi_a = 3$. The tapering of the waveguide boundary causes a dramatic change in the decay lengths of $I_v(z)$. (b) Numerically calculated $I_v(z)$ of the maximum transmission eigenchannel in the disordered waveguides of constant width $W = 10.2 \mu\text{m}$ (solid blue line), increasing width with $W_1 = 5.1 \mu\text{m}$, $W_2 = 10.2 \mu\text{m}$ (dotted green line), and decreasing width with $W_1 = 10.2 \mu\text{m}$, $W_2 = 5.1 \mu\text{m}$ (dashed red line). All waveguides have $L = 20 \mu\text{m}$ and $L/\xi_a = 3$. Despite of the reduced waveguide dimensions, the maximum transmission channels exhibit a qualitatively similar structure to the experimentally measured intensities, indicating the intensity distribution inside a strongly absorbing random medium is determined by the structure of the maximum transmission channel. 102

6.6 Transmission eigenchannels and intensity decay in a diffusive waveguide of bowtie geometry. (a) Top-view SEM image of a fabricated quasi-2D waveguide with bowtie geometry. The length of waveguide is $L = 80 \mu\text{m}$. The width of waveguide decreases linearly from $60 \mu\text{m}$ at $z = 0$ to $10 \mu\text{m}$ at $z = L/2$ and then again increases linearly to $60 \mu\text{m}$ at $z = L$. (b) Numerically-calculated cross-section-averaged intensity $I_v(z)$ of the 19th (solid line) and 20th (dashed line) transmission eigenchannels of bowtie waveguide. The length L of the waveguide is $20 \mu\text{m}$, the width at $z = 0, L$ is $10.2 \mu\text{m}$ (35 propagating modes) and the width of constriction at $z = L/2$ is $5.1 \mu\text{m}$ (17 propagating modes). The abrupt changes in the decay rate of $I_v(z)$ before and after $z = L/2$ indicate the conversion from propagating wave to evanescent wave and back. The evanescent decay rate varies from one channel to another. (c) Numerically-calculated $I_v(z)$ (green dashed line) and cross-section-integrated intensity $I_t(z)$ (blue solid line) for the maximum transmission channel of the same waveguide as in (b) but with absorption $L/\xi_a = 3$. The constriction causes a significant change in the intensity distribution of the maximum transmission channel. (d) Experimentally measured $I_v(z)$ (green dashed line) and $I_t(z)$ (blue solid line) inside the disordered waveguide shown in (a). Both intensity distributions follow those of the maximum transmission channel. 105

6.7 Transmission eigenchannels and energy distribution in a diffusive waveguide of lantern geometry. (a) Top-view SEM image of a fabricated quasi-2D disordered waveguide with lantern geometry. The length of waveguide is $L = 80 \mu\text{m}$. The width of waveguide increases linearly from $10 \mu\text{m}$ at $z = 0$ to $60 \mu\text{m}$ at $z = L/2$ and then again decreases linearly to $10 \mu\text{m}$ at $z = L$. (b) Numerically calculated cross-section-averaged intensity $I_v(z)$ for the 5th (dashed line) and 19th (solid line) transmission eigenchannels of lantern geometry. The length L of the waveguide is $20 \mu\text{m}$, the width at $z = 0$, L is $5.1 \mu\text{m}$ (17 propagating modes) and width at $z = L/2$ is $10.2 \mu\text{m}$ (35 propagating modes). $I_v(z)$ of the 19th transmission eigenchannel exhibits the conversion of the evanescent wave to a propagating wave near the input end and then back to the evanescent wave near the output end due to the variation of the waveguide width. In contrast, the 5th channel remains propagating wave across the entire waveguide. (c) Numerically calculated $I_r(z)$ (green dashed line) and cross-section-integrated intensity $I_t(z)$ (blue solid line) for the maximum transmission channel of the same waveguide as in (b) but with absorption $L/\xi_a = 3$. Both intensity profiles are opposite to those in the bow-tie waveguide. (d) Experimentally measured $I_v(z)$ (green dashed line) and $I_t(z)$ (blue solid line) inside the disordered waveguide shown in (a). The intensity profiles are similar to those of the maximum transmission channel shown in (c). 108

- 7.1 On-chip disordered waveguide with a tapered lead. (a) Top-view scanning electron micrograph (SEM) of a fabricated silicon waveguide. A ridge waveguide (lead) is tapered from the width $W_1 = 330 \mu\text{m}$ at the edge of the wafer to the width $W = 15 \mu\text{m}$, in order to increase the degree of control of the light that is injected to the disordered waveguide. (b) Magnified SEM of the disordered region of the waveguide that consists of a random array of air holes (diameter = 90 nm). (c) Magnified SEM showing the air holes distributed randomly within the waveguide with a filling fraction of 6 %. (d) The sidewalls of the waveguide are made of a triangular lattice of air holes (diameter = 360 nm) with a lattice constant of 505 nm, which supports a full photonic bandgap at the wavelength $\lambda = 1.51 \mu\text{m}$ 120
- 7.2 Semi-log plot of the eigenvalues of the covariance matrix $C(y, y')$ for the electric field $E_m(y, z = L_1)$ at the end of a tapered lead with $W_1 = 85 \mu\text{m}$, $W = 15 \mu\text{m}$, and $L_1 = 100 \mu\text{m}$. The inset is a schematic of the geometry. The sudden drop of eigenvalues gives the number of significant eigenvalues, $M = 56$, which is equal to the number of waveguide modes $N = 56$ at the end of the lead $z = L_1$ 120

7.3 Wavefront shaping experiment to control intensity distribution inside a disordered waveguide. (a) A schematic of the experimental setup. A laser (HP 8168F) output at $\lambda = 1510$ nm is collimated (by lens L_1), expanded (by L_2, L_3) and linearly polarized (by a polarized beam splitter PBS) before being modulated by a phase-only SLM (Hamamatsu X10468). Two lens (L_4, L_5) are used to project the SLM plane to the pupil plane of an objective O_1 ($100\times$, NA = 0.7), and the edge of the wafer is placed at the focal plane. The SLM imposes phase modulation only in one direction in order to generate a line at the front end of the coupling waveguide. A sample phase pattern on the SLM is shown. The light scattered out of the sample plane is collected by another objective O_2 ($100\times$, NA = 0.7) and imaged to an InGaAs camera (Xenics XEVA 1.7-320) by a tube lens (L_6). M_1 and M_2 are mirrors, BS is beam splitter. (b) An optical image of the illumination line ($330 \times 1.1 \mu\text{m}$) on the waveguide facet. The input intensity is modulated along the line. (c) An image of the spatial distribution of light intensity inside the disordered waveguide for a random input wavefront. The spatial resolution is about $1.1 \mu\text{m}$. The ratio S of the integrated intensities over the two rectangles at the back and front side of the waveguide is used as feedback for optimizing the input wavefront.123

- 7.4 Experimental control of intensity distribution inside the disordered waveguide. (a, b, c) Two-dimensional intensity distribution $I(y, z)$ inside the disordered waveguide shown in Fig. 7.1 for (a) random input fields, (b) optimized input for maximum light penetration (maximizing S). (c) optimized input for minimum light penetration (minimizing S). (d, e, f) The cross-section-averaged intensity, $I(z)$, obtained from $I(y, z)$ in (a, b, c). Dashed lines are experimental data and solid lines are simulation results. 125
- 7.5 Numerical simulation of wavefront shaping experiment. (a,c) Weight $w(\tau)$ of each transmission eigenchannel in the input field obtained by maximizing (a) or minimizing (c) light penetration into the disordered waveguide with the cost function S (black solid line). For comparison, $w(\tau)$ for the random input field (blue solid line), and for the input field of the maximum (a) or minimum (c) transmission eigenchannel after removal of amplitude modulation (red dotted line) are also shown. (b,d) Cross-section-averaged intensity distribution $I(z)$ for the maximized (b) or minimized (d) S (black solid line), as well as the maximum (b) or minimum (d) transmission channel with (green dash-dotted line) and without amplitude modulation (red dotted line). 128

- 8.1 2D disordered waveguide with inhomogeneous scattering and loss. (a) Top-view scanning electron micrograph (SEM) of the fabricated silicon waveguide that consists of randomly positioned air holes. The waveguide width $W = 20 \mu\text{m}$, and length $L = 60 \mu\text{m}$. A circular region of diameter $10 \mu\text{m}$ at the center of the waveguide has larger and denser air holes (hole diameter = 150 nm , the air filling fraction = 15%). Outside this region, the air holes are smaller (diameter = 90 nm) and the filling fraction is lower (6%). The sidewalls of the waveguide are made of a triangular lattice of air holes (diameter = 360 nm , lattice constant = 505 nm), which supports an in-plane photonic bandgap at the wavelength $\lambda = 1.51 \mu\text{m}$. (b) Magnified SEM of the central region of the disordered waveguide showing air holes of two different sizes and densities. 135
- 8.2 A schematic of the wavefront shaping experiment setup. A laser beam (HP 8168F) at $\lambda = 1510 \text{ nm}$ is collimated (by lens L_1), expanded (by L_2, L_3), and linearly polarized (by a polarized beam splitter PBS) before being modulated by a phase-only SLM (Hamamatsu X10468). Two lens (L_4, L_5) are used to project the SLM plane to the pupil plane of an objective O_1 ($100\times$, $\text{NA} = 0.7$), and the edge of the coupling waveguide is placed at the focal plane of the objective. The light scattered out of the sample plane is collected by a second objective O_2 ($100\times$, $\text{NA} = 0.7$) and imaged to an InGaAs camera (Xenics XEVA 1.7-320) by a tube lens (L_6). M_1 and M_2 are mirrors. BS is an unpolarized beam splitter. The inset is an optical image of the illumination line on the front facet of the coupling waveguide, created by modulating the phase of the SLM pixels. 136

8.3	Optimizing the incident wavefront to enhance light transmission through the disordered waveguide with spatially inhomogeneous scattering and loss. Experimentally measured 2D intensity distribution $I(y, z)$ inside the waveguide shown in Fig. 8.1 for (a) unoptimized input fields, (b) optimized input for maximum cost function S . The white box marks the boundary of the disordered waveguide.	137
8.4	Numerical simulation of the ensemble averaged Poynting vector $\vec{J}(y, z)$ of light inside the 2D disordered waveguide with spatially inhomogeneous scattering and loss. The magnitude of $\vec{J}(y, z)$ is shown by color plot, and its direction is shown by the arrows. The input field in (a) is optimized to maximize total transmission. With optimized input wavefront, the optical waves bypass the region of higher scattering and loss in the middle of the waveguide (denoted by a white circle). (b) shows $\vec{J}(y, z)$ for the maximum transmission channel, which is nearly identical to that in (a), indicating the optimized input field couples mostly to the maximum transmission channel.	138

- 9.1 Frequency splitting between the CW and CCW modes in a circular dielectric microdisk of radius $R = 590$ nm and $n = 3$ in free space ($n = 1$) as a function of the normalized rotation speed $\Omega R/c$. The circles are the FDTD simulation results for a rotating closed cavity for a WG mode ($l = 1, m = 7, \lambda = 1009.8$ nm) and the solid line is the analytical result from Eq. (20). Squares are the FDTD simulation results for the same mode ($l = 1, m = 7, \lambda = 1131.48$ nm) in the rotating microdisk with open boundary. Dotted line represents the frequency shifts obtained from the FDTD simulation of the stationary microdisk with the effective indices of refraction (inside and outside the disk) that include the rotation-induced changes. The insets show the mode profiles for the closed and open cavities and the black circle marks the boundary of the cavity. 151
- 10.1 Calculated quality factors for the $l = 1, m = \pm 7$ modes as a function of normalized rotation speed $\Omega R/c$. The squares are obtained from the FDTD simulation of a rotating microdisk of $R = 590$ nm and $n = 3$ in free space, and the crosses from the stationary microdisk with the effective indices of refraction (inside and outside the disk) that include rotation-induced changes described in chapter 9. The dotted lines are linear fits showing that the Q changes exponentially with rotation speed. 160

- 10.2 Relative change in Q factor $\frac{\Delta Q}{Q_0}$ (squares) and the normalized frequency splitting $\frac{\Delta k}{k_0}$ (circles) as a function of the normalized rotation speed $\Omega R/c$ for the WG mode of $l = 1$, $m = -7$ in the dielectric microdisk of $R = 590$ nm and $n = 3$. The dotted lines are the linear fits. 161
- 10.3 Rotation-induced changes in the resonances of elliptical cavities. (a) A 2D microcavity of elliptical shape. The length of minor (major) axis is $2a$ ($2b$). (b,c) Spatial distribution of the electric field magnitude ($|E_z|$) for a pair of quasi-degenerate modes in the elliptical cavity with $a/b = 0.88$ and refractive index $n = 3.0$. (d) A schematic showing the frequency splitting Δk_0 of a quasi-degenerate pair of modes (solid lines) in an elliptical cavity without rotation, and the frequency splitting Δk_r with rotation. The higher-frequency (lower-frequency) mode of the quasi-degenerate pair is blue (red) shifted by rotation (dashed lines). (e) Normalized frequency shift $\Delta k_r R$ as a function of the normalized rotation speed $\Omega R/c$ for a pair of quasi-degenerate modes with $m = 11$ and $l = 1$ in the ellipse with $a/b = 0.88$ (red dashed line) and 0.92 (black solid line). (f) Magnitude of rotation-induced changes in Q , $|\Delta Q|$, for the same pair of modes in (b). Black solid line and red dashed line correspond to $a/b = 0.92$ and 0.88 respectively. (g) Relative changes in the resonant frequency $\Delta k_r/k_0$ and the quality factor $\Delta Q/Q_0$ for the corresponding modes in (c,f). The vertical axis is shown in log scale to show the differences in magnitudes. 164

10.4 Evolution of far-field emission patterns of elliptical microcavities with rotation. The deformation of the ellipse is $a/b = 0.92$ in (a-c) and 0.88 (d-f). (a,d) Angular distribution of far-field intensity $I(\theta)$ (at $r = 50R$) of quasi-degenerate pairs of modes shown in Fig. 10.3 at $\Omega R/c = 0$. The blue solid (green dashed) curve represents the mode with even (odd) symmetry with respect to the x axis. (b,e) Angular distribution of far-field intensity for the CW and CCW wave components in the stationary resonances shown in (a,d). The solid (dashed) curve represents the CW (CCW) wave. The output directions of CW and CCW waves are symmetric with respect to the horizontal axis. (c,f) Angular distribution of far-field intensity $I(\theta)$ (at $r = 50R$) of the modes in (a,d) at $\Omega R/c = 10^{-4}$. The interference fringes in the output intensity patterns of stationary cavity (a,d) vanishes, as the modes evolve from standing wave to traveling wave with rotation. The emission patterns of the two traveling-wave modes at high rotation speed are not symmetric with respect to the horizontal axis. 165

10.5 Comparison of Sagnac effect in a rotating microcavity with chiral symmetry ($\eta = 1$, dashed line) and without chiral symmetry ($\eta = 0.1$, solid line). The value of $\eta|V|^2$ is kept the same. (a) (Dimensionless) frequency splitting for a pair of quasi-degenerate modes as a function of rotation frequency Ω . (b,c) Evolution of CW (thick line) and CCW (thin line) traveling-wave components in the quasi-degenerate modes with rotation. In the symmetric cavity ($\eta = 1$), at low rotation speed the eigenmodes remain standing-wave modes with equal weights of CCW and CW components, and their frequency difference is barely changed by rotation. When the rotation speed is sufficiently high, one mode evolves to a CCW traveling-wave mode, the other one to a CW traveling-wave mode; and their frequency difference starts to grow significantly with Ω . In a chiral cavity ($\eta = 0.1$), the evolution of frequency splitting with rotation is identical to the symmetric cavity. Without rotation both modes are dominated by CCW traveling waves, but one of them (b) transforms into a CW traveling wave mode at high Ω 171

10.6 A pair of quasi-degenerate modes ($\lambda = 598$ nm) in a non-rotating dielectric disk ($n = 3.0$) of asymmetric limaçon shape ($R = 591$ nm, $\epsilon_1 = 0.1$, $\epsilon_2 = 0.075$, $\delta = 1.94$). (a,b) Spatial distributions of electric field intensity (inset) and angular momentum components (main panel) inside the cavity. Both modes have more CW wave ($m < 0$) than CCW wave ($m > 0$). 172

10.7	Far-field emission intensity patterns of a pair of quasi-degenerate modes ($\lambda = 598$ nm) in a non-rotating dielectric disk ($n = 3.0$) of asymmetric limaçon shape ($R = 591$ nm, $\epsilon_1 = 0.1$, $\epsilon_2 = 0.075$, $\delta = 1.94$). (a) Angular distributions of emission intensities at a distance of $r = 50R$ from the cavity center for both modes, which have similar output directions. (b) Far-field patterns of CW (red solid line) and CCW (blue dashed line) wave components in the resonances, exhibiting distinct output directions.	173
10.8	Emission from the rotating asymmetric limaçon cavity with the same parameters as the stationary one in Fig. 10.7. (a,b) Spatial distributions of field intensities for a pair of degenerate modes, which correspond to the stationary modes in Fig. 10.7, at the normalized rotation frequency $\Omega R/c = 10^{-3}$. The intensities outside the cavity are enhanced to illustrate the main output directions of the two modes are different, even though they have the same output directions without rotation [Fig. 10.7(a)]. (c) Spatial distribution of field intensity for one of the quasi-degenerate modes in the non-rotating cavity. It is dominated by CW wave. When the cavity rotates in the CCW direction, this mode switches from CW to CCW wave, and the main output direction is changed dramatically. (d) Angular distribution of far field intensity for the pair of modes shown in (a,b) in the rotating cavity.	175

10.9 Rotation-induced change in emission pattern of the same cavity as the one in Fig. 10.8, when both quasi-degenerate modes are excited simultaneously. (a) Angular distribution of the emission intensity I_e at a distance of $r = 3R$ from the cavity center at three rotation speeds. To show the change in the emission profile, $I_e(\theta)$ is normalized ($\int_0^{2\pi} I_e(\theta)d\theta = 1$). (b) Relative changes in the main emission peak intensity (at $\theta = 0.73$) (solid squares and solid line) and in the ratio of main peak intensity over the secondary peak intensity (at $\theta = 2.79$) (crosses and dashed line) vs. the normalized rotation frequency $\Omega R/c$. Both peak intensities are integrated over a range of emission angle marked by the double-arrowed segments in (a). For comparison, relative changes of resonant frequencies, $\frac{\Delta k}{k_0}$, are plotted for circular cavities with the same area and refractive index (open circles and dotted line). The symbols represent the numerical data, and the straight lines are linear fit of the data in the log-log plot, which gives the slope. The values of the slope are (from top to bottom) 2.4×10^3 , 1.2×10^3 , and 5.7×10^{-1} respectively. The rotation-induced changes of output intensity are much larger than that of the resonance frequency. 177

- 10.10 Output sensitivity to rotation for the asymmetric limaçon cavity with varying degree of spatial chirality. The cavity parameters are the same as those in Fig. 10.6 except the value of δ . (a) Relative change of the emission intensity in the main output direction (solid squares and dashed line) as a function of spatial chirality α for the quasi-degenerate modes in Fig. 10.7. The rotation frequency is fixed at $\Omega R/c \simeq 1.5 \times 10^{-5}$. The difference between the emission patterns for CW and CCW waves in the non-rotating cavity is quantified by β (solid circles and solid line), which is also plotted against α . With increasing spatial chirality α , CW and CCW outputs become more distinct, enhancing the emission sensitivity to rotation. (b,c) Far-field patterns for CW wave (red solid line) and CCW wave (blue dashed line) in two cavities with $\delta = 0$ (b), and 2.75 (c). At $\delta = 0$, both CW and CCW waves emit predominantly in the direction close to $\theta = \pi/2$ (b), and the slight difference of their emission directions is a result of wave effects in the wavelength-scale cavity. As δ increases from 0 to π , the main emission direction of the CW wave moves towards $\theta = 0$, and the CCW wave towards $\theta = \pi$; meanwhile, the secondary emission peak, which is in the opposite direction of the main peak, grows monotonically. 179
- 10.11 The quality (Q) factor of the non-rotating asymmetric limaçon cavity with varying δ . The refractive index of the cavity is $n = 3.0$ and the radius is $R = 591$ nm. The deformation parameters are $\epsilon_1 = 0.1$ and $\epsilon_2 = 0.075$. The Q is the mean of the quasi-degenerate pair of resonances at $\lambda \simeq 598$ nm. 180

- 10.12 The minimum detectable rotation speed Ω_c as a function of the radius R of the asymmetric limaçon cavity. The refractive index of the cavity is $n = 3.0$, the deformation parameters are $\epsilon_1 = 0.1$ and $\epsilon_2 = 0.075$, $\delta = 1.94$. The wavelength is kept at $\lambda = 598$ nm. 181
- 10.13 Relative changes in the main emission peak intensity as a function of refractive index n of an asymmetric limaçon cavity with $R = 591$ nm, $\epsilon_1 = 0.1$, $\epsilon_2 = 0.075$, and $\delta = 1.94$. The resonant modes in all the cases have $\lambda/n \sim 200$ nm where λ is the vacuum wavelength and n is the refractive index of the asymmetric limaçon cavity. The rotation speed is fixed at $\Omega R/c \simeq 3 \times 10^{-5}$ 182
- 10.14 Absolute change in output intensity by rotation, ΔI_o , as a function of the cavity size R for fixed wavelength and rotation speed. The variation of ΔI_o with R depends on the values of f and g of the resonant modes. (a) When $f = 0.1$ and $g = 0.12$, ΔI_o first increases exponentially and then decreases exponentially. At the turning point R_0 , the radiation rate is equal to the absorption rate, $\gamma_r(R_0) = \gamma_a$. (b) When $f = 0.08$ and $g = 0.04$, ΔI_o keeps increasing exponentially with R , but the exponent decreases at large R . As the absorption rate reduces, the turning point R_0 moves to a larger value. In both panels, the solid line corresponds to $R_0 \sim 15\mu\text{m}$, and the dashed line to $R_0 \sim 25\mu\text{m}$ 184

Acknowledgements

Throughout my time at Yale, I have had the honor and pleasure of working with many brilliant minds and this thesis would not have been possible without their support and guidance.

First of all, I want to thank my thesis advisor, Professor Hui Cao for having faith in me and providing direction, motivation, insight and guidance. I would also like to thank Prof. Hong Tang and Prof. Paul Fluey for their valuable suggestions and advice throughout this entire journey. I thank Prof. Owen Miller for agreeing to be part of my thesis committee.

Many thanks to all my fellow group members who were a great support during this journey. Special thanks to Dr. Heeso Noh and Dr. Seng Fatt Liew for teaching and introducing me to various numerical simulation techniques and experimental methods. I would like to thank Dr. Brandon Redding for teaching me electron beam lithography as well as for teaching me how to build optical setups. I am grateful to other former group members Dr. Sebastien Popoff, Dr. Sebastian Knitter, and Dr. Yaron Bromberg for their immense support and guidance in various projects. I am also grateful to all the present group members Dr. Chia Wade Hsu, Dr. Hasan Yilmaz, Dr. Stefan Bittner, and Wen Xiong for all the stimulating discussions and ideas.

I want to extend my gratitude to all the people that I have collaborated in various research projects throughout my PhD. I want to thank Prof. Alexey Yamilov who along with being a collaborator was also a mentor and provided me with guidance and helped me to gain insight in the field of random media. My special thanks to Prof. Jan Wiersig and Prof. Li Ge for collaborating with me in the study of rotating microcavities. Prof. Li Ge was a great support and taught me a lot about microcavities. I want to thank Prof. Boris Shapiro for teaching and introducing me to the field of long range correlations in random media. I thank Prof. Douglas Stone for his valuable suggestions related to various projects. I also thank Prof. Peter Rakich and his group members for sharing their knowledge about silicon fabrication. I wish to offer my gratitude to Michael Power, James Agresta and Christopher Tillinghast for teaching me how to use the reactive ion etcher and various other instruments in the cleanroom. I am grateful to Dr. Michael Rooks for his valuable guidance related to sample fabrication. Last but not the least, I thank the department secretaries, Maria Rao and Giselle DeVito for their great support.

I feel extremely humbled and blessed for knowing and being able to work with many talented people in Becton, especially the students and post-docs working in the basement. I want to thank all of them as they all made my experience at Yale a memorable one. Finally, I would like to thank my parents for their support throughout this experience. I am also very grateful to all my family members, friends and well wishers who were extremely supportive and without whom I would not have been able to complete this journey.

Chapter 1

Introduction

1.1 Light Transport in Random Media

Multiple scattering of waves in random media is a phenomenon widely seen in nature. Examples are scattering of optical waves by biological tissues, scattering of sunlight by clouds or sound waves being scattered by water droplets in a foggy day. Because of its wide prevalence, the phenomenon of multiple scattering is studied in diverse fields ranging from adaptive optics, ocean acoustics, radio physics, condensed matter physics, seismology to biomedical imaging.

One approach to understand multiple scattering of waves such as light is to use the concept of diffusion. Diffusion describes multiple scattering as a random walk of photons and if the spatial gradient of the energy density is not too large, the flux is linearly proportional to the gradient. The approach of using the concept of diffusion is elegant as it requires knowledge of a single parameter, D , the diffusion constant, regardless of the underlying microscopical mechanisms of transport. The diffusion constant D is proportional to the transport mean free path ℓ which is the distance the wave travels inside the medium before its propagation direction is randomized by

scattering events. It is given by $D = \frac{1}{d}v\ell$, where v is the transport velocity of the photons, and $d = 2$ ($d = 3$) for two-dimensional (three-dimensional) random medium. ℓ signifies the scattering strength inside a random media and higher the scattering inside a medium, smaller is the value of ℓ . If $\ell \gg L \gg \lambda$, where L is the system length and λ is the wavelength, the waves undergo ballistic transport and mostly travel in the forward direction with few scattering events. When $L \gg \ell \gg \lambda$, the waves undergo multiple scattering and the wave transport becomes diffusive.

Although the theory of diffusion can predict the average behaviors of wave transport in a multiple scattering medium, it is however an approximation as it ignores interference effects [1-4]. When scattering is weak or correspondingly ℓ is much longer than λ , diffusion is a good approximation as interference effects are negligible. However, when scattering becomes very strong such that $\ell \sim \lambda$, interference effects start dominating the wave transport. One such example is Anderson localization where strong wave interference from different scattering events leads to suppression of wave diffusion and waves become exponentially localized within the medium [5].

Interference effects due to multiple scattering of waves were originally studied in the context of electron transport in disordered conductors. In electronic transport, such effects exist in the mesoscopic length scale which refers to a system length L at which the phase coherence length of electrons is comparable or greater than L . In such mesoscopic length scales, the quantum wave effects can dominate transport behaviors compared to classical particle-based predictions. Since such mesoscopic effects are essentially wave interference effects, similar effects also exist for classical waves such as light propagating through a scattering medium. The advantage of studying these effects with photons is that the unlike electronic samples, which have to be cooled down below 1 K to suppress electron-phonon interactions to preserve the

temporal coherence throughout the entire sample, for photons the temporal phase coherence is preserved when they are scattered by static disorder. In addition, unlike photons which do not mutually interact, Coulomb interaction between electrons is unavoidable.

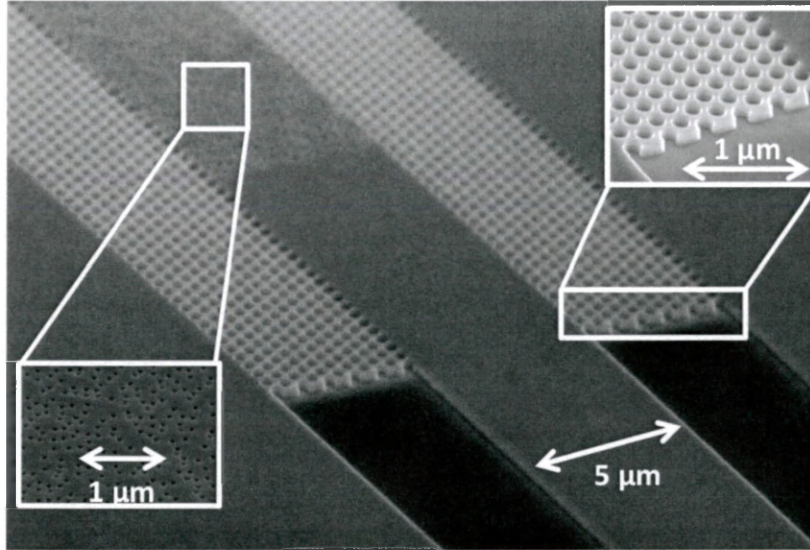


Figure 1.1: Side-view scanning electron microscope (SEM) image of a fabricated two dimensional random waveguide. The two sidewalls of the waveguide consist of triangular lattices of air holes. They possess a 2D photonic bandgap and behave like reflecting walls for light incident from all angles in the waveguide. The probe light is coupled from a silicon ridge waveguide to an empty photonic crystal waveguide, then impinging onto a random array of air holes

In this thesis, we study experimentally some of these mesoscopic or interference effects in light transport inside a scattering medium. The monochromatic coherent input light is from a CW laser source and the static scattering medium studied is a two dimensional disordered silicon waveguide with air holes as scatterers and photonic crystal sidewalls. Fig. 1.1 shows a scanning electron microscope (SEM) image of one such fabricated random waveguide. We directly probe the mesoscopic effects inside the medium and show how these effects spatially evolve. We further demonstrate that these effects can be controlled efficiently by changing the geometry of the medium and without having to change the intrinsic disorder. With the recent development of spatial light modulators, optical waves offer many advantages towards studying these

interference effects as now we can control the optical states. We take advantage of that and show that by controlling the phase of the input light state, we can control the interferences inside the scattering medium and thereby have diverse transport behaviors of light inside a scattering medium.

There are many advantages of using the two dimensional planar waveguide geometry for studying mesoscopic effects inside the random medium. The disorder strength which depends on the density and size of the air holes can be precisely controlled. The light that propagates through the random medium gets scattered both in-plane and out of the waveguide plane. The out-of-plane scattering allows us to monitor the light transport inside the medium from the vertical direction thus enabling us to directly probe the mesoscopic effects inside the random waveguide. The cross-section of the waveguides can be spatially varied which allows us to study independently the effect of geometry on the mesoscopic effects. Finally, in these two dimensional disordered waveguides, the magnitude of the interference effects is determined by its localization length given by $\xi = (\pi/2)N\ell$, where $N = 2W/(\lambda/n_e)$ is the number of propagating modes in the waveguide, W is the waveguide width, λ is the optical wavelength in vacuum, and n_e is the effective index of refraction of the random medium. Since N scales linearly with W , ξ can be easily tuned by varying the waveguide width and by changing the waveguide geometry (L, W), we can reach both the diffusion regime ($\ell < L < \xi$) and localization regime ($L > \xi$) [6, 7]. Therefore, even if scattering is relatively weak ($k\ell \gg 1$, where k is the wavenumber), the waveguide length L can easily exceed ξ so that the localization effect is strong enough [6, 7].

The two-dimensional disordered waveguides are fundamentally different from 3D random media. In a 3D random medium, there exists a quantum phase transition from localization to diffusion which depends on the disorder strength [5]. This transition was first shown by Anderson in the context of the metal-insulator transition [5], but it exists for all waves [8, 9]. For both quantum and classical waves, the character

of transport in a 3D random medium depends upon the closeness to the localization threshold of the phase transition separating diffusion and localization. Ioffe and Regel proposed that for 3D random medium, the threshold criterion for localization is given by the Ioffe-Regel criterion, $k\ell \sim 1$ [10]. Because of their reduced dimensionality, the 2D disordered waveguides on the other hand are always localized in the limit $L \rightarrow \infty$. Although in such structures there does not exist a mobility edge [11], the same is not necessary to investigate any of the mesoscopic effects studied in this thesis and the effects exist even for finite sized diffusive samples. In the following subsections, we discuss in detail the mesoscopic effects studied in this thesis.

1.1.1 Renormalization of diffusion coefficient

In a diffusive medium with negligible inelastic scattering, there exists a probability of a wave to return to the same position it has previously visited after a random walk. The wave can therefore form a closed loop and the probability of such loops happening increases with increase in scattering strength. For every such loop there always exists the time-reversed loop which yields an identical phase delay. This is shown in Fig. 1.2. Since both the loops yield the same phase delay, constructive interference of the waves from the reversed loops increases the energy density at the original position and decreases the net flux through the random medium. This gives rise to the so-called weak localization effect [12]. This is the basic mechanism which eventually suppresses the wave diffusion leading to Anderson localization. In case of Anderson localization, the return probability is close to unity and the wave becomes exponentially localized within the medium.

One theory that can describe such suppression of diffusion due to interferences between the waves traveling in the time-reversed paths is the self-consistent theory of

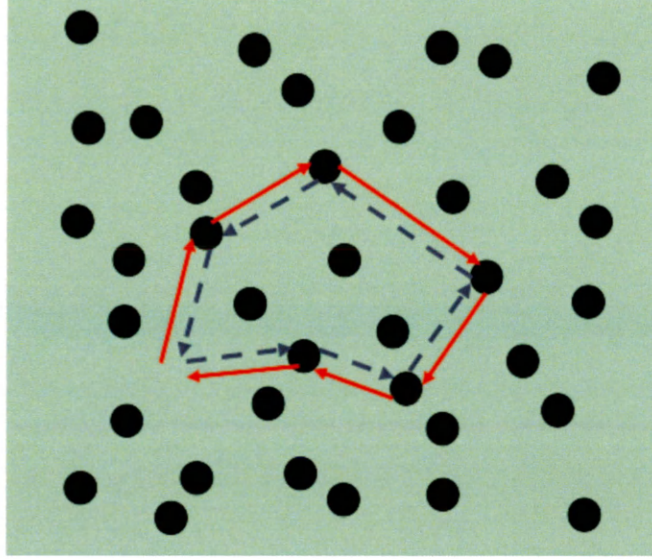


Figure 1.2: Weak localization effect. Constructive interference of the waves from the reversed loops increases the energy density at the original position and decreases the net flux through the random medium.

localization [13,14]. It can predict quantitatively not only the magnitude of the interferences inside the medium but can also predict modification of these interferences due to absorption, finite size of the medium or variation of boundary conditions. The major ingredient of the self-consistent theory is that the suppression of diffusion due to the weak localization effects is accounted for by a renormalized diffusion coefficient D where the amount of renormalization is proportional to the return probability of the waves via the looped paths.

In a random media of finite size and open boundaries, compared to an infinite medium, the return probability is reduced as the waves propagating through the longer loops may reach the boundary and escape. The magnitude of renormalization of D of any finite random media therefore depends on the system size. In addition, the chance of the waves escaping from the boundaries is higher and therefore the renormalization of D is also weaker in that region. In contrast, at the center of the medium the chances of the waves escaping are lowest and therefore the renormal-

ization of D is also largest. This implies that along with renormalization, the value of D is no longer a constant and becomes a spatially varying function [15–17]. In addition to finite size, another parameter that effects the renormalization of D is absorption. In presence of absorption, the long loops are cut as the waves can get absorbed. Absorption therefore reduces the renormalization of D . It also sets a length scale beyond which the waves will not reach the boundary, and D becomes position independent [18].

Although the self-consistent theory of localization has been used to interpret several experimental results [19–21], its key prediction of position dependent diffusion has not been experimentally demonstrated. In chapter 2 of this thesis, we will present the first direct experimental evidence of position dependent diffusion inside a random waveguide. We will present studies of random waveguides of different widths, lengths, scattering strengths and absorption and will demonstrate their effect on renormalization of the diffusion coefficient. In chapter 4, we will further demonstrate that it is possible to change local diffusion within a single random waveguide without changing the properties of the disorder by just varying the geometry of the system. By varying the geometry, we vary the renormalization of the diffusion coefficient spatially which changes the local diffusion within a single random waveguide. This is possible because position dependent diffusion is caused by the nonlocal wave interference effects that depend on the exact position of the boundary.

1.1.2 Intensity correlations in speckle patterns

When we shine a laser through a scattering medium such as a scotch tape and look at the output intensity pattern, we observe a complex intensity pattern consisting of bright and dark spots. The intensity pattern is due to the interference between scat-

tered waves and is referred as speckle pattern. Fig. 1.3 shows an example of a speckle pattern. Although the speckle pattern looks random, it is in fact not completely random and there exists intensity-intensity correlations within the pattern [2,22,23]. The speckle pattern in fact can be considered as a “signature” of the scattering medium and important information about the scattering medium can be extracted by measuring the correlations existing in the pattern. The correlations in a speckle pattern are an outcome of the non-self-averaging nature of coherent wave transport in a multiple scattering medium.

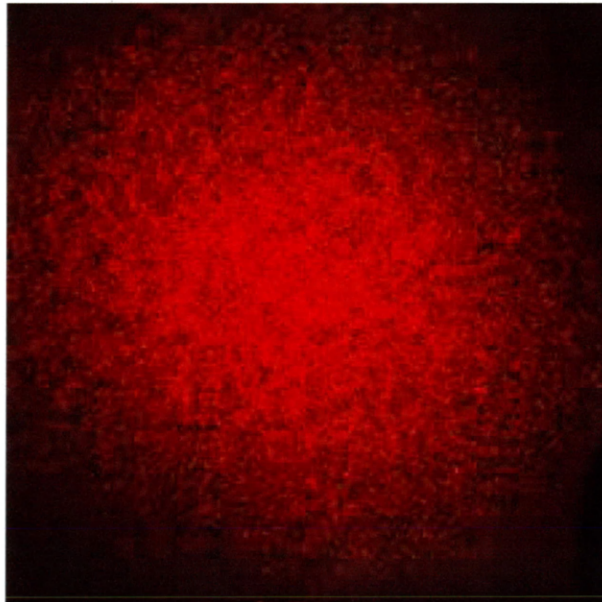


Figure 1.3: Typical output speckle pattern of laser light transmitted through a diffusive medium

The intensity-intensity correlation function C of a speckle pattern can be computed theoretically by means of a perturbative approach in which the disorder is treated as a small parameter [22]. Calculation of C requires consideration of all possible multiple-scattering paths that light can take inside a scattering medium. However, most of the correlations among the different paths reduce to zero upon ensemble averaging and only a subset of paths yield non-vanishing correlations and

contribute to C . Fig. 1.4 is a schematic showing the three possible subsets of paths that contribute to C [22,24-30]. The first and the most obvious one (Fig. 1.4(a)), consisting of independent scattering paths, gives rise to the short range correlation C_1 . It has the largest contribution to C and is of the order unity. In the spatial domain, C_1 correlation implies that the intensity within a speckle spot is correlated. In the angular domain, C_1 correlation leads to “memory effect” in a random medium which implies that a small shift in the direction of the incoming beam, results on average in a shift of the same angle in the outgoing intensity speckle pattern [22,25].

The next contribution to the correlation arises when two sets of diffusing paths cross somewhere in the middle of the sample (Fig. 1.4(b)). Because of the crossing, two paths can “exchange” information in propagating through the sample and this can lead to a long range correlation, C_2 . Since this can only happen for two sets of diffusion paths which meet once inside the system, the magnitude of C_2 correlation is less from the previous C_1 correlation by the probability of two diffusion paths going through the sample and crossing somewhere in the sample which is about $1/g$ where g is the dimensionless conductance of the scattering medium [22,25]. The long range C_2 correlation implies that two speckles spots of the transmitted speckle pattern and separated by distances much larger than ℓ are correlated and if a given speckle spot in the transmission far field is brighter than average, all the other spots also tend to be a little brighter.

The final contribution to the correlation arises when two sets of diffusing paths cross twice somewhere in the middle of the sample (Fig. 1.4(c)) [22,25]. Such crossings lead to “infinite range” correlations, C_3 . The C_3 correlations results in all pairs of input and output channels of a random media to be correlated to each other and is responsible for the universal conductance fluctuations. Since C_3 correlations are

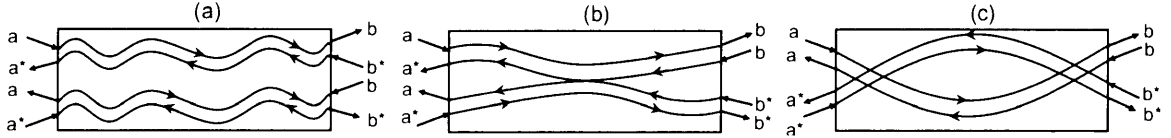


Figure 1.4: Subset of paths that contribute to the correlations in the speckle pattern. a and b correspond to input and output channels respectively and the reversed arrow signifies the time-reversed path. (a) Independent scattering paths contribute to C_1 . (b) One crossing of scattering paths lead to long-range correlations C_2 . Its magnitude is on the order of $1/g$. (c) Two crossing of scattering paths inside the random medium lead to infinite range correlations C_3 . Since it requires two crossings, therefore the magnitude is on the order of $1/g^2$.

formed due to two crossings of the diffusion paths, its magnitude is therefore on the order of $1/g^2$.

The correlations in the speckle pattern besides being of fundamental importance are also important from application point of view. With the recent advances in wavefront shaping it is now possible to focus light in a speckle spot inside or outside a random media with possible applications ranging from deep tissue imaging, laser surgery, radiation treatments to optogenetics. It has been observed that focusing light on a single speckle simultaneously brightens nearby speckles due to long range correlations resulting in reduction of the contrast of focusing. In addition, it has also been shown that the long range correlations of intensity inside the random medium determines not only focusing contrast but also energy deposition inside the sample [31–33]. Although experimentally, long range correlations of intensity have been investigated, but most measurements were performed either on transmitted or reflected light outside the random media [34–42]. It is interesting to probe the long range correlations developed inside the random media as that will indicate how the focusing contrast or energy deposition will vary spatially inside the random medium. Only one experiment in microwaves has been done until now where a detector (antenna) was inserted into the random media to measure the intensity inside the medium to calculate the

correlations [34]. In chapter 3 of this thesis, we present experimental results of direct probing of the long range correlations of multiply scattered optical waves inside a random waveguide. We demonstrate how the long range correlations evolve spatially and also vary the degree of long range correlations by modifying the g of the random waveguides. In chapter 5, we further demonstrate experimentally an effective approach of tailoring the spatial dependence of long-range intensity correlation functions inside the random system. This is accomplished by fabricating photonic random waveguides with the cross section varying along their length. The functional form of the long-range correlation is modified inside waveguides of different shapes because the crossing probability of scattering paths is affected non-uniformly in space.

1.1.3 Open and closed channels in random media

Another fascinating effect resulting from interferences of multiply scattered waves inside random media is the creation of transmission eigenchannels which are eigenvectors of the matrix $t^\dagger t$, where t is the field transmission matrix (TM). The transmission eigenchannels of lossless random media can be broadly classified as open and closed [43–51]. The open channels have transmission eigenvalues τ close to 1 and dominate the propagation of the waves through the medium, while the closed channels with τ close to 0 dominate the reflection. Since the existence of open channels allows the possibility for an optimally prepared coherent input beam to be transmitted through a lossless diffusive medium with order unity efficiency, the open channels have been extensively studied in the recent times [31, 52–57].

Besides transmission, the energy density distribution of multiply scattered waves inside a disordered medium is also determined by the spatial profiles of the transmission eigenchannels that are excited by the input light. Recently, it has been

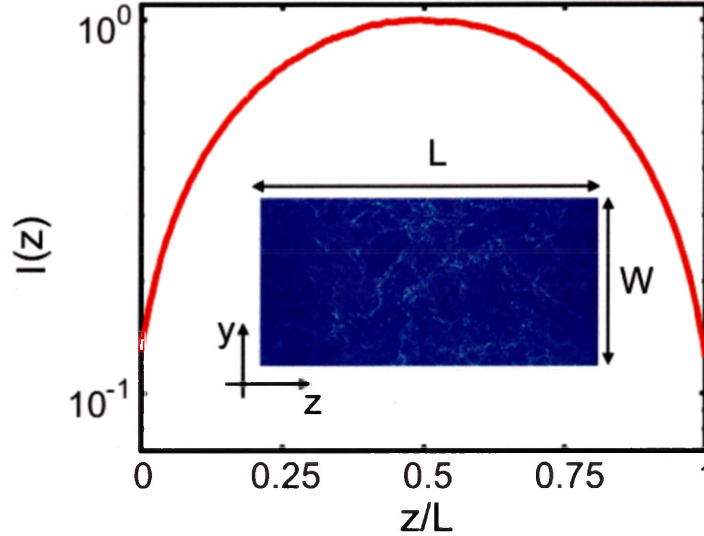


Figure 1.5: Spatial profile (cross section averaged intensity $I(z)$) of maximum transmission channel of a diffusive waveguide of $W = 5.1 \mu\text{m}$ and $L = 10.2 \mu\text{m}$. The dimensionless conductance is $g = 3$. The inset shows the 2D intensity distribution of the maximum transmission channel. The 2D intensity distribution is averaged over y to obtain the spatial profile $I(z)$.

shown that the spatial profiles of the transmission eigenchannels are distinct and the the maximum transmission channel has a universal spatial profile (inside a diffusive waveguide with uniform cross section), which cannot be changed by varying disorder strength or by adjusting the width or length of the random media [58]. Fig. 1.5 is a numerical simulation result which shows the spatial profile of the energy density of a maximum transmission channel in a diffusive waveguide. The inset shows the 2D intensity distribution inside the waveguide. In chapter 6 of this thesis we show that by varying the geometry of a random waveguide, the spatial structure of open channels can actually be significantly and deterministically altered from the universal ones. This enables tuning the depth profile of energy density inside the random medium, thus controlling how much energy is concentrated inside the sample and where it is concentrated. We show that by gradually increasing the waveguide cross-section, we can convert evanescent channels to propagating channels. In addition, perfect reflection channels can be created in certain confined geometries, which do not exist in

waveguides with uniform cross-section. We show that, unlike high-reflection channels in uniform waveguides that exhibit shallow penetration into the disordered system, a perfect reflection channel can penetrate almost through the entire system but does not transmit any light.

Recent developments in the field of adaptive wavefront shaping technique have made it possible to selectively couple input light to the open channels to enhance the total transmission or focusing through a random medium [59–63]. A major constraint that limits the efficiency of such experiments is incomplete control of the input [63–65]. In chapter 7 of this thesis, we implement the adaptive wavefront shaping technique to our on-chip random nanostructures and with a careful design of the coupling waveguide achieve a complete control of the input. Taking the advantage of the fact that open and closed channels have different spatial profiles and transmission, we demonstrate an unprecedented enhancement and control of the transmission and energy density inside the random nanostructures by selectively coupling the input light to these channels. Finally in chapter 8, we extend the adaptive wavefront shaping technique to random waveguides with inhomogeneous scattering and loss and demonstrate the power of wavefront shaping in such structures. We show that by selectively coupling input light to the open channels, regions of higher scattering and loss can be bypassed by the light propagating in such structures.

1.2 Rotating Dielectric Microcavities

In the final part of this thesis, we study numerically the effect of rotation on resonant modes of two dimensional dielectric microcavities. Unlike random media, microcavities are homogeneous structures which do not have a spatially varying refractive

index profile. The light inside such structures is confined by total internal reflection. The simplest example of a two dimensional microcavity is a circular disk. The light beam inside a circular disk propagates via consecutive reflections from the boundary. Because of the symmetry of the cavity the angle of incidence remains the same and the condition for total internal reflection is maintained at each bounce. When the frequency of the light propagating inside the cavity is such that the phase it accumulates after one round trip is equal to $2\pi n$ ($n = 1, 2, 3..$), the field reaches a steady state and forms a resonant mode of the cavity. Fig. 1.6 shows the electric field distribution of a resonant mode of a circular microcavity with closed and open boundaries.

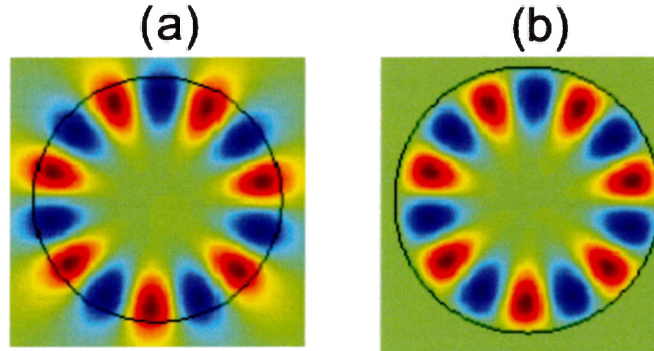


Figure 1.6: Electric field distribution of a resonant mode in a circular disk with open (a) and closed boundaries (b). The radius of the disk is 591 nm and refractive index is 3. The resonant wavelengths for (a) and (b) are $\lambda = 1131.48$ nm and $\lambda = 1009.8$ nm respectively. For the open cavity, the Q factor of the resonant mode is ~ 9000 . The black circle marks the boundary of the cavity for both (a) and (b).

Although the light inside the circular cavity is confined by total internal reflection, the confinement is not perfect. The curvature of the cavity boundary leads to an evanescent leakage and in absence of any additional loss, the leakage rate determines the finite lifetime or the quality factor (Q) of the resonant mode. For a circular cavity, as seen in Fig. 1.6, because of the rotational symmetry of the shape, the leakage of light is always isotropic. To achieve anisotropic directional emission, various asymmetric shapes of microcavities have been investigated [66–68].

Microcavities have been extensively studied for both fundamental physics as well as practical applications such as filters, modulators, switches, bio-chemical sensors and lasers [69, 70]. One application that has recently been proposed is to use microcavities to detect rotation [71–84]. Possible advantages of using microcavities as gyroscopes will be on-chip integration and miniaturization. In a rotating frame of reference, the effective refractive index of the resonant modes of a cavity gets modified and becomes a function of the rotation speed [72]. This leads to a shift of the resonant frequencies of the cavity that is proportional to the rotation speed. This frequency shift is called the Sagnac effect [71–73, 77, 79, 85–87]. The Sagnac effect in microcavities has been proposed to be used as a measure to detect rotation [71, 72]. The Sagnac effect however scales as the size of the cavity and is therefore extremely small for micron sized cavities [71, 72].

In the previous studies which investigated the Sagnac effect, cavities with only closed boundaries were investigated [72, 73, 76]. In reality the cavities have leakage due to open boundaries and therefore rotation along with the resonant frequencies can also affect the Q factor and emission intensity pattern of the resonant modes. In chapter 9 of this thesis, we present a Finite Difference Time Domain (FDTD) algorithm that we have developed to study two dimensional microcavities of any shape in a rotating frame with both closed and open boundaries. Using the FDTD Algorithm, along with the Sagnac effect, we also study the Q factor and the emission intensity pattern of resonant modes of cavities of different shapes. In chapter 10, we present the numerical results and demonstrate that emission intensity pattern as compared to Sagnac effect is much more sensitive to rotation and can therefore be a better candidate for rotation sensing.

Bibliography

- [1] A. Ishimaru, *Wave Propagation and Scattering in Random Media* (Academic Press, 1978).
- [2] *Scattering and Localization of Classical Waves in Random Media*, edited by P. Sheng (World Scientific, Singapore, 1990).
- [3] M. C. van Rossum and T. M. Nieuwenhuizen, *Rev. Mod. Phys.* **71**, 313 (1999).
- [4] E. Akkermans and G. Montambaux, *Mesoscopic Physics of Electrons and Photons* (Cambridge University Press, Cambridge, 2007).
- [5] P. W. Anderson, *Phys. Rev.* **109**, 1492 (1958).
- [6] D. J. Thouless, *Phys. Rev. Lett.* **39**, 1167 (1977).
- [7] A. Z. Genack and A. A. Chabanov, *J. Phys. A* **38**, 10465 (2005).
- [8] S. John, *Phys. Rev. Lett.* **53**, 2169 (1984).
- [9] P. W. Anderson, *Phil. Mag. Lett.* **52**, 505 (1985).
- [10] A. Ioffe and A. R. Regel, *Prog. Semicond.* **4**, 237 (1960).
- [11] E. Abraham, P. W. Anderson, D. C. Licciardello, and T. V. Ramakrishnan, *Phys. Rev. Lett.* **42**, 673 (1979).
- [12] L. Gor'kov, A. Larkin, and D. Khmel'nitskii, *JETP Lett.* **30**, 228 (1979).

- [13] D. Vollhardt and P. Wölfle, *Phys. Rev. B* **22**, 4666 (1980).
- [14] J. Kroha, C. M. Soukoulis, and P. Wölfle, *Phys. Rev. B* **47**, 11093 (1993).
- [15] B. A. van Tiggelen, A. Lagendijk, and D. S. Wiersma, *Phys. Rev. Lett.* **84**, 4333 (2000).
- [16] N. Cherroret and S. E. Skipetrov, *Phys. Rev. E* **77**, 046608 (2008).
- [17] C. Tian, *Phys. Rev. B* **77**, 064205 (2008).
- [18] A. Yamilov and B. Payne, *Optics Express* **21**, 11688 (2013).
- [19] M. Störzer, P. Gross, C. Aegerter, and G. Maret, *Phys. Rev. Lett.* **96**, 063904 (2006).
- [20] H. Hu, A. Strybulevych, J. H. Page, S. E. Skipetrov, and B. A. van Tiggelen, *Nat. Phys.* **4**, 945 (2008).
- [21] T. Sperling, W. Bührer, C. M. Aegerter, *Nat. Phot.* **7**, 48 (2013).
- [22] R. Berkovits and S. Feng, *Phys. Rep.* **238**, 135 (1994).
- [23] P. Sheng, *Introduction to Wave Scattering, Localization, and Mesoscopic Phenomena* (Academic, Boston, 1995).
- [24] M. J. Stephen and G. Cwilich, *Phys. Rev. Lett.* **59**, 285 (1987).
- [25] R. Pnini, *Correlation of Speckle in Random Media, Proceedings of the International Physics School on Waves and Imaging through Complex Media*, 391412 (1999: Cargse, France) edited by P Sebbah (Kluwer Academic Publishers, Dordrecht, 2001).
- [26] S. Feng, C. Kane, P. A. Lee, and A. D. Stone, *Phys. Rev. Lett.* **61**, 834 (1988).
- [27] S. Feng and P. A. Lee, *Science* **251**, 633 (1991).

- [28] F. Scheffold and G. Maret, *Phys. Rev. Lett.* **81**, 5800 (1998).
- [29] R Pnini and B.Shapiro,*Phys. Rev. B* **39**, 6986 (1989).
- [30] R. Pnini and B. Shapiro, *Phys. Lett. A* **157**, 265 (1991).
- [31] I. M. Vellekoop and A. P. Mosk, *Phys. Rev. Lett.* **101**, 120601 (2008).
- [32] M. Davy, Z. Shi, and A. Z. Genack, *Phys. Rev. B* **85**, 035105 (2012).
- [33] X. Cheng and A. Z. Genack, *Optics Letters* **39**, 6324 (2014).
- [34] A. Z. Genack, N. Garcia, and W. Polkosnik, *Phys. Rev. Lett.* **65**, 2129 (1990).
- [35] M. P. van Albada, J. F. de Boer, and A. Lagendijk, *Phys. Rev. Lett.* **64**, 2787 (1990).
- [36] J. F. de Boer, M. P. van Albada, and Ad Lagendijk, *Phys. Rev. B* **45**, 658 (1992).
- [37] N. Garcia, A.Z. Genack, R. Pnini, and B. Shapiro, *Phys. Lett. A* **176**, 458 (1993).
- [38] F. Scheffold, W. Härtl, G. Maret, and Egon Matijević, *Phys. Rev. B* **56**, 10942 (1997).
- [39] P. Sebbah, R. Pnini, and A. Z. Genack,*Phys. Rev. E* **62**, 7348 (2000).
- [40] P. Sebbah, B. Hu, A. Z. Genack, R. Pnini, and B. Shapiro, *Phys. Rev. Lett.* **88**, 123901 (2002).
- [41] A. A. Chabanov, N. P. Trégourès, B. A. van Tiggelen, and A. Z. Genack, *Phys. Rev. Lett.* **92**, 173901 (2004).
- [42] O. L. Muskens, T. van der Beek, and A. Lagendijk, *Phys. Rev. B* **84**, 035106 (2011).

- [43] O. N. Dorokhov, *Solid State Commun.* **44**, 915 (1982).
- [44] O. N. Dorokhov, *Solid State Commun.* **51**, 381 (1984).
- [45] J. L. Pichard and G. André, *Europhys. Lett.* **2**, 477 (1986).
- [46] Y. Imry, *Europhys. Lett.* **1**, 249 (1986).
- [47] K. A. Muttalib, J. L. Pichard, and A. D. Stone, *Phys. Rev. Lett.* **59**, 2475 (1987).
- [48] P. A. Mello, P. Pereyra, and N. Kumar, *Ann. Phys.* **181**, 290 (1988).
- [49] J. B. Pendry, A. MacKinnon, and P. J. Roberts, *Proc. Math. Phys. Sc.* **437**, 67 (1992).
- [50] Y. V. Nazarov, *Phys. Rev. Lett.* **73**, 134 (1994).
- [51] C. W. Beenakker, *Rev. Mod. Phys.* **69**, 731 (1997).
- [52] W. Choi, A. P. Mosk, Q. H. Park, and W. Choi, *Phys. Rev. B* **83**, 134207 (2011).
- [53] A. P. Mosk, A. Lagendijk, G. Lerosey, and M. Fink, *Nat. Photon.* **6**, 283 (2012).
- [54] A. Pena, A. Girschik, F. Libisch, S. Rotter, and A. A. Chabanov, *Nat. Commun.* **5** (2014).
- [55] S. F. Liew, S. M. Popoff, A. P. Mosk, W. L. Vos, and H. Cao, *Phys. Rev. B* **89**, 224202 (2014).
- [56] Z. Shi and A. Z. Genack, *Phys. Rev. Lett.* **108**, 043901 (2012).
- [57] B. Gerardin, J. Laurent, A. Derode, C. Prada, and A. Aubry, *Phys. Rev. Lett.* **113**, 173901 (2014).

- [58] M. Davy, Z. Shi, J. Park, C. Tian, and A.Z. Genack, *Nat. Commun.* **6**, 6893 (2015).
- [59] I. M. Vellekoop and A. P. Mosk, *Phys. Rev. Lett.* **101**, 120601 (2008).
- [60] W. Choi, A. P. Mosk, Q. H. Park, and W. Choi, *Phys. Rev. B* **83**, 134207 (2011).
- [61] M. Kim, Y. Choi, C. Yoon, W. Choi, J. Kim, Q. H. Park, and W. Choi, *Nat. Photon.* **6**, 581 (2012).
- [62] H. Yu, T. R. Hillman, W. Choi, J. O. Lee, M. S. Feld, R. R. Dasari, and Y. K. Park, *Phys. Rev. Lett.* **111**, 153902 (2013).
- [63] S. M. Popoff, A. Goetschy, S. F. Liew, A. D. Stone, and H. Cao, *Phys. Rev. Lett.* **112**, 133903 (2014).
- [64] A. Goetschy and A. D. Stone, *Phys. Rev. Lett.* **111**, 063901 (2013).
- [65] H. Yilmaz, W. L. Vos, and A. P. Mosk, *Biomed. Opt. Express* **4**, 1759 (2013).
- [66] J. U. Nockel and A. D. Stone, *Nature (London)* **385**, 45 (1997).
- [67] J. Wiersig and M. Hentschel, *Rev. Mod. Phys.* **100**, 033901 (2008).
- [68] H. Cao and J. Wiersig, *Rev. Mod. Phys.* **87**, 61 (2015).
- [69] *Optical Processes in Microcavities*, edited by R. K. Chang and A. J. Campillo, Advanced Series in Applied Physics (World Scientific, Singapore, 1996).
- [70] *Optical Microcavities*, edited by K. J. Vahala, Advanced Series in Applied Physics (World Scientific, Singapore, 2004).
- [71] S. Sunada and T. Harayama, *Phys. Rev. A* **74**, 021801(R) (2006).
- [72] S. Sunada and T. Harayama, *Opt. Express* **15**, 16245 (2007).

- [73] T. Harayama, S. Sunada, and T. Miyasaka, *Phys. Rev. E* **76**, 016212 (2007).
- [74] J. Scheuer, *Opt. Express* **15**, 15053 (2007).
- [75] C. Peng, Z.B. Li, and A. S. Xu, *Appl. Opt.* **46**, 4125 (2007).
- [76] S. Sunada, S. Tamura, K. Inagaki, and T. Harayama, *Phys. Rev. A* **78**, 053822 (2008).
- [77] M. Terrel, M. J. F. Digonnet, and S. Fan, *Laser Photon. Rev.* **3**, 452 (2009).
- [78] M. A. Terrel, M. J. F. Digonnet, and S. Fan, *J. Lightwave Technol.* **27**, 47 (2009).
- [79] C. Ciminelli, F. Dell’Olio, C. E. Campanella, and M. N. Armenise, *Adv. Opt. Photon.* **2**, 370 (2010).
- [80] M. J. F. Digonnet, *J. Lightwave Technol.* **29**, 3048 (2011).
- [81] C. Sorrentino, J. R. E. Toland, and C. P. Search, *Optics Express* **20**, 354 (2012).
- [82] D. Kalantarov, and C. P. Search, *J. Opt. Soc. Am. B* **30**, 377 (2013).
- [83] Li Ge, R. Sarma, and H. Cao, *Phys. Rev. A* **90**, 013809 (2014).
- [84] Li Ge, R. Sarma, and H. Cao, *Optica* **2**, 323 (2015).
- [85] E. J. Post, *Rev. Mod. Phys.* **39**, 475 (1967).
- [86] F. Aronowitz, *The Laser Gyro*, in *Laser Applications*, edited by M. Ross (Academic, New York, 1971).
- [87] W. W. Chow, J. Gea-Banacloche, L. M. Pedrotti, V. E. Sanders, W. Schleich, and M. O. Scully, *Rev. Mod. Phys.* **57**, 61 (1985).

Chapter 2

Experimental demonstration of position dependent diffusion in disordered waveguides

2.1 Introduction

¹ The concept of diffusion has been successfully applied to diverse phenomena such as heat, sound, or electron transport. It has also been used to describe light transport through multiple scattering media such as clouds, colloidal solutions, paint, and biological tissues [2–5]. For electromagnetic waves such as light or any other kinds of waves, diffusion however is an approximation as it disregards interference effects [6].

In a multiple scattering medium with negligible inelastic scattering, there exists a probability of a wave to return to the same position it has previously visited after a random walk. The wave can therefore form a closed loop and the probability of such loops happening increases with increase in scattering strength. For every such loop there always exists the time-reversed loop which yields an identical phase delay. Since

1. The results shown in this chapter have been published in ref. [1].

both the loops yield the same phase delay, constructive interference of the waves from the reversed loops increases the energy density at the original position and decreases the net flux through the random medium. This gives rise to the so-called weak localization effect [7]. This is the basic mechanism which eventually suppresses the wave diffusion leading to Anderson localization [8].

This effect of suppression of diffusion due to interferences between the waves traveling in the time-reversed paths has been accounted for by a renormalized diffusion coefficient D in the self-consistent theory of localization [9,10]. The amount of renormalization is proportional to the return probability, which is determined by the scattering strength, finite size, and position inside the random media. The dependence of return probability on finite size and spatial position comes from the fact that in an open system of finite size the longer loops may reach the boundary where waves can escape. The chance of escape of the waves is higher near the boundary resulting in lower return probability compared to the center of the medium. The renormalization of D is therefore weaker near the boundaries compared to the center of the random medium implying that the value of D is not only just renormalized but also varies spatially [11-13].

The renormalization of the diffusion coefficient also depends on absorption or dissipation. In the presence of dissipation, the long loops are cut, thus reducing the renormalization of the diffusion coefficient compared to a passive system of similar size and scattering strength. Furthermore, dissipation introduces an effective length scale beyond which the wave will not reach the boundary of the system and the diffusion coefficient becomes position independent [14].

Although self-consistent theory of localization in open random media has been used to understand several experimental results [15-17], its key prediction of position-dependent diffusion (PDD) has not been observed directly. This is partly because it is difficult to probe wave transport inside three dimensional random medium. In

this chapter, we report the first direct experimental observation of PDD by analyzing light that escapes from the two-dimensional random structures via out-of-plane scattering [18,19]. We demonstrate the effects of finite size, scattering strength and absorption on the renormalization of the diffusion coefficient D . The experimental results presented in this chapter, provides an experimental confirmation for the interpretation of localization in open random media as position-dependent suppression of diffusion, put forward in the self-consistent theory [11,12] and the supersymmetric theory [13]. Although the experiment has been performed with light, the conclusions drawn from this work directly apply to the transport of other types of waves such as acoustic waves, microwaves and de Broglie waves of electrons.

2.2 Two dimensional disordered waveguides

The random media what we study in this experiment are two dimensional disordered waveguides that are designed and fabricated in a 220 nm silicon layer on top of 3 μm buried oxide. The patterns are written by electron beam lithography and etched in an inductively coupled plasma reactive ion etcher. As shown in the scanning electron microscope (SEM) image in Fig. 2.1, the random waveguide has photonic crystal sidewalls made of a triangular lattice of air holes (lattice constant 440 nm, hole radius 154 nm). The photonic crystal sidewalls are designed to have a 2D photonic bandgap for all incident angles of TE polarized light in the wavelength range of 1450 nm - 1550 nm. The Bragg length of the photonic crystal is approximately two lattice constants. For providing optical confinement of the light in the plane of the waveguide, it is essential to have a photonic crystal that reflects light for all incident angles as the light can be scattered by the air holes in all directions. The index difference between silicon and air is not sufficient for in-plane optical confinement as the critical angle for silicon-air interface is only ~ 21 degrees. For all the random waveguide samples

studied in this chapter and also in the subsequent chapters, the parameters of the photonic crystal are kept the same. In addition, the range of the probe light for all the experiments described in this thesis is chosen such that it falls within the range of the photonic bandgap. The incident light enters the waveguide from an open

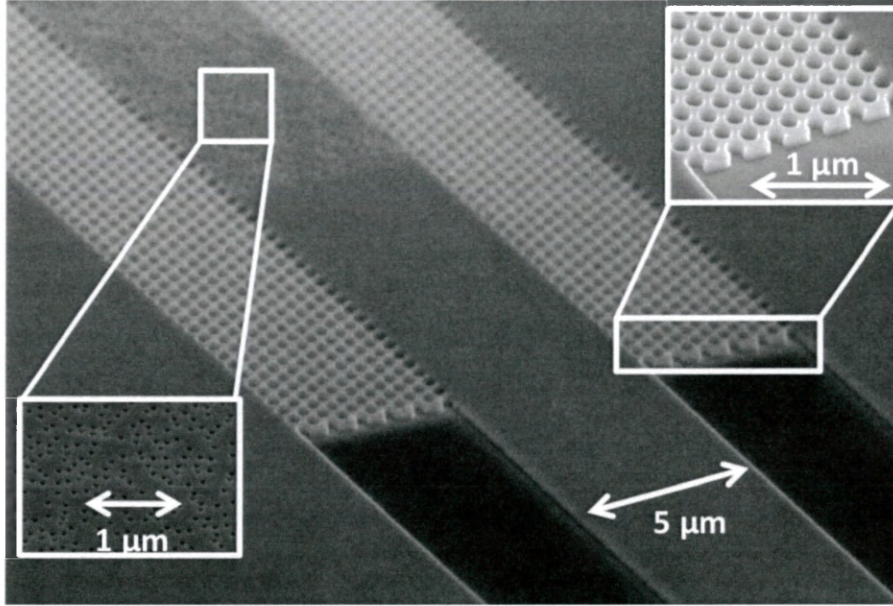


Figure 2.1: Side-view scanning electron microscope (SEM) image of a fabricated quasi-2D disordered photonic waveguide. The two sidewalls of the waveguide consist of triangular lattices of air holes (lattice constant 440 nm, hole radius 154 nm). They possess a 2D photonic bandgap and behave like reflecting walls for light incident from all angles in the waveguide. The probe light (in the wavelength range of 1500 nm - 1520 nm) is coupled from a silicon ridge waveguide to an empty photonic crystal waveguide, then impinge onto a random array of air holes (hole diameter 100 nm, and areal density 6 %) inside the waveguide.

end and is incident onto a 2D array of air holes inside the waveguide. The random pattern of air holes causes light to scatter while going through the waveguide. The transport mean free path ℓ is determined by the size and density of air holes. Light localization will occur if the length of the random array L exceeds the localization length $\xi = (\pi/2)N\ell$, where $N = 2W/(\lambda/n_e)$ is the number of propagating modes in the waveguide, W is the waveguide width, λ is the optical wavelength in vacuum, and n_e is the effective index of refraction of the random medium. Since N scales

linearly with W . ξ can be easily tuned by varying the waveguide width. Therefore, by changing the waveguide geometry (L, W), we can reach both the diffusion regime ($\ell < L < \xi$) and localization regime ($L > \xi$) [20, 21].

One important factor that we need to consider in these random waveguides is the dissipation of light. The wavelength range of the probe light is chosen such that light absorption by silicon is negligible. Hence, light scattering out of the waveguide plane by the random array of air holes is the dominant loss mechanism. Such scattering allows us to study the effect of PDD by monitoring the intensity distribution inside the system from the vertical direction. However, we need to address the question whether the out-of-plane scattering can be treated as incoherent dissipation in the calculations. In a random array of scatterers, the fields are correlated [22, 23] only within a distance on the order of one transport mean free path ℓ , and waves from different coherent regions of size $\ell \times \ell$ have uncorrelated phases. Since there are a large number of such coherence regions $\ell \times \ell$ in the random waveguide of size $W \times L$, the overall leakage may be considered incoherent and thus can be treated effectively as material absorption. The absorption strength in the random medium can be quantified by the diffusive dissipation length in the random system which is $\xi_a = \sqrt{D_0 \tau_a}$, where τ_a is the ballistic dissipation time. In the experimental structures, similar to ℓ , the magnitude of ξ_a also depends on the size and density of the air holes.

The planar waveguide geometry we use is well suited for studying the effect of PDD. It allows a precise fabrication of the desired system using lithography so that the parameters such as ℓ and ξ_a can be accurately controlled. The localization length $\xi \propto W$ can be varied by changing the waveguide width, while the diffusive dissipation length ξ_a remains fixed. This allows us to separate the effects of localization and dissipation by testing waveguides of different width. The additional confinement of light by the waveguide sidewalls makes ξ scale linearly with ℓ . Even if scattering is relatively weak ($k\ell \gg 1$, where k is the wavenumber), the waveguide length L can

easily exceed ξ so that the localization effect is strong enough to modify diffusion.

2.3 Experimental demonstration of PDD

A schematic of the experimental setup is shown in Fig. 2.2(a). Experimentally light from a wavelength-tunable laser (HP 8168F) is coupled to the silicon ridge waveguide through a single-mode polarization-maintaining lensed fiber. The transverse-electric (TE) polarization (electric field in the plane of the waveguide) of the incident light is chosen. An optical image of the spatial distribution of light intensity across the structure surface is taken by collecting light scattered out of plane using a $50\times$ objective lens (numerical aperture 0.42) and recorded by an InGaAs camera (Xenics Xeva 1.7-320) (Fig. 2.2(b)). The intensity is integrated over the cross section of the waveguide to obtain the evolution $I(z)$ along the waveguide (parallel to the z axis). For each configuration (width W , length L , transport mean free path ℓ) of the disordered waveguides, $I(z)$ is averaged over two random realizations of air holes and fifty input wavelengths equally spaced between 1500 nm and 1520 nm. The wavelength spacing is chosen to produce independent intensity distributions. Additional measures are taken to enhance the signal to noise ratio in the experiments. One major issue that is addressed is the issue of stray light. The lensed fiber which is tapered at the end to focus the laser beam, focuses the light from the laser to a spot of diameter ~ 2.5 μm at the edge of the wafer. The ridge waveguide has the same width as the random waveguide it is connected to, which varies from 5 micron to 60 micron (Fig. 2.3(a,b)). However, the height of the silicon ridge waveguide is merely 220 nm, so some of the input light does not couple into the waveguide: instead it propagates above or below the waveguide. To avoid such stray light, the ridge waveguide is tilted by 30 degrees with respect to the incident direction of the light from the fiber (approximately normal to the edge of the wafer). In addition, the ridge waveguide is made 2.5 mm long.

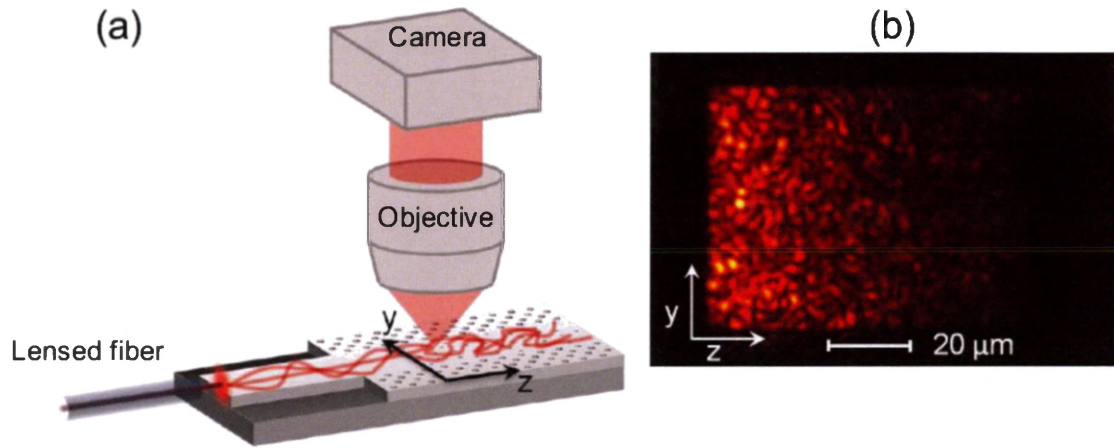


Figure 2.2: (a) A schematic of the experimental setup. A lensed fiber couples the light to the structure and another 50 \times objective lens (NA = 0.42) collects the light scattered by the air holes out of the waveguide plane and projects onto a camera. (b) Optical image of the intensity of light scattered out-of-plane from the disordered waveguide. The wavelength of the probe light is 1505 nm.

so that the random waveguide structure is far from the direct path of the stray light (Fig. 2.3(a,b)). This approach is adopted for all experimental samples studied in this thesis. The camera used in the experiment (Xenics Xeva 1.7-320) is thermo-electric

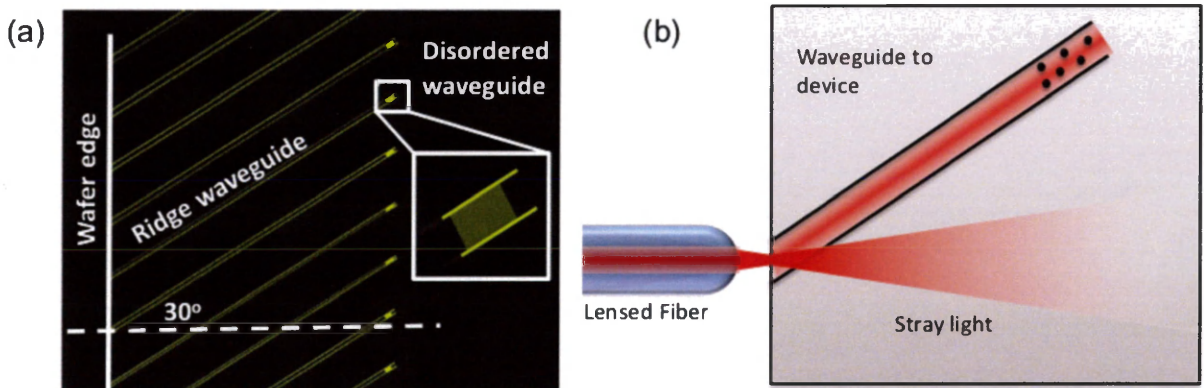


Figure 2.3: (a) Schematic of the sample layout showing the ridge waveguides coupling the probe light from the edge of the wafer to the random waveguides with photonic crystal sidewalls (b) Layout of the fabricated structures studied experimentally.

cooled in three stages to reduce the noise in the experiments. The image generated by the camera is 14 bit which enables us to record intensities with a dynamic range up to 4 orders of magnitude. In addition, measurements with different input powers

and gain settings of the camera are taken to further enhance the signal to noise ratio. The signal to noise limit is set by the background signal due to the stray light.

2.3.1 PDD in disordered waveguides of different widths

Figure 2.4(a) shows the measured $I(z)$ inside random waveguides of W varying from $60 \mu\text{m}$ to $5 \mu\text{m}$ (blue solid lines). All other parameters are kept the same. L is fixed at $80 \mu\text{m}$, the diameter of air holes is 100 nm , and the average (center-to-center) distance of adjacent holes is 390 nm . ℓ and ξ_a are obtained by fitting the $W = 60 \mu\text{m}$ sample, with the self-consistent theory of localization (red dashed line). We find that $\ell = 2.2 \mu\text{m}$ and $\xi_a = 30 \mu\text{m}$. With the parameters found from the $W=60 \mu\text{m}$ sample, the self-consistent theory of localization successfully predicts the decay for $I(z)$ in all the other samples with widths $W=40 \mu\text{m}$, $20 \mu\text{m}$, $10 \mu\text{m}$, $5 \mu\text{m}$ (red solid lines). We stress that the agreement with the experimental data is obtained without any free parameter except for the vertical intensity scale. The PDD coefficient $D(z)$ corresponding to the red curves in Fig. 2.4(a) are shown in Fig. 2.4(b). We can clearly see that the diffusion coefficient is reduced inside the sample, and its value varies along z . Farther away from the open boundary, D has a smaller value. As the width gets smaller, the reduction of $D(z)$ is enhanced due to stronger localization effects. The maximum reduction of $D(z)$ is for the $W = 5 \mu\text{m}$ waveguide and D is reduced to $0.65D_0$.

Instead of calculating the experimental parameters ℓ and ξ_a using numerical simulations based on given air hole radius, density and effective indices of the substrate, the approach of fitting the experimental data of $W = 60 \mu\text{m}$ sample to extract the experimental parameters is taken as the air cylinders of the fabricated random media do not have perfectly smooth vertical walls. In addition, the exact radius of the fabricated air cylinders of the random media may slightly vary from the target radius depending on the exposure used during the lithography process. Since the radius

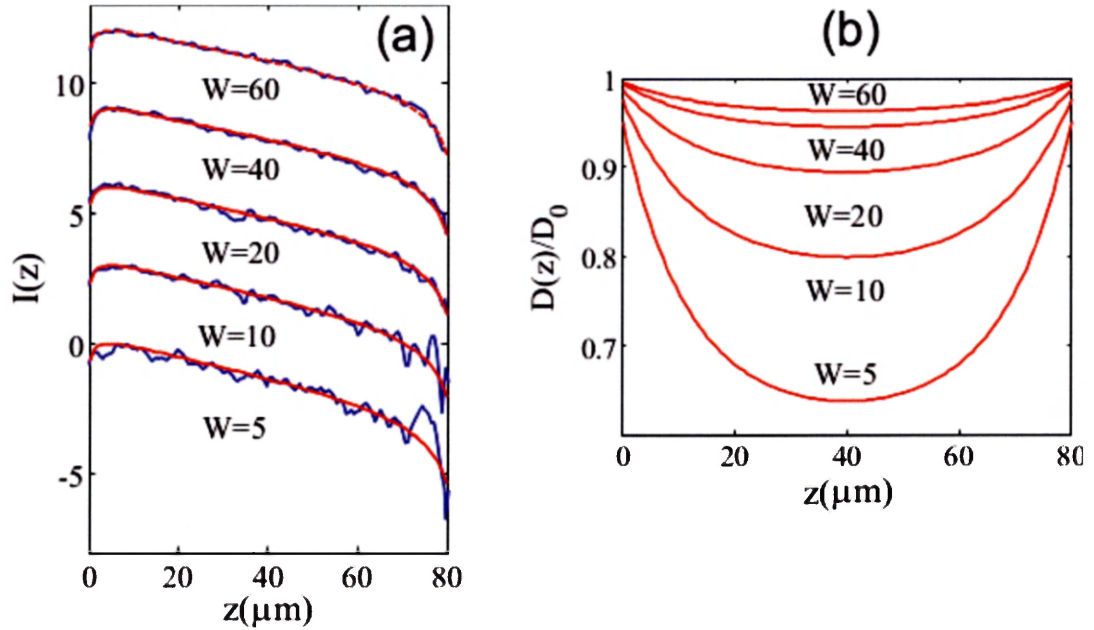


Figure 2.4: (a) Experimentally measured light intensity $I(z)$ inside random waveguides of different width W and constant length $L=80 \mu\text{m}$ (blue solid lines). The curves are vertically shifted for a clear view. The y axis is in natural log scale. $\ell=2.2 \mu\text{m}$ and $\xi_a=30 \mu\text{m}$ are found by fitting the $W=60 \mu\text{m}$ sample with the self-consistent theory of localization (red dashed line). With these parameters, the self-consistent theory of localization predicts $I(z)$ for other samples of $W=40 \mu\text{m}$, $20 \mu\text{m}$, $10 \mu\text{m}$, $5 \mu\text{m}$ (red solid curves), which agrees well with the experimental data. (b) Position-dependent diffusion coefficients for the five samples in (a).

of the air cylinder as well as smoothness of the vertical walls affects the scattering cross-section which eventually determines the disorder strength of the random media, it therefore becomes difficult to extract the parameters ℓ and ξ_a accurately using numerical simulations. Since ℓ and ξ_a essentially determines the magnitude of all the mesoscopic effects studied in this thesis, we therefore fit the experimental data numerically to extract the exact experimental parameters.

2.3.2 PDD in disordered waveguides of different scattering strengths

Next, we demonstrate the effect of dissipation on PDD. In strongly dissipative disordered waveguides, when ξ_a becomes smaller than the localization length ξ , the effect of dissipation is significant. The suppression of diffusion is weakened by the dissipation, and a plateau for the renormalized diffusion coefficient is developed inside the disordered system. This result can be understood as follows. Dissipation suppresses feedback from long propagation paths, limiting the effective size of the system to the order of diffusive dissipation length for any position that is more than one ξ_a away from the open boundary ($\xi_a < z < L - \xi_a$) [14,24]. Thus, the renormalized D reaches a constant value equal to that of an open system of dimension $\sim 2\xi_a$. In the remaining regions that are within one ξ_a to the boundary ($z < \xi_a$ and $L - z < \xi_a$), the diffusion coefficient is still position dependent due to leakage through the boundary and D increases toward the value of D_0 . We note that the extent of these regions ξ_a is much greater than the transport mean free path ℓ . The latter determines the boundary region where the diffusion approximation is not accurate even without wave interference [5].

To demonstrate this effect experimentally, we increase the density and size of the scatterers in the disordered waveguides. Larger and denser scatterers along with increased in-plane scattering also increases the out-of-plane scattering resulting in

larger dissipation. The enhanced dissipation enables us to reach the deep saturation region $\xi_a \ll L$. In this case, in the fabricated structures, the diameter of air holes is 150 nm, and the average distance between adjacent holes is 370 nm. Waveguide length L is set at 80 μm and W varies from 5 μm to 60 μm . Experimental data of measured intensity $I(z)$ inside the random waveguides are presented in Fig. 2.5(a). Using the same procedure described above, we obtain the values of $D(z)$ shown in Fig. 2.5(b). Although we observe renormalization of $D(z)$, but larger out-of-plane loss (shorter ξ_a), leads to a well-developed plateau of $D(z)$ inside all the samples.

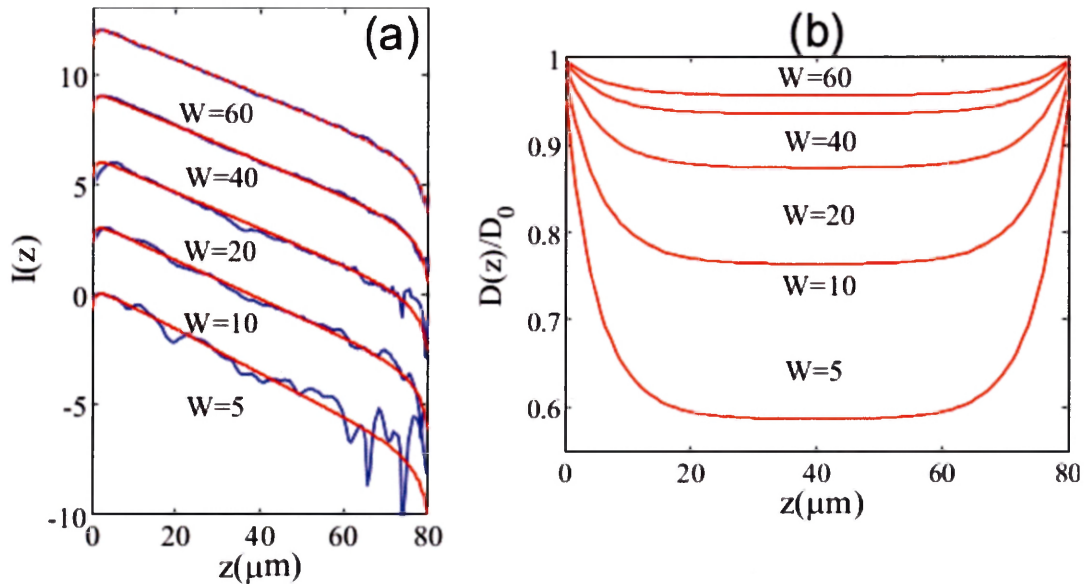


Figure 2.5: (a) Experimentally measured light intensity $I(z)$ inside random waveguides of different width W and constant length $L=80$ μm in the deep saturation regime $\xi_a \ll L$ (blue solid lines). The curves are vertically offset for a clear view. The y axis is in natural log scale. $\ell = 1.0$ μm and $\xi_a = 13$ μm are found by fitting the $W=60$ μm sample with the self-consistent theory of localization (red dashed line). These values are then used to predict $I(z)$ for other samples $W=40$ μm , 20 μm , 10 μm , 5 μm (red solid curves), which is in good agreement with the experimental data with no fitting parameters except the vertical intensity scale. (b) Diffusion coefficients $D(z)$ for all samples in (a) are saturated in the region $\xi_{a0} < z < L - \xi_a$.

2.3.3 PDD in disordered waveguides of different lengths

Finally, we demonstrate the effect of increasing the system length on PDD of dissipative disordered waveguides. We fabricate two waveguides of same widths and scattering strengths but different lengths. The size and density of the air holes are same as the samples studied in the first case (Fig. 2.4). The widths of the two waveguides are $W = 5 \mu\text{m}$ and lengths are $L = 80 \mu\text{m}$ and $160 \mu\text{m}$. Fig. 2.6(a) plots the measured $I(z)$ along with the prediction of the self-consistent theory. Fig. 2.6(b) plots the values of $D(z)$. Although we double the length of the random system L from $80 \mu\text{m}$ to $160 \mu\text{m}$, the minimal D no longer decreases, instead it saturates in the middle of the random waveguide. This behavior is attributed to dissipation which suppresses localization as seen in the previous case. As the system length L becomes much larger than the diffusive dissipation length ξ_a , $D(z)$ saturates to a constant value inside the disordered waveguide, similar to the results shown in Fig. 2.5. To summarize, we have presented the first direct experimental evidence of position-dependent suppressed diffusion of light inside random systems. We have shown that the renormalization of the diffusion coefficient D which has long been considered as a theoretical approach to account for localization corrections is an actual physical phenomenon. We demonstrated the effects of finite size, shape and scattering strength of the random system on PDD. By controlling these parameters we could manipulate the strength of wave interferences and thereby could control the degree of renormalization of D . We further showed that the presence of dissipation prevents D from approaching zero and sets a limit for the minimal value of the renormalized diffusion constant that can be reached by the localization effects.

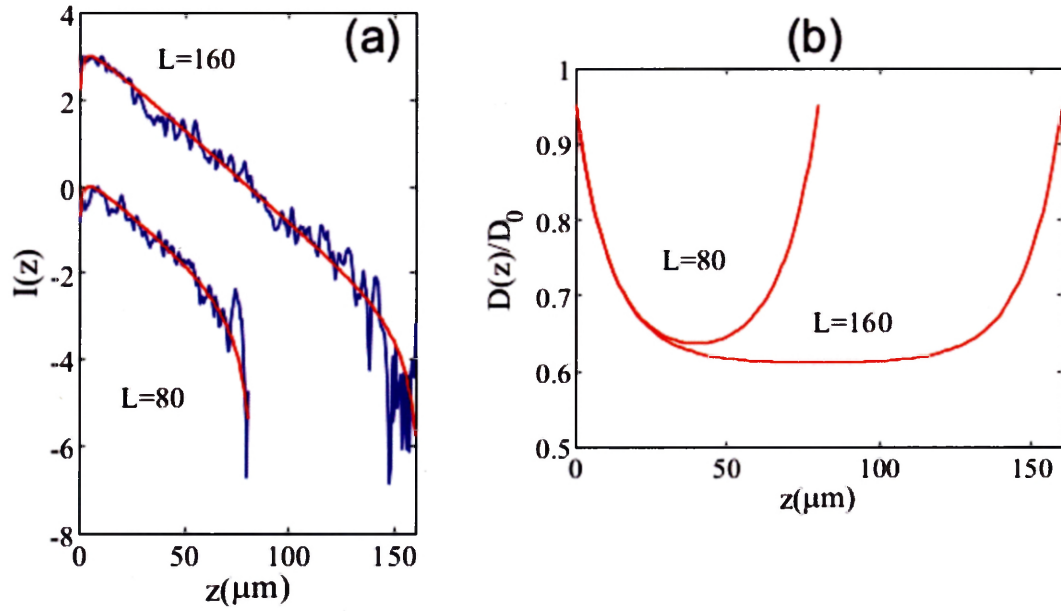


Figure 2.6: (a) Experimentally measured $I(z)$ of two waveguides with the same width $W=5 \mu\text{m}$ but different length, $L=80 \mu\text{m}$, $160 \mu\text{m}$ (blue solid curves). The y axis is in natural log scale. Red solid curves represent the prediction of the self-consistent theory of localization using the same values of ℓ and ξ_a as in Fig. 2.4(a). (b) Diffusion coefficients $D(z)$ for the two samples in (a), showing the saturation of D inside the longer sample $L=160 \mu\text{m}$.

Bibliography

- [1] A.Yamilov, R. Sarma, B. Redding, B. Payne, H. Noh, and H. Cao, *Phys. Rev. Lett.* **112**, 023904 (2014).
- [2] *Scattering and Localization of Classical Waves in Random Media*, edited by P. Sheng (World Scientific, Singapore, 1990).
- [3] A. Ishimaru, *Wave Propagation and Scattering in Random Media* (Academic Press, 1978).
- [4] M. C. van Rossum and T. M. Nieuwenhuizen, *Rev. Mod. Phys.* **71**, 313 (1999).
- [5] E. Akkermans and G. Montambaux, *Mesoscopic Physics of Electrons and Photons* (Cambridge University Press, Cambridge, 2007).
- [6] Ping Sheng, *Introduction to Wave Scattering, Localization, and Mesoscopic Phenomena* (Academic, Boston, 1995).
- [7] L. Gor'kov, A. Larkin, and D. Khmel'nitskii, *JETP Lett.* **30**, 228 (1979).
- [8] P. W. Anderson, *Phys. Rev.* **109**, 1492 (1958).
- [9] D. Vollhardt and P. Wölfle, *Phys. Rev. B* **22**, 4666 (1980).
- [10] J. Kroha, C. M. Soukoulis, and P. Wölfle, *Phys. Rev. B* **47**, 11093 (1993).
- [11] B. A. van Tiggelen, A. Lagendijk, and D. S. Wiersma, *Phys. Rev. Lett.* **84**, 4333 (2000).

- [12] N. Cherroret and S. E. Skipetrov, *Phys. Rev. E* **77**, 046608 (2008).
- [13] C. Tian, *Phys. Rev. B* **77**, 064205 (2008).
- [14] A. Yamilov and B. Payne, *Optics Express* **21**, 11688 (2013).
- [15] M. Störzer, P. Gross, C. Aegerter, and G. Maret, *Phys. Rev. Lett.* **96**, 063904 (2006).
- [16] H. Hu, A. Strybulevych, J. H. Page, S. E. Skipetrov, and B. A. van Tiggelen, *Nat. Phys.* **4**, 945 (2008).
- [17] T. Sperling, W. Bührer, C. M. Aegerter, *Nat. Phot.* **7**, 48 (2013).
- [18] J. Topolancik, B. Ilic, and F. Vollmer, *Phys. Rev. Lett.* **99**, 253901 (2007).
- [19] F. Riboli, P. Barthelemy, S. Vignolini, F. Intonti, A. D. Rossi, S. Combrie, and D. S. Wiersma, *Optics Letters* **36**, 127 (2011).
- [20] D. J. Thouless, *Phys. Rev. Lett.* **39**, 1167 (1977).
- [21] A. Z. Genack and A. A. Chabanov, *J. Phys. A* **38**, 10465 (2005).
- [22] B. Shapiro, *Phys. Rev. Lett.* **57**, 2168 (1986).
- [23] S. Feng, C. Kane, P. A. Lee, and A. D. Stone, *Phys. Rev. Lett.* **61**, 834 (1988).
- [24] P. W. Brouwer, *Phys. Rev. B* **57**, 10526 (1998).

Chapter 3

Direct probing of long-range intensity correlation inside a random waveguide

3.1 Introduction

¹ Light propagation in disordered media has been a topic of intense studies for nearly three decades [2-4]. In analogy with electronic transport in disordered metals, fundamental issues related to diffusion and localization have been addressed [5,6]. One interesting example is long-range intensity correlation [7], which characterizes mesoscopic transport of both classical and quantum waves, and reflects the closeness to the Anderson localization threshold [8]. Experimentally, correlation in time, space, frequency, angle, and polarization have been investigated, but most measurements are performed on transmitted or reflected light outside the random media [9-17]. It would be interesting to probe correlation inside the random media and to monitor how long-range correlation build up as light propagates through the random medium.

1. This chapter is primarily based on the journal article published in ref. [1].

However, it is very difficult to probe transport inside three-dimensional (3D) random media. Only in microwave experiment was a detector (antenna) inserted into the random media to measure the intensity inside [9]. As shown in chapter 2, alternatively we design and fabricate quasi-2D disordered waveguides to probe light transport inside from the third dimension. This approach will allow us to directly measure intensity correlation and fluctuations inside random structures. Furthermore, we can vary the degree of long-range intensity correlation by changing the waveguide geometry.

The intensity-intensity correlation function C consists of three terms, short-range C_1 , long-range C_2 and an infinite-range C_3 correlation. Intuitively interferences between waves scattered along independent paths give rise to C_1 , one crossing of paths generates C_2 , and two crossings cause C_3 [18,19]. The spatial correlation term C_1 decays exponentially with increasing distance and vanishes beyond the transport mean free path ℓ . C_2 also decays but much more slowly, while C_3 has a constant contribution. The long-range correlation dominates fluctuations of total transmission $T_a \equiv \sum_b T_{ab}$, where T_{ab} is the transmission from an incoming wave mode a to an outgoing mode b . The magnitude of C_2 is on the order of $1/g$, and C_3 of $1/g^2$, where $g \equiv \sum_a T_a$ is the conductance [13,20]. When $g \gg 1$, C is dominated by C_1 . To measure C_2 , the spatial distance must exceed the transport mean free path so that C_1 dies out. Alternatively, C_2 can be measured by collecting all transmitted light using an integrating sphere. This method, however, cannot be used to measure C_2 inside the sample. Instead, we integrate light intensity over the waveguide cross-section to average out the short-range fluctuation, and directly measure the long-range correlation inside the disordered planar waveguide. The conductance of the waveguide is $g = (\pi/2)N\ell/L$, where $N = 2W/(\lambda/n_c)$ is the number of propagating modes in the waveguide. L is the waveguide length, W is the waveguide width, λ is the light wavelength in vacuum, and n_c is the effective index of refraction of the random medium [21]. Hence, by decreasing W , we are able to reduce g and enhance the

magnitude of C_2 without modifying the structural disorder.

This chapter is organized as follows. First we describe the design and fabrication of 2D disordered waveguides as well as the optical measurement of intensity correlation inside the waveguide. The next section contains the calculation of long-range correlation inside the disordered waveguides and the formula for the physical quantities that are measured experimentally. The final section presents the experimental data and comparison to the theory.

3.2 2D random nanostructures

Similar to random waveguides shown in chapter 2, the 2D disordered waveguides are fabricated in a silicon-on-insulator (SOI) wafer with a 220 nm silicon layer on top of a 3 μm buried oxide [Fig. 3.1]. The patterns are written by electron beam lithography and etched in an inductively-coupled-plasma (ICP) reactive-ion-etcher (RIE). Each waveguide contains a 2D random array of air holes that scatter light. The air hole diameters are 100 nm and the average (center-to-center) distance of adjacent holes is 390 nm. The waveguide walls are made of photonic crystals (triangle lattice of air holes, the lattice constant = 440 nm, the hole radius = 154 nm) that have complete 2D bandgap for in-plane confinement of light. However, light is scattered out of plane, and this leakage allows us to observe light transport inside the disordered waveguide from the vertical direction.

The monochromatic light from a tunable CW laser source (HP 8168F) is coupled by an objective lens of numerical aperture (NA) = 0.4 into the empty waveguide. To ensure efficient confinement inside the waveguide, the light is transverse-electric (TE) polarized (electric field in the plane of the waveguide). The light is subsequently incident onto the random array of air holes inside the waveguide and undergoes multiple scattering [Fig. 3.2(a)]. The optical image of the spatial distribution of light intensity

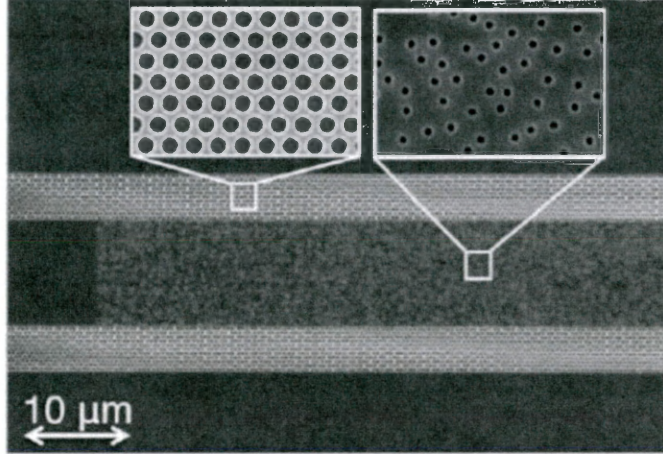


Figure 3.1: Top-view scanning electron microscope (SEM) image of a quasi-2D disordered photonic waveguide. Light is injected from the left end of the empty waveguide and incident onto the random array of air holes. The waveguide wall is made of a triangle lattice of air holes which forms a 2D photonic bandgap to confine light inside the waveguide.

across the structure is taken by collecting light scattered out of plane using a $50\times$ objective lens ($\text{NA} = 0.42$) and then recorded by an InGaAs camera (Xeva 1.7-320). The spatial resolution is limited by the NA of the objective lens, and estimated to be $\sim 2 \mu\text{m}$. Figure 3.2(b) is a typical optical image, which exhibits short-range intensity fluctuations.

The 2D intensity distribution inside the waveguide $I(y, z)$ is extracted from the optical image [Fig. 3.2(b)]. $I(y, z)$ is then integrated along the cross-section of the waveguide (y direction) to give the variation along the waveguide axis (z direction) $I(z)$. The spatial intensity correlations $\tilde{C}(z_1, z_2)$ are then computed from $I(z)$ as:

$$\tilde{C}(z_1, z_2) = \frac{\langle I(z_1)I(z_2) \rangle}{\langle I(z_1) \rangle \langle I(z_2) \rangle} - 1 \quad (3.1)$$

where $\langle \dots \rangle$ represents an ensemble average. $\tilde{C}(z_1, z_2)$ is measured for various combinations of z_1 and z_2 inside the disordered waveguides. The ensemble averaging is done over ten random configurations of air holes and 25 input wavelengths equally spaced between 1500 nm and 1510 nm. The wavelength spacing is chosen to produce

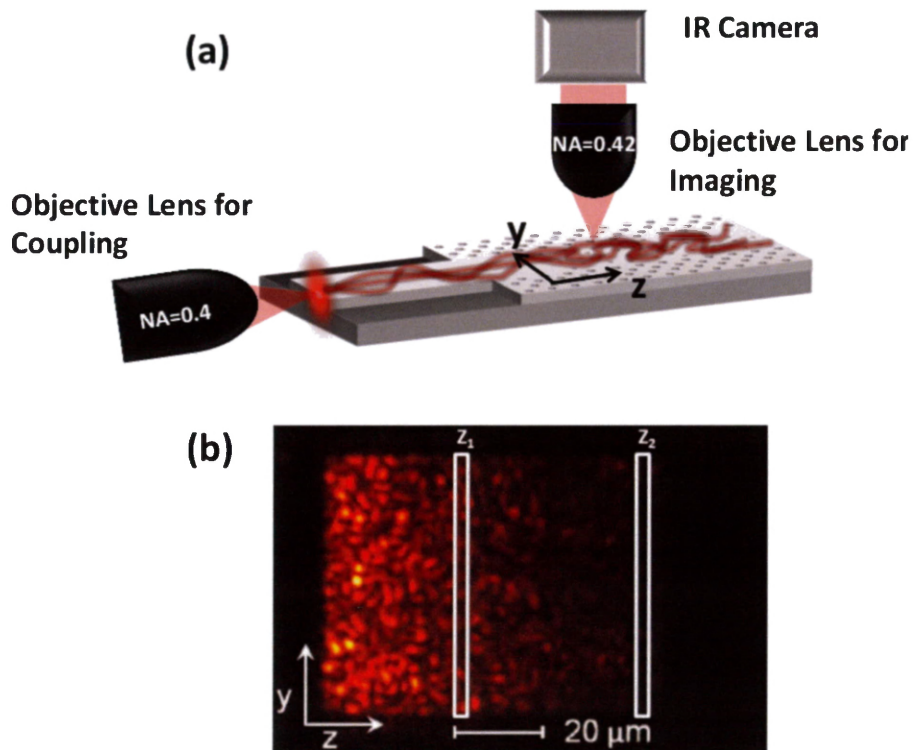


Figure 3.2: (a) A schematic of the optical measurement setup. One objective lens ($\text{NA} = 0.4$) couples the light from a tunable laser source to the waveguide, and another objective lens ($50\times$, $\text{NA} = 0.42$) collects the light scattered by the air holes out of the waveguide plane and images onto a camera. (b) An optical image of the intensity of scattered light from the disordered waveguide. The wavelength of the probe light is 1510 nm . The intensity distribution exhibits short-range fluctuations. z_1 and z_2 represent the axial positions of two cross-sections inside the disordered waveguide.

different intensity distributions. Further averaging is done by generating different intensity distributions by slightly moving the input coupling spot along the transverse direction y . Nevertheless, since long range correlation depend on the size and shape of the input beam [22], we ensure that the random array of air holes is illuminated uniformly along the y direction, so that diffusion occurs only along the z direction.

The relevant parameters for light propagation in the disordered waveguide are the transport mean free path ℓ and the diffusive dissipation length ξ_a . The transport mean free path ℓ depends on the size and density of the air holes. The dissipation mostly comes from out-of-plane scattering since the silicon absorption at the probe wavelength is negligible. As shown in chapter 2, this vertical leakage of light can be treated like absorption and described by the diffusive dissipation length $\xi_a = \sqrt{D\tau_a}$, where τ_a is the ballistic absorption time and D is the diffusion coefficient. For the disordered waveguides in Fig. 3.1, we find $\xi_a = 30 \mu\text{m}$ and $\ell = 2.2 \mu\text{m}$ by fitting the measured $I(z)$ with the diffusion equation as shown in chapter 2. The waveguide length is $80 \mu\text{m}$, and the width varies from $10 \mu\text{m}$ to $60 \mu\text{m}$. Thus the conductance g is between 1.6 and 9.9.

3.3 Theory of long-range intensity correlation

Spatial intensity correlation defined by Eq. (3.1) involve intensities integrated over the cross-section of the waveguide. Such integration suppresses the contribution from the short-range correlation C_1 so that only C_2 and C_3 remain. At the output end of the disordered waveguide ($z_1 = z_2 = L$), these two contributions reduce to the normalized variance of total transmission and the normalized variance of conductance respectively [6, 15]. C_2 and C_3 in lossy systems, such as those in our experiment, have been investigated before [8, 23]. Although the expressions for C_2 and C_3 in Ref. [8, 23] have been derived for diffusive samples ($g > 1$), it has been shown to also apply to

the localized samples ($g \leq 1$) [24]. For the disordered waveguides in our experiment, C_2 is much larger than C_3 . Thus we ignore C_3 and assume $\tilde{C} \simeq C_2$.

Next we obtain an expression for $C_2(z_1, z_2)$ which can be compared to the spatial correlation function defined in Eq. (3.1). Such expression has been derived using the Langevin approach in Refs. [11, 25-27]. For a waveguide geometry we obtain,

$$C_2(z_1, z_2) = \frac{2}{gL} \frac{\int_0^L \frac{\partial K(z_1, z')}{\partial z'} \frac{\partial K(z_2, z')}{\partial z'} \langle I(z') \rangle^2 dz'}{\langle I(z_1) \rangle \langle I(z_2) \rangle}, \quad (3.2)$$

where $K(z, z')$ is the solution of

$$\frac{\partial^2 K(z, z')}{\partial z^2} - \frac{K(z, z')}{\xi_a^2} = -\delta(z - z') \quad (3.3)$$

with boundary conditions $K(0, z') = K(L, z') = 0$. Such boundary condition neglects surface effects which can also lead to additional terms in Eq. (3.2). They are significant at $0 < z \lesssim \ell$, $L - \ell \lesssim z < L$ [27], particularly for large index mismatch between inside and outside of random medium. However, in our system of air holes in dielectric, the effective refractive index of the random medium is less than that outside. In this case surface reflections are not pronounced [4]. Hence our choice of boundary conditions is reasonable for our samples with $\ell \ll L$.

Solution to Eq. (3.3) is

$$K(z, z') = \frac{\sinh \zeta_{<} \sinh(\mathcal{L} - \zeta_{>})}{\xi_a^{-1} \sinh \mathcal{L}}, \quad (3.4)$$

where $\mathcal{L} = L/\xi_a$, $\zeta_{<} = \min[z, z']/\xi_a$ and $\zeta_{>} = \max[z, z']/\xi_a$. In the same approximation $\langle I(z) \rangle \propto \sinh(\mathcal{L} - \zeta)/\sinh \mathcal{L}$. Substituting this expression as well as Eq. (3.4) into Eq. (3.2) we get $C_2(z_1, z_2)$. The final expression is cumbersome in presence of loss, so we only list several limiting cases.

Case 1: Vanishing loss. In this case we take the limit $\xi_a \rightarrow \infty$ and get

$$C_2(z_1, z_2) = \frac{2z_1}{3gL^2} \frac{(2L - z_1)(L - z_1) + (L - z_2)^2}{L - z_1}, \quad (3.5)$$

which reduces to a well known result $C_2(L, L) = 2/3g$ at the output end.

Case 2: $z_2 = L$. This corresponds to correlating the intensity at the output surface with an intensity inside random medium. We get

$$C_2(z_1, L) = \frac{-8\zeta_1 + 4\zeta_1 \cosh 2\mathcal{L} + 3(\sinh 2\mathcal{L} - \sinh 2\zeta_1) - 3 \sinh 2(\mathcal{L} - \zeta_1)}{16 g \mathcal{L} \sinh^2 \mathcal{L}} + \frac{4(\mathcal{L} - \zeta_1) \cosh \mathcal{L} \operatorname{csch}(\mathcal{L} - \zeta_1) \sinh \zeta_1}{16 g \mathcal{L} \sinh^2 \mathcal{L}}. \quad (3.6)$$

where, $\zeta_1 = z_1/\xi_a$. In lossless random medium the above expression reduces to $C_2(z_1, L) = 2(2L - z_1)z_1/(g L^2)$, in agreement with the expression in Ref. [25, 28].

Case 3: $z_1 = z_2 \equiv z$. Under this condition we obtain the normalized variance of the cross-section integrated intensity inside the waveguide,

$$C_2(z, z) = \frac{4\zeta \cosh 2\mathcal{L} + 5 \sinh 2\mathcal{L} - \sinh 2(\mathcal{L} - 2\zeta)}{[16 g \mathcal{L} \sinh^2 \mathcal{L}]} + \frac{\operatorname{csch}^2(\mathcal{L} - \zeta)(-4(\mathcal{L} - \zeta) + \sinh 4(\mathcal{L} - \zeta)) \sinh^2 \zeta}{[16 g \mathcal{L} \sinh^2 \mathcal{L}]} - \frac{4(2\zeta + \sinh 2(\mathcal{L} - \zeta) + \sinh 2\zeta)}{[16 g \mathcal{L} \sinh^2 \mathcal{L}]}. \quad (3.7)$$

In the limit $z = L$ this quantity reduces to the normalized variance of the total transmission. In lossless medium Eq. (3.7) reduces to a compact expression $C_2(z, z) = (2z/gL)(1 - 2z/3L)$. We note that this function takes the maximum value $(9/8)C_2(L, L)$ at $z = 3L/4$, for any L .

In the following section we will compare the above theoretical predictions to the experimental data obtained for 2D disordered waveguides. Because of their reduced dimensionality, the waveguides are always localized in the $L \rightarrow \infty$ limit. The extent

of the localization effects can be controlled by varying the ratio between system length L and the localization length $\xi = (\pi/2)N\ell$. Since N scales linearly with W , ξ can be easily tuned by varying the waveguide width without changing transport mean free path and, hence, maintaining constant diffusive absorption length ξ_a . Therefore, by changing the waveguide geometry (e.g. L or W), we can reach both the diffusion regime ($\ell < L < \xi$) and the localization regime ($\xi < L$) [29]. In this thesis, we concentrate on the diffusion regime.

3.4 Comparison of experimental results and theory

Figure 3.3 shows the measured $\tilde{C}(z_1, z_2)$ for a disordered waveguide of $L = 80 \mu\text{m}$, $W = 60 \mu\text{m}$, $\xi_a = 30 \mu\text{m}$, $\ell = 2.2 \mu\text{m}$. z_1 is varied between 0 and L while z_2 is fixed at L or $L/2$. As the distance between z_1 and z_2 increases, $\tilde{C}(z_1, z_2)$ decays gradually. Even when the distance becomes much larger than the transport mean free path, the intensity correlation does not vanish. The correlation builds up further into the sample. As shown in the inset of Fig. 3.3, for a fixed distance $\Delta z = z_2 - z_1 = 10 \mu\text{m}$, \tilde{C} grows as z_2 moves from $L/4$ to L . The experimentally observed long-range correlations inside the random system agree well to the theoretical predictions represented by the solid lines in Fig. 3.3.

Next we demonstrate the ability to manipulate the long-range correlation by adjusting the the width W of the waveguide while keeping the length L and the degree of disorder the same. Figure 4 compares $\tilde{C}(z_1, z_2)$ for two disordered waveguides of length $L = 80 \mu\text{m}$ and $W = 10 \mu\text{m}$, $60 \mu\text{m}$. z_1 is moved from 0 and L while z_2 is set at L . The localization length ξ , falls from $788 \mu\text{m}$ for $W = 60 \mu\text{m}$ to $131 \mu\text{m}$ for $W = 10 \mu\text{m}$. Hence, the former is in the diffusion regime ($\ell \ll L \ll \xi$), while the latter approaches the localization regime ($L \sim \xi$). The conductance g , which is

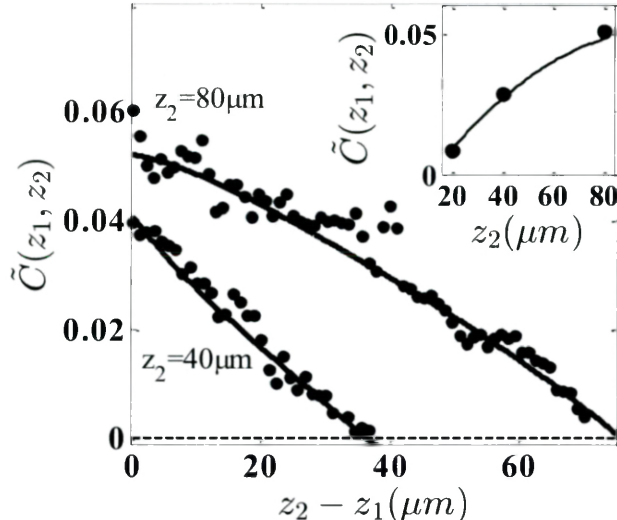


Figure 3.3: Long-range intensity correlation $\tilde{C}(z_1, z_2)$ in a disordered waveguide of $L = 80 \mu\text{m}$, $W = 60 \mu\text{m}$, $\xi_a = 30 \mu\text{m}$, $\ell = 2.2 \mu\text{m}$. z_1 is varied between 0 and L while z_2 is fixed at L or $L/2$. Solid circles are experimental data and solid lines represent the theoretical predictions of Eqs. (3.2,3.6). The dashed line corresponds to the background taken outside the waveguide. The inset shows $\tilde{C}(z_1, z_2)$ for $\Delta z = z_2 - z_1 = 10 \mu\text{m}$ and $z_2 = L, L/2, L/4$. Solid circles are experimental data and solid line represents the theoretical prediction of Eqs. (3.2). For a fixed Δz , $\tilde{C}(z_1, z_2)$ increases when moving deeper into the sample.

proportional to W , drops by a factor of 6 from 9.85 to 1.64. The probability for two scattering paths crossing, which scales as $1/g$, is thus enhanced by a factor of 6. This leads to a six-fold increase of the long-range intensity correlation, as indeed observed experimentally and in agreement with the theory in the previous section. We note that the enhancement of long-range correlation is caused purely by the change of waveguide geometry with no modification of the scattering strength.

Finally, we measured the normalized variance of the cross-section-integrated intensity $I(z)$ inside the disordered waveguides. As mentioned above, the normalized variance, $\text{var}[I(z)]/\langle I(z) \rangle^2 = \tilde{C}(z_1 = z, z_2 = z)$, becomes equal to the normalized variance of total transmission when $z = L$. Figure 3.5 shows the measured variance inside two disordered waveguides of width $W = 10 \mu\text{m}, 60 \mu\text{m}$. The other parameters are the same as in Fig. 3.4. z is changed from 0 to L . The normalized fluctuations of $I(z)$ grow with the depth of the random system. In a narrower waveguide, the fluc-

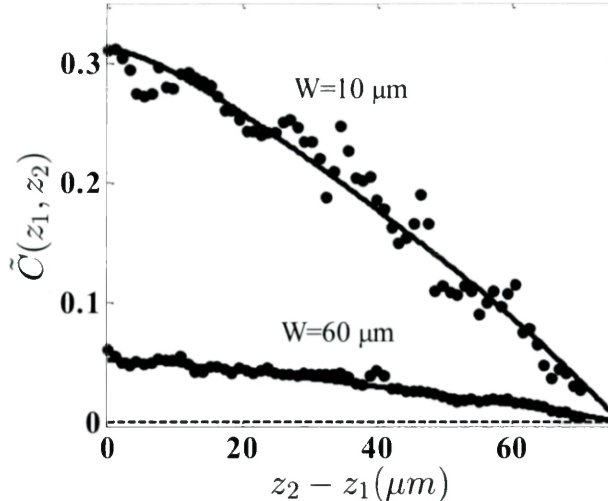


Figure 3.4: Long-range intensity correlation $\tilde{C}(z_1, z_2)$ for two waveguides with the same length $L = 80 \mu\text{m}$ and the degree of disorder ($k\ell = 26$) but different widths $W = 60 \mu\text{m}$ and $W = 10 \mu\text{m}$. z_1 is moved from 0 to L and z_2 is set at L . Solid circles are experimental data and solid lines represent the theoretical predictions of Eqs. (3.6). The dashed line corresponds to the background taken outside the waveguide. The six-times reduction of the waveguide width results in a six-fold increase in the magnitude of intensity correlation.

tuation is larger due to more pronounced localization effect (smaller conductance).

In summary, we directly measured the long-range spatial intensity correlation inside the quasi-two-dimensional disordered waveguides. Light scattered out of the waveguide plane allowed us to probe the internal transport from the third dimension. The long-range intensity correlation gradually build up as light propagates through the random system. The fluctuations of cross-section integrated intensity also grow with the depth into the disordered waveguide. Good agreements between experiment and theory are obtained. By reducing the waveguide width, we are able to enhance the long-range intensity correlation and the relative intensity fluctuations, without modifying the degree of disorder. Such use of geometry may provide a new approach for manipulation of long-range spatial correlation of light intensity inside random media as we will see in the subsequent chapters.

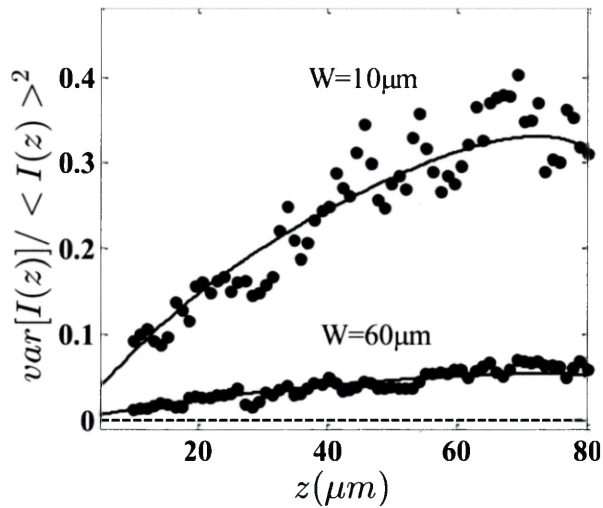


Figure 3.5: Normalized variance of the cross-section integrated intensity $I(z)$, $\text{var}[I(z)]/\langle I(z) \rangle^2$, for two waveguides with the same length $L = 80 \mu\text{m}$ and degree of disorder ($k\ell = 26$) but different widths $W = 60 \mu\text{m}$ and $W = 10 \mu\text{m}$. z is changed from 0 to L . The solid circles are experimental data and solid lines represent the theoretical predictions of Eqs. (3.7). The dashed line corresponds to the background taken outside the waveguide. The six-times reduction of the waveguide width results in a six-fold increase in the magnitude of intensity fluctuations.

Bibliography

- [1] R. Sarma, A. Yamilov, P. Neupane, B. Shapiro, and H. Cao, *Phys. Rev. B* **90**, 014203 (2014).
- [2] *Scattering and Localization of Classical Waves in Random Media*, edited by P. Sheng (World Scientific, Singapore, 1990).
- [3] R. Berkovits and S. Feng, *Phys. Rep.* **238**, 135 (1994).
- [4] M. C. van Rossum, and T. M. Nieuwenhuizen, *Rev. Mod. Phys.* **71**, 313 (1999).
- [5] P. Sheng, *Introduction to Wave Scattering, Localization, and Mesoscopic Phenomena* (Academic, Boston, 1995).
- [6] E. Akkermans and G. Montambaux, *Mesoscopic Physics of Electrons and Photons* (Cambridge University Press, Cambridge, 2007).
- [7] M. J. Stephen and G. Cwilich, *Phys. Rev. Lett.* **59**, 285 (1987).
- [8] R. Pnini, *Correlation of Speckle in Random Media, Proceedings of the International Physics School on Waves and Imaging through Complex Media*, 391412 (1999: Cargse, France) edited by P Sebbah (Kluwer Academic Publishers, Dordrecht, 2001).
- [9] A. Z. Genack, N. Garcia, and W. Polkosnik, *Phys. Rev. Lett.* **65**, 2129 (1990).

- [10] M. P. van Albada, J. F. de Boer, and A. Lagendijk, *Phys. Rev. Lett.* **64**, 2787 (1990).
- [11] J. F. de Boer, M. P. van Albada, and Ad Lagendijk, *Phys. Rev. B* **45**, 658 (1992).
- [12] N. Garcia, A.Z. Genack, R. Pnini, and B. Shapiro, *Phys. Lett. A* **176**, 458 (1993).
- [13] F. Scheffold, W. Härtl, G. Maret, and Egon Matijević, *Phys. Rev. B* **56**, 10942 (1997).
- [14] P. Sebbah, R. Pnini, and A. Z. Genack, *Phys. Rev. E* **62**, 7348 (2000).
- [15] P. Sebbah, B. Hu, A. Z. Genack, R. Pnini, and B. Shapiro, *Phys. Rev. Lett.* **88**, 123901 (2002).
- [16] A. A. Chabanov, N. P. Trégourès, B. A. van Tiggelen, and A. Z. Genack, *Phys. Rev. Lett.* **92**, 173901 (2004).
- [17] O. L. Muskens, T. van der Beek, and A. Lagendijk, *Phys. Rev. B* **84**, 035106 (2011).
- [18] S. Feng, C. Kane, P. A. Lee, and A. D. Stone, *Phys. Rev. Lett.* **61**, 834 (1988).
- [19] S. Feng and P. A. Lee, *Science* **251**, 633 (1991).
- [20] F. Scheffold and G. Maret, *Phys. Rev. Lett.* **81**, 5800 (1998).
- [21] C. P. Lapointe, P. Zakharov, F. Enderli, T. Feurer, S. E. Skipetrov, and F. Scheffold, *EPL* **105**, 34002 (2014).
- [22] R Pnini and B.Shapiro, *Phys. Rev. B* **39**, 6986 (1989).
- [23] P. W. Brouwer, *Phys. Rev. B* **57**, 10526 (1998).
- [24] A. Yamilov and H. Cao, *Phys. Rev. E* **70**, 037603 (2004).

- [25] R. Pnini and B. Shapiro, *Phys. Lett. A* **157**, 265 (1991).
- [26] A. A. Lisyansky and D. Livdan, *Phys. Lett. A* **170**, 53 (1992).
- [27] A. A. Lisyansky and D. Livdan, *Phys. Rev. B* **47**, 14157 (1993).
- [28] E. Kogan and M. Kaveh, *Phys. Rev. B* **45**, 1049 (1992).
- [29] A. Yamilov, R. Sarma, B. Redding, B. Payne, H. Noh, and H. Cao, *Phys. Rev. Lett.* **112**, 023904 (2014).

Chapter 4

Control of light diffusion inside a random waveguide using geometry

4.1 Introduction

¹ The concept of diffusion is widely used to study the propagation of light through multiple scattering media such as clouds, colloidal solutions, paint, and biological tissues [2-5]. Diffusion, however, is an approximation as it neglects wave interference effects [6]. Most of the scattered waves follow independent paths and have uncorrelated phases, so their interference is averaged out. However, a wave may return to a position it has previously visited after multiple scattering, and there always exists the time-reversed path which yields identical phase delay. Constructive interference between the waves traveling in the time-reversed paths increases the energy density at the original position, thus suppressing diffusion [7] and eventually leading to localization [8]. This effect has been accounted for by a renormalized diffusion coefficient D in the self-consistent theory of localization [9,10]. The amount of renormalization depends on the return probability, which is determined by the size of a random

1. This chapter is primarily based on the journal article published in ref. [1].

medium as well as the position inside [11–14]. In chapter 2, we demonstrated a direct observation of the position-dependent diffusion coefficient in disordered waveguides. By changing the waveguide width, we tuned the diffusion coefficient by varying the strength of wave interference. However, the width of each waveguide was kept constant, and we switched between the waveguides to control diffusion.

In this chapter, we fabricate disordered waveguides with a variable cross-section and thus achieve control of light transport in the same system. In these structures that we have designed, it is necessary to account for spatial variation of diffusion coefficient D in two dimensions (2D) due to the modulation of the waveguide width. Experimentally we fabricate a random array of air holes in a waveguide geometry on a silicon wafer, and probe light propagation inside the 2D structure from the third dimension. The measured spatial distribution of light intensity inside the disordered waveguide agrees well with the prediction of the self-consistent theory of localization [12, 14]. Instead of changing the degree of disorder, we demonstrate that the wave diffusion can be manipulated by changing the geometry (cross-section) of the random waveguide nanostructures.

The proposed approach of using geometry to control the interference effects in multiple scattering media is of both a fundamental and a practical importance. For example, coherent control of the total transmission of light through three dimensional random media was demonstrated by shaping the wave front of the input light [15]. The degree of such coherent control is limited by the number of modes that can be controlled. For 2D planar waveguide structures, the overall geometry can provide additional degree of freedom and can be used along with wavefront shaping techniques to more efficiently control the total transmission through the random media. Understanding the effect of geometry on transport through disordered media is also important to explore new functionalities of on-chip photonic devices using random media. For example, a two-dimensional disordered media has been proposed to pro-

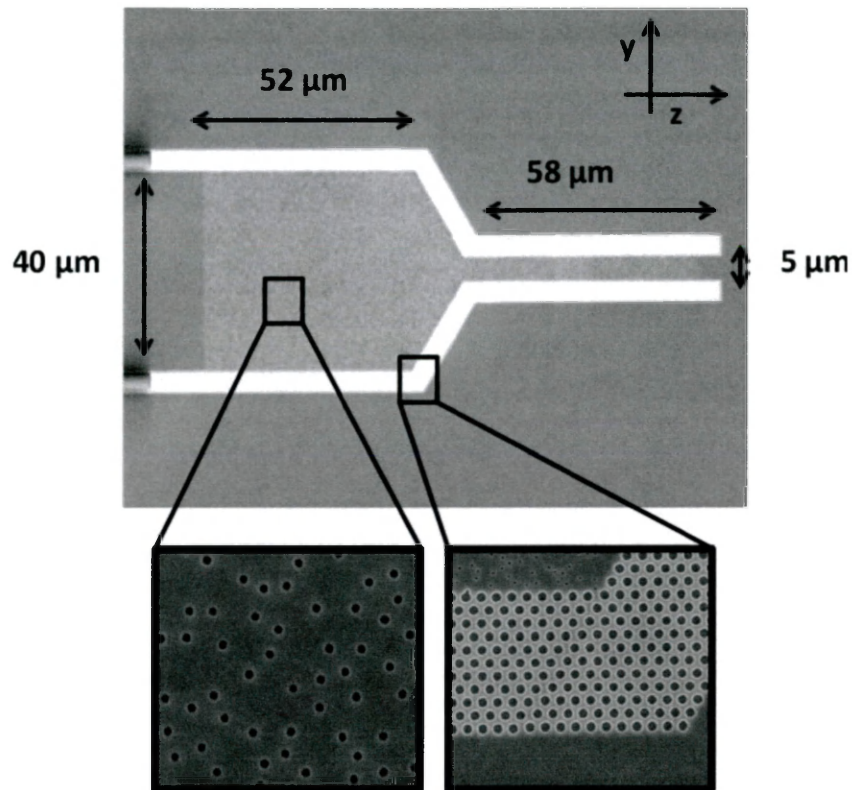


Figure 4.1: Top-view scanning electron microscope (SEM) image of a quasi-2D disordered photonic waveguide. Light is injected from the left end of the waveguide and incident onto the random array of air holes. The waveguide wall is made of a triangle lattice of air holes which forms a 2D photonic bandgap to confine light inside the waveguide. The width of the random waveguide is changed gradually from $40 \mu\text{m}$ to $5 \mu\text{m}$ through a tapered region.

vide efficient broad band coupling of light to a thin film at a wide range of incident angles for solar cell applications [16]. Our experiments demonstrate that for fixed disordered structures, coherent control of light diffusion in the plane of the film is possible simply by varying the geometry. In addition, on-chip multiple scattering media have also been recently applied to spectrometer applications [17]. Studying the effect of geometry of the random structure is important to enhance the sensitivity and resolution of such devices.

4.2 2D disordered waveguide and experimental setup

The disordered waveguides in this experiment are fabricated with a silicon-on-insulator (SOI) wafer where the thickness of the silicon layer and the buried oxide are 220 nm and 3 μm respectively. The patterns are written by electron beam lithography and etched in an inductively-coupled-plasma (ICP) reactive-ion-etcher (RIE). Figure 4.1 is a scanning electron microscope (SEM) image of a fabricated sample. The waveguide contains a 2D random array of air holes. The hole diameters are 120 nm, and the average (center-to-center) distance of neighboring holes is about 385 nm. The total length L of the random waveguide is 120 μm , and the waveguide width W is changed from $W_1 = 40 \mu\text{m}$ to $W_2 = 5 \mu\text{m}$ via a tapered region. The lengths of wider (W_1) and narrower (W_2) sections are $L_1 = 52 \mu\text{m}$ and $L_2 = 58 \mu\text{m}$ respectively. The tapered section is 10 μm long, with a tapering angle of 60 degrees. The waveguide walls are made of a triangular lattice of air holes (lattice constant 440 nm, hole radius 154 nm) that produces a complete 2D photonic bandgap.

In the optical experiment, we use a lensed fiber to couple monochromatic light (wavelength ~ 1500 nm) from a tunable CW laser source (HP 8168F) into the waveguide [Fig. 4.2(a)]. The polarization of input light is transverse-electric (TE) (electric field parallel to the waveguide plane). Light is scattered by the air holes inside the waveguide and undergoes diffusion. The waveguide walls provide in-plane confinement of the scattered light. However, some of the light is scattered out of the waveguide plane. This leakage allows us to observe light propagation inside the disordered waveguide from the vertical direction. The spatial distribution of light intensity across the waveguide is projected by a $50\times$ objective lens [numerical aperture (NA) = 0.42] onto an InGaAs camera (Xeva 1.7-320). Figure 4.2(b) shows a typical optical image, from which we extract the 2D intensity distribution inside the waveguide $I(y, z)$.

The ensemble averaging is done over three random configurations of air holes and 25 input wavelengths equally spaced between 1500 nm and 1510 nm. The wavelength

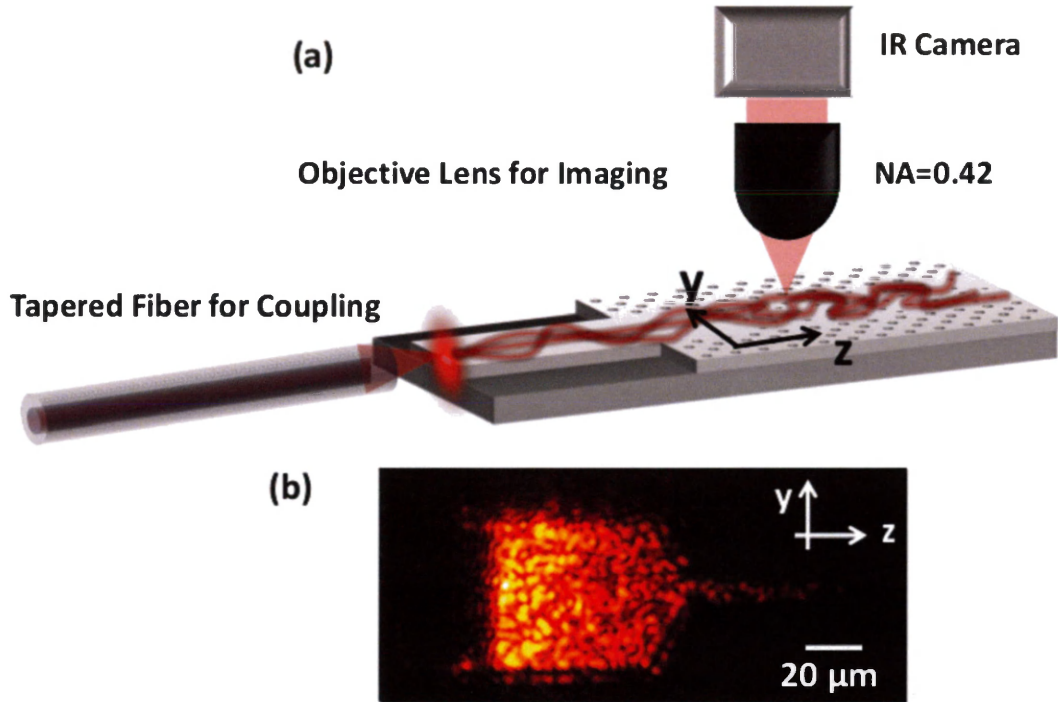


Figure 4.2: (a) A schematic of the experimental setup. A lensed fiber couples the light to the structure and another $50\times$ objective lens ($NA = 0.42$) collects the light scattered by the air holes out of the waveguide plane and projects onto a camera. (b) Optical image of the intensity of light scattered out-of-plane from the disordered waveguide. The wavelength of the probe light is 1505 nm.

spacing is chosen to produce different intensity distributions. Further averaging is done by slightly moving the input beam position along the transverse y direction. Nevertheless, the front surface of the random structures is always uniformly illuminated by the incident light.

The relevant parameters for light propagation in the disordered waveguide are the transport mean free path ℓ and the diffusive dissipation length ξ_a . The transport mean free path ℓ depends on the size and density of the air holes. The dissipation mostly comes from out-of-plane scattering as the silicon absorption at the probe wavelength is negligible. As shown in the work in chapter 2, this vertical loss of light can be treated

as dissipation (or absorption) and described by the characteristic length $\xi_a = \sqrt{D_0\tau_a}$, where τ_a is the ballistic dissipation time and D_0 is the diffusion coefficient without localization corrections.

There are three main advantages of using the planar waveguide geometry. First, it allows a precise fabrication of the designed structure so that the parameters such as the transport mean free path can be accurately controlled. Second, we can easily monitor the in-plane diffusion by collecting the out-of-the-plane scattered light. Third, the localization length ξ can be tuned by changing the waveguide width W , because $\xi = (\pi/2)N\ell$, where $N = 2W/(\lambda/n_e)$ is the number of propagating modes in the waveguide, which is proportional to W . By varying the width of a single waveguide, we adjust the strength of the localization effect along the waveguide. The localization length in the wider section of the waveguide ($W_1 = 40 \mu\text{m}$) is 8 times longer than that in the narrower section ($W_2 = 5 \mu\text{m}$). Hence, the suppression of diffusion by wave interference is enhanced approximately 8 times in the narrower section of the waveguide.

4.3 Numerical simulation of position dependent diffusion

For a quantitative description of light transport in a random waveguide of variable width, we use the self-consistent theory of localization to calculate the diffusion coefficient $D(y, z)$ inside the waveguide. The renormalization of D depends on the return probability, which is position dependent [11–13]. The maximum renormalization happens inside the random media at a location where the return probability is the highest, and the renormalization is lowest near the open boundaries of the random media. As shown below, the return probability takes the maximum value in the narrow portion of the structure and not at the geometrical center as in waveguides with a uniform

cross-section. The renormalization of the diffusion coefficient also depends on the amount of dissipation, which suppresses feedback from long propagation paths and sets an effective system size beyond which the wave will not return [18, 19].

In order to compare the experimental results with the self-consistent theory, we compute $D(y, z)$ using the commercial package COMSOL Multiphysics after setting the values of the transport mean free path ℓ and the diffusive dissipation length ξ_a . First the return probability is calculated at every point in the waveguide [14]. This is done by moving a point source throughout the structure and by calculating the light intensity at the source for each source position. This intensity is taken as the return probability which is then used to renormalize $D(y, z)$. The modified $D(y, z)$ is then used to recalculate the return probability. Several iterations of this procedure are performed until the changes in $D(y, z)$ between iterations become small enough to be negligible. Once we obtain the final value of $D(y, z)$, it is used to calculate the intensity $I(y, z)$ inside the waveguide.

The calculation of $D(y, z)$ is repeated for various combinations of ℓ and ξ_a until the calculated $I(y, z)$ matches the measured intensity distribution. The parameters that gave the best agreement for the measured experiment data are $\ell = 2.9 \mu\text{m}$ and $\xi_a = 35 \mu\text{m}$. Figure 4.3(a) plots the calculated return probability, which is greatly enhanced by the stronger transverse confinement (along the y direction) in the narrower section of the waveguide. Consequently, the renormalized diffusion coefficient $D(y, z)$, shown in Fig. 4.3(b), reaches the minimum value close to the middle of the narrower section. Note that in the tapered region, D changes not only along z , but also along y . The smaller D near the boundary is attributed to the enhancement of return probability due to reflection from the photonic crystal wall. Figure 4.3(c) shows the spatial distribution of in-plane diffusive light intensity $I(y, z)$ inside the waveguide.

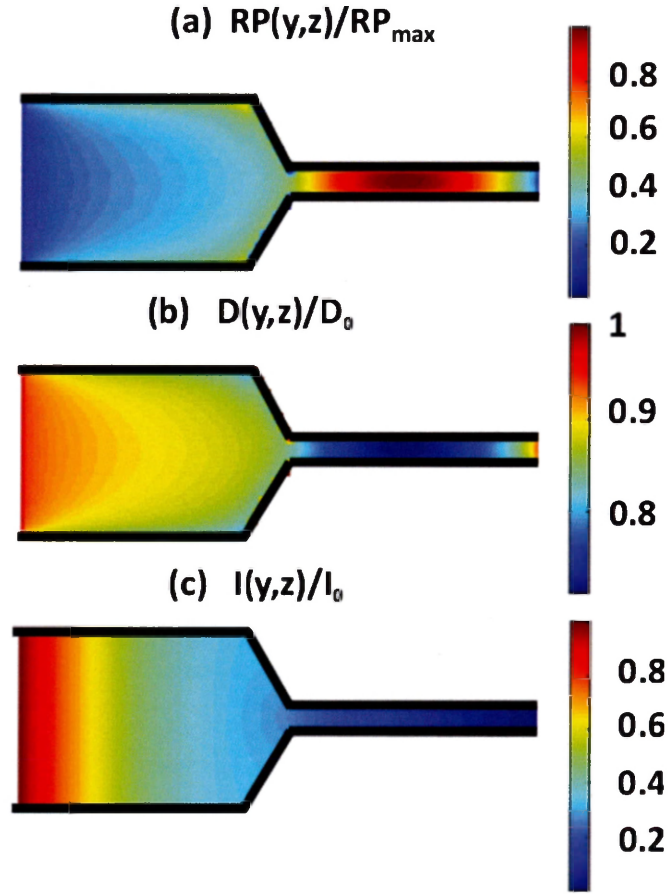


Figure 4.3: (a) Calculated return probability in the disordered waveguide shown in Fig. 4.1. $\ell = 2.9\mu\text{m}$, and $\xi_a = 35\mu\text{m}$. (b) 2D renormalized position dependent diffusion coefficient $D(y, z)/D_0$ for the same structure as in (a). (c) Intensity distribution $I(y, z)/I_0$ inside the random structure obtained from $D(y, z)/D_0$ in (b).

4.4 Comparison of experimental results and numerical simulation

From the experimentally measured $I(y, z)$, we compute the cross-section integrated intensity $I_t(z) = \int_{-W(z)/2}^{W(z)/2} I(y, z) dy$ and the cross-section averaged intensity $I_v(z) = I_t(z)/W(z)$. The former quantity is proportional to the z -component of total energy flux through the cross-section of the waveguide, while the latter quantity, $I_v(z)$, is related to the energy density.

As shown in Fig. 4.4(a), $I_t(z)$ decays more slowly with z in the wider section of the waveguide than in the narrower one. The narrowing of the waveguide width leads to a sharp drop of I_t (energy flux), as part of the diffusive light is reflected back. The dashed curve in Fig. 4.4(a) is the calculated $I_t(z)$ using self-consistent theory, which agrees well with the experimental data. The inset to Fig. 4.4(a) plots the experimental data of $I_t(\tilde{z})$ for the wider (dashed line) and narrower sections (solid line) on top of each other. The maximum intensity of both cases are normalized to 1. For the wider section, $\tilde{z} = z/L_1$ and for the narrower section, $\tilde{z} = (z - (L_1 + 10))/L_2$. We can clearly see the difference in the exponential decay (slope) of $I_t(\tilde{z})$ for the two cases. This difference can be attributed to two factors. (i) reflection from the boundary of the tapered region. (ii) enhanced localization effect in the narrower section of waveguide. Reflection only modifies the decay in the wider section of the waveguide. However, this modification is only dominant towards the end of the wider section as can be seen by a flattening of $I_t(z)$ near $z = 50$. From the experimental data (see inset of Fig. 4.4(a)), we observe that the decays of the wider and narrower section are different from the beginning (i.e. $\tilde{z} \sim 0.1$). This is a clear indication of the finite size effects or enhanced localization effect in the narrow section of the waveguide. In the absence of localization effects, the intensity decays for both sections will be similar until at least $\tilde{z} \sim 0.5$, beyond which the decay in the wider section will be slightly reduced due to

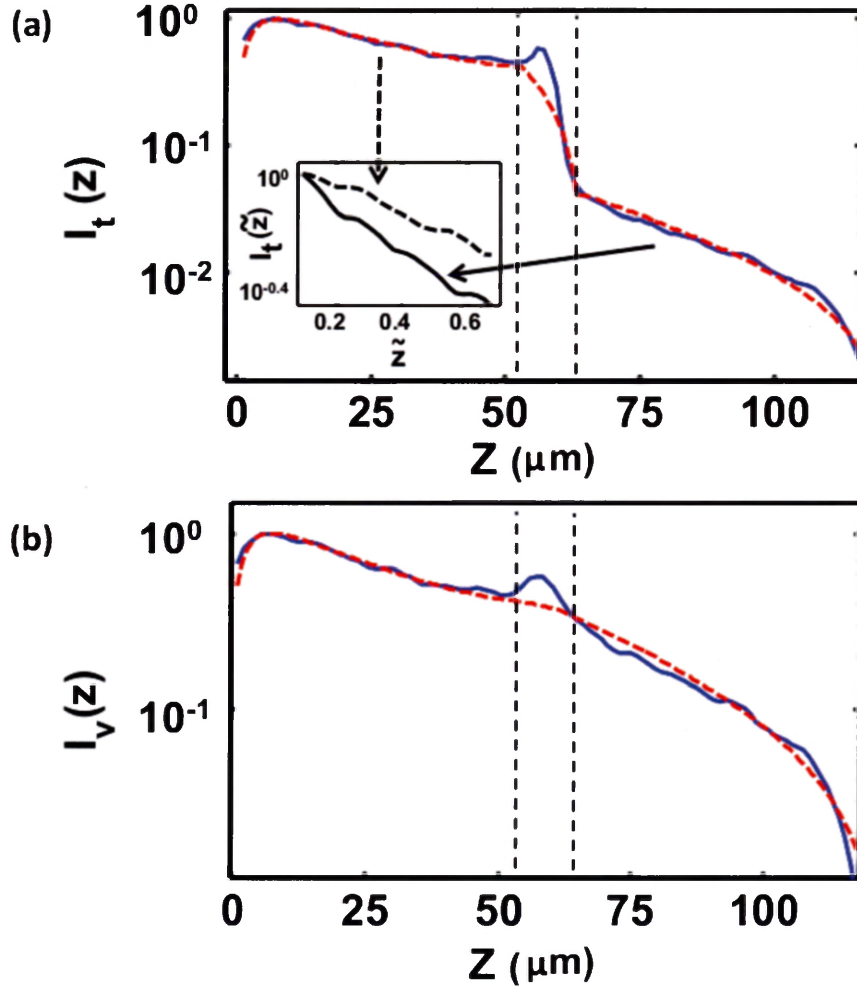


Figure 4.4: (a) Comparison of the measured cross-section integrated intensity $I_t(z)$ of the entire structure (solid blue line) to numerical calculations based on self-consistent theory (dashed red line). The inset plots the measured $I_t(\tilde{z})$ for both the wider (dashed line) and narrower (solid line) sections of the waveguide on top of each other. $\tilde{z} = z/L_1$ for the wide section, and $\tilde{z} = (z - (L_1 + 10))/L_2$ for the narrow section. In the inset, for both cases, $I_t(\tilde{z})$ is normalized to 1 to demonstrate the clear difference in the exponential decay rate (slope). (b) Measured cross-section averaged intensity $I_v(z)$ (solid blue line) in comparison with the results of self consistent theory (dashed red line). The vertical dotted lines in (a,b) marks the starting point and the end point of the tapered region.

reflection from the boundary of the tapered section.

Figure 4.4(b) plots the measured $I_r(z)$ together with the calculated one. Similar to previous case, $I_r(z)$ also decays more slowly with z in the wider section of the waveguide than in the narrower one. Again we see a good agreement except at $z \sim 60 \mu\text{m}$. The optical image [Fig. 4.2(b)] reveals that near the photonic crystal wall of the tapered section, the abrupt backward scattering leads to the formation of a standing wave, thus the intensity is enhanced compared to the diffusive prediction. The spatial extent of this effect is determined by the transport mean free path ℓ beyond which the direction of the reflected wave is randomized. The inherent inability of a diffusive description to describe transport on scales shorter than ℓ explains the deviation of the experimentally measured intensity from the theoretical prediction, as exhibited in Fig. 4.4(b) by a small bump at $z \sim 60 \mu\text{m}$.

In summary, in this chapter we demonstrated an effective way of manipulating light diffusion in a disordered photonic waveguide. Instead of changing the degree of structural disorder, we varied the waveguide geometry (its cross-section). By modulating the width in a single waveguide, we manipulated the interference of scattered light and made the diffusion coefficient vary spatially in two dimensions. We measured the intensity distribution inside the quasi-2D random structures by probing from the third dimension and the experimental results agreed well with the predictions of the self-consistent theory of localization. Although, the experiments in this work were done with light, the outlined approach to control diffusion is also applicable to other types of waves, such as acoustic waves, microwaves and the de Broglie waves of electrons.

Bibliography

- [1] R. Sarma, T. Golubev, A. Yamilov, and H. Cao. *Appl. Phys. Lett.* **105**, 041104 (2014).
- [2] *Scattering and Localization of Classical Waves in Random Media*, edited by P. Sheng (World Scientific, Singapore, 1990).
- [3] A. Ishimaru, *Wave Propagation and Scattering in Random Media* (Academic Press, 1978).
- [4] M. C. van Rossum and T. M. Nieuwenhuizen, *Rev. Mod. Phys.* **71**, 313 (1999).
- [5] E. Akkermans and G. Montambaux, *Mesoscopic Physics of Electrons and Photons* (Cambridge University Press, Cambridge, 2007).
- [6] Ping Sheng, *Introduction to Wave Scattering, Localization, and Mesoscopic Phenomena* (Academic, Boston, 1995).
- [7] L. Gor'kov, A. Larkin, and D. Khmel'nitskii, *JETP Lett.* **30**, 228 (1979).
- [8] P. W. Anderson, *Phys. Rev.* **109**, 1492 (1958).
- [9] D. Vollhardt and P. Wölfle. *Phys. Rev. B* **22**, 4666 (1980).
- [10] J. Kroha, C. M. Soukoulis, and P. Wölfle. *Phys. Rev. B* **47**, 11093 (1993).
- [11] B. A. van Tiggelen, A. Lagendijk, and D. S. Wiersma. *Phys. Rev. Lett.* **84**, 4333 (2000).

- [12] N. Cherroret and S. E. Skipetrov, *Phys. Rev. E* **77**, 046608 (2008).
- [13] C. Tian, *Phys. Rev. B* **77**, 064205 (2008).
- [14] B. Payne, A. Yamilov, and S. E. Skipetrov, *Phys. Rev. B* **82**, 024205 (2010).
- [15] S. M. Popoff, A. Goetschy, S. F. Liew, A. D. Stone, and H. Cao, *Phys. Rev. Lett.* **112**, 133903 (2014).
- [16] K. Vynck, M. Burrese, F. Riboli, D. S. Wiersma , *Nature Materials* **11**, 1017 (2012).
- [17] B. Redding, S. F. Liew, R. Sarma, and H. Cao, *Nature Photonics* **7**, 746 (2013).
- [18] P. W. Brouwer, *Phys. Rev. B* **57**, 10526 (1998).
- [19] A. Yamilov and B. Payne, *Optics Express* **21**, 11688 (2013).

Chapter 5

Using geometry to manipulate long-range correlation of light inside random media

5.1 Introduction

¹ The diffusion model has been widely utilized to describe wave propagation in disordered media, e.g., light in biological tissues, ultrasonic waves through cracked metals, and electron wavefunctions in disordered conductors. It, however, ignores the interferences of scattered waves, which lead to many prominent phenomena including Anderson localization, universal conductance fluctuations, and enhanced backscattering [2–4]. Extensive theoretical and experimental studies in the past three decades have illustrated that mesoscopic transport of both classical and quantum mechanical waves is governed by wave interference effects [5,6].

As shown in chapter 3, one important consequence of wave interferences in random media is the correlations in the fluctuations of scattered intensities [7,8]. The

1. This chapter is primarily based on the journal article published in ref. [1].

interference between waves scattered along independent paths gives rise to intensity correlation on the scale of wavelength, one crossing of paths generates long-range correlation beyond the mean free path, and two crossings leads to an infinite-range correlation [9, 10].

The non-local correlations have a direct consequence for the coherent control of light transmission through random media via wavefront shaping [11], which has advanced rapidly in the past few years due to potential applications to deep tissue imaging [12–14]. Indeed focusing light to a single speckle simultaneously brightens nearby speckles, and hence reducing the contrast of focusing [15, 16]. It has been shown that the spatial correlation of intensity inside the random medium [17–21] determines not only focusing contrast but also energy deposition into the sample [22]. Therefore, manipulating the non-local correlation can open up a new avenue to controlling waves inside random media.

Typically the magnitude of long-range correlation is small, but it becomes significant in strongly scattering media, especially when localization regime [4] is approached [9, 10, 23–26]. Experimentally long-range correlations have been observed not only in space, but also in time, frequency, angle, and polarization, but most measurements are performed on transmitted or reflected light, i.e. outside the random media [18, 20, 27–33]. Modifications of the correlations of transmitted light have been realized with two techniques: (i) varying the spot size of an incident beam on a wide disordered slab [17, 20, 25], and (ii) inserting a constriction, e.g., a pin hole, inside a random medium [29, 34]. However, the possibility of manipulating long-range correlations inside the random media has not been explored. This is at least in part due to the experimental challenge of gaining a noninvasive access to the interior of a random structure where light propagates.

In chapter 3, we showed quasi-two-dimensional random waveguides that we fabricated to probe the transport inside from the third dimension [21, 35, 36]. This

experimental setup has enabled us to monitor directly how the long-range spatial correlations build up inside diffusive systems [21]. Moreover, by reducing (or increasing) the width of a rectangular waveguide, we were able to enhance (or suppress) the crossing probabilities of scattering paths throughout the system and, therefore, to modify the magnitude of long-range correlation function. However, the functional form of correlation remained unchanged, as it is known to be universal for diffusive waveguides with uniform width [17, 19].

In this chapter, we experimentally demonstrate an effective approach of tailoring the spatial dependence of long-range intensity correlation function inside a random system. This is accomplished by fabricating photonic waveguides with cross-section varying along their length. The functional form of the long-range correlation is modified inside waveguides of different shapes because the crossing probability of scattering paths is affected non-uniformly in space. Our approach enables global optimization of non-local effects via system geometry and it is applicable to other types of waves such as acoustic waves and matter waves. Besides the fundamental importance, manipulating the long-range correlation of waves inside random systems is useful for imaging and focusing into multiply scattering media using wavefront shaping [11, 22, 37] because it affects such aspects as focusing contrast as well as energy deposition inside the medium. Therefore, our approach can provide an additional degree of freedom for controlling wave transport in scattering media.

5.2 Numerical simulations

To illustrate the effects of waveguide geometry on long-range spatial correlation, we first present numerical results of two-dimensional (2D) disordered waveguides. The structures have reflecting sidewalls which confine the light inside the waveguide where scattering and diffusion take place within $\mathbf{r} = (y, z)$ plane with z being the axial

direction. Light transport in the random waveguide is diffusive, and the non-local intensity correlation is dominated by the long-range correlation C_2 [7, 23]. The 2D correlation function $C_2(\mathbf{r}_1; \mathbf{r}_2)$ between two points $\mathbf{r}_1 = (y_1, z_1)$ and $\mathbf{r}_2 = (y_2, z_2)$ is calculated with the Langevin approach [19, 20, 38–40], similar to chapter 3.

Let us consider the simplest case of linear tapering where the waveguide width ($W(z)$) increases or decreases linearly along the waveguide axis z . Figure 5.1 shows the magnitude of C_2 , $C_2(\mathbf{r}; \mathbf{r})$, in three waveguides with $W(z)$ being constant (a), linear increasing (b) or linear decreasing (c). The 2D distributions of C_2 across the waveguides are clearly different in the three cases, revealing that the waveguide geometry has a significant impact on the growth of C_2 . In Fig. 5.1(d-f), the correlation functions $C_2(z_1; z_2)$ of the cross-section averaged intensity further illustrates the difference: in the waveguide of increasing $W(z)$, the correlation function stay nearly constant for most values of z_1 and z_2 , while in the waveguide of decreasing width, the correlation function exhibits more rapid variation over z_1 and z_2 . These results suggest that the range of spatial correlation is increased (or decreased) in the gradually expanding (or contracting) waveguide, as compared to the waveguide of constant width.

For a more quantitative comparison, the magnitude of C_2 of the cross-section averaged intensity, i.e., $C_2(z; z)$, is plotted in Fig. 5.2(a) for six waveguides of same length but different geometry. To compare the shape of these curves, the maximum value of each curve is set to 1. After the normalization, the two curves for the constant widths of 10 μm and 60 μm coincide and agree to the universal functional form. In the expanding waveguide, $C_2(z; z)$ increases more rapidly at the beginning and levels off when light diffuses deeper into the waveguide. This is attributed to the higher crossing probability of scattering paths near the front end of the waveguide where the cross section is narrower. As the width increases with z , the crossing probability is reduced, and the enhancement of C_2 is slowed down. The contracting waveguide

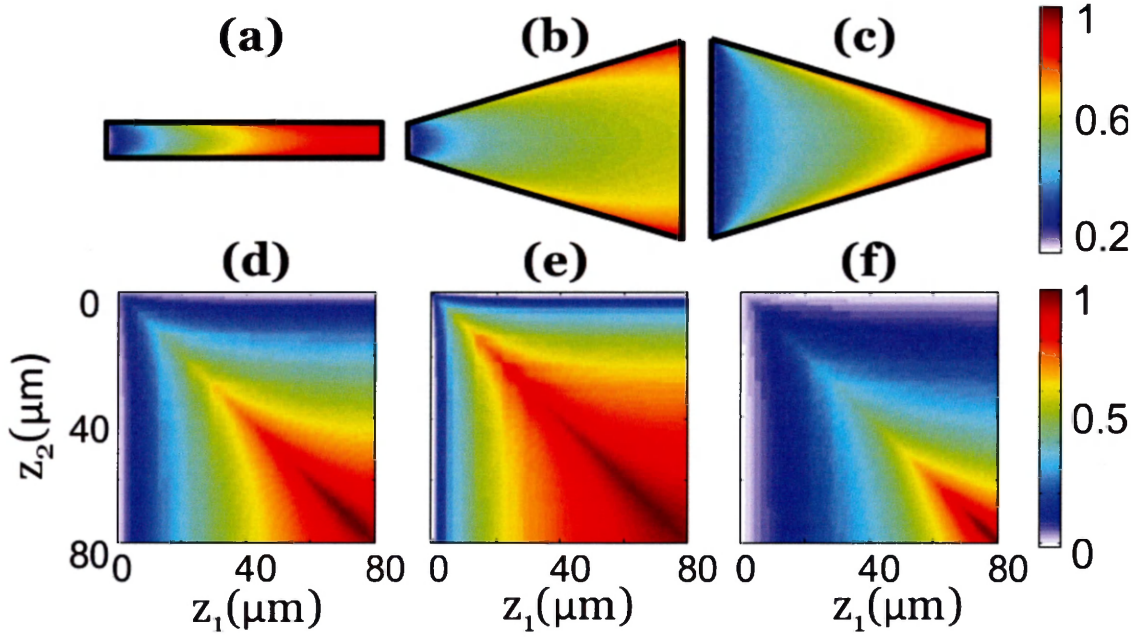


Figure 5.1: Calculated spatial long-range intensity correlation for the constant-width and two types of tapered 2D random waveguides. The waveguide length $L = 80 \mu\text{m}$, the transport mean free path $\ell = 2.2 \mu\text{m}$, and the diffusive absorption length $\xi_a = 26 \mu\text{m}$. The waveguide in (a,d) has a constant width $W = 10 \mu\text{m}$; in (b,e) $W(z)$ increases linearly from $10 \mu\text{m}$ to $60 \mu\text{m}$, while in (c,f) $W(z)$ decreases linearly from $60 \mu\text{m}$ to $10 \mu\text{m}$. (a-c) show spatial distribution of the magnitude of long-range correlation function, $C_2(\mathbf{r}; \mathbf{r})$ for three geometries. (d-f) show long-range correlation function $C_2(z_1; z_2)$ of cross-section averaged intensity for the same geometries. The maximum value is normalized to 1 for comparison. The differences in these plots reveal that the waveguide geometry has a significant impact on the magnitude and range of C_2 .

exhibits the opposite trend: the magnitude of C_2 grows more quickly in the second half of the waveguide due to enhanced crossing probability. We can further conclude that by enhancing the tapering of the waveguide cross section, the change in the spatial dependence of C_2 can be made larger.

Figure 5.2(b) plots the correlation function $C_2(z; L)$ for two points z and L of cross-section averaged intensity of the six waveguides. After normalizing the maximum value to 1, $C_2(z; L)$ for the two constant-width waveguides coincide; in the expanding waveguide the spatial range of correlation is enhanced while in the contracting waveguide the range is reduced. To be more quantitative, we find the correlation length Δz from $C_2(L - \Delta z; L) = C_2(L; L)/2$. The constant-width waveguides have the same $\Delta z = 48 \mu\text{m}$, whereas the waveguide tapered from $10 \mu\text{m}$ to $60 \mu\text{m}$ has $\Delta z = 65 \mu\text{m}$ and the one from $60 \mu\text{m}$ to $10 \mu\text{m}$ has $\Delta z = 27 \mu\text{m}$. Hence, the correlation length inside the random waveguide can be tuned by geometry.

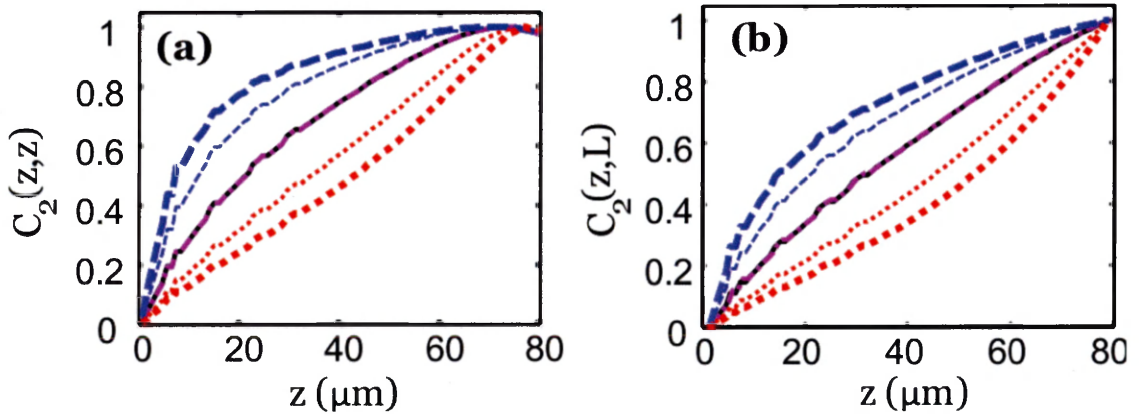


Figure 5.2: Comparison of calculated long-range correlation in six waveguides with different degrees of taper: two with constant widths of $10 \mu\text{m}$ (solid black line) and $60 \mu\text{m}$ (dash-dotted magenta line); two with width linearly increasing from $10 \mu\text{m}$ (thick dashed blue line) or $20 \mu\text{m}$ (thin dashed blue line) to $60 \mu\text{m}$; and two with width linearly decreasing from $60 \mu\text{m}$ to $10 \mu\text{m}$ (thick dotted red line) or $20 \mu\text{m}$ (thin dotted red line). Other parameters are the same as in Fig. 5.1. Both $C_2(z; z)$ (a) and $C_2(z; L)$ (b) clearly demonstrate that while the functional form of long-range correlation is universal for uniform waveguides, it is strongly modified in the tapered ones.

An intuitive model has been developed in the previous studies of expanding dif-

fusive beams inside absorption less disordered slabs [25,29]. The long-range intensity correlation function for the transmitted light is determined by the crossing probability of scattering paths inside the slab, which is on the order of $1/g$, where g is the dimensionless conductance. To account for the effect of diffuse spreading of the intensity, $1/g$ is obtained by integrating over short sections of increasing width at different depths inside the slab. While this model can predict the long-range correlations of transmitted light, it fails inside the random medium. This is because the magnitude of long-range intensity correlation C_2 at depth z is not determined simply by the conductance of the waveguide section from 0 to z , which only takes into account the crossing probability of scattering paths between 0 and z . The diffusive waves that pass through z may return to it after multiple scattering and crossing in the section between z and L , thus contributing to C_2 at z as well. The change in the functional form of the long-range correlation function therefore cannot be explained by the effective conductance model. This model, which was developed in the previous studies of expanding diffusive beams inside disordered slabs [25,29], can only predict the correlations of light outside random media.

To demonstrate this, let us consider a simplest example of a diffusive waveguide with constant width and no absorption. Since the dimensionless conductance $g(z)$ decreases linearly with depth z , $C_2(z; z) \approx 1/g(z) \approx z$ would increase linearly with z . Figure 5.3(a) plots the $C_2(z; z)$ calculated using the Langevin approach [39,40], which displays a nonlinear increase with z . We further compare the $C_2(z; z)$ inside tapered waveguides to the prediction by the effective conductance model. As shown in Fig. 5.3(b, c), indeed the calculated C_2 inside the random waveguide of either constant or varying cross-section differ not just quantitatively but also qualitatively from the prediction of the effective conductance model. For example, the effective conductance model predicts a monotonic increase of $C_2(z; z)$ with z , the actual $C_2(z; z)$ in the tapered waveguides decreases with z near the rear end. The significant differences

confirm that the changes in the functional form of the C_2 inside the random system cannot be explained by the z dependence of g .

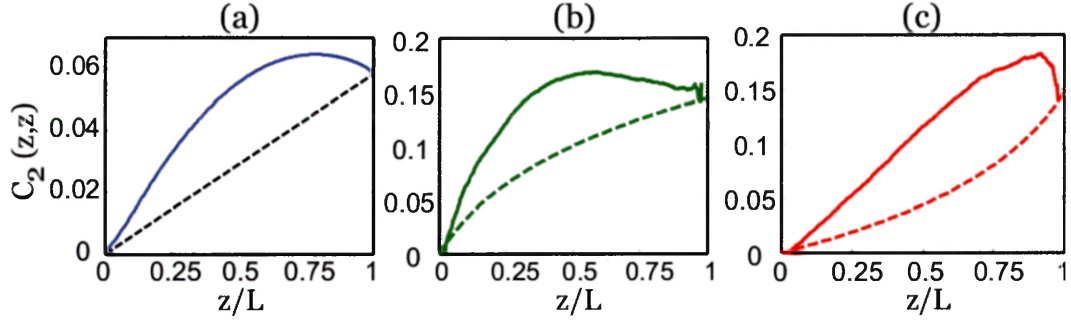


Figure 5.3: Comparison of calculated long-range correlation function $C_2(z; z)$ for the cross-section averaged intensity inside passive diffusive waveguides (solid line) with same scattering strength as Fig. 5.1 to the prediction of the effective conductance model (dashed line). (a) The waveguide has constant width $W = 60 \mu\text{m}$. (b) The waveguide width increases linearly from $10 \mu\text{m}$ to $60 \mu\text{m}$. (c) The waveguide width decreases linearly from $60 \mu\text{m}$ to $10 \mu\text{m}$. All three waveguides have the same length $L = 80 \mu\text{m}$. The effective conductance model fails to predict $C_2(z; z)$ inside all three waveguides.

5.3 Experimental results and comparison to numerical simulations

In this section we present the experimental results and compare them to numerical simulations. We fabricate 2D disordered waveguides of various shapes in a silicon-on-insulator (SOI) wafer with a 220 nm silicon layer on top of a $3 \mu\text{m}$ buried oxide. The structures are patterned by electron beam lithography and etched in an inductively-coupled-plasma (ICP) reactive-ion-etcher (RIE). Each waveguide contains a 2D random array of air holes that scatter light. The air hole diameters are 100 nm and the average (center-to-center) distance of adjacent holes is 390 nm. The waveguide walls are made of triangle lattice of air holes (the lattice constant of 440 nm, the hole radius of 154 nm) that has a complete 2D photonic bandgap for the in-plane confinement of light.

The experimental setup used is same as the one shown in the chapter 3. The monochromatic beam from a tunable CW laser source (HP 8168F) is coupled into the empty waveguide by an objective lens of numerical aperture (NA) 0.4. The light is transverse-electric (TE) polarized, i.e., the electric field is in the plane of the waveguide. After propagating through the empty waveguide, the light is incident onto the random array of air holes inside the waveguide. The front end of the random array is uniformly illuminated along the y direction. The light undergoes multiple scattering in the 2D plane of waveguide. Some of the light is scattered out of plane and imaged by a $50\times$ objective lens (NA = 0.42) onto an InGaAs camera (Xeva 1.7-320).

From the optical image, the spatial distribution of light intensity inside the waveguide $I(y, z)$ is extracted. To smooth out the short-range fluctuations, $I(y, z)$ is averaged over the cross-section of the waveguide to obtain the cross-section-averaged intensity $I_v(z)$. The spatial intensity correlation $C(z_1, z_2)$ is then computed from $I_v(z)$. With the short-range contribution removed, $C(z_1, z_2)$ is dominated by long-range correlation C_2 . The contribution of C_3 , which is on the order of $1/g^2$ (where g is the dimensionless conductance), is negligible as $g \gg 1$ in our waveguides.

As described in the previous chapters, the relevant parameters for light transport in the disordered waveguide are the transport mean free path ℓ and the diffusive dissipation length ξ_a . The transport mean free path ℓ depends on the size and density of the air holes. The dissipation results from out-of-plane scattering as the silicon absorption at the probe wavelength is negligible. As shown in chapter 2, this vertical leakage of light can be treated similarly as absorption and described by the diffusive dissipation length $\xi_a = \sqrt{D\tau_a}$, where τ_a is the ballistic dissipation time and D is the diffusion coefficient [35]. To determine these two parameters, ℓ and ξ_a , for all the waveguides of different shapes, we extracted their values by fitting the measured cross-section averaged intensity, $I_v(z)$, and the magnitude of correlations $C(z, z)$ of

$I_r(z)$ in a waveguide with constant width. $W = 60\mu\text{m}$ and $L = 80\mu\text{m}$. The numerical calculations were done with the same method as described in chapter 3 and the parameters extracted from the fitting are $\xi_a = 26\mu\text{m}$ and $\ell = 2.2\mu\text{m}$. Figure 5.4 (c) and (d) show the experimental data along with the fitted curves obtained from the numerical calculations. For the waveguides of different shapes, we keep the size and density of the air holes the same and therefore all waveguides of different shapes have the same ξ_a and ℓ .

Figure 5.5(a,b) are the scanning electron microscope (SEM) images of an expanding waveguide and a contracting waveguide. The measured correlation functions for the cross-section averaged intensity inside the two waveguides, $C(z_1 = z, z_2 = L)$, are plotted in Figure 5.5(c). The ensemble averaging is done over 4 random configurations of air holes and 25 input wavelengths equally spaced between 1500 nm and 1510 nm. Additional averaging is carried out by slightly moving the incident beam spot on the input facet of the empty waveguide to generate different intensity patterns with uniform envelope at the front end of the random array. The experimental data clearly show that the dependence of $C(z, L)$ on z is very different for the two tapered waveguides, which agree well to the calculation results.

Since the waveguide geometry in Fig. 5.5(b) is the mirror image of the one in Fig. 5.5(a), the $C(z, L)$ for light input from the left end of the former is equivalent to that with input from the right end of the latter. As C is dominated by long-range correlation function, this result implies C_2 becomes asymmetric. Note that the asymmetry exists only inside the random medium. The C_2 for the transmitted light remains symmetric, as it is determined by the dimensionless conductance g which has the same value for the two waveguides. The difference in the correlation functions in expanding and contracting waveguides reveals that $C_2(\mathbf{r}_1; \mathbf{r}_2)$ is no longer symmetric because one waveguide is a mirror image of the other. In other words, the long-range intensity correlation function for light input from one end of the tapered waveguide

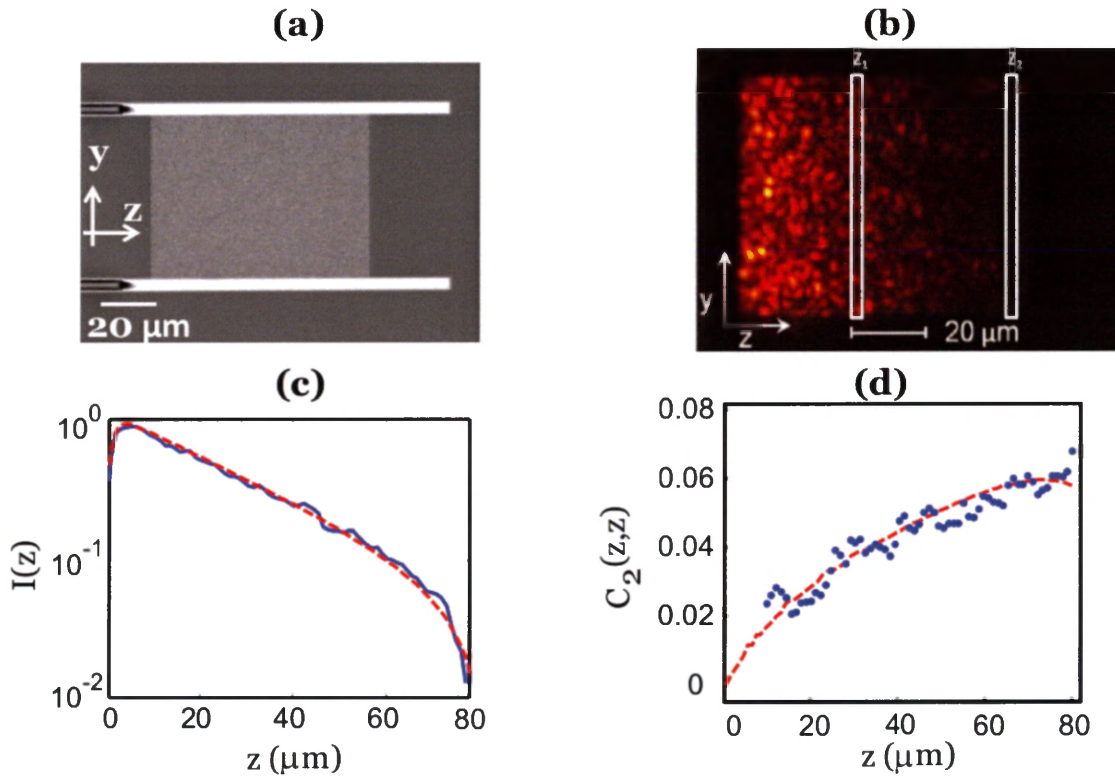


Figure 5.4: (a) Top-view scanning electron microscope (SEM) image of a quasi-2D disordered waveguide with $W = 60 \mu\text{m}$ and $L = 80 \mu\text{m}$. The waveguide wall is made of a triangle lattice of air holes which forms a 2D photonic bandgap to confine light inside the waveguide. (b) An optical image of the intensity of scattered light from the disordered waveguide shown in (a). The wavelength of the probe light is 1500 nm. The white boxes mark two cross-sections at depths z_1 and z_2 in the disordered waveguide. (c,d) Fitting of experimental data to extract scattering and dissipation parameters. The solid blue line in (c) represents the experimentally measured ensemble and cross-section averaged intensity inside the waveguides shown in (a). The solid blue circles in (d) are the measured $C(z, z)$ for the cross-section averaged intensity in the waveguide shown in (a). The dashed red lines in (c) and (d) are obtained by numerical calculation with parameters $\xi_a = 26 \mu\text{m}$ and $\ell = 2.2 \mu\text{m}$, which have the best fit to the experimental data.

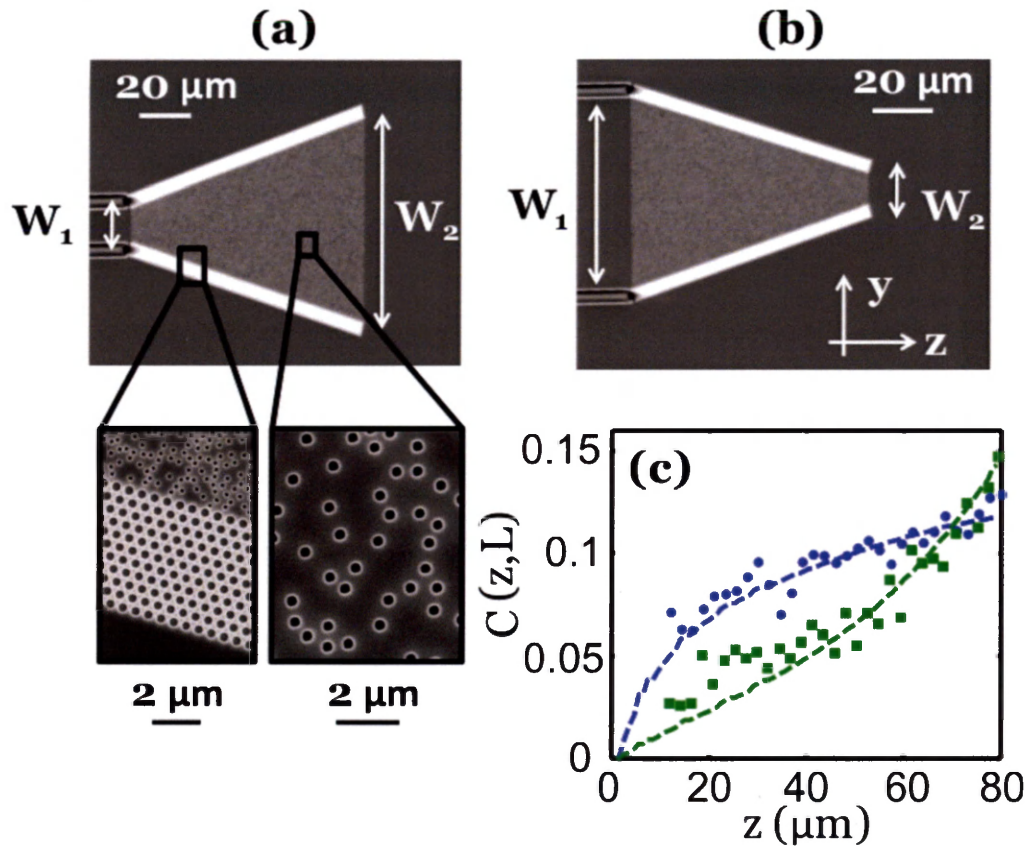


Figure 5.5: Experimental measurement of long-range intensity correlation inside the tapered waveguides. (a,b) Top-view SEM images of fabricated quasi-2D disordered waveguides with linearly increasing (a) or decreasing (b) width. The width of waveguide in (a) increases from $10\ \mu\text{m}$ to $60\ \mu\text{m}$, and in (b) it is opposite. Both have the same length $L = 80\ \mu\text{m}$. Magnified SEM images show the air holes distributed randomly in the tapered section of the waveguide and the triangle lattice of air holes in the reflecting sidewalls. (c) Measured long-range correlation function for the cross-section-averaged intensity $C(z, L)$ inside the tapered waveguides shown in (a) and (b). The blue circles (green squares) represent experimental data for the waveguides with increasing (decreasing) width, and the dashed lines are theoretical results.

is different from that with input from the other end. This behavior is distinct from that of the constant-width waveguide whose two ends are equivalent.

Next, we vary the waveguide cross section in a non-monotonic manner for further manipulation of long-range intensity correlation inside the random waveguide. The waveguide shown in Fig. 5.6(a) has the width W increasing linearly in the first half of the waveguide and decreasing in the second half. This geometry, unlike the tapered waveguides studied above, is symmetric with respect to the center ($z = L/2$), thus the spatial intensity correlation function is the same for light incident from either end of the waveguide. Figure 5.6(b) shows the spatial distribution of light intensity inside the waveguide with input from the left end. The short-range intensity fluctuations seen in Fig. 5.6(b) are smoothed out after the intensity is averaged over the cross section, leaving only the long-range contributions to the intensity correlation function $C(z_1, z_2)$. Figure 5.6(c) plots $C(z, L)$, which increases initially at a slow rate as z approaches $L/2$, but turns into a sharp rise once z passes $L/2$ and approaches L . This is because the crossing probability of scattering paths is first reduced as the waveguide is expanding in $z < L/2$, and then enhanced in $z > L/2$ as the cross section decreases. Therefore, the crossing probability can be controlled by modulating the waveguide width, which changes the spatial dependence of long-range correlation function. Figure 5.6(d) shows the intensity correlation function $C(z, L/2)$. It first increases monotonically as z moves from 0 to $L/2$, and then decreases slightly for z from $L/2$ to L . The experimental data (solid circles) are in good agreement to the theoretical results (dashed lines) in Fig. 5.6(c,d).

5.4 Discussion

Finally, in this section we illustrate the significance of controlling long-range correlations by geometry in focusing of light inside a highly scattering medium. We perform

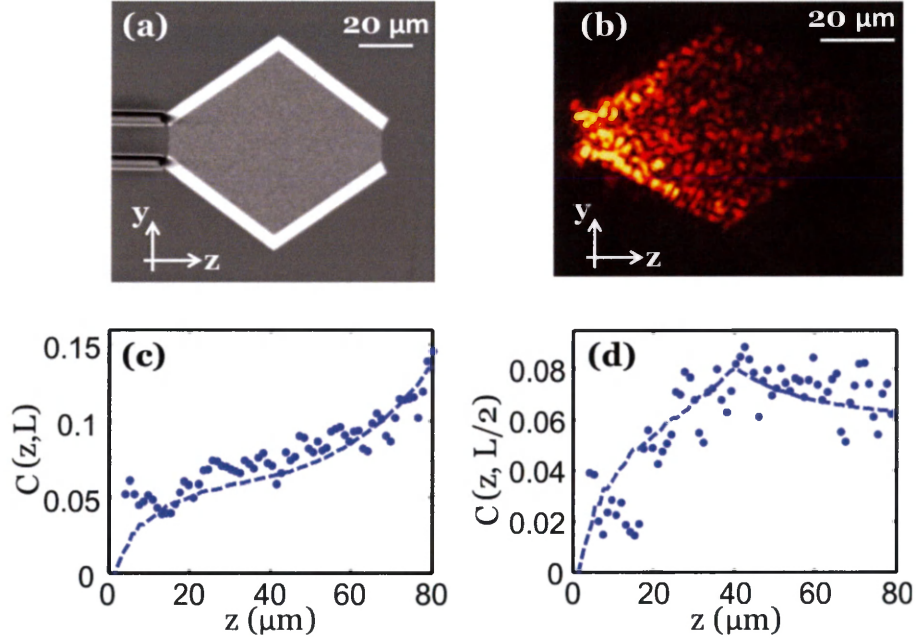


Figure 5.6: Long-range correlation in a quasi-2D disordered waveguide whose width varies non-monotonically. (a) Top-view SEM image showing the waveguide width W increases linearly from $10 \mu\text{m}$ at $z = 0$ to $60 \mu\text{m}$ at $z = 40 \mu\text{m}$ and then reduces linearly down to $10 \mu\text{m}$ at $z = 80 \mu\text{m}$. Other structural parameters are the same as the waveguides in Fig. 5.5. (b) An optical image of the intensity of scattered light from the disordered waveguide. The wavelength of the probe light is 1510 nm . (c) Long-range correlation function $C(z, L)$ for the cross-section averaged intensities at z and L in the waveguide shown in (a). $C(z, L)$ displays a sharp change in the growth rate before and after z passes $L/2$. (d) Long-range correlation function for the cross-section averaged intensities at z and $L/2$ in the waveguide shown in (a). $C(z, L/2)$ increases monotonically in the first half of the waveguide and decreases slightly in the second half. In (c, d), solid circles represent experimental data and the dashed curves are obtained by numerical calculation.

a numerical simulation of wavefront shaping experiment where we focus the input light to a point inside the random waveguide by adjusting the relative phase of electric field in the guided modes of the lead waveguide at the input. Then we normalize the light intensity at the focal point, $\mathbf{r} = (0, z)$, to 1, and average the intensities at all other points of the same cross-section (same z) to obtain the focusing background intensity I_b . Figure 5.7 plots I_b versus z in two diffusive waveguides, one tapered from $10 \mu\text{m}$ to $60 \mu\text{m}$, the other from $60 \mu\text{m}$ to $10 \mu\text{m}$. The variation of the background intensity with depth is dramatically different for the two waveguides, and $I_b(z)$ follows the spatial dependence of C_2 inside these two waveguides as shown in Fig. 5.2. Therefore, by tailoring the long-range correlation function, we are able to tune the focusing contrast via geometry. Since focusing light into a highly scattering sample by wavefront shaping opens the possibility of probing inside opaque media, our approach of controlling the quality of focusing will be important to applications of sensing and imaging into turbid media.

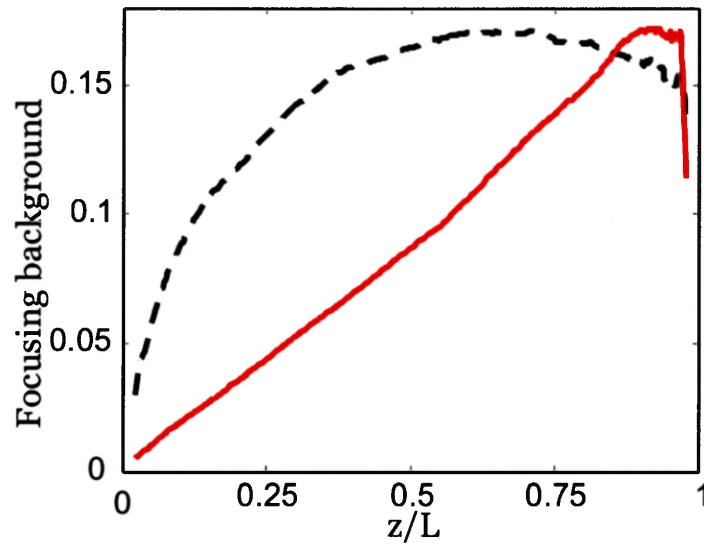


Figure 5.7: Numerical simulation of focusing of light inside a diffusive waveguide by shaping the input wavefront. The light intensity at the focal spot, $\mathbf{r} = (0, z)$, is normalized to 1. Black dashed curve (solid red curve) represents the background intensity I_b vs. depth z inside a random waveguide of width tapered linearly from $10 \mu\text{m}$ ($60 \mu\text{m}$) to $60 \mu\text{m}$ ($10 \mu\text{m}$). Both waveguides have the same length $L = 80 \mu\text{m}$, and they are identical to the ones shown in Fig. 5.1. $I_b(z)$ follows the spatial variation of C_2 , as shown in Fig. 5.2, in both waveguides.

Bibliography

- [1] R. Sarma, A. Yamilov, P. Neupane, and H. Cao, *Phys. Rev. B* **92**, 180203(R) (2015).
- [2] P. Sheng, *Introduction to Wave Scattering, Localization, and Mesoscopic Phenomena* (Academic, Boston, 1995).
- [3] E. Akkermans and G. Montambaux, *Mesoscopic Physics of Electrons and Photons* (Cambridge University Press, Cambridge, 2007).
- [4] A. Lagendijk and B. van Tiggelen and D. S. Wiersma, *Phys. Today* **62**, 24 (2009).
- [5] B. L. Altshuler and P. A. Lee and R. A. Webb, *Mesoscopic Phenomena in Solids* (North Holland, Amsterdam, 1991).
- [6] M. C. van Rossum, and T. M. Nieuwenhuizen, *Rev. Mod. Phys.* **71**, 313 (1999).
- [7] R. Berkovits and S. Feng, *Phys. Rep.* **238**, 135 (1994).
- [8] R. Pnini, *Correlation of Speckle in Random Media, Proceedings of the International Physics School on Waves and Imaging through Complex Media*. 391412 (1999: Cargse, France) edited by P Sebbah (Kluwer Academic Publishers, Dordrecht, 2001).
- [9] S. Feng, C. Kane, P. A. Lee, and A. D. Stone, *Phys. Rev. Lett.* **61**, 834 (1988).
- [10] S. Feng and P. A. Lee, *Science* **251**, 633 (1991).

- [11] A. P. Mosk, A. Lagendijk, G. Lerosey, and M. Fink, *Nature Photonics* **6**, 283 (2012).
- [12] Z. Yaqoob, D. Psaltis, M. S. Feld, and C. Yang, *Nat. Photon.* **2**, 110 (2008).
- [13] X. Xu, H. Liu, and L. V. Wang, *Nat. Photon.* **5**, 154 (2011).
- [14] H. Yu, J. Park, K. Lee, J. Yoon, K. Kim, S. Lee, and Y. K. Park, *Curr. Appl. Phys.* **15**, 632 (2015).
- [15] I. M. Vellekoop and A. P. Mosk, *Phys. Rev. Lett.* **101**, 120601 (2008).
- [16] M. Davy, Z. Shi, and A. Z. Genack, *Phys. Rev. B* **85**, 035105 (2012).
- [17] R. Pnini and B. Shapiro, *Phys. Rev. B* **39**, 6986 (1989).
- [18] A. Z. Genack, N. Garcia, and W. Polkosnik, *Phys. Rev. Lett.* **65**, 2129 (1990).
- [19] A. A. Lisyansky and D. Livdan, *Phys. Rev. B* **47**, 14157 (1993).
- [20] J. F. de Boer, M. P. van Albada, A. Lagendijk, *Phys. Rev. B* **45**, 658 (1992).
- [21] R. Sarma, A. Yamilov, P. Neupane, B. Shapiro, and H. Cao, *Phys. Rev. B* **90**, 014203 (2014).
- [22] X. Cheng and A. Z. Genack, *Optics Letters* **39**, 6324 (2014).
- [23] M. J. Stephen and G. Cwilich, *Phys. Rev. Lett.* **59**, 285 (1987).
- [24] A. A. Chabanov, M. Stoytchev and A. Z. Genack, *Nature* **404**, 850 (2000).
- [25] T. Strudley, T. Zehender, C. Blejean, E. Bakkers, and O. L. Muskens, *Nat. Photonics.* **7**, 413 (2013).
- [26] C. P. Lapointe, P. Zakharov, F. Enderli, T. Feurer, S. E. Skipetrov, and F. Scheffold, *EPL* **105**, 34002 (2014).

- [27] M. P. van Albada, J. F. de Boer, and A. Lagendijk, *Phys. Rev. Lett.* **64**, 2787 (1990).
- [28] N. Garcia, A.Z. Genack, R. Pnini, B. Shapiro, *Phys. Lett. A* **176**, 458 (1993).
- [29] F. Scheffold, W. Hartl, G. Maret, and E. Matijevic, *Phys. Rev. B* **56**, 10942 (1997).
- [30] P. Sebbah, R. Pnini, and A. Z. Genack, *Phys. Rev. E* **62**, 7348 (2000).
- [31] P. Sebbah, B. Hu, A. Z. Genack, R. Pnini, and B. Shapiro, *Phys. Rev. Lett.* **88**, 123901 (2002).
- [32] A. A. Chabanov, N. P. Tregoures, B. A. van Tiggelen, and A. Z. Genack, *Phys. Rev. Lett.* **92**, 173901 (2004).
- [33] O. L. Muskens, T. van der Beek, and A. Lagendijk, *Phys. Rev. B* **84**, 035106 (2011).
- [34] F. Scheffold and G. Maret, *Phys. Rev. Lett.* **81**, 5800 (1998).
- [35] A.Yamilov. R. Sarma. B. Redding. B. Payne. H. Noh. and H.Cao *Phys. Rev. Lett.* **112**, 023904 (2014).
- [36] R. Sarma, A. Yamilov, T. Golubev, and H. Cao, *Appl. Phys. Lett.* **105**, 041104 (2014).
- [37] N. Fayard, A. Caze, R. Pierrat, and R. Carminati, *arxiv*: **1504.06267** (2015).
- [38] B. Z. Spivak and A. Y. Zyuzin, *Mesoscopic Phenomena in Solids*, edited by B. L. Altshuler, P. A. Lee, and R. A. Webb, (Elsevier Science Publishers, Amsterdam, 1991) Chap. 2.
- [39] R. Pnini and B. Shapiro, *Phys. Lett. A* **157**, 265 (1991).

[40] E. Kogan and M. Kavch. *Phys. Rev. B* **45**, 1049 (1992).

Chapter 6

Control of mesoscopic transport by modifying transmission channels using geometry

6.1 Introduction

¹ The diffusive transport of particles in a confined geometry can be effectively controlled by varying the boundary shape. This approach has been widely adopted in natural and artificial systems including channels in biological membranes, nanoporous materials, microfluidics, and artificial ion channels [2–8]. A large variety of quasi one-dimensional (1D) structures with modulated cross-section have been developed for applications in controlled drug delivery, biochemical sensing, particle sorting, Brownian motors, and ion pumps [8–11]. However, this powerful method has not been extensively applied to the control of diffusive transport of waves such as light, microwave or acoustic waves.

While wave diffusion is often described by the Brownian motion, it has a fun-

1. This chapter is primarily based on the journal article published in ref. [1].

damental difference from particle diffusion, i.e., the scattered waves interfere and produce many important phenomena in mesoscopic physics, e.g., Anderson localization, universal conductance fluctuations, and enhanced backscattering [12–15]. Our aim is to control the mesoscopic transport by manipulating wave interference effects in a confined geometry.

A prominent interference effect in a lossless diffusive medium is the creation of open and closed channels, which are eigenvectors of the matrix $t^\dagger t$, where t is the field transmission matrix (TM). The transmission eigenvalues are close to 1 or 0, leading to a bimodal distribution [16–24]. The open channels (with transmission eigenvalues τ close to 1) have dominant contributions to the propagation of waves through random media, while the closed channels ($\tau \sim 0$) determine the reflected waves. Thus by modifying these channels, one would be able to control wave transport. The key question is, then, how to modify these channels.

A recent study has shown that the maximum transmission channel has a universal spatial profile (inside a diffusive waveguide with uniform cross section), which cannot be changed by varying disorder strength or by adjusting the width or length of the random media [25]. The wavefront shaping technique has been successfully developed for selective coupling of light into open channels to enhance the total transmission or focusing through a random medium [26–30], but it cannot modify the transmission eigenchannels. Therefore, an efficient method for deterministic tailoring of the spatial structure of transmission channels is still missing.

In this chapter, we propose and demonstrate an effective approach to manipulate the transmission eigenchannels to control diffusive wave transport. We show that similar to long range correlations and renormalization of diffusion coefficient as shown in previous chapters, by varying the geometry of a random waveguide, the spatial structure of open channels can also be significantly and deterministically altered from the universal ones. This enables tuning the depth profile of energy density inside

the random medium, thus controlling how much energy is concentrated inside the sample and where it is concentrated. By gradually increasing the waveguide cross-section, we are able to convert evanescent channels to propagating channels. In addition to controlling transmission, perfect reflection channels can be created in certain confined geometries, which do not exist in waveguides with uniform cross-section. We show that, unlike high reflection channels in uniform waveguides that exhibit shallow penetration into the disordered system, a perfect reflection channel can penetrate almost through the entire system but does not transmit any light. Furthermore, in the presence of absorption, we can vary the decay length of energy flux inside a diffusive waveguide by modulating the cross-section of the waveguide along its axis. This cannot be achieved in a waveguide of uniform cross-section, as the flux decay length is independent of the waveguide dimension and is determined only by the intrinsic disorder and dissipation.

Optical absorption is ubiquitous and it often weakens the localization effects [31–39], but the approach of using geometry to control wave transport by manipulating the structure of eigenchannels proves to be effective and robust against strong absorption. Therefore the confined geometries enable us to control not only the amount of light being transmitted or reflected, but also the amount of energy concentrated inside the random media. Although strong localization effects, absorption or asymmetric reflection from edges can modify the universal structure of transmission channels, but such effects also remove the open channels with perfect transmission [34, 40, 41]. Unlike these effects, the approach of varying shape of confined geometries gives the significant advantage and freedom to alter the spatial structures of eigenchannels while retaining the open eigenchannels with perfect transmission.

Aside from the fundamental importance, the ability of tailoring the spatial distribution of energy density of transmission eigenchannels can be exploited to manipulate light-matter interactions in highly scattering media, e.g., light absorption, emission,

amplification, and nonlinear optical processes [25, 42]. The potential applications range from laser surgery, photovoltaics, to random laser and energy-efficient lighting [43–50]. Our results suggest that the perfect reflection channels may greatly benefit sensing and imaging applications, as the light in such a channel would penetrate to a certain depth and then fully reflected to ensure an efficient collection of the probe signal. The conversion of evanescent waves to propagative waves and vice versa may be used to tailor optical excitations inside the random media. Since the application of wavefront shaping technique to focusing or imaging through turbid media as well as enhancing total transmission depends on the properties of high transmission channels, the approach of modifying the transmission eigenvalues and eigenvectors by geometry provides a complementary degree of control. While the efficiency of wavefront shaping approach is reduced by incomplete channel control and measurement noise [30, 51, 52], the approach of using geometry is immune to such external factors. Although the above results are obtained for light, they are also applicable to other classical and quantum mechanical waves.

6.2 Quasi-two-dimensional random waveguide

To manipulate transmission eigenchannels, we design and fabricate quasi two - dimensional (2D) waveguides of various geometries. The waveguide structures are fabricated in a 220 nm silicon layer on top of 3 μm buried oxide by electron beam lithography and reactive ion etching [53]. Figure 6.1 shows the scanning electron microscope (SEM) images of two fabricated waveguides. The waveguide contains a 2D random array of air holes that serve as scatterers for light. The air hole diameter is 100 nm and the average (center-to-center) distance of adjacent holes is 390 nm. The waveguide walls are made of triangle lattice of air holes (lattice constant = 440 nm, hole radius = 154 nm) that has a complete 2D photonic bandgap for the in-plane confinement of light.

The waveguide is connected to a lead which is an empty waveguide (without any air holes) with a constant width to couple light in.

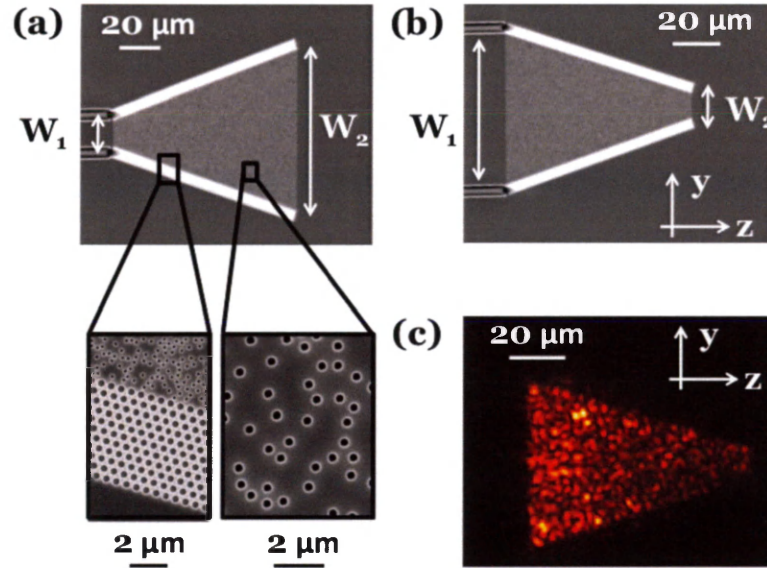


Figure 6.1: Quasi-two-dimensional random waveguides of different geometry. (a,b) Top-view SEM images of fabricated quasi-2D disordered waveguides with linearly increasing (a) or decreasing (b) width. The width of waveguide in (a) increases from $W_1 = 10 \mu\text{m}$ to $W_2 = 60 \mu\text{m}$, and in (b) it is opposite. Both have the same length $L = 80 \mu\text{m}$. Magnified SEM images show the air holes distributed randomly in the tapered section of the waveguide and the triangle lattice of air holes in the reflecting sidewalls. (c) An optical image of the intensity of scattered light from the disordered waveguide. The wavelength of the probe light is 1500 nm.

A monochromatic beam of light from a tunable CW laser source (HP 8168F) is focused by an objective lens (numerical aperture $NA = 0.4$) onto the lead waveguide. The light is transverse-electric (TE) polarized, with the electric field parallel to the plane of the waveguide ($y - z$ plane). After propagating through the lead, the light is incident onto the random array of air holes and undergoes multiple scattering in the 2D plane of waveguide. Some of the light is scattered out of plane, part of which is collected by a $50\times$ objective lens ($NA = 0.42$) and imaged onto an InGaAs camera (Xeva 1.7-320). From the optical image [Fig. 6.1(c)], the spatial distribution of light intensity inside the waveguide $I(y, z)$ is extracted. Ensemble averaging is done by recording the intensity profile for 50 different wavelengths around $\lambda = 1500 \text{ nm}$

and three distinct configurations of air holes. Further averaging is done by slightly shifting the input beam spot on the lead waveguide in the transverse direction y to produce distinct speckle illumination for the random array of air holes, nevertheless, the incident intensity profile is always kept uniform across y .

All disordered waveguides studied in this work exhibit diffusive transport. The relevant parameters for light transport in the disordered waveguide are the transport mean free path ℓ and the diffusive dissipation length ξ_a . The transport mean free path ℓ depends on the density and diameter of the air holes. The dissipation results from out-of-plane scattering, since the silicon absorption at the probe wavelength is negligible. This vertical leakage of light can be treated similarly as absorption and described by the diffusive dissipation length $\xi_a = \sqrt{D\tau_a}$, where τ_a is the ballistic dissipation time and D is the diffusion coefficient [53]. The values of ℓ and ξ_a are $2.2 \mu\text{m}$ and $26 \mu\text{m}$ respectively, which were extracted from the measured intensity distribution inside a waveguide of rectangle shape [53]. Since these two parameters depend only on the size and density of the air holes, we keep them the same for all waveguides with different geometries. This ensures the modification of light transport is purely due to the change in geometry instead of structural disorder or dissipation.

6.3 Linear tapering of waveguide width

In Fig. 6.1, the two waveguides have their width $W(z)$ increase or decrease linearly along the waveguide axis z . To illustrate how the transmission channels are modified by the linear tapering of the waveguide boundary, we first perform numerical modeling by excluding the effect of dissipation. This enables us to separate the effect of geometry from that of dissipation, which will be discussed in the next section. In the simulation, the wavelength, refractive index, and polarization of light are the same as in the experiment. However, the dimension of the waveguide and the transport mean

free path are scaled down to reduce the computing time. This should not change the conclusion of our results because the systems are still in the diffusive regime.

The disordered waveguide has perfectly reflecting sidewalls and is connected to two leads (empty waveguides) at both ends. The refractive index in the empty waveguide is determined by the vertical waveguiding in the silicon layer, and its value is calculated to be $n = 2.85$. In the disordered waveguide, the presence of air holes ($n = 1$, radius = 75 nm, filling fraction = 0.15) reduces the effective index of refraction to $n = 2.62$. The (vacuum) wavelength of the probe light is $\lambda = 1.5 \mu\text{m}$, and the transport mean free path is $\ell = 1.1 \mu\text{m}$. The length of the disordered waveguide L is set to be much larger than ℓ to ensure multiple scattering and diffusion of light. Since the localization length (ξ) is proportional to the width of the waveguide (W), the value of W is chosen to make $\xi \gg L$ so that localization effects are negligible.

We calculate the electromagnetic field inside the disordered waveguide by solving the Maxwell equations using a finite element simulation software (COMSOL Multiphysics). To construct the transmission matrix t of the disordered waveguide, we use the guided modes in the leads as the basis. The input (output) lead waveguide has a constant width equal to the same width W_1 (W_2) of the disordered waveguide at the front (back) end $z = 0$ ($z = L$), and it supports $M = W_1/\lambda/2n$ ($N = W_2/\lambda/2n$) guided modes. Thus t is a $N \times M$ matrix, and its element t_{ij} represents the field transmission from the input j -th mode to the output i -th mode. The reflection matrix is constructed in a similar way by computing the reflected waves, and its dimension is $M \times M$.

A singular value decomposition of the transmission matrix t gives $t = U\Lambda V^\dagger$. Λ is a $N \times M$ diagonal matrix with $\min[N, M]$ non-negative real numbers, $\sqrt{\tau_m}$, where τ_m is the eigenvalue of $t^\dagger t$ and represents the transmittance of the m^{th} transmission eigenchannel. V is a $M \times M$ unitary matrix that maps the field in the guided modes of the input lead to the eigenchannels of the disordered waveguide, and U is a $N \times N$

unitary matrix that maps the eigenchannels to the output waveguide modes. Each column of V represents an input singular vector, whose elements are the complex coefficients for the input waveguide modes that combine to couple light into a single transmission eigenchannel. The output field of a single transmission eigenchannel is represented by the column of U , which is called the output singular vector. Similarly the reflection eigenvalues ρ_n can be obtained by singular value decomposition of the reflection matrix r .

For comparison, we also compute the transmission eigenchannels in the waveguide of constant width W . For $W = 5.1 \mu\text{m}$, $M = N = 19$, and there are 19 transmission eigenchannels. Figure 6.2(a) plots the transmission eigenvalues, 2 of which ($m = 18$ and 19) are many orders of magnitude smaller than the others and are not shown as they fall below the numerical accuracy. This is because the lead waveguide has larger refractive index than the disordered waveguide and support more guided modes. The disordered waveguide can support only $N - 2 = 17$ propagating modes, thus 2 of the 19 transmission channels cannot propagate inside the disordered waveguide and become evanescent. Light can be coupled to these two evanescent channels with the extra modes that can be supported by the input lead waveguide.

Therefore, the eigenchannels of the transmission matrix can be divided into two categories: propagating channels and evanescent channels. The propagating channel has a spatial structure that varies on the scale of the mean free path. The evanescent channel features an intensity decay on the order of the wavelength, which is much shorter than the mean free path, and the corresponding transmission eigenvalue is essentially zero.

A gradual increase of the waveguide width along its axis increases the number of propagating modes that can be supported inside the disordered waveguide, converting the evanescent channels to the propagating channels. This is observed, as an example, in the tapered waveguide whose width is increased from $W_1 = 5.1 \mu\text{m}$ at $z = 0$ to W_2

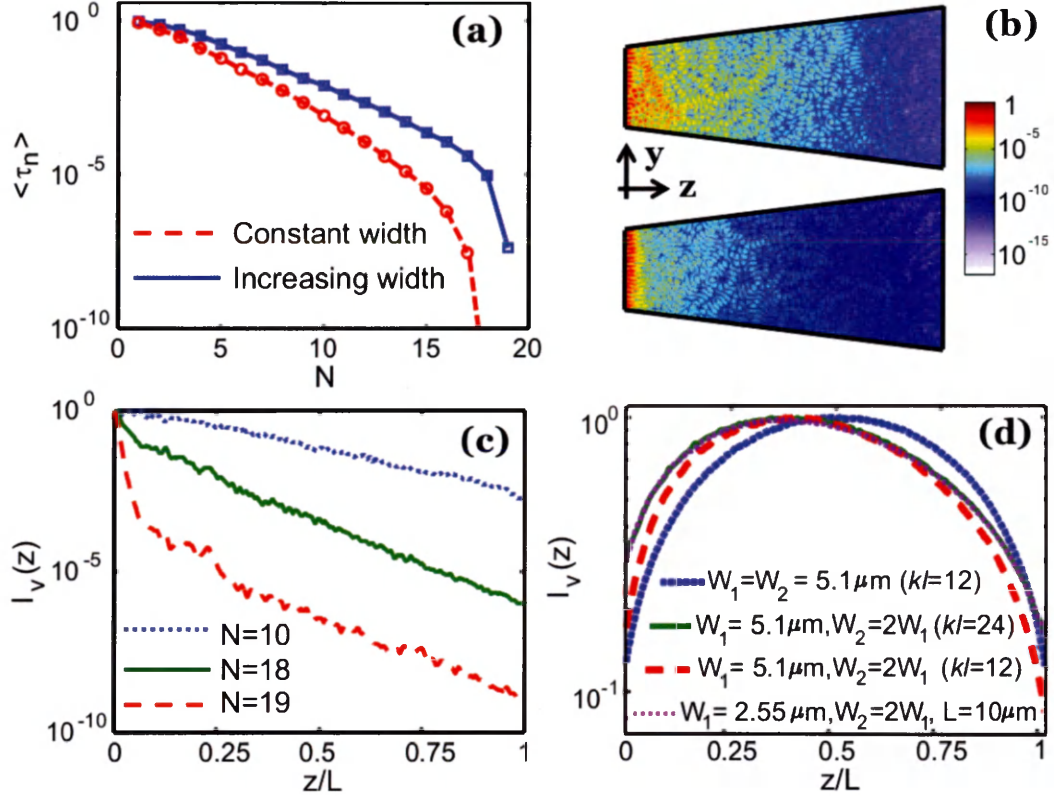


Figure 6.2: Comparison of transmission eigenvalues and eigenchannels in constant-width and increasing-width random waveguides. (a) Numerically-calculated ensemble-averaged transmission eigenvalues of random waveguides with constant width (dashed line with circles) and increasing width (solid line with squares). The constant-width waveguide ($W = 5.1 \mu\text{m}$, $L = 20 \mu\text{m}$) supports 19 transmission eigenchannels of which 17 are propagating channels and 2 are evanescent channels, whereas the expanding waveguide ($W_1 = 5.1 \mu\text{m}$, $W_2 = 10.2 \mu\text{m}$, $L = 20 \mu\text{m}$) has 19 propagating channels of higher transmittance. (b) Spatial distribution of electric field intensity inside the waveguide with increasing width for the 18th and 19th transmission eigenchannels. Both transform from evanescent waves at the entrance of the waveguide to propagating waves due to the increase of waveguide width. (c) Cross-section-averaged intensity, $I_v(z)$, for the 18th (solid line) and 19th (dashed line) channels shown in (b). The conversion from evanescent wave to propagating wave causes a sudden change in the decay length of $I_v(z)$ near the front end of the waveguide. For comparison, $I_v(z)$ for the 10th eigenchannel (dotted line) of the same waveguide is added and it shows a constant decay length. (d) Comparison of the cross-section-averaged intensity, $I_v(z)$, of the maximum transmission channel ($m = 1$) in the disordered waveguides with constant width (blue dotted line) and increasing width with two different disorder strengths (red dashed line and green solid line) and different dimensions (dotted magenta line). Tapering of the waveguide width breaks the symmetry of the spatial structure of the open channel and moves the peak of $I_v(z)$ from the center of the waveguide towards the front end. The position of the peak does not depend on the disorder strength.

$= 10.2 \mu\text{m}$ at $z = L$ [Fig. 6.1(a)]. With $M = 19$ and $N = 38$, the transmission matrix $t_{38 \times 19}$ still supports 19 transmission eigenchannels, but all of them have non-vanishing τ_m [Fig. 6.2(a)].

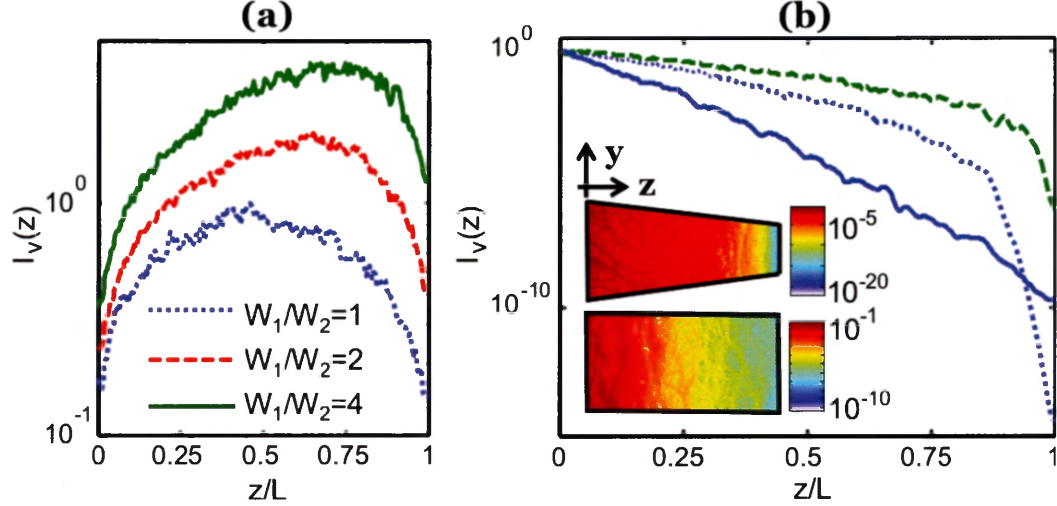


Figure 6.3: Transmission eigenchannels in tapered waveguide of decreasing width. (a) Comparison of cross-section-averaged intensity, $I_v(z)$, of the maximum transmission channel ($m = 1$) in two waveguides with different tapering angles and a constant-width waveguide. All waveguides have the same length $L = 20 \mu\text{m}$. The constant-width waveguide has $W_1 = W_2 = 10.2 \mu\text{m}$ (blue dotted line). The two tapered waveguides have $W_1 = 10.2 \mu\text{m}$ and $W_1/W_2 = 2$ (red dashed line), 4 (green solid line). The $I_v(z)$ curves are offset along the y axis for clarity. The intensity peak shifts from the waveguide center ($W_1/W_2 = 1$) towards the output end ($W_1/W_2 > 1$), and the shift is larger for higher tapering angle (larger W_1/W_2). (b) Cross-section-averaged intensity, $I_v(z)$, of a perfect reflection channel for the same tapered waveguides as in (a). The blue dotted line corresponds to tapering of $W_1/W_2 = 2$ and green dashed line corresponds to $W_1/W_2 = 4$. $I_v(z)$ of a high reflection channel of the constant-width waveguide (blue solid line) is added for comparison. The insets show the spatial distribution of electric field intensity for the high reflection channel of the constant-width waveguide and the perfect reflection channel of the tapered waveguide with $W_1/W_2 = 2$. The perfect reflection channel in a tapered waveguide exhibits slower intensity decay inside the random medium (followed by a sharp drop near the rear end) and thus can penetrate much deeper into the turbid medium than the high reflection channel in the constant-width waveguide. The penetration length increases with the tapering angle.

Figure 6.2(b) shows the spatial distribution of electric field intensity inside the tapered waveguide for the 18th and 19th transmission eigenchannels which have the lowest transmittance. Both these channels have been converted from evanes-

cent channels in a constant-width waveguide with $W = 5.1 \mu\text{m}$ to propagating channels in the tapered waveguide. $I(y, z)$ exhibits a sharp drop near the front side of the waveguide. For a quantitative analysis, the cross-section-averaged intensity, $I_v(z) = [1/W(z)] \int I(y, z) dy$, is plotted in Fig. 6.2(c) for these two channels. For comparison, $I_v(z)$ for the $N = 10$ eigenchannel is added to the plot, and it displays an exponential decay with a constant rate. In contrast, $I_v(z)$ for the 19th eigenchannel first decays very rapidly at small z/L , and then changes to a much slower decay at $z/L \sim 0.07$. The number of guided modes in the waveguide is $N(z) = 2W(z)/(\lambda/n)$, where $W(z)$ is the waveguide width at depth z , and n is the effective index of refraction of the disordered waveguide. As W increases with z , the waveguide becomes wide enough to support additional modes. For example, at $z/L \sim 0.07$, N is increased from 18 to 19, thus the 19th mode is transformed from evanescent wave to propagating wave. Consequently, the decay length of $I_v(z)$ increases from $\sim 0.14 \mu\text{m}$ (comparable to $\lambda/2\pi n$) to $\sim 1.8 \mu\text{m}$ (much larger than $\lambda/2\pi n$). Similarly, the 18th eigenchannel is transformed from evanescent to propagating at a smaller value of $z/L \sim 0.05$, where N is increased from 17 to 18. Hence, this conversion can be attributed to the gradual increase of the number of propagating modes that can be supported by the tapered waveguide at different depths.

If λ and n are fixed, the spatial position (z/L) inside the tapered waveguide where the conversion from evanescent wave to propagating wave takes place is determined by the width at that position, thus the spatial position where such conversion occurs can be easily controlled by tuning the tapering angle. The disorder strength does not affect directly the location of conversion, however, a change in the disorder strength is often accompanied by a change in the effective index of refraction n , which would modify the conversion depth.

The increase of the waveguide width also enhances the transmittance of all other transmission eigenchannels (albeit not as large an enhancement as the above two)

which are also propagating channels in the constant width waveguide. Consequently, the dimensionless conductance $g = \sum \tau_m$ is larger, but the number of input modes remains the same. This behavior is distinct from the constant-width waveguide, where the increase of width also enhances g , but the number of input modes increases simultaneously requiring additional degree of control of the input field for coupling into a single eigenchannel. The waveguide with increasing width can therefore be useful for applications related to enhancing transmission through random media by wavefront shaping technique with incomplete degree of control of the input field.

Furthermore, the spatial profiles of open channels are modified in the tapered waveguide. Figure 6.2(d) compares the cross-section-averaged intensity $I_v(z)$ of the maximum transmission channel in the disordered waveguides with constant and increasing widths. In the waveguide with uniform cross-section, $I_v(z)$ exhibits a symmetric profile with peak in the middle of the waveguide ($z = L/2$). It corresponds to the universal structure of the maximum transmission channel in a constant-width waveguide [25]. In the waveguide with increasing widths, $I_v(z)$ becomes asymmetric and its peak shifts from the center towards the front end of the waveguide ($z < L/2$). As seen in Fig. 6.2(d), when the tapering angle of the waveguide boundary is merely 14° , the peak of the maximum transmission channel has already moved significantly from the center $z/L = 0.5$ to $z/L = 0.35$. This shift does not depend on the disorder strength or the actual dimension of the diffusive waveguide. As a confirmation, Fig. 6.2(d) shows the spatial profiles of the highest transmission channel in two more tapered waveguides, one has L, W_1, W_2 all reduced to half, but $k\ell$ unchanged ($k = 2\pi/\lambda/n$); the other has the same L, W_1, W_2 , but $k\ell$ is doubled. Although their profiles are slightly different, the peak positions are identical.

Next we investigate the disordered waveguide with linearly decreasing width, as shown in Fig. 6.1(b). This geometry is the mirror image of the one in Fig. 6.1(a), thus light injection from the left end of waveguide in Fig. 6.1(b) is identical to light

injection from the right end of the waveguide in Fig. 6.1(a). The transmission matrix of the waveguide in Fig. 6.1(b), $t_{19 \times 38}$, is the transpose of that in Fig. 6.1(a), and it also supports 19 transmission eigenchannels with the same transmittance. Thus the conductance g is identical for the two waveguides in Fig. 6.1. However, the spatial structure of the open channels is different.

Figure 6.3(a) shows the cross-section-averaged intensity $I_r(z)$ for the maximum transmission channel in the waveguide with decreasing width. Its peak shifts from the center of the waveguide towards the output end ($z > L/2$), opposite to that of the waveguide with increasing width in Fig. 6.2(d). The two profiles are mirror image, and the peak always shifts towards the narrower section of the tapered waveguide. How much the peak shifts from the waveguide center depends on the angle of tapering. By changing the tapering angle, the location of the intensity peak can be tuned deterministically, as seen in Fig. 6.3(a). This result illustrates that the maximum of the energy density can be positioned to different depths inside a random system by tailoring its geometry.

While the number of the transmission eigenchannels for the two waveguides in Fig. 6.1 is identical, the number of reflection channels differs. In the expanding waveguide [Fig. 6.1(a)], the reflection matrix $r_{19 \times 19}$ has 19 eigenchannels, which have one-to-one correspondence with the transmission eigenchannels. However, in the contracting waveguide [Fig. 6.1(b)], the input lead waveguide supports 38 guided modes, and the output only 19 modes. Consequently there are 19 transmission eigenchannels, but 38 reflection channels. While 19 of the reflection channels have the corresponding transmission channels, the rest 19 do not. In other words, the reflection matrix $r_{38 \times 38}$ has 38 eigenvalues, of which 19 of them are equal to unity. They represent perfect reflection channels with all incident light being reflected.

The 2-D spatial distribution of field intensity for a perfect reflection channel in the tapered waveguide with $W_1/W_2 = 2$ is shown in the inset of Fig. 6.3(b). For

comparison, a high reflection channel in a waveguide of uniform cross-section is also shown. We can clearly see that the high reflection channel in the constant-width waveguide has a uniform decay of intensity inside the random structure. In contrast, the intensity of the perfect reflection channel exhibits a much slower decay almost throughout the entire random structure and then a sharp drop close to the rear end ($z \sim L$).

The main panel of Fig. 6.3(b) plots the cross-section-averaged intensity, $I_v(z)$, for one of the perfect reflection channels in two tapered waveguides with different tapering angles and a high reflection channel in the constant-width waveguide. The high reflection channel of a constant-width waveguide has shallow penetration into the random medium due to a rapid intensity decay. The perfect reflection channel, however, has a much slower decay and thus a longer penetration depth. A sharp drop of its intensity near the rear end corresponds to the cutoff beyond which no light propagates. The cutoff occurs at the position where the waveguide width is just large enough to support $N + 1$ modes (where N is the number of propagating modes in the output lead). Since the cutoff position depends on the tapering angle of the random waveguide, both the decay length of the intensity and the cutoff position in a perfect reflection channel can be deterministically and effectively controlled by tuning the tapering angle. For example, by increasing the tapering angle we are able to increase the penetration depth by shifting the cutoff position closer to the output end, as seen in Fig. 6.3(b).

Since light in the perfect reflection channels can penetrate deep into the scattering system, such channels can be used for probing inside turbid media. Despite of the deeper penetration, all the light exits from the input end, making the collection efficiency of probe signal 100%, which is extremely useful for sensing or imaging applications. The penetration depth can be precisely tuned via tapering the boundary of a confined random system.

Unlike high reflection or closed channels of random waveguides with uniform cross-section, the perfect reflection channels of the tapered waveguides cannot be deduced from the transmission matrix and will require measurement of the complete reflection matrix of the tapered waveguide. Since the cutoff position of the intensity of the perfect reflection channels is near the rear end of the waveguide, an optimization of transmission using adaptive wavefront shaping technique (described and demonstrated in the next chapter) cannot be used either. Experiments requiring coupling of input light to the perfect reflection channels will therefore require modification from the current experimental setup as it will require measurement of the reflected light as opposed to light inside the random media. Nevertheless, one possible advantage of measuring the reflected light can be that it may have better signal to noise ratio compared to measurements of light inside the random media as more light is usually reflected from the surface of the random media compared to light that penetrates the random media.

6.4 Effect of Absorption

In this section, we study the effect of light dissipation, which was not included the last section. Previous studies have shown that loss has a profound impact on the transmission channels. It not only modifies the statistical distribution of the transmission eigenvalues [34], but also changes the structure of eigenchannels [41, 54]. In case of passive diffusive waveguides, the probability density distribution of transmission eigenvalues, $P(\tau)$, has 2 peaks, one at 1 and the other at 0. Thus, there are many channels (the number is determined by g) with comparable values of $\tau \sim 1$. Therefore, the total intensity inside the random medium is the sum of intensities of all these high transmission eigenchannels.

In case of strongly absorbing waveguides ($L \gg \xi_a$), the peak at $\tau = 1$ disappears

and $P(\tau)$ has a cutoff at τ_{max} which is determined by L/ξ_a . In such absorbing waveguides, $P(\tau)$ decays strongly with τ with a faster decay near τ_{max} . This implies that the τ 's will be arranged as $\tau_1 > \tau_2 > \tau_3 > \dots$. Furthermore, because $P(\tau)$ decays fast toward τ_{max} , τ_1 will be much greater than $\tau_2, \tau_3, \tau_4 \dots$ and the total intensity inside the random media will therefore be dominated by the eigenchannel with the maximum transmission.

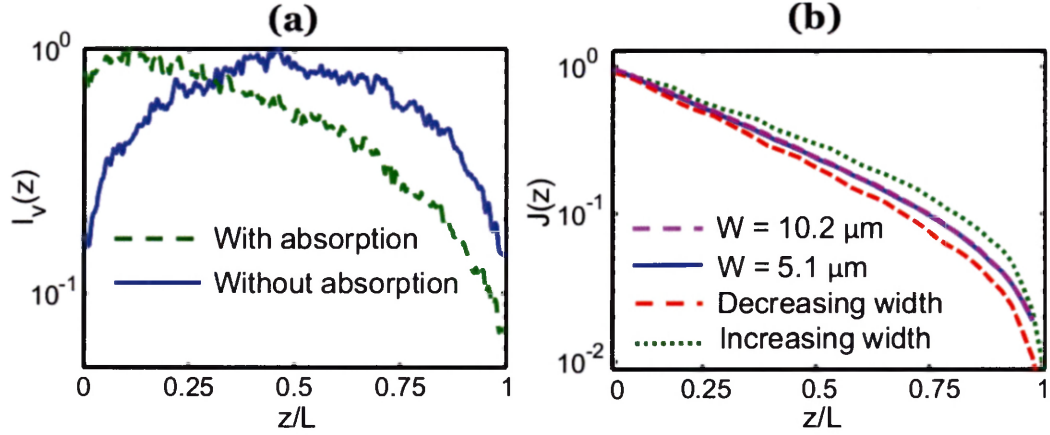


Figure 6.4: Effect of absorption on the maximum transmission eigenchannel and energy flux decay in the constant-width and tapered waveguides. (a) Comparison of the cross-section-averaged intensity, $I_v(z)$, of the maximum transmission channel in a constant-width ($W = 5.1 \mu\text{m}$, $L = 20 \mu\text{m}$) disordered waveguide with (dashed line) and without (solid line) absorption. In the absorbing waveguide, $L/\xi_a = 3$. Absorption modifies the spatial profile of the maximum transmission channel. (b) Comparison of spatial decay of energy flux $J(z)$ in random waveguides with constant widths $W = 5.1 \mu\text{m}$ (blue solid line) and $W = 10.2 \mu\text{m}$ (dashed magenta line), increasing width of $W_1 = 5.1 \mu\text{m}$, $W_2 = 10.2 \mu\text{m}$ (green dotted line) and decreasing width of $W_1 = 10.2 \mu\text{m}$ and $W_2 = 5.1 \mu\text{m}$ (red dashed line). For all waveguides, $L = 20 \mu\text{m}$, $L/\xi_a = 3$ and $J(z)$ is normalized to 1 at $z = 0$. While the flux decay length remains the same for the two rectangle waveguides of different widths, it is lengthened in the expanding waveguide and shortened in the contracting waveguide.

For the quasi-2D waveguides we fabricate, the dissipation results from out-of-plane scattering of light, which can be treated as absorption [53]. We simulate it in the 2D waveguide by introducing an imaginary part of the refractive index. The diffusive dissipation length is $\xi_a = \sqrt{\ell_a/2}$, where ℓ_a is the ballistic dissipation length. The ratio of L/ξ_a is set to 3.0, which is close to the value of the fabricated waveguides. At

$L/\xi_a = 3$, absorption causes a notable change in the spatial profile of the maximum transmission channel as seen in Figure 6.4(a). The intensity peak of the maximum transmission channel, which is located at the middle ($z/L \sim 0.5$) of the passive waveguide, moves to the front end ($z/L \sim 0$) due to absorption.

Although it reduces the throughput, loss allows us to manipulate the spatial decay of energy flux inside the random waveguide by geometry. In the absence of loss, the net flux $J(z)$, integrated over the cross-section of the waveguide, points in the z direction and its value is constant along z . By tailoring the boundary shape of the waveguide, the magnitude of J changes, but it remains invariant with z . With the addition of loss, $J(z)$ decays exponentially along z . If the waveguide has a uniform cross-section, the decay length is determined by ξ_a , which is independent of the waveguide width or length. However, the decay length can be varied by tapering the waveguide width along z . Figure 6.4(b) plots $J(z)$ in four waveguides with random input fields. To compare the spatial profile of $J(z)$, its value at $z = 0$ is normalized to 1. Two of the waveguides have uniform width, $W = 5.1 \mu\text{m}$, $10.2 \mu\text{m}$, and their $J(z)$ overlaps after the normalization. With a linear increase of W with z , the decay of $J(z)$ becomes slower, while a linear decrease of the waveguide width accelerates the flux decay. Hence, by varying the waveguide width along the cross-section, we can tune the decay of energy flux inside the random media. Such tuning of flux decay rate by geometry can be achieved only in the presence of loss, illustrating additional degree of control enabled by combination of dissipation and geometry.

6.5 Intensity decay inside random media

Experimentally we measured the 2D intensity distribution inside the tapered waveguides shown in Fig. 6.1(c). From $I(y, z)$ we obtain the cross-section-averaged intensity $I_r(z)$ which gives the depth profile of the average energy density inside the random

waveguide. In the tapered waveguides, the intensity decay rates become significantly different as seen in Fig. 6.5(a). $I_v(z)$ decays much faster inside the expanding waveguide than that in the constant-width waveguide, while the contracting waveguide leads to a much slower decay of $I_v(z)$. Such behavior is attributed to the variation of the waveguide width along z .

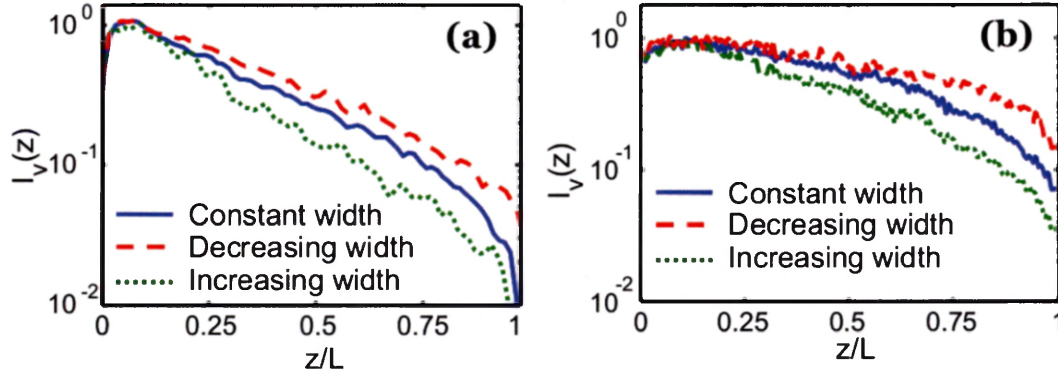


Figure 6.5: Experimentally measured intensity decays inside disordered waveguides in comparison to numerically calculated spatial profiles of the maximum transmission eigenchannels. (a) Experimentally measured cross-section-averaged intensity $I_v(z)$ inside quasi-2D waveguides of constant width $W = 60 \mu\text{m}$ (solid blue line), increasing width with $W_1 = 10 \mu\text{m}$, $W_2 = 60 \mu\text{m}$ (dotted green line), and decreasing width with $W_1 = 60 \mu\text{m}$, $W_2 = 10 \mu\text{m}$ (dashed red line). All the waveguides have $L = 80 \mu\text{m}$ and $L/\xi_a = 3$. The tapering of the waveguide boundary causes a dramatic change in the decay lengths of $I_v(z)$. (b) Numerically calculated $I_v(z)$ of the maximum transmission eigenchannel in the disordered waveguides of constant width $W = 10.2 \mu\text{m}$ (solid blue line), increasing width with $W_1 = 5.1 \mu\text{m}$, $W_2 = 10.2 \mu\text{m}$ (dotted green line), and decreasing width with $W_1 = 10.2 \mu\text{m}$, $W_2 = 5.1 \mu\text{m}$ (dashed red line). All waveguides have $L = 20 \mu\text{m}$ and $L/\xi_a = 3$. Despite of the reduced waveguide dimensions, the maximum transmission channels exhibit a qualitatively similar structure to the experimentally measured intensities, indicating the intensity distribution inside a strongly absorbing random medium is determined by the structure of the maximum transmission channel.

For comparison, we also measure the intensity decay inside two constant-width waveguides. Despite of a factor of 6 difference in the waveguide width ($W=10 \mu\text{m}$, $60 \mu\text{m}$), I_v decays exponentially in the two waveguides with nearly the same rate (not shown). This result confirms that the intensity decay is independent of the waveguide width as long as W is invariant with z and localization effect is negligible [53].

As mentioned before, the two tapered waveguides with the same tapering angle are mirror image of each other with respect to $z = L/2$. Thus the transport of light with input from one end ($z = 0$) of one waveguide is equivalent to that with input from the opposite end ($z = L$) of the other waveguide. Hence, the difference in the intensity decay in the two waveguides with injection from the same end ($z = 0$) illustrates asymmetric transport of light in such tapered waveguides.

Since our fabricated waveguides are in the regime of strong dissipation ($L \gg \xi_a$), the intensities inside the structures are dominated by the maximum transmission channel. The experimentally measured intensities should therefore reflect qualitatively the intensity profiles of the maximum transmission channels. In Figure 6.5(b), we plot the numerically calculated $I_v(z)$ for the maximum transmission eigenchannels in waveguides of constant widths and tapered geometries (with reduced dimensions due to limited computing power). They exhibit qualitatively similar structures, indicating the intensity distribution inside a strongly dissipative random system is determined by the maximum transmission channel whose spatial profile can be tuned by geometry.

6.6 Non-monotonic variation of waveguide cross-section

Finally, we change the waveguide width non-monotonically along the axis for further control of transmission channels. Figure 6.6(a) shows a “bow-tie” waveguide whose width W decreases linearly in the first half and then increases in the second half. While the input and output ends have identical widths, the waveguide has a constriction in the middle that reduces the energy flow. The total number of transmission eigenchannels is still determined by the waveguide width at the input/output. However, only a fraction of these channels (determined by the width of the constriction)

can propagate through the constriction. The rest are converted to evanescent waves in the vicinity of the construction due to the reduction in the number of propagating modes. As the waveguide width increases after the constriction, the evanescent wave that can tunnel through the constriction may convert back to propagating wave. This is seen in the intensity profiles of the transmission channels in Fig. 6.6(b). $I_v(z)$ decays gradually in the first part of the bow-tie waveguide, then suddenly changes to a much faster decay near the constriction, after the constriction the decay slows down again. The abrupt changes in the decay length, from much larger than the evanescent decay length, $\lambda/2\pi n$, to smaller than $\lambda/2\pi n$ and back, indicate the conversion from propagating wave to evanescent wave and back. The accelerated decay rate near the constriction differs from one channel to another [Fig. 6.6(b)]. Hence, evanescent waves with different decay rates are created inside a diffusive waveguide by the constriction.

In the bow-tie waveguide, the number of transmission eigenchannels that diffuse through the constriction without being converted to evanescent waves is determined by the width of the constriction. When the constriction width W_c is reduced to below the transport mean free path ℓ , light propagation in the vicinity of the constriction is changed from 2D diffusion to quasi-1D diffusion. However, the number of waveguide modes supported by the constriction can still be much larger than 1, as long as $W_c \gg \lambda$, allowing light diffusion through the constriction. However, if $W_c < \lambda$, light transport at the constriction changes to evanescent tunneling.

The bow-tie geometry also modifies the high transmission channels, even in the presence of strong absorption. In Fig. 6.6 (c) along with the cross-section-averaged intensity $I_r(z)$ we also plot the cross-section-integrated intensity $I_l(z) = I_r(z)W(z)$. While the former only gives the depth profile of the average energy density inside the random waveguide, the latter tells the total amount of energy concentrated at certain depth z . The cross-section-averaged intensity $I_r(z)$ for the maximum transmission

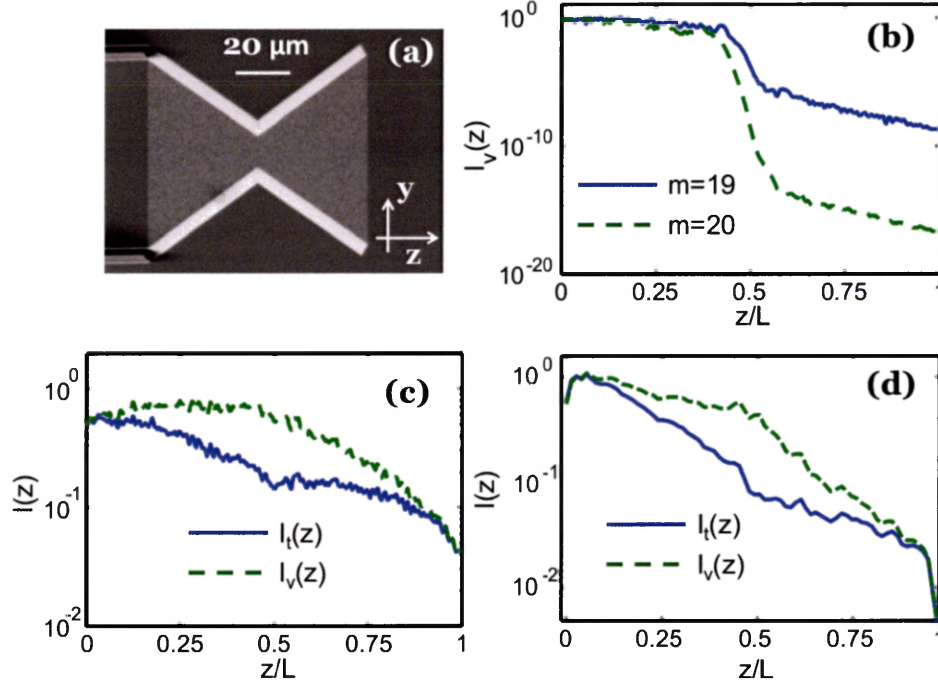


Figure 6.6: Transmission eigenchannels and intensity decay in a diffusive waveguide of bowtie geometry. (a) Top-view SEM image of a fabricated quasi-2D waveguide with bowtie geometry. The length of waveguide is $L = 80 \mu\text{m}$. The width of waveguide decreases linearly from $60 \mu\text{m}$ at $z = 0$ to $10 \mu\text{m}$ at $z = L/2$ and then again increases linearly to $60 \mu\text{m}$ at $z = L$. (b) Numerically-calculated cross-section-averaged intensity $I_v(z)$ of the 19th (solid line) and 20th (dashed line) transmission eigenchannels of bowtie waveguide. The length L of the waveguide is $20 \mu\text{m}$, the width at $z = 0, L$ is $10.2 \mu\text{m}$ (35 propagating modes) and the width of constriction at $z = L/2$ is $5.1 \mu\text{m}$ (17 propagating modes). The abrupt changes in the decay rate of $I_v(z)$ before and after $z = L/2$ indicate the conversion from propagating wave to evanescent wave and back. The evanescent decay rate varies from one channel to another. (c) Numerically-calculated $I_v(z)$ (green dashed line) and cross-section-integrated intensity $I_t(z)$ (blue solid line) for the maximum transmission channel of the same waveguide as in (b) but with absorption $L/\xi_a = 3$. The constriction causes a significant change in the intensity distribution of the maximum transmission channel. (d) Experimentally measured $I_v(z)$ (green dashed line) and $I_t(z)$ (blue solid line) inside the disordered waveguide shown in (a). Both intensity distributions follow those of the maximum transmission channel.

channel exhibits a small bump at the constriction, while the cross-section-integrated intensity $I_t(z)$ has a dip. This is because the reduction in the cross-section increases the energy density but suppresses the total flux at the center of the waveguide. Figure 6.6(d) plots the experimentally measured intensity of light inside the bow-tie waveguide. $I_v(z)$ decays slower in the first half ($z < L/2$) than in the second half ($z > L/2$). $I_t(z)$ exhibits opposite behavior. The qualitative agreement between the measured intensity decay and the calculated profile of the highest transmission eigenchannel again confirms that the energy distribution inside the bow-tie waveguide is determined by the maximum transmission channel.

The spatial structure of the open channel in the bow-tie waveguide can be tuned by shifting the constriction away from the center of the waveguide. Unlike varying the constriction width which would modify the transmission eigenvalue and the dimensionless conductance, changing the location of the constriction only modifies the transmission eigenchannels, but not the eigenvalues. It thus provides an efficient way of tailoring the energy distribution inside the diffusive waveguide while keeping the transmittance constant.

Complementary to the bow-tie waveguide, we fabricate the “lantern” waveguide whose width W increases linearly in the first half and decreases in the second half [Fig. 6.7(a)]. In contrast to the bowtie geometry, the number of propagating modes that can be supported in the lantern waveguide increases in the middle due to larger cross-section, thus increasing energy throughput. In particular, a transmission eigenchannel, which is evanescent at the input end of the random waveguide (due to the refractive index difference from the lead waveguide), transforms to propagating wave as the waveguide becomes wider. However, close to the rear end of the waveguide, the propagating wave becomes evanescent again due to the decrease of the waveguide width. Such behavior is shown in Fig. 6.7(b), where $I_r(z)$ for the $m = 19$ eigenchannel exhibits a fast decay near the front end of the lantern waveguide, then the decay

is slowed down in the middle, but near the back end the decay becomes fast again. Since light can only tunnel out of the waveguide, there is a strong buildup of energy inside the lantern waveguide, especially near the center where the number of waveguide modes is maximum. For comparison, $I_v(z)$ of another transmission eigenchannel ($m = 5$) is also plotted. Unlike $m = 19$, $I_v(z)$ for $m = 5$ eigenchannel does not display a dip in the intensity at $z/L \sim 0$ as it does not start with an evanescent wave at the front side of the waveguide, instead it exhibits a uniform decay of intensity across the entire waveguide.

The high transmission channels also experience a significant change in the lantern waveguide. As seen in Fig. 6.7(c), the maximum transmission channel displays an opposite behavior to that of the bow-tie waveguide [Fig. 6.6(c)]. $I_v(z)$ drops faster in the first half of the waveguide ($z < L/2$) than in the second half ($z > L/2$), while $I_t(z)$ is the opposite. The difference from the bow-tie waveguide is expected because the cross-section is modulated in opposite manner in the two waveguides. Consequently, the intensity distribution inside the lantern waveguide is very different from that in the bow-tie waveguide. The measured $I_v(z)$ and $I_t(z)$ in Fig. 6.6(d) exhibit distinct decay rates for $z < L/2$ and $z > L/2$, which agree qualitatively to those of the maximum transmission channel. This confirms the change in energy distribution inside the lantern waveguide can be very well represented by the change in the structure of the maximum transmission channel by geometry.

6.7 Discussion

To conclude, we have demonstrated an effective approach to modify transmission eigenchannels of confined disordered media. Using geometry, we can change the spatial profiles of the transmission channels significantly and deterministically from the universal one. It allows us to control the depth profile of the total energy as well

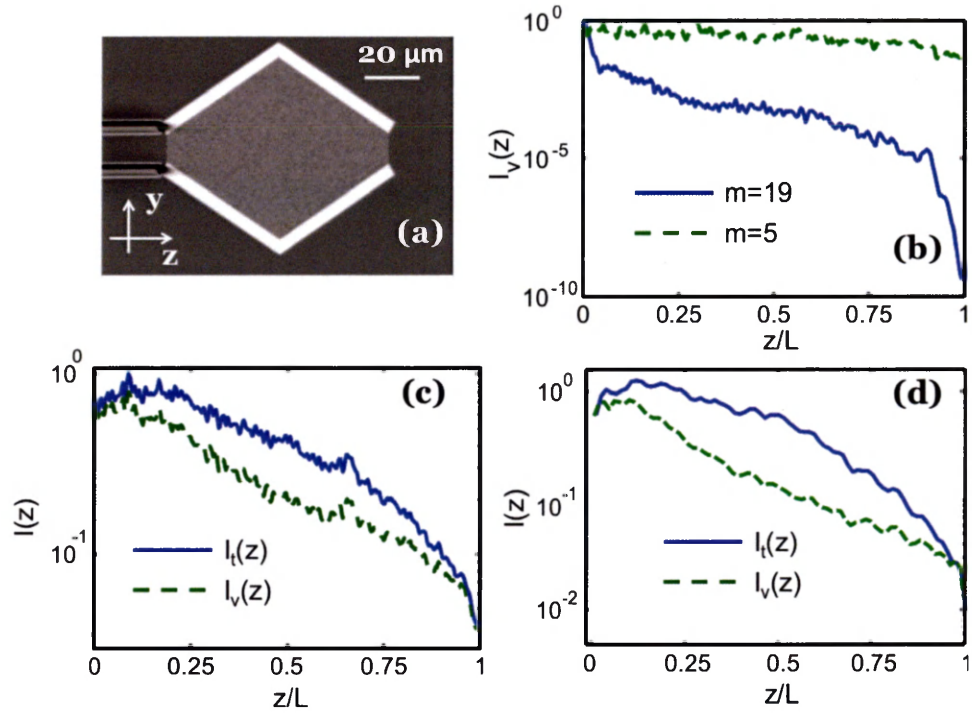


Figure 6.7: Transmission eigenchannels and energy distribution in a diffusive waveguide of lantern geometry. (a) Top-view SEM image of a fabricated quasi-2D disordered waveguide with lantern geometry. The length of waveguide is $L = 80 \mu\text{m}$. The width of waveguide increases linearly from $10 \mu\text{m}$ at $z = 0$ to $60 \mu\text{m}$ at $z = L/2$ and then again decreases linearly to $10 \mu\text{m}$ at $z = L$. (b) Numerically calculated cross-section-averaged intensity $I_v(z)$ for the 5th (dashed line) and 19th (solid line) transmission eigenchannels of lantern geometry. The length L of the waveguide is $20 \mu\text{m}$, the width at $z = 0, L$ is $5.1 \mu\text{m}$ (17 propagating modes) and width at $z = L/2$ is $10.2 \mu\text{m}$ (35 propagating modes). $I_v(z)$ of the 19th transmission eigenchannel exhibits the conversion of the evanescent wave to a propagating wave near the input end and then back to the evanescent wave near the output end due to the variation of the waveguide width. In contrast, the 5th channel remains propagating wave across the entire waveguide. (c) Numerically calculated $I_v(z)$ (green dashed line) and cross-section-integrated intensity $I_t(z)$ (blue solid line) for the maximum transmission channel of the same waveguide as in (b) but with absorption $L/\xi_a = 3$. Both intensity profiles are opposite to those in the bow-tie waveguide. (d) Experimentally measured $I_v(z)$ (green dashed line) and $I_t(z)$ (blue solid line) inside the disordered waveguide shown in (a). The intensity profiles are similar to those of the maximum transmission channel shown in (c).

as the energy density inside the random medium, thus controlling how much energy is concentrated inside the sample and where it is concentrated. The ability to tailor the spatial distribution of energy density can be exploited to manipulate light-matter interactions in scattering media, which will be useful for numerous applications.

By gradually increasing the cross-section, we can enhance the transmittance of all the transmission eigenchannels while keeping the number of input modes the same. Such geometries can be useful for applications related to enhancement of total transmission by shaping the input wavefront, as in such structures there will be more open channels due to larger conductance. Moreover, since the waveguide cross-section at the input end does not change, the number of input channels remains the same, and additional degree of control of the input field is not necessary for coupling into any one of the open channels. In addition, using geometry we can also convert evanescent channels to propagating channels and vice versa. In a waveguide with the output cross-section smaller than the input one, perfectly reflecting channels are created. The light injected to such a channel would penetrate inside the scattering media to a certain depth and then get fully reflected back to the input end. The penetration depth of such channels can be further tuned by geometry. Such channels have potential applications for probing deep inside turbid media. Since all the light exits from the input end, the collection efficiency of probe signal would be 100%. We can further design geometries with opposite taperings to have the same transmission eigenvalues but very different eigenchannel profiles. By breaking the reflection symmetry of confined geometry, the transmission eigenchannels become asymmetric. In a diffusive waveguide with non-monotonic tapering boundary such as the lantern geometry, energy can buildup inside the random medium, which will benefit the applications of energy harvesting and tailoring of optical excitations inside scattering media.

Unlike the localization effects shown in chapter 2 and 4 which are suppressed by absorption, the approach of using geometry to control light transport is effective even

in the presence of strong absorption and does not require any change of structural disorder. Thus this approach can truly complement the wavefront shaping technique to control mesoscopic transport of light with an additional advantage that the efficiency is not reduced by external factors such as incomplete channel control and measurement noise [30]. The results discussed in this chapter are also applicable to other waves such as microwaves, acoustics or matter waves.

Finally, we stress that the confined geometry enables manipulating the spatial structures of transmission eigenchannels while retaining the open channels with perfect transmission. This is advantageous compared to other approaches that rely on localization effects like shown in chapter 2 and 4, absorption [41] or asymmetric surface reflections from edges [40] to modify the transmission channels as those approaches will also remove the open channels with perfect transmission. Although in this chapter we have focused only on the maximum transmission channel, in general using geometry the spatial profiles of the other low transmission channels can also be deterministically and significantly modified. Since changing the confined geometry of a random medium corresponds to modifying its boundary condition, we expect that the Green's function inside the random system can also be tailored. This implies that our approach of manipulating geometry in general may be applied to control any mesoscopic effect that depends on the Green's functions inside the random media such as non-local intensity correlations, renormalization of the diffusion coefficient, the density of states etc.

Bibliography

- [1] R. Sarma, A. Yamilov, S. F. Liew, M. Guy, and H. Cao, *Phys. Rev. B* **92**, 214206 (2015).
- [2] J. Kaerger and D. M. Ruthven, *Diffusion in Zeolites and Other Microporous Solids* (Wiley, New York, 1992).
- [3] F. J. Keil, R. Krishna, and M.-O. Coppens, *Rev. Chem. Eng.* **16**, 71 (2000).
- [4] B. Hille, *Ion Channels of Excitable Membranes, 3rd edition*, (Sinauer, Sunderland, 2001).
- [5] Lindner, J. Garca-Ojalvo, A. Neiman, and L. Schimansky-Geier, *Phys. Rep.* **392**, 321 (2004).
- [6] H. X. Zhou, G. N. Rivas, and A. P. Minton, *Annu. Rev. Biophys.* **37**, 375 (2008).
- [7] H. Bruus, *Theoretical Microfluidics, Oxford Master Series in Condensed Matter Physics* (Oxford University Press, Oxford, 2008).
- [8] P. Hänggi and F. Marchesoni, *Rev. Modern Physics.* **81**, 387 (2009).
- [9] P. S. Dittrich and A. Manz, *Nat. Rev. Drug. Discov.* **5**, 210 (2006).
- [10] C. Dekker, *Nature Nanotech.* **2**, 209 (2007).
- [11] C. Zhao and C. Yang, *Microfluid Nanofluid* **13**, 179 (2012).

- [12] P. Sheng, *Introduction to Wave Scattering, Localization, and Mesoscopic Phenomena* (Academic, Boston, 1995).
- [13] M. C. W. van Rossum and T. M. Nieuwenhuizen, *Rev. Mod. Phys.* **71**, 313 (1999).
- [14] E. Akkermans and G. Montambaux, *Mesoscopic Physics of Electrons and Photons* (Cambridge University Press, Cambridge, 2007).
- [15] A. Lagendijk, B. van Tiggelen, and D. S. Wiersma, *Phys. Today* **62**, 24 (2009).
- [16] O. N. Dorokhov, *Solid State Commun.* **44**, 915 (1982).
- [17] O. N. Dorokhov, *Solid State Commun.* **51**, 381 (1984).
- [18] J. L. Pichard and G. André, *Europhys. Lett.* **2**, 477 (1986).
- [19] Y. Imry, *Europhys. Lett.* **1**, 249 (1986).
- [20] K. A. Muttalib, J. L. Pichard, and A. D. Stone, *Phys. Rev. Lett.* **59**, 2475 (1987).
- [21] P. A. Mello, P. Pereyra, and N. Kumar, *Ann. Phys.* **181**, 290 (1988).
- [22] J. B. Pendry, A. MacKinnon, and P. J. Roberts, *Proc. Math. Phys. Sc.* **437**, 67 (1992).
- [23] Y. V. Nazarov, *Phys. Rev. Lett.* **73**, 134 (1994).
- [24] C. W. Beenakker, *Rev. Mod. Phys.* **69**, 731 (1997).
- [25] M. Davy, Z. Shi, J. Park, C. Tian, and A.Z. Genack, *Nat. Commun.* **6**, 6893 (2015).
- [26] I. M. Vellekoop and A. P. Mosk, *Phys. Rev. Lett.* **101**, 120601 (2008).
- [27] W. Choi, A. P. Mosk, Q. H. Park, and W. Choi, *Phys. Rev. B* **83**, 134207 (2011).

- [28] M. Kim, Y. Choi, C. Yoon, W. Choi, J. Kim, Q. H. Park, and W. Choi, *Nat. Photon.* **6**, 581 (2012).
- [29] H. Yu, T. R. Hillman, W. Choi, J. O. Lee, M. S. Feld, R. R. Dasari, and Y. K. Park, *Phys. Rev. Lett.* **111**, 153902 (2013).
- [30] S. M. Popoff, A. Goetschy, S. F. Liew, A. D. Stone, and H. Cao, *Phys. Rev. Lett.* **112**, 133903 (2014).
- [31] S. John, *Phys. Rev. Lett.* **53**, 2169 (1984).
- [32] V. Freilikher, M. Pustilnik, and I. Yurkevich, *Phys. Rev. Lett.* **73**, 810 (1994).
- [33] T. Sh. Misirpashaev, J. C. J. Paasschens, and C. W. J. Beenakker, *Physica A* **236**, 189 (1997).
- [34] P. W. Brouwer, *Phys. Rev. B* **57**, 10526 (1998).
- [35] A. A. Chabanov, M. Stoytchev, and A. Z. Genack, *Nature* **404.6780**, 850 (2000).
- [36] L. I. Deych, A. Yamilov, and A. A. Lisyansky, *Phys. Rev. B* **64**, 024201 (2001).
- [37] A. Yamilov, and H. Cao *Phys. Rev. E* **70**, 037603 (2004).
- [38] A. G. Yamilov and B. Payne, *Opt. Express* **21**, 11688 (2013).
- [39] L. Y. Zhao, C. S. Tian, Z. Q. Zhang, and X. D. Zhang, *Phys. Rev. B* **88**, 155104 (2013).
- [40] L. Zhao, C. Tian, Y. P. Bliokh, and V. Freilikher, *arxiv*: **1506.03685**, (2015).
- [41] S. F. Liew, S. M. Popoff, A. P. Mosk, W. L. Vos, and H. Cao, *Phys. Rev. B* **89**, 224202 (2014).
- [42] X. Cheng and A. Z. Genack, *Opt. Lett.* **39**, 6324 (2014).

- [43] M. Gratzel, *J. Photochem. Photobiol. C* **4**, 145 (2003).
- [44] H. Cao, *J. Phys. A: Math. Gen.* **38**, 10497 (2005).
- [45] I. M. Vellekoop, A. Lagendijk, and A. P. Mosk, *Nat. Photon.* **4**, 320 (2010).
- [46] S. Popoff, G. Lerosey, M. Fink, A. C. Boccarda, and S. Gigan, *Nat. Commun.* **1**, 1 (2010).
- [47] A. P. Mosk, A. Lagendijk, G. Lerosey, and M. Fink, *Nat. Photon.* **6**, 283 (2012).
- [48] W. L. Vos, T. W. Tukker, A. P. Mosk, A. Lagendijk, and W. L. IJzerman, *Appl. Opt.* **52**, 2602 (2013).
- [49] H. Cao, *Coherent Control of Light Transmission and Absorption in Random Scattering Media*, 45th Winter Colloquium on the Physics of Quantum Electronics, PQE Book of Abstracts (2015).
- [50] M. Kim, W. Choi, C. Yoon, G. H. Kim, S. Kim, G. Yi, Q. Park, and W. Choi, *Opt. Express* **23**, 12740 (2015).
- [51] A. Goetschy and A. D. Stone, *Phys. Rev. Lett.* **111**, 063901 (2013).
- [52] H. Yilmaz, W. L. Vos, and A. P. Mosk, *Biomed. Opt. Express* **4**, 1759 (2013).
- [53] A. Yamilov, R. Sarma, B. Redding, B. Payne, H. Noh, and H. Cao, *Phys. Rev. Lett.* **112**, 023904 (2014).
- [54] S. F. Liew and H. Cao, *Opt. Express* **23**, 11043 (2015).

Chapter 7

Control of energy density inside disordered medium by coupling to open or closed channels using adaptive wavefront shaping

7.1 Introduction

¹ It has long been known that in disordered media there are many fascinating and surprising effects resulting from interferences of multiply scattered waves [2, 3]. As described in chapter 6, one of such effects is the creation of transmission eigenchannels which can be broadly classified as either open or closed [4, 5]. The existence of high-transmission (open) channels allows for an optimally prepared coherent input beam to be transmitted through a lossless diffusive medium with order unity efficiency. In contrast, waves injected into low-transmission (closed) channels barely penetrate the medium and are mostly reflected. As seen in chapter 6, in general, the penetration

1. This chapter is primarily based on the journal article published in ref. [1].

depth and energy density distribution of multiply scattered waves inside a disordered medium are determined by the spatial profiles of the transmission eigenchannels that are excited by the incident light. The distinct spatial profiles of open and closed channels suggest that selective coupling of incident light to these channels enables effective control of total transmission and energy distribution inside the random medium [6,7]. Since the energy density determines the light-matter interactions inside a scattering system, manipulating its spatial distribution opens the door to tailoring optical excitations as well as linear and nonlinear optical processes such as absorption, emission, amplification, and frequency mixing inside turbid media. The potential applications range from photovoltaics [8,9], white LEDs [10] and random lasers [11], to biomedical sensing [12] and radiation treatments [13].

In recent years there have been numerous theoretical and experimental studies on transmission eigenchannels [6,14–18]. While by knowing the transmission matrix, one can determine their profiles [19–22], it is difficult to directly probe their spatial profiles inside three-dimensional (3D) random media. So far, the open and closed channels have been observed only with acoustic wave inside a two-dimensional (2D) disordered waveguide [23], but controlling the energy density distribution has not been realized due to lack of an efficient wavefront modulator for acoustic wave or microwave radiation. The advantage of optical waves is the availability of spatial light modulators (SLMs) with many degrees of freedom. However, the commonly used samples in optical experiment have an open slab geometry, thus making it impossible to control all input modes due to limited numerical aperture of the imaging optics. Such incomplete control dramatically weakens the open channels [24], although a notable enhancement of total transmission has been achieved [21,25]. Furthermore, an enhancement of total energy stored inside a 3D scattering sample has been reported [26], but a direct probe and control of the optical intensity distribution inside the scattering medium are still missing.

In this chapter, we demonstrate experimentally the control of the energy density distribution inside a scattering medium. Instead of the open slab geometry, we fabricate a silicon waveguide that contains scatterers and has reflecting sidewalls. The intensity distribution inside the two-dimensional waveguide is probed from the third dimension. With careful design of the on-chip coupling waveguide, we can access all the input modes. Such control of the incident wavefront enables an order of magnitude enhancement of the total transmission or a 50 times suppression. A direct probe of the optical intensity distribution inside the disordered waveguide reveals that selective excitation of open channels results in the buildup of energy deep inside the scattering medium, while the excitation of closed channels greatly reduces the penetration depth. Compared to the linear decay for random input fields, the optimized wavefront can produce an intensity profile that is either peaked near the center of the waveguide or decays exponentially with depth. The total energy stored inside the waveguide is increased 3.7 times or decreased 2 times.

7.2 Design of the coupling waveguide and the disordered nanostructures

The 2D waveguide structure for this experiment is fabricated in a 220 nm silicon layer on top of 3 μm buried oxide by electron beam lithography and reactive ion etching [7]. As shown in Fig. 7.1, air holes are randomly distributed within the waveguide whose sidewalls are a photonic crystal that reflects light. At the probe wavelength $\lambda = 1.51 \mu\text{m}$, the transport mean free path $\ell = 2.5 \mu\text{m}$ is much less than the length $L = 50 \mu\text{m}$ of the disordered waveguide, so that light transport is diffusive. The out-of-plane scattering, which provides a direct probe of light transport inside the random structure, can be treated as loss and the diffusive dissipation length is $\xi_a = 31 \mu\text{m}$. The values of ℓ and ξ_a are extracted from the measured intensity distribution and intensity

fluctuations inside the disordered waveguide for uncontrolled illumination [27]. The waveguide of width $W = 15 \mu\text{m}$ supports $N = 56$ transmission eigenchannels, among which ~ 5 are open channels and the rest are closed channels. The total transmission for uncontrolled illumination is about 4.8%.

The probe light is injected into the waveguide from the edge of the wafer. Due to the large mismatch of the refractive index between silicon and air, the light can be coupled only to the lower-order modes of the ridge waveguide. This limits the number of input modes that can be controlled by wavefront shaping. To increase the degree of input control, the coupling waveguide (lead) is tapered at an angle of 15° [Fig. 7.1(a)]. The wider waveguide at the front end supports many more lower-order modes, which can be excited by the incident light and then converted to high-order modes by the taper.

To select the parameters for the tapered lead, we compute the degree of control for the optical field at the end of the lead that will be injected to the disordered waveguide. We simulate light propagation through the tapered waveguide using the Finite Element Method (COMSOL) and KWANT [28]. At the entrance of the lead ($z = 0$), only low-order modes (up to $M_1 - \text{th}$ order) of the waveguide (of width W_1) are excited with constant amplitude and random phase. The incident electric field can be written as

$$E(y, z = 0) = \sum_{m=1}^{M_1} e^{i\theta_m} \phi_m(y).$$

where $\phi_m(y)$ represents the transverse field profile for the $m - \text{th}$ guided mode, and θ_m is the initial phase. We calculate electric field distribution at the end of the lead $E_n(y, z = L_1)$, where the subscript n denotes different set of random phases θ_m assigned to the input field. L_1 is the length of the tapered lead. Then we construct the covariance matrix,

$$C(y, y') = \langle E_n(y) E_n^*(y') \rangle_n,$$

where $\langle \rangle_n$ represents averaging over random input wave-fields. The eigenvalues of $C(y, y')$ are computed and plotted in Fig. 7.2 for a tapered waveguide of $W_1 = 85 \mu\text{m}$, $W = 15 \mu\text{m}$, and $L_1 = 100 \mu\text{m}$. The sudden drop of the eigenvalues in Fig. 7.2 gives the number of significant eigenvalues, which corresponds to the number of independent spatial modes M that are controlled by varying the input field [Fig. 7.2]. We compute M for many tapered waveguides of different dimensions, and find $M = N$ as long as M_1 exceeds the number of transverse modes N at the end of the lead (of width W).

In the experiment, the number of low-order modes in the coupling waveguide that are excited by the incident light, M_1 , depends on the numerical aperture (NA) of the objective we use to couple light into the silicon waveguide, the refractive index contrast at the silicon/air interface, the width W_1 and NA of the silicon waveguide. For the fabricated sample in Fig. 7.1, $W_1 = 330 \mu\text{m}$, the total number of waveguide modes at the front of the taper is 1245. The numerical aperture of the objective (NA = 0.7) determines the range of incident angle for light illuminating the front facet of the silicon waveguide. From the silicon/air index contrast, we calculate the angular range of light that is coupled into the waveguide, and then obtain the number of waveguide modes that are excited by the incident light, $M_1 = 359$. We intentionally make M_1 much larger than $N = 56$, to ensure all input modes to the disordered waveguide are accessed experimentally. In addition, we adjust the incident beam size to completely fill the pupil of the objective, so that the entire numerical aperture of the objective is used to couple light into the lead.

7.3 Wavefront shaping experiment

The wavefront shaping experiment is shown schematically in Fig. 7.3(a). A monochromatic laser beam is phase modulated by an SLM and then focused to the edge of the

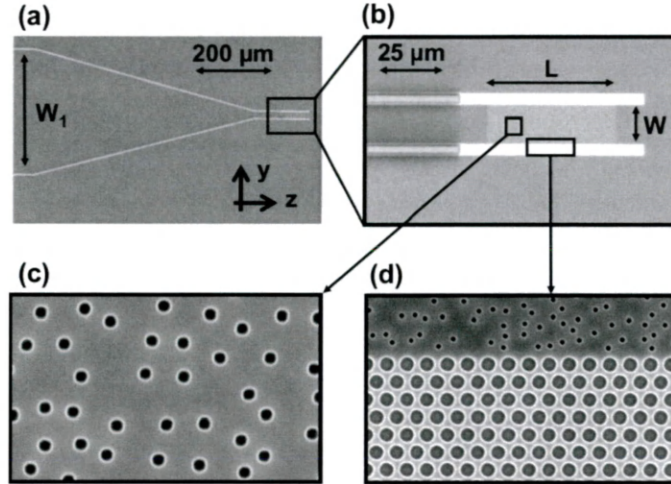


Figure 7.1: On-chip disordered waveguide with a tapered lead. (a) Top-view scanning electron micrograph (SEM) of a fabricated silicon waveguide. A ridge waveguide (lead) is tapered from the width $W_1 = 330 \mu\text{m}$ at the edge of the wafer to the width $W = 15 \mu\text{m}$, in order to increase the degree of control of the light that is injected to the disordered waveguide. (b) Magnified SEM of the disordered region of the waveguide that consists of a random array of air holes (diameter = 90 nm). (c) Magnified SEM showing the air holes distributed randomly within the waveguide with a filling fraction of 6 %. (d) The sidewalls of the waveguide are made of a triangular lattice of air holes (diameter = 360 nm) with a lattice constant of 505 nm, which supports a full photonic bandgap at the wavelength $\lambda = 1.51 \mu\text{m}$.

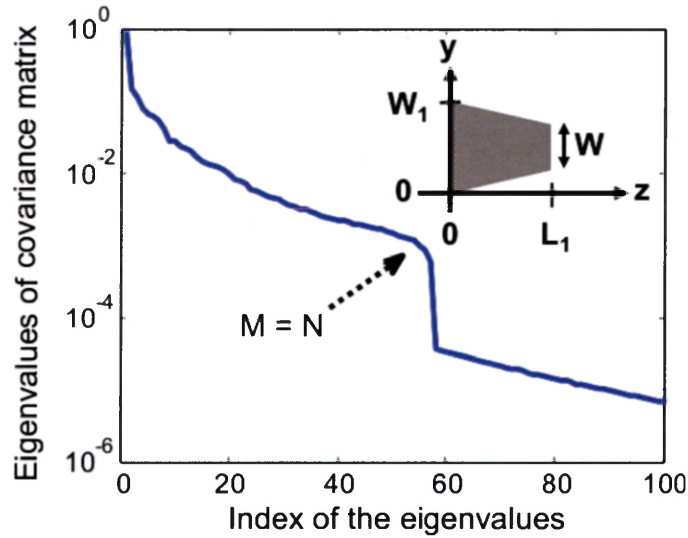


Figure 7.2: Semi-log plot of the eigenvalues of the covariance matrix $C(y, y')$ for the electric field $E_m(y, z = L_1)$ at the end of a tapered lead with $W_1 = 85 \mu\text{m}$, $W = 15 \mu\text{m}$, and $L_1 = 100 \mu\text{m}$. The inset is a schematic of the geometry. The sudden drop of eigenvalues gives the number of significant eigenvalues, $M = 56$, which is equal to the number of waveguide modes $N = 56$ at the end of the lead $z = L_1$.

wafer by a microscope objective of numerical aperture (NA) 0.7. To produce a line of illumination at the input facet of the coupling waveguide, the SLM imposes phase modulation only along one dimension that is parallel to the transverse direction of the waveguide, as shown by the 2D phase mask in Fig. 7.3(a). The light that is scattered out of plane by the random array of air holes is collected by an objective and projected to an InGaAs Camera to obtain the spatial distribution of the intensity, $I(y, z)$, inside the disordered structure [Fig 7.3(c)]. In the wavefront shaping experiment, we modulate the phases of 300 macro-pixels on the SLM. Each macro-pixel is a group of 2×792 SLM pixels, and has the dimension 0.04×15.8 mm. Since the SLM plane is projected onto the pupil plane of the objective (O_1), the phase modulation is applied to the phase space instead of the real space.

Two wavefront shaping approaches have been developed for the transmission enhancement, one is based on the measurement of transmission matrix [29,30]; the other relies on feedback [31]. While the open channels can be obtained from the measured transmission matrix, the closed channels are subject to measurement noise due to nearly vanishing transmission. Here we took the feedback approach, and optimized the procedure using the continuous sequential algorithm [31] to control the energy density inside the disordered waveguide.

To optimize the throughput of the disordered waveguide, we choose the cost function S to be the ratio of light intensity integrated over an area in the back part of the waveguide to that in the front part [marked by two rectangles in Fig. 7.3(c)]. To smooth out the fluctuation, the intensity is integrated over an area of length d and width W . Experimentally we varied d from $2l$ to $7l$, where $l = 2.5 \mu\text{m}$ is the transport mean free path, and the final results obtained via optimization are robust. If d is less than $2l$, the spatial averaging is not sufficient to smooth out the intensity fluctuation. The data shown in Fig. 7.4 are obtained with $d = 4.5l$. To ensure the convergence of the optimization algorithm, the phases of all macro-pixels are ad-

justed in two sequential rounds. The final value of the cost function S depends on the initial phase pattern for the optimization algorithm, but the variation is less than 10%. The final distribution of light intensity across the disordered waveguide $I(y, z)$ also changes with the initial phase pattern, but the cross-section-averaged intensity $I(z)$ has almost the same profile. Thus the data obtained from different initial phase patterns are averaged to reduce fluctuations.

To avoid experimental artifacts it is crucial to optimize the intensity ratio instead of the intensity integrated over the entire scattering sample, because the adaptive wave front shaping can change not only the energy distribution inside the sample, but also the transmission through the optical system that delivers light from the SLM to the sample. If we were to maximize or minimize the total energy within the disordered waveguide, the optimization algorithm might find a wavefront that enhances or suppresses the light delivery to the sample through the lens and the objective [25].

7.4 Experimental results and comparison to numerical simulations

First we maximize S to enhance light penetration into the scattering structure. Figure 7.4(b) shows the final intensity distribution $I(y, z)$ for the optimized input. In Fig. 7.4(e) we plot the cross-section-averaged intensity $I(z) = \int_0^W I(y, z)dy$, further averaged over four wavelengths and three initial phase patterns that served as the seed to the optimization algorithm. $I(z)$ is peaked near the center of the disordered waveguide in Fig. 7.4(e), which is dramatically different from the monotonic decay with random input fields in Fig. 7.4(d). The latter profile is in agreement with the prediction of the diffusion theory and the slight deviation from a linear decay is caused by the out-of-plane scattering loss. The dissipation causes an asymmetry

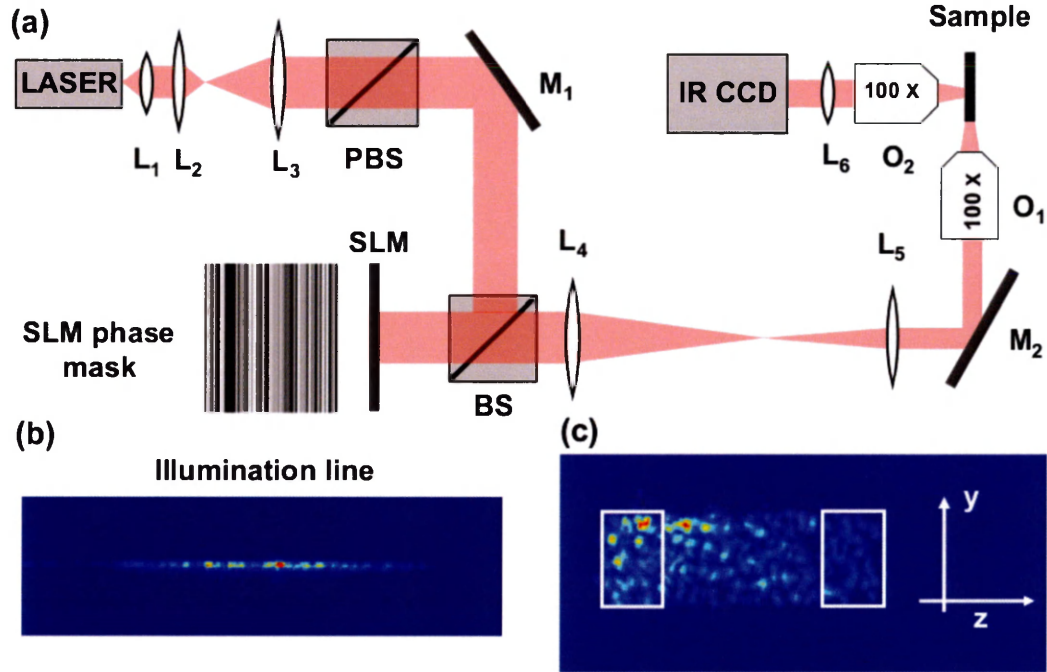


Figure 7.3: Wavefront shaping experiment to control intensity distribution inside a disordered waveguide. (a) A schematic of the experimental setup. A laser (HP 8168F) output at $\lambda = 1510$ nm is collimated (by lens L_1), expanded (by L_2 , L_3) and linearly polarized (by a polarized beam splitter PBS) before being modulated by a phase-only SLM (Hamamatsu X10468). Two lens (L_4 , L_5) are used to project the SLM plane to the pupil plane of an objective O_1 (100 \times , NA = 0.7), and the edge of the wafer is placed at the focal plane. The SLM imposes phase modulation only in one direction in order to generate a line at the front end of the coupling waveguide. A sample phase pattern on the SLM is shown. The light scattered out of the sample plane is collected by another objective O_2 (100 \times , NA = 0.7) and imaged to an InGaAs camera (Xenics XEVA 1.7-320) by a tube lens (L_6). M_1 and M_2 are mirrors, BS is beam splitter. (b) An optical image of the illumination line ($330 \times 1.1 \mu\text{m}$) on the waveguide facet. The input intensity is modulated along the line. (c) An image of the spatial distribution of light intensity inside the disordered waveguide for a random input wavefront. The spatial resolution is about $1.1 \mu\text{m}$. The ratio S of the integrated intensities over the two rectangles at the back and front side of the waveguide is used as feedback for optimizing the input wavefront.

in the optimized intensity distribution with respect to the center of the waveguide ($z/L = 0.5$), as the peak of $I(z)$ in Fig. 7.4(b) shifts towards the input end. The resemblance of the optimized $I(z)$ to the spatial profile of open channels indicates that the optimized wavefront couples light to the high-transmission eigenchannels.

Next we minimize S by adapting the input wavefront, and the resulting intensity distribution is presented in Fig. 7.4(c). The cross-section-averaged intensity $I(z)$ in Fig. 7.4(f) exhibits a much faster decay with depth than the random input. Moreover, the decay is clearly exponential, resembling the spatial profile of closed channels. Despite the presence of measurement noise, the optimized wavefront couples effectively to the low-transmission eigenchannels.

To confirm the experimental results, we simulate a 2D disordered waveguide with all parameters equal to the experimental values [28]. The phase-only modulation is imposed on the input wavefront to optimize the same cost function S with the continuous sequential algorithm. The solid curves in Fig. 7.4(d,e,f) represent the simulation results, which agree well with the experimental data. The curves are normalized such that the total incoming flux is equal to unity in all cases. Therefore, the intensity profiles can be quantitatively compared to get the order of magnitude of intensity amplification within the scattering sample.

By projecting the optimized fields onto the transmission eigenchannels, we obtain the contributions from individual channels. Figure 7.5(a) presents the weight w of each channel as a function of the transmission eigenvalue τ in the case that the cost function S is maximized [Fig. 7.4(b,e)]. In comparison to a random input field which has equal contributions from all channels $w(\tau) = 1/N$, the optimized field for maximum S has greatly enhanced contributions from the high transmission channels and reduced contributions from the low-transmission channels [Fig. 7.5(a)]. While the maximum transmission channel has the largest weight, a few channels with slightly lower transmission also make significant contributions. Thus the energy

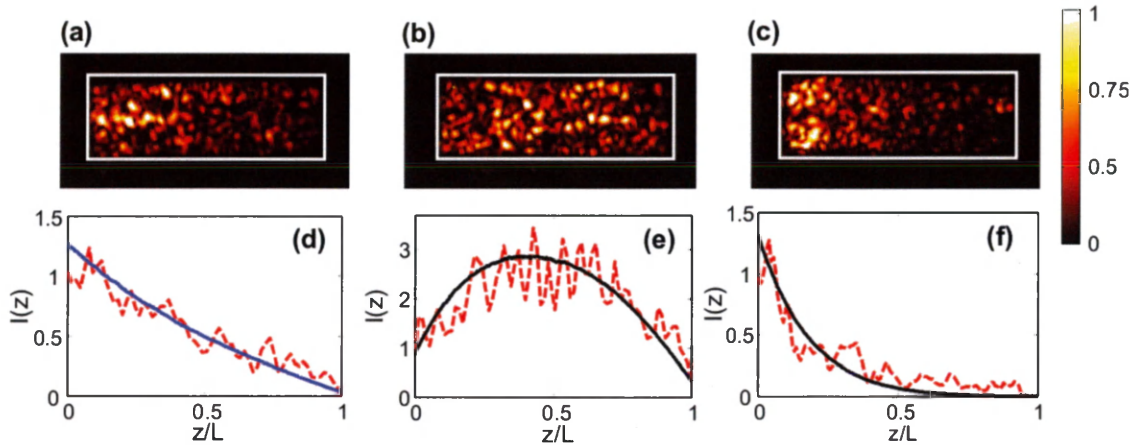


Figure 7.4: Experimental control of intensity distribution inside the disordered waveguide. (a, b, c) Two-dimensional intensity distribution $I(y, z)$ inside the disordered waveguide shown in Fig. 7.1 for (a) random input fields, (b) optimized input for maximum light penetration (maximizing S). (c) optimized input for minimum light penetration (minimizing S). (d, e, f) The cross-section-averaged intensity, $I(z)$, obtained from $I(y, z)$ in (a, b, c). Dashed lines are experimental data and solid lines are simulation results.

density distribution $I(z)$ is slightly lower than that of the maximum transmission channel, and shifted a bit towards the front end of the waveguide [Fig. 7.5(b)]. As shown in Fig. 7.5(a), the weight $w(\tau)$ increases exponentially with τ , in contrast to the linear increase of w with τ in the case of focusing (maximizing intensity of a single speckle) through a random medium. This difference indicates maximizing S is more efficient for enhancing the contribution of the maximum transmission channel over all other channels.

When S is minimized [Fig. 7.4(c,f)], the weights of high-transmission channels are strongly suppressed, especially the highest transmission channel [Fig. 7.5(c)]. While many low-transmission channels have slightly increased weights as compared to the random input field, none of them becomes dominant. Since the low-transmission channels have exponential decay with different decay lengths, the total intensity distribution $I(z)$ obtained by minimizing S also decays exponentially, but the decay

length is longer than that of the minimum transmission channel [Fig. 7.5(d)].

The numerical simulation confirms that our wavefront shaping experiment results in selective coupling of the input light to open or closed channels, which leads to distinct intensity distribution inside the scattering waveguide. The total transmission is increased from $\sim 4.8\%$ (for random input fields) to $\sim 47\%$ (when S is maximized), and the total energy inside the disordered structure is enhanced 3.7 times. The minimization of S makes the total transmission drop to $\sim 0.1\%$, and the total energy inside is reduced by a factor of 2.

Finally we compare numerically the feedback-based approach to the transmission-matrix approach by computing the transmission eigenchannels from the field transmission matrix. With phase-only modulation, the input field for a transmission eigenchannel is decomposed by the waveguide modes, and the amplitude of the decomposition coefficients are set to a constant. The removal of amplitude modulation mixes the maximum transmission channel with other channels, as seen in Fig. 7.5(a). While the weight of the maximum transmission channel decreases from unity to $\pi/4$ [32], all other channels have a constant weight $(1 - (\pi/4))/(N - 1)$. The cross-section-averaged intensity distribution $I(z)$ is nearly identical to that obtained by maximizing S [Fig. 7.5(b)]. Similarly, elimination of amplitude modulation from the minimum transmission channel introduces contributions from all other channels [Fig. 7.5(c)]. Their weights are equal (independent of their transmission), albeit smaller than that of the minimum transmission channel. Consequently, $I(z)$ displays a rapid decay at shallow depths, due to the dominant contribution from the minimum transmission channel; it is followed by a much slower decay at large depth due to the contributions of the remaining channels including the highly transmitting ones. The total transmission is $\sim 1\%$, approximately an order of magnitude higher than that obtained by minimizing S . This is attributed to the stronger suppression of the higher transmission channels by the feedback approach, i.e., the higher the transmission eigenvalue, the

lower the weight. Therefore, with phase-only modulation of incident wavefront, the feedback approach is far more efficient in minimizing the total transmission than the transmission-matrix approach.

In summary, we apply the adaptive wavefront shaping technique to on-chip disordered nanostructures. Careful design of the coupling waveguide enables access to all input modes and allows us to reach the maximum or minimum transmission that is achievable with phase-only modulation. Selective excitation of the open or closed channels results in the variation of the optical intensity distribution from an exponential decay to a linear decay and to a profile peaked near the center of the random system. The coherent control of multiple-scattering interference leads to diverse transport behaviors in contrast to universal diffusion, highlighting the possibility of controlling light-matter interactions in turbid media.

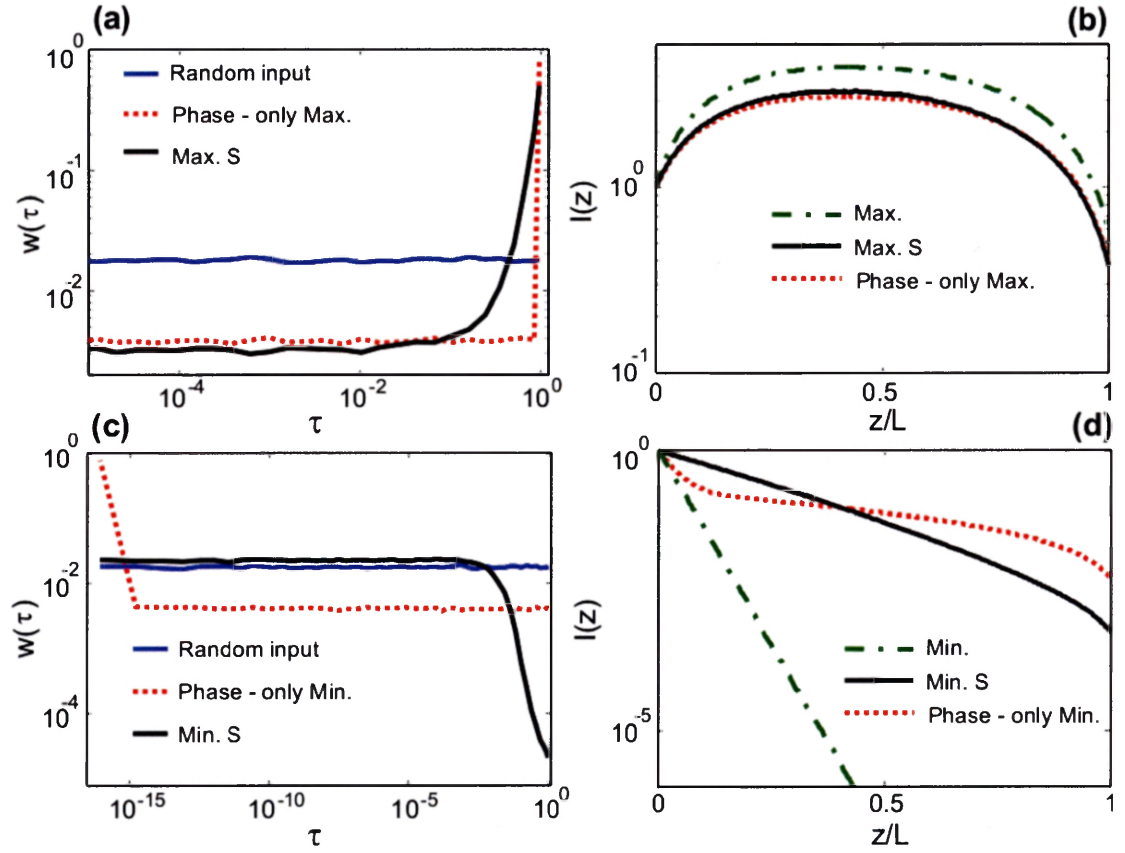


Figure 7.5: Numerical simulation of wavefront shaping experiment. (a,c) Weight $w(\tau)$ of each transmission eigenchannel in the input field obtained by maximizing (a) or minimizing (c) light penetration into the disordered waveguide with the cost function S (black solid line). For comparison, $w(\tau)$ for the random input field (blue solid line), and for the input field of the maximum (a) or minimum (c) transmission eigenchannel after removal of amplitude modulation (red dotted line) are also shown. (b,d) Cross-section-averaged intensity distribution $I(z)$ for the maximized (b) or minimized (d) S (black solid line), as well as the maximum (b) or minimum (d) transmission channel with (green dash-dotted line) and without amplitude modulation (red dotted line).

Bibliography

- [1] R. Sarma, A. Yamilov, S. Petrenko, Y. Bromberg, and H. Cao, *Phys. Rev. Lett.* **117**, 086803 (2016).
- [2] M. C. W. van Rossum and T. M. Nieuwenhuizen, *Rev. Mod. Phys.* **71**, 313 (1999).
- [3] E. Akkermans and G. Montambaux, *Mesoscopic Physics of Electrons and Photons* (Cambridge University Press, Cambridge, 2007).
- [4] O. N. Dorokhov, *Solid State Commun.* **51**, 381 (1984).
- [5] Y. Imry, *Europhys. Lett.* **1**, 249 (1986).
- [6] M. Davy, Z. Shi, J. Park, C. Tian, and A.Z. Genack, *Nat. Commun.* **6**, 6893 (2015).
- [7] R. Sarma, A. Yamilov, S. F. Liew, M. Guy, and H. Cao, *Phys. Rev. B* **92**, 214206 (2015).
- [8] K. Vynck, M. Burreli, F. Riboli, and D. S. Wiersma, *Nat. Mat.* **11**, 1017 (2012).
- [9] D. S. Wiersma, *Nat. Photon.* **7**, 188 (2013).
- [10] V. Y. F. Leung, A. Lagendijk, T. W. Tukker, A. P. Mosk, W. L. Ijzerman, and W. L. Vos, *Opt. Exp.* **22**, 8190 (2014).
- [11] X. Cheng and A. Z. Genack, *Opt. Lett.* **39**, 6324 (2014).

- [12] Q. Song, S. Xiao, Z. Xu, V. M. Shalaev, and Y. L. Kim, *Opt. Lett.* **35**, 2624 (2010).
- [13] J. Yoon, M. Lee, K. Lee, N. Kim, J. M. Kim, J. Park, H. Yu, C. Choi, W. Do Heo, and Y. Park, *Scientific Reports* **5** (2015).
- [14] I. M. Vellekoop and A. P. Mosk, *Phys. Rev. Lett.* **101**, 120601 (2008).
- [15] A. P. Mosk, A. Lagendijk, G. Lerosey, and M. Fink, *Nat. Photon.* **6**, 283 (2012).
- [16] W. Choi, A. P. Mosk, Q. H. Park, and W. Choi, *Phys. Rev. B* **83**, 134207 (2011).
- [17] A. Pena, A. Girschik, F. Libisch, S. Rotter, and A. A. Chabanov, *Nat. Commun.* **5** (2014).
- [18] S. F. Liew, S. M. Popoff, A. P. Mosk, W. L. Vos, and H. Cao, *Phys. Rev. B* **89**, 224202 (2014).
- [19] S. M. Popoff, G. Lerosey, R. Carminati, M. Fink, A. C. Boccara, and S. Gigan, *Phys. Rev. Lett.* **104**, 100601 (2010).
- [20] Z. Shi and A. Z. Genack, *Phys. Rev. Lett.* **108**, 043901 (2012).
- [21] M. Kim, Y. Choi, C. Yoon, W. Choi, J. Kim, Q. H. Park, and W. Choi, *Nat. Photon.* **6**, 581 (2012).
- [22] H. Yu, T. R. Hillman, W. Choi, J. O. Lee, M. S. Feld, R. R. Dasari, and Y. K. Park, *Phys. Rev. Lett.* **111**, 153902 (2013).
- [23] B. Gerardin, J. Laurent, A. Derode, C. Prada, and A. Aubry, *Phys. Rev. Lett.* **113**, 173901 (2014).
- [24] A. Goetschy and A. D. Stone, *Phys. Rev. Lett.* **111**, 063901 (2013).

- [25] S. M. Popoff, A. Goetschy, S. F. Liew, A. D. Stone, and H. Cao, *Phys. Rev. Lett.* **112**, 133903 (2014).
- [26] O. S. Ojambati, H. Yilmaz, A. Lagendijk, A. P. Mosk, and W. L. Vos, *New Jour. of Phys.* **18**, 043032 (2016).
- [27] R. Sarma, A. Yamilov, P. Neupane, and H. Cao, *Phys. Rev. B* **92**, 180203 (2015).
- [28] C. W. Groth, M. Wimmer, A. R. Akhmerov, and X. Waintal, *New Jour. of Phys.* **16**, 063065 (2014).
- [29] M. Kim, W. Choi, Y. Choi, C. Yoon, and W. Choi, *Optics Express* **23**, 12648 (2015).
- [30] H. Yu, J. Park, K. Lee, J. Yoon, K. Kim, S. Lee, and Y. Park, *Current Applied Physics* **15**, 632 (2015).
- [31] I. M. Vellekoop, *Optics Express* **23**, 12189 (2015).
- [32] I. M. Vellekoop, E. G. Van Putten, A. Lagendijk, and A. P. Mosk, *Optics Express* **16**, 67 (2008).

Chapter 8

Control of light transport inside a random medium with inhomogeneous scattering and loss

8.1 Introduction

¹ In recent years there have been rapid advances in coherent control of light propagation in strong scattering media [2]. It has been shown that light can be focused inside or through a turbid medium by shaping the input wavefront [3], which enables image transmission through an opaque material [4]. As shown in the previous chapter and other experiments, wavefront shaping techniques have also been used to enhance the total transmission of light through a diffusive system via selective coupling of incident light to high transmission channels [5–10]. These studies have important implications in biophotonics and biomedical applications [11,12]. However, in real samples such as biological tissues, the amount of light scattering often varies spatially. So far all the samples in wavefront shaping experiments are homogeneous, namely, the scattering

1. This chapter is primarily based on the journal article published in ref. [1].

strength is constant everywhere. Coherent control of light transport has not been demonstrated in inhomogeneous samples and the power of wavefront shaping in such systems is not known.

Light absorption is common in optical systems, and it can strongly modify high transmission channels. With strong absorption uniformly spread across a scattering medium, the diffusive transport of light in the maximum transmission channel turns into quasi-ballistic [13]. In reality, optical absorbers are often distributed non-uniformly in random samples, and the high transmission channels redirect the energy flow to circumvent the absorbing regions to minimize attenuation [14]. These results are obtained from numerical simulations, and there has been no experimental study yet. Further, it is not clear what will happen when both scattering and absorption are spatially inhomogeneous.

In this chapter, we adopt the adaptive wavefront shaping approach to enhance light transmission through a disordered waveguide with spatially inhomogeneous scattering and loss. The silicon waveguide contains randomly distributed air holes within photonic crystal sidewalls. The degree of input control is much higher than that in the open slab geometry, thanks to an on-chip tapered lead. Light transport inside the two dimensional waveguide can be directly probed from the third dimension. After optimizing input wavefront to enhance the total transmission, we observe that optical waves bypass the region of higher scattering and loss in the waveguide. The spatial inhomogeneity of scattering and loss leads to redirecting of energy flux to optical paths with less scattering and loss, in order to maximize the total energy transported through the system. The experimental data agree to the numerical simulation results, revealing how a high transmission channel is modified by spatially inhomogeneous scattering and loss.

8.2 2D random waveguide with inhomogeneous scattering and loss

The disordered waveguide is fabricated in a silicon-on-insulator (SOI) wafer. The thickness of the silicon layer and of the buried oxide are 220 nm and 3 μm , respectively. The patterns are made by electron beam lithography and etched by an inductively-coupled-plasma (ICP) reactive-ion-etcher (RIE). Figure 8.1 is the scanning electron microscope (SEM) image of a fabricated sample. The waveguide is $L = 60 \mu\text{m}$ long and $W = 20 \mu\text{m}$ wide. It contains a two-dimensional (2D) random array of air holes. While propagating in the waveguide, light is scattered both in plane and out of plane by the air holes. The out-of-plane scattering can be treated as loss, and the material absorption at the probe wavelength ($\lambda = 1510 \text{ nm}$) is negligible [15].

To introduce spatially inhomogeneous scattering and loss, we vary the size and density of air holes in the waveguide. In a central region of diameter 10 μm , the air holes are larger and denser (hole diameter = 150 nm, air filling fraction = 15 %), leading to stronger in-plane scattering and out-of-plane scattering. Outside this region the scattering and loss are weaker, as the air holes are smaller (diameter = 90 nm) and the filling fraction is lower (6 %).

The relevant parameters to describe light propagation in the disordered waveguide are the transport mean free path ℓ and the diffusive dissipation length ξ_a . Their values in the two regions of different air hole size and density are extracted from the measurement of intensity distributions and fluctuations in two separate waveguides with homogeneous scattering and loss [16]. In the central region, $\ell = 1 \mu\text{m}$ and $\xi_a = 13 \mu\text{m}$; in the surrounding region, $\ell = 2.5 \mu\text{m}$ and $\xi_a = 31 \mu\text{m}$.

The waveguide has reflecting sidewalls made of a triangular lattice of air holes (diameter = 360 nm, lattice constant = 550 nm). It supports an in-plane photonic bandgap at the probe wavelength, that confines the scattered light within the wave-

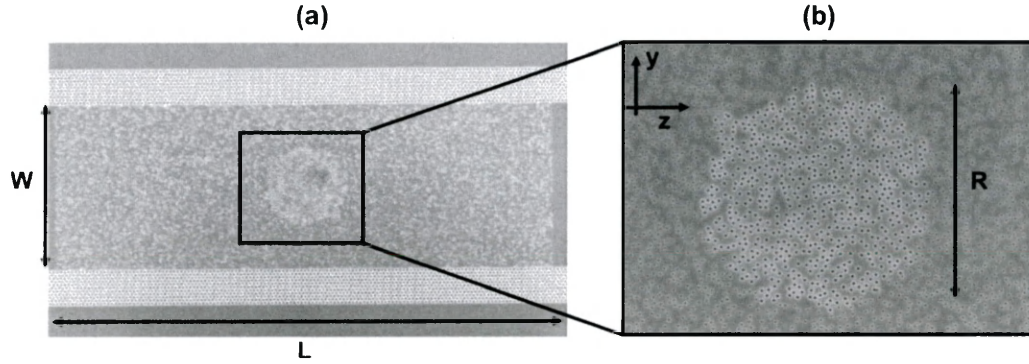


Figure 8.1: 2D disordered waveguide with inhomogeneous scattering and loss. (a) Top-view scanning electron micrograph (SEM) of the fabricated silicon waveguide that consists of randomly positioned air holes. The waveguide width $W = 20 \mu\text{m}$, and length $L = 60 \mu\text{m}$. A circular region of diameter $10 \mu\text{m}$ at the center of the waveguide has larger and denser air holes (hole diameter = 150 nm , the air filling fraction = 15%). Outside this region, the air holes are smaller (diameter = 90 nm) and the filling fraction is lower (6%). The sidewalls of the waveguide are made of a triangular lattice of air holes (diameter = 360 nm , lattice constant = 505 nm), which supports an in-plane photonic bandgap at the wavelength $\lambda = 1.51 \mu\text{m}$. (b) Magnified SEM of the central region of the disordered waveguide showing air holes of two different sizes and densities.

uide. The incident light is injected from the edge of the wafer to a silicon ridge waveguide. Due to the refractive index mismatch between silicon and air, the light can only excite the lower-order modes of the ridge waveguide, limiting the number of input modes that could be controlled by wavefront shaping. As shown in the previous chapter, to increase the degree of input control, we design and fabricate a tapered waveguide that serves as a lead to the disordered waveguide [10]. The tapering angle is 15° , and the waveguide width is reduced from $330 \mu\text{m}$ to $20 \mu\text{m}$ over a length of $578 \mu\text{m}$. The wider waveguide at the input supports many more lower-order modes that are converted to higher-order modes by the taper. The numerical simulation confirmed that the number of waveguide modes excited at the air-silicon interface by the incident light is significantly larger than the number of transmission channels in the disordered waveguide $N = 75$.

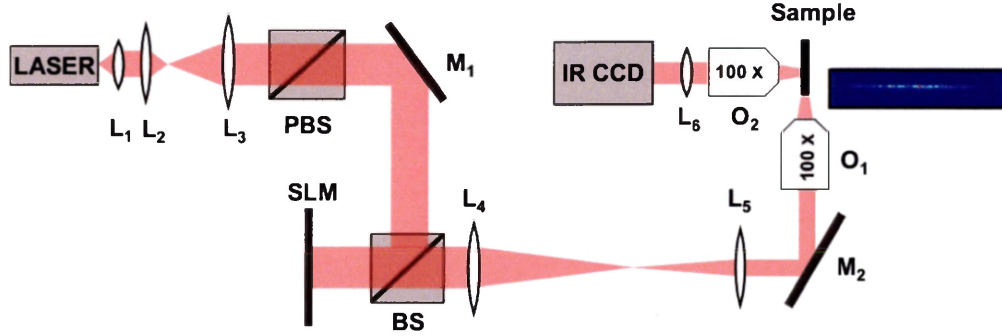


Figure 8.2: A schematic of the wavefront shaping experiment setup. A laser beam (HP 8168F) at $\lambda = 1510$ nm is collimated (by lens L_1), expanded (by L_2 , L_3), and linearly polarized (by a polarized beam splitter PBS) before being modulated by a phase-only SLM (Hamamatsu X10468). Two lens (L_4 , L_5) are used to project the SLM plane to the pupil plane of an objective O_1 (100 \times , NA = 0.7), and the edge of the coupling waveguide is placed at the focal plane of the objective. The light scattered out of the sample plane is collected by a second objective O_2 (100 \times , NA = 0.7) and imaged to an InGaAs camera (Xenics XEVA 1.7-320) by a tube lens (L_6). M_1 and M_2 are mirrors, BS is an unpolarized beam splitter. The inset is an optical image of the illumination line on the front facet of the coupling waveguide, created by modulating the phase of the SLM pixels.

8.3 Experimental setup and results

To control light transport in the disordered waveguide, we adopt the adaptive wavefront shaping scheme that we implemented for 2D on-chip waveguides in the previous chapter. The setup is shown again schematically in Fig. 8.2. A monochromatic laser beam is collimated, expanded and linearly polarized. It is then phase modulated by a spatial light modulator (SLM). The SLM plane is demagnified and projected to the pupil plane of an objective. At the focal plane of objective lies the front facet of the coupling waveguide. We impose one-dimensional phase modulation on the SLM to create a line of illumination for the coupling waveguide, as shown in the inset of Fig. 8.2. To map the spatial distribution of light intensity, $I(y, z)$, inside the disordered structure, the out-of-plane scattered light is collected by a second objective and projected to an InGaAs camera.

To enhance the total transmission through the disordered waveguide, we choose the feedback-based optimization technique, which is robust against measurement

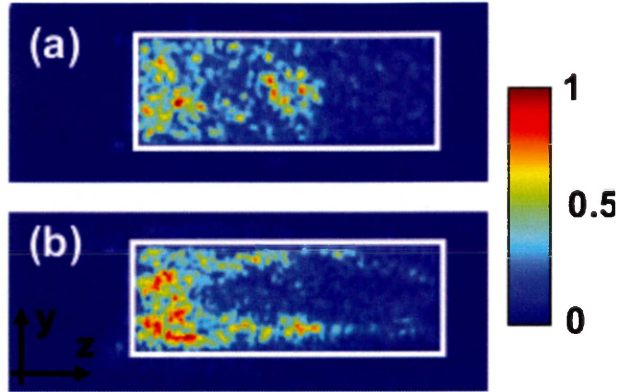


Figure 8.3: Optimizing the incident wavefront to enhance light transmission through the disordered waveguide with spatially inhomogeneous scattering and loss. Experimentally measured 2D intensity distribution $I(y, z)$ inside the waveguide shown in Fig. 8.1 for (a) unoptimized input fields, (b) optimized input for maximum cost function S . The white box marks the boundary of the disordered waveguide.

noise as shown in the previous chapter. The cost function S is given by the ratio of the cross-section integrated intensity of light at the back end of the waveguide to that at the front end. We use the continuous sequential algorithm to maximize S by adjusting the phase of SLM pixels [3]. Figures 8.3(a) and (b) show the intensity distribution $I(y, z)$ for an unoptimized input and an optimized input, respectively. When the input wavefront is not optimized, the light intensity decreases with the depth in the disordered waveguide. Stronger out-of-plane scattering brightens the central region that has larger and denser air holes. In contrast, the optimized input wavefront makes the central region dark, meanwhile the intensities on both sides of this region increases. Such changes indicate that light bypasses the central region with higher scattering and loss to maximize the total energy transported through the medium.

8.4 Numerical simulations

For a better understanding of the experimental results, in order to understand the energy flow for optimized input, we perform a numerical simulation [17] to calcu-

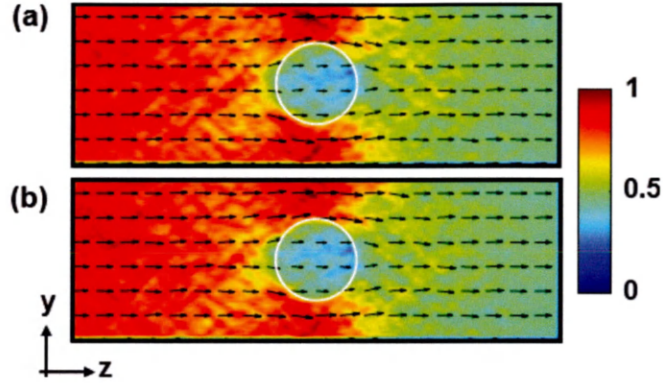


Figure 8.4: Numerical simulation of the ensemble averaged Poynting vector $\vec{J}(y, z)$ of light inside the 2D disordered waveguide with spatially inhomogeneous scattering and loss. The magnitude of $\vec{J}(y, z)$ is shown by color plot, and its direction is shown by the arrows. The input field in (a) is optimized to maximize total transmission. With optimized input wavefront, the optical waves bypass the region of higher scattering and loss in the middle of the waveguide (denoted by a white circle). (b) shows $\vec{J}(y, z)$ for the maximum transmission channel, which is nearly identical to that in (a), indicating the optimized input field couples mostly to the maximum transmission channel.

late the ensemble averaged Poynting vector $\vec{J}(y, z)$ for an optimized input of a 2D disordered waveguide with all parameters equal to the experimental values. Similar to the previous chapter, the continuous sequential algorithm is used to optimize the total transmission via phase-only modulation of the input wavefront. The total transmission increases from 3.2% with unoptimized input to 42% with optimized input. Figure 8.4(a) plots the magnitude and direction of $\vec{J}(y, z)$ in the disordered waveguide for an optimized input. The optimized input wavefront makes the energy flux circumvent the central region with higher scattering and loss, in agreement to the experimental result. Further, Fig. 8.4(b) shows the magnitude and direction of $\vec{J}(y, z)$ of the maximum transmission channel, which resembles that of the optimized input in Fig. 8.4(a). This result suggests that with the optimized input wavefront, light transport is dominated by the maximum transmission channel. We confirmed this by decomposing the optimized input wavefront by the transmission eigenchannels. The contribution from the maximum transmission channel is significantly larger than all other channels. Therefore, the optimization of incident wavefront leads to selective

coupling of light to the high transmission channels.

In summary, we enhanced light transmission through a 2D waveguide with spatially inhomogeneous scattering and loss by shaping the wavefront of incident light. Using a tapered lead, we are able to access all input modes by a spatial light modulator. The optimized wavefront selectively couples light to high transmission channels, which bypass the regions of higher scattering and loss. This work demonstrates the power of wavefront shaping in controlling light transport in inhomogeneous scattering samples, which are common in real applications. In addition, these results may trigger further studies of on-chip disordered photonic nanostructures with spatially varying scattering strength and loss to mold the flow of light [18].

Bibliography

- [1] R. Sarma, A. Yamilov, and H.Cao, *arxiv* : **1610.06881**. (2016) (under review in Applied Physics Letters).
- [2] A. P. Mosk, A. Lagendijk, G. Lerosey, and M. Fink, *Nat. Photon.* **6**, 283 (2012).
- [3] I. M. Vellekoop, *Optics Express* **23**, 12189 (2015).
- [4] S. Popoff, G. Lerosey, M. Fink, A. C. Boccara, and S. Gigan, *Nat. Commun.* **1**, 81 (2010).
- [5] I. M. Vellekoop and A. P. Mosk, *Phys. Rev. Lett.* **101**, 120601 (2008).
- [6] W. Choi, A. P. Mosk, Q. H. Park, and W. Choi, *Phys. Rev. B* **83**, 134207 (2011).
- [7] M. Kim, Y. Choi, C. Yoon, W. Choi, J. Kim, Q. H. Park, and W. Choi, *Nat. Photon.* **6**, 581 (2012).
- [8] H. Yu, T. R. Hillman, W. Choi, J. O. Lee, M. S. Feld, R. R. Dasari, and Y. K. Park, *Phys. Rev. Lett.* **111**, 153902 (2013).
- [9] S. M. Popoff, A. Goetschy, S. F. Liew, A. D. Stone, and H. Cao, *Phys. Rev. Lett.* **112**, 133903 (2014).
- [10] R. Sarma, A. Yamilov, S. Petrenko, Y. Bromberg, and H.Cao, *Phys. Rev. Lett.* **117**, 086803 (2016).

- [11] M. Kim, W. Choi, Y. Choi, C. Yoon, and W. Choi, *Optics Express* **23**, 12648 (2015).
- [12] H. Yu, J. Park, K. Lee, J. Yoon, K. Kim, S. Lee, and Y. Park, *Current Applied Physics* **15**, 632 (2015).
- [13] S. F. Liew, S. M. Popoff, A. P. Mosk, W. L. Vos, and H. Cao, *Phys. Rev. B* **89**, 224202 (2014).
- [14] S. F. Liew and H. Cao, *Opt. Express* **23**, 11043 (2015).
- [15] A. Yamilov, R. Sarma, B. Redding, B. Payne, H. Noh, and H. Cao, *Phys. Rev. Lett.* **112**, 023904 (2014).
- [16] R. Sarma, A. Yamilov, P. Neupane, and H. Cao, *Phys. Rev. B* **92**, 180203 (2015).
- [17] C. W. Groth, M. Wimmer, A. R. Akhmerov, and X. Waintal, *New Jour. of Phys.* **16**, 063065 (2014).
- [18] M. Koirala and A. Yamilov, *Opt. Lett.* **41**, 3860 (2016).

Chapter 9

Finite Difference Time Domain Algorithm for Rotating Dielectric Structures

9.1 Introduction

¹ Optical gyroscopes have been widely used in industrial and military applications ranging from inertial navigation systems in aircrafts and vessels to control, stabilization, and positioning systems for robotics and virtual reality applications [2]. Compared to the mechanical gyros, optical gyros have higher sensitivity and lower drift rates. All optical rotation sensors exploit the Sagnac effect which is the phase difference between two counter-propagating waves along a closed-loop fiber or waveguide. Recently slow light structures, e.g., photonic crystals [3, 4] and coupled microresonators [5–9], have been explored for the realization of high-sensitivity miniaturized optical gyroscopes. In addition to the phase shift, a rotation-induced photonic bandgap has been suggested and studied [10]. All these optical gyros are passive

1. This chapter is primarily based on the journal article published in ref. [1].

in the sense that the light sources are external. The active gyros produce the two counter-propagating beams within the structures, and their frequency difference is often used as a measure of the rotation speed. Microcavity lasers have recently been investigated for ultrasmall active optical gyroscopes [11–14]. Wavelength-scale microdisk cavities have small footprints and can be made with current semiconductor fabrication technologies [11–13].

In the theoretical investigations of optical gyroscopes, diverse strategies have been undertaken, e.g., the direct modal analysis of time-dependent Maxwell equations in the laboratory frame [15, 16], the extension of tight-binding theory to electrodynamics of a rotating medium [3], and the two-dimensional Greens function in a rotating environment [17]. The numerical approaches include the extended transfer matrix method [6] and the finite-difference time-domain (FDTD) algorithm in a rotating frame [18]. The FDTD method is an ab-initio, time domain method that can simulate both steady state and transient processes. Analytical results are often difficult to be obtained for complex photonic structures with open boundaries, and the FDTD simulation provides a vital tool for the design and optimization of rotation sensors. An extensive and detailed analysis of the numerical dispersion, the dielectric boundary condition and the perfectly matched layer absorbing boundary conditions in the rotating FDTD model has been performed previously [18].

In this chapter, we modify the standard FDTD algorithm for stationary frame to rotating frame by incorporating the modified constitutive relations due to rotation, and simulate a wavelength-scale optical gyroscope based on a circular microdisk. Different from the previous FDTD model, which calculates only E and H , we calculate E , H , D , and B by solving simultaneously and separately the Maxwell equations and the constitutive relations in the rotating frame. We validate our FDTD codes by comparing the simulated frequency splitting of resonant modes of a circular disk to the analytical results.

9.2 FDTD algorithm for rotating frame

Basic physical laws governing electromagnetic fields are invariant under coordinate transformation including noninertial ones [18,19]. Maxwell equations therefore retain their form, and the transformation from the stationary frame to a rotating frame is manifested by the changes in the constitutive relations. Assume the medium rotates slowly with a constant angular velocity Ω around a fixed axis, such that $|\Omega L| \ll c$, where L is the maximum distance from the rotation axis, and c is the velocity of light in vacuum. The constitutive relations in the rotating frame to the first order of Ω are [14, 18, 19]:

$$\epsilon \vec{E} = \vec{D} + c^{-2} \vec{\Omega} \times \vec{r} \times \vec{H} \quad (9.1)$$

$$\mu \vec{H} = \vec{B} - c^{-2} \vec{\Omega} \times \vec{r} \times \vec{E} \quad (9.2)$$

We consider a dielectric disk of radius R in free space. The disk is in the $x - y$ plane and rotates around its center with $\vec{\Omega} = \Omega \hat{z}$. The disk can be considered as a two-dimensional system with an effective index of refraction n . It has been shown that in a rotating two-dimensional system the electromagnetic fields can be decomposed into transverse electric (TE) and transverse magnetic (TM) modes [17]. Without loss of generality, we concentrate on the TM modes in this thesis. For TM modes, the non-vanishing field components are E_z, D_z, H_x, H_y, B_x , and B_y , and the constitutive relations are reduced to

$$\epsilon E_z = D_z - c^{-2}(\Omega y H_y + \Omega x H_x) \quad (9.3)$$

$$\mu H_x = B_x - c^{-2}(\Omega x E_z) \quad (9.4)$$

$$\mu H_y = B_y - c^{-2}(\Omega y E_z) \quad (9.5)$$

The Maxwell equations remain the same in the rotating frame, and there are no free charges or currents in the microdisk systems. We adopt the Yee lattice and leapfrog scheme in our FDTD algorithm. All field components are updated with the Maxwell equations and the constitutive relations in a particular order:

$$\frac{\partial D_z}{\partial t} = \frac{\partial H_y}{\partial x} - \frac{\partial H_x}{\partial y} \quad (9.6)$$

$$\epsilon E_z = D_z - c^{-2}(\Omega y H_y + \Omega x H_x) \quad (9.7)$$

$$\frac{\partial B_x}{\partial t} = \frac{\partial E_z}{\partial y} \quad (9.8)$$

$$\frac{\partial B_y}{\partial t} = \frac{\partial E_z}{\partial x} \quad (9.9)$$

$$\mu H_x = B_x - c^{-2}(\Omega x E_z) \quad (9.10)$$

$$\mu H_y = B_y - c^{-2}(\Omega y E_z) \quad (9.11)$$

Equations 9.6, 9.8, and 9.9 are identical to those in the stationary frame, and we discretize them in space and time following the standard procedure of Yee algorithm for a stationary frame. Equations 9.6, 9.8, and 9.9 update D_z , B_x , and B_y , respectively. Equations 9.7, 9.10, and 9.11, which update E_z , H_x , and H_y , respectively, contain additional terms from rotation, which make the discretization complicated. For example, the discretized form of Eq. 9.7 in terms of Yee notation where time step

is given by superscript and spatial stepping is given by subscript is

$$\begin{aligned} \epsilon_{i-1/2,j+1/2} E_z|_{i-1/2,j+1/2}^n = D_z|_{i-1/2,j+1/2}^n - c^{-2}(\Omega y H_y|_{i-1/2,j+1/2}^n \\ + \Omega x H_x|_{i-1/2,j+1/2}^n) \end{aligned} \quad (9.12)$$

The semi-implicit-approximation or temporal average of E_z gives [20] :

$$\begin{aligned} \epsilon_{i-1/2,j+1/2} E_z|_{i-1/2,j+1/2}^n = \epsilon_{i-1/2,j+1/2} (E_z|_{i-1/2,j+1/2}^{n+1/2} \\ + E_z|_{i-1/2,j+1/2}^{n-1/2})/2 \end{aligned}$$

and a similar expression for D_z . The leapfrog scheme does not calculate the value of H_y at $(i - 1/2, j + 1/2)$, and we therefore use a spatial average as an approximation

$$H_y|_{i-1/2,j+1/2}^n = (H_y|_{i-1,j+1/2}^n + H_y|_{i,j+1/2}^n)/2$$

Similar spatial average is applied to H_x . After substituting these expressions into Eq. 9.12 we get

$$\begin{aligned} \epsilon_{i-1/2,j+1/2} E_z|_{i-1/2,j+1/2}^{n+1/2} = -\epsilon_{i-1/2,j+1/2} E_z|_{i-1/2,j+1/2}^{n-1/2} \\ + (D_z|_{i-1/2,j+1/2}^{n+1/2} + D_z|_{i-1/2,j+1/2}^{n-1/2}) - c^{-2}(\Omega y (H_y|_{i-1,j+1/2}^n \\ + H_y|_{i,j+1/2}^n) + \Omega x (H_x|_{i-1/2,j+1}^n + H_x|_{i-1/2,j}^n)) \end{aligned} \quad (9.13)$$

Equation 9.13 is the final form that we use in our algorithm to update E_z . To update H_x and H_y with Eqs. 9.10 and 9.11, we follow the same procedure, but use the semi-implicit approximation or temporal averaging for H_x and H_y , and perform the spatial

averaging for E_z :

$$\begin{aligned} \mu_{i-1/2,j+1} H_x|_{i-1/2,j+1}^{n+1} &= -\mu_{i-1/2,j+1} H_x|_{i-1/2,j+1}^n \\ &+ (B_x|_{i-1/2,j+1}^{n+1} + B_x|_{i-1/2,j+1}^n) - c^{-2} (\Omega x (E_z|_{i-1/2,j+1/2}^{n+1/2} \\ &\quad + E_z|_{i-1/2,j+3/2}^{n+1/2})) \end{aligned} \quad (9.14)$$

$$\begin{aligned} \mu_{i,j+1/2} H_y|_{i,j+1/2}^{n+1} &= -\mu_{i,j+1/2} H_y|_{i,j+1/2}^n \\ &+ (B_y|_{i,j+1/2}^{n+1} + B_y|_{i,j+1/2}^n) - c^{-2} (\Omega y (E_z|_{i+1/2,j+1/2}^{n+1/2} \\ &\quad + E_z|_{i-1/2,j+1/2}^{n+1/2})) \end{aligned} \quad (9.15)$$

Our algorithm therefore uses Maxwell equations to update D and B from E and H , and the constitutive relations to update E and H from D and B . Although it includes additional quantities and equations compared to the previous FDTD algorithm, our algorithm is actually simpler as there are no time derivatives or spatial derivatives in the extra equations. This improves the numerical stability and accuracy of the FDTD simulation.

For simulating a stationary or rotating closed cavity, we use Dirichlet Boundary conditions in our FDTD algorithm. For stationary or rotating open cavities, we terminate the main grid by a uniaxial perfectly matched layer (UPML) designed for a stationary frame. The condition for vanishing reflection from the UPML has been obtained in the stationary frame [20]. In a rotating frame, since the constitutive relations are changed, the zero reflection condition cannot be perfectly satisfied [18]. To determine the applicability of the UPML designed for a stationary frame in a rotating frame, we estimate the error caused by residual reflection from the UPML. The test region and benchmark region share the center, and both have a square-shaped main grid terminated by UPML. However the main grid of the benchmark

region is five times bigger than that of the test region. We launch a hard source at the centre of both the test region and the benchmark region at the initial time step $n = 0$, and calculate the global error [20]

$$e_{global}|^n = \sum_i \sum_j |E_{z,T}|_{i,j}^n - E_{z,B}|_{i,j}^n|^2 \quad (9.16)$$

at various time steps n , where $E_{z,T}|_{i,j}^n$ is the value of E_z at time step n and position (i, j) in the test region and $E_{z,B}|_{i,j}^n$ is in the benchmark region. After the source has propagated and reached the UPML of the test region but not the UPML of the benchmark region, Eq. 9.16 gives an estimation of the reflection from the UPML.

We observed, for a stationary main grid terminated by a stationary UPML, the maximum global error is $\sim 1.3 \times 10^{-12}$. For a rotating main grid with the maximum $v/c \sim 0.01$ and terminated by stationary UPML, the maximum global error is $\sim 2.1 \times 10^{-6}$. The global error increases by a factor of $\sim 10^6$ but still is small enough and the reflection does not corrupt the results as shown in the next sections.

9.3 Sagnac effect in a microdisk cavity

In this section, we present the analytical result of Sagnac effect in a rotating microdisk. In the rotating frame, the wave equation for electric field of TM polarized light can be written in the polar coordinates as [11, 13, 14]:

$$\left[\frac{\partial^2}{\partial r^2} + \left(\frac{1}{r} \right) \left(\frac{\partial}{\partial r} \right) + \frac{1}{r^2} \frac{\partial^2}{\partial \theta^2} + 2ik \frac{\Omega}{c} \frac{\partial}{\partial \theta} + n^2 k^2 \right] E_z = 0 \quad (9.17)$$

In a circular disk, $E_z(r, \theta) = f(r) \exp(-im\theta)$, where m is an integer, and

$$\left[\frac{\partial^2}{\partial r^2} + \left(\frac{1}{r} \right) \left(\frac{\partial}{\partial r} \right) - \frac{m^2}{r^2} + K_m^2 \right] f(r) = 0 \quad (9.18)$$

where

$$K_m^2 = k^2 \left[n^2 + 2m \frac{\Omega}{\omega} \right] \quad (9.19)$$

Equation 9.19 implies that rotation induces a change in the dielectric constant or the refractive index, which is given by $n_{eff}^2 = n^2 + 2m \frac{\Omega}{\omega}$ [14]. For a given direction of rotation, the clockwise (CW) and counter-clockwise (CCW) waves inside the cavity experience different n_{eff} as they have opposite signs of the azimuthal number, m . The wave traveling in the same direction of rotation acquires a higher n_{eff} than that traveling in the opposite rotation. Thus rotation lifts the degeneracy of WG modes. For a closed cavity, where Dirichlet Boundary conditions are applied at the boundary, the frequency splitting between the CW and CCW modes can be obtained analytically to the first order of Ω [11]:

$$\Delta\omega = 2 \left(\frac{m}{n^2} \right) \Omega \quad (9.20)$$

Equation 9.20 corresponds to the Sagnac effect in a closed cavity. For an open cavity, n_{eff} is modified both inside and outside the cavity. Since for a whispering gallery mode, $m \sim \frac{2\pi R}{\lambda}$ (where λ and R are resonant wavelength and radius of the cavity), Eq. 9.20 implies that Sagnac effect scales linearly with the size of the cavity.

9.4 Validation of the FDTD algorithm

Using our FDTD algorithm, we simulate a rotating microdisk cavity with both closed and open boundary. The circular disk has a radius $R = 590$ nm and a refractive index $n_0^{disk} = 3$. In order to find the frequencies of resonant modes in a stationary open cavity, we first launch a seed pulse with a broad bandwidth centered at $\lambda = 2R$ to excite many cavity resonances. The modes with shorter lifetime will decay faster in time, and the Fourier transform of the field inside the cavity at a later time will give

the frequencies of the surviving modes with longer lifetime. We investigate the mode at $\lambda = 1131.48$ nm with radial number $l = 1$ and azimuthal number $m = 7$. The wavelength of the same mode in the closed cavity can be found from the zero of Bessel Function, which gives $\lambda = 1009.8$ nm. Once we get the resonant frequencies of the stationary cavities, for our simulations of rotating open and closed cavities, we excite only that particular mode by launching a seed pulse with bandwidth narrower than the frequency spacing between the adjacent modes. The rotation induces a frequency splitting of the CW and CCW modes, which causes a temporal beating of the fields. The Fourier transform of the intracavity electric field gives the frequencies of the two split modes. The frequency difference $\Delta\omega$ for the WG modes with $m = \pm 7, l = 1$ in a closed cavity of $R = 590$ nm and $n_0^{disk} = 3$ is plotted by the circles in Fig. 9.1, and the solid line is the analytical result from Eq. 9.20. Their excellent agreement validates our FDTD model.

To test the applicability of the UPML to the rotating case, we simulate a rotating dielectric cavity of $R = 590$ nm and n_0^{disk} in free space, and calculate the frequency splitting $\Delta\omega$ for the WG modes with $m = \pm 7, l = 1$ (squares in Fig. 9.1). The effect of rotation can also be treated as a change of the refractive index. According to Eq. 9.19, the effective index of refraction as a function of the rotation velocity Ω is $(n_{\Omega}^{disk})^2 = (n_0^{disk})^2 + 2m(\Omega/\omega)$, which for $(\Omega/\omega) \ll 1$ gives $n_{\Omega}^{disk} \sim n_0^{disk} + \left(\frac{m\Omega}{n_0^{disk}\omega}\right)$, where n_{Ω}^{disk} and n_0^{disk} are the refractive indices for the stationary disk and rotating disk, respectively. Along with the disk, we also change the refractive index outside the cavity in a similar way. The rotation induced change of the resonant frequency can be calculated with an index change in the stationary case. The frequency splitting calculated in this way for the WG modes of $m = \pm 7, l = 1$ is plotted by the dotted line in Fig. 9.1, and it agrees well to the FDTD simulation in the rotating frame. Such agreement indicates the residual reflection from the UPML has negligible effect. Fig. 9.1 shows that an open cavity has a larger frequency splitting between the CW

and CCW modes than a closed cavity. It can be attributed to the increased mode size in the open cavity because the field can extend beyond the disk edge.

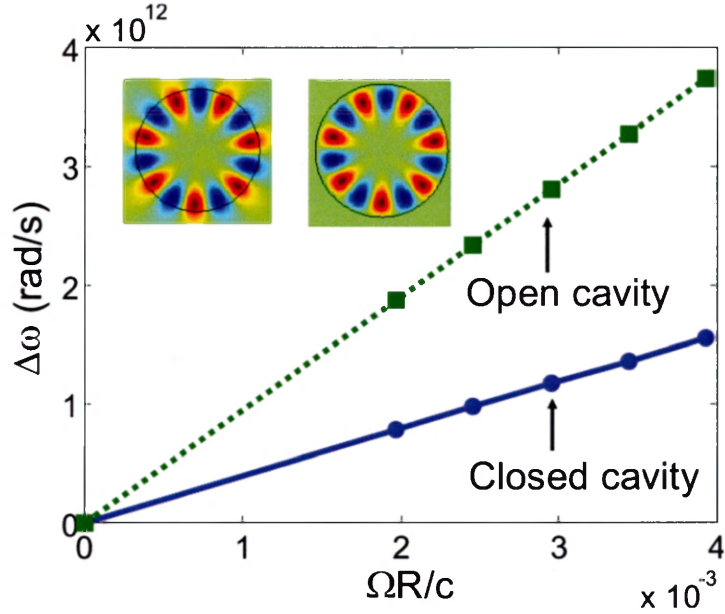


Figure 9.1: Frequency splitting between the CW and CCW modes in a circular dielectric microdisk of radius $R = 590$ nm and $n = 3$ in free space ($n = 1$) as a function of the normalized rotation speed $\Omega R/c$. The circles are the FDTD simulation results for a rotating closed cavity for a WG mode ($l = 1$, $m = 7$, $\lambda = 1009.8$ nm) and the solid line is the analytical result from Eq. (20). Squares are the FDTD simulation results for the same mode ($l = 1$, $m = 7$, $\lambda = 1131.48$ nm) in the rotating microdisk with open boundary. Dotted line represents the frequency shifts obtained from the FDTD simulation of the stationary microdisk with the effective indices of refraction (inside and outside the disk) that include the rotation-induced changes. The insets show the mode profiles for the closed and open cavities and the black circle marks the boundary of the cavity.

9.5 Discussion

In this chapter, we present the FDTD algorithm that we developed to simulate photonic structures in a rotating frame. The Maxwell equations solved using the FDTD algorithm assumes that the rotation angular velocity Ω is constant in time, and the maximal speed $v = \Omega R$ to be small in magnitude compared to the speed of light. The results therefore do not take into account relativistic effects. In addition, the effect of

rotation on the electronic structure of the materials is not taken into account. Under these assumptions, good agreement between the FDTD simulations of the Sagnac effect in 2D closed cavities and the analytical results is obtained and that validates our simulation algorithm. For open cavities, UPML for stationary frame is adapted and the residual reflection from the UPML is shown to have negligible effects on the rotation-induced frequency shift of the wavelength-scale microdisk cavities as long as the maximal speed $v \ll c$. Our numerical results illustrate that the frequency splitting in an open microdisk cavity is larger than that in a closed cavity of same size. This is attributed to an increase of mode size in the open cavity.

Unlike the previous FDTD model which substitutes the constitutive relations into the Maxwell equations and updates only E and H in time stepping [18], in our algorithm we calculate both E , H , and D , B by solving simultaneously and separately the Maxwell equations (identical to that in a stationary frame) and the modified constitutive relations in the rotating frame. In the previous approach [18], the spatial derivatives associated with rotation require the values of the fields at the time mid-steps which are missing, and a linear extrapolation in time is used to evaluate the missing values based on the two previously calculated values. As a consequence of the linear extrapolation based on values of the fields in the previous time steps, the algorithm becomes unstable for all time steps and gives rise to non-physical exponentially growing fields as shown analytically in Ref. [21]. This instability increases with faster rotation speeds and longer running times. In our algorithm, we avoid this issue by incorporating D and B in addition to E and H fields and using time interpolation into the algorithm instead of extrapolation. For same grid size and time-stepping, our algorithm however takes more computation time as it calculates 4 quantities instead of 2. The running time eventually puts a limit on the maximum size of microcavity and the minimum rotation speed that can be simulated.

Finally, in this chapter we studied only the rotation induced changes in the res-

onant frequencies. As described above, the change in resonant frequency due to rotation can be attributed to change in refractive index and a linear change in refractive index due to rotation leads to a linear change in resonant frequency. For open cavities, the curvature of the cavity boundary leads to an evanescent leakage and in absence of any additional loss, the leakage rate determines the finite lifetime or the quality factor (Q) of the resonant mode and the shape determines the output intensity pattern. Since the Q and output intensity both originate from an evanescent tunneling process, where the tunneling barrier is determined by the refractive index of the cavity, unlike the resonant frequency these two quantities are exponentially sensitive to change in refractive index. Further, as shown above, the change in refractive index due to rotation is linearly proportional to azimuthal number m of the mode which is again linearly proportional to the radius of the cavity R . This implies that as compared to Sagnac effect which will increase linearly with cavity size, the magnitude of rotation induced changes in Q and emission pattern will show a much superior exponential scaling with the cavity size. In the next chapter, based on this motivation, we explore these two quantities and show that they indeed are more sensitive compared to Sagnac effect. In the simulations presented in this thesis, due to computation limitations, we simulate only small cavities and correspondingly the rotation speeds are very high. This however should not change the conclusions and as shown in the next chapter, the results of larger cavities can be inferred from the results of small cavities using scaling arguments.

Bibliography

- [1] R. Sarma, H. Noh, and H. Cao, *J. Opt. Soc. Am. B* **29**, 1648 (2012).
- [2] C. Ciminelli, F. Dell Olio, C. E. Campanella, and M. N. Armenise, *Adv. Opt. Photon.* **2**, 370 (2010).
- [3] B. Z. Steinberg, *Phys. Rev. E* **71**, 056621 (2005).
- [4] B. Z. Steinberg and A. Boag, *J. Opt. Soc. Am. B* **23**, 1442 (2006).
- [5] A. B. Matsko, A. A. Savchenkov, V. S. Ilchenko, and L. Maleki, *Opt. Commun.* **233**, 107 (2004).
- [6] J. Scheuer and A. Yariv, *Phys. Rev. Lett.* **96**, 053901 (2006).
- [7] C. Peng, Z. Li, and A. Xu, *Opt. Express* **15**, 3864 (2007).
- [8] C. Sorrentino, J. R. E. Toland, and C. P. Search, *Opt. Express* **20**, 354 (2012).
- [9] R. Novitski, B. Z. Steinberg, and J. Scheuer, *Phys. Rev. A* **85**, 023813 (2012).
- [10] B. Z. Steinberg, J. Scheuer, and A. Boag, *J. Opt. Soc. Am. B* **24**, 1216 (2007).
- [11] S. Sunada and T. Harayama, *Phys. Rev. A* **74**, 021801(R) (2006).
- [12] T. Harayama, S. Sunada, and T. Miyasaka, *Phys. Rev. E* **76**, 016212 (2007).
- [13] S. Sunada and T. Harayama, *Opt. Express* **15**, 16245 (2007).

- [14] J. Scheuer, *Opt. Express* **15**, 15053 (2007).
- [15] M. Skorobogatiy and J. D. Joannopoulos, *Phys. Rev. B* **61**, 5293 (2000).
- [16] M. Skorobogatiy and J. D. Joannopoulos, *Phys. Rev. B* **61**, 15554 (2000).
- [17] B. Z. Steinberg, *Phys. Rev. E* **74**, 016608 (2006).
- [18] C. Peng, R. Hui, X. Luo, Z. Li, and A. Xu, *Opt. Express* **16**, 5227 (2008).
- [19] T. Shiozawa, *Proc. IEEE* **61**, 1694 (1973).
- [20] A. Taflove, *Computational Electrodynamics: The Finite-Difference Time-Domain Method* (Artech House, 1995).
- [21] R. Novitski, J. Scheuer, and B. Z. Steinberg, *Phys. Rev. E* **87**, 023303 (2013).

Chapter 10

Rotation induced changes in optical resonances of dielectric microcavities

10.1 Introduction

¹ Optical microcavities have been explored for various applications such as coherent light sources in integrated photonic circuits, single-photon emitters, and biochemical sensors [4, 5]. One potential application that has received attention recently is ultrasmall on-chip optical gyroscope [1, 2, 6–19]. Almost all conventional optical gyroscopes rely on the Sagnac effect for rotation sensing [12, 14, 20, 21]. The Sagnac effect refers to rotation-induced phase shift between two counter-propagating waves in an optical loop or frequency splitting in a resonant cavity as described in chapter 9. Since the Sagnac effect scales linearly with the cavity size [20, 22], microcavities have much lower frequency response to rotation. As such, rotation-induced changes in other characteristics of microcavity resonances, such as the quality (Q) factor have

1. This chapter is primarily based on the journal articles published in ref. [1–3].

been investigated. For example, in circular Bragg microlasers, the rotation-induced intensity modulation has been shown to have exponential dependence on the rotation velocity [9].

Stationary microcavities with shape deformed from circle have generated a lot of interest in the past two decades, with the quest to achieve optimal directional radiation from microlasers. Deformed microcavities have also been explored for rotation sensing, with the focus on rotation-induced changes in resonant frequencies of closed cavities [7, 8, 11, 18, 20]. Unfortunately the shape deformation often lifts the frequency degeneracy of cavity modes, causing a threshold behavior for the Sagnac effect. For deformed cavities with open boundaries, it is however interesting to study how rotation modifies the emission intensity patterns and investigate its sensitivity to rotation.

In this chapter, we present a detailed numerical study on the effects of rotation on optical resonances in microcavities of various shapes with open boundary. We start with a circular cavity where we investigate the rotation induced changes in Q factors and compare that to the Sagnac effect. We show that the Q factor, which determines the lasing threshold and the output power, is more sensitive to rotation than the resonant frequency. In the second section we study a deformed elliptical cavity. We investigate how deformation effects the threshold behavior of the Sagnac effect. In addition, we also show how rotation modifies the emission intensity patterns. In the final section, we concentrate on deformed cavities with broken chiral symmetry. We show that emission intensity pattern of such cavities can be extremely sensitive to rotation and can be used to detect rotation. Further, by tuning the degree of spatial chirality with cavity shape, we show that we are able to maximize the emission sensitivity to rotation without spoiling the quality factor.

Various methods have been developed to study photonic structures in rotating frame [23–29]. In this chapter, we numerically calculate the cavity resonances using

the finite-difference time-domain (FDTD) method described in Chapter 9. In all the simulations, we consider the dielectric microdisk in free space, the disk thickness is much less than its radius, so it can be approximated as a 2D cavity with an effective index of refraction n . We present the results of the transverse magnetic (TM) resonances with the electric field perpendicular to the disk plane (parallel to the z axis) and the magnetic field parallel to the plane (the $x - y$ plane). The disk rotates about the z axis in the counter-clockwise direction with a constant angular velocity of rotation Ω . The rotation is slow enough that $\Omega R \ll c$, where R is the disk radius, and we keep only the leading-order terms of $\Omega R/c$ in the wave equation. In the rotating frame where the disk is stationary, the Maxwell equations retain their form, but the constitutive relations are modified [1, 23, 24, 30].

10.2 Rotation induced changes in Q factor of resonances of a circular microcavity

In this section, we simulate the same circular cavity and the resonant mode that we studied in the previous chapter. The circular disk has a radius $R = 590$ nm and a stationary refractive index $n_0^{disk} = 3$. The wavelength of the resonant mode is $\lambda = 1131.48$ nm, radial number $l = 1$, and azimuthal number $m = 7$. In an open cavity, along with the resonant frequency, rotation also changes the quality factor of a resonant mode, because the contrast of refractive index inside and outside the disk varies with the rotation and affects the degree of optical confinement by the cavity. For a rotating dielectric microdisk, the refractive index changes both inside and outside the disk, and the refractive index difference is given by

$$n_{\Omega}^{disk} - n_{\Omega}^{outside} \sim (n_0^{disk} - n_0^{outside}) + \left(\frac{m\Omega}{\omega} \right) \left[\frac{1}{n_0^{disk}} - \frac{1}{n_0^{out}} \right] \quad (10.1)$$

Equation 10.1 simplifies for the case of a disk in free space $n_0^{outside} = 1$ as

$$n_{\Omega}^{disk} - n_{\Omega}^{outside} \sim (n_0^{disk} - 1) + \left(\frac{m\Omega}{\omega}\right) \left[\frac{1}{n_0^{disk}} - 1\right] \quad (10.2)$$

Equation 10.2 implies the rotation increases the refractive index difference for negative m . Thus the Q factor for the counter-propagating mode increases with the rotation speed Ω . For the co-propagating mode with positive m , the Q factor decreases with rotation. In the case of a microdisk, the change in the refractive index contrast is symmetric and opposite for the clockwise (CW) and counter-clockwise (CCW) modes. Figure 10.1 plots the Q values obtained from the simulation (given by the squares) for the CW and CCW modes for different rotation speeds. For the $m = 7$ mode, we see a decrease in the Q factor whereas the Q factor for the $m = -7$ mode increases. The change has the same magnitude but opposite sign for the two modes. Within the range of rotation speed in the simulation, we observe an exponential dependence of $\Delta Q = Q_{CW}(\Omega) - Q_{CW}(\Omega = 0)$ on Ω . This is because $\frac{\Omega}{\omega} \ll 1$ and the rotation-induced change of the refractive index scales linearly with Ω . The Q factor of a TIR-based whispering gallery (WG) mode depends exponentially on the difference in the refractive index inside and outside the disk, which scales linearly with the rotation speed according to Eq. 10.2.

In the simulation, the Q factor of a cavity mode is extracted from the temporal decay of the field. At a given rotation speed, a single mode at frequency ω is excited by a seed pulse launched near the disk edge. By making the bandwidth of the pulse narrower than the frequency difference between the CW and CCW modes, we ensure only one mode is excited and eliminate beating in the time trace of E_z . $E_z(t)$ displays an exponential decay after the seed pulse is gone, and from the decay time τ we obtain $Q = \omega\tau$, where ω is the resonant frequency. An important point to notice is that, the sensitivity of the Q factor to rotation is more than one order of magnitude higher

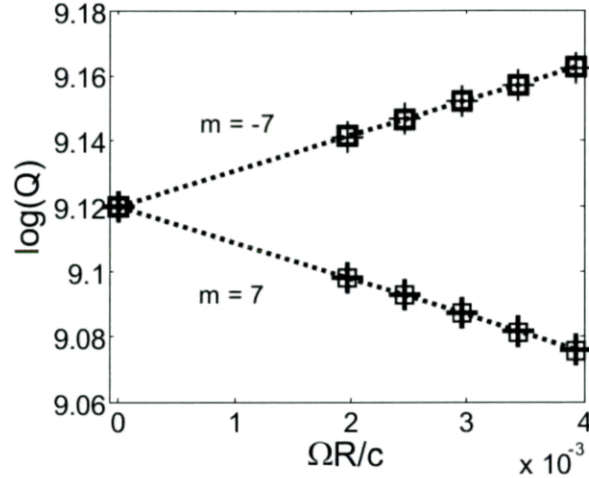


Figure 10.1: Calculated quality factors for the $l = 1$, $m = \pm 7$ modes as a function of normalized rotation speed $\Omega R/c$. The squares are obtained from the FDTD simulation of a rotating microdisk of $R = 590$ nm and $n = 3$ in free space, and the crosses from the stationary microdisk with the effective indices of refraction (inside and outside the disk) that include rotation-induced changes described in chapter 9. The dotted lines are linear fits showing that the Q changes exponentially with rotation speed.

compared to the change in frequency. Figure 10.2 plots the relative change in Q , $\frac{\Delta Q}{Q_0}$, as a function of Ω , in comparison with the normalized frequency splitting $\frac{\Delta k}{k_0}$, where Q_0 is the Q factor of the stationary cavity, $k_0 = \omega_0/c$ is the normalized resonant frequency of the stationary cavity, and $\Delta k = \Delta\omega/c$ is the normalized rotation induced splitting of the resonant frequency. Both scale linearly with Ω , and the slope for $\frac{\Delta Q}{Q_0}$ versus Ω is 2.16×10^{-12} , whereas the slope for $\frac{\Delta k}{k_0}$ versus Ω is 1.12×10^{-13} . The Q factor for this cavity is therefore ~ 20 times more sensitive to rotation than the resonant frequency. The Q not only determines the threshold pump level for lasing, but also affects the output power above the threshold. Thus the change of Q by rotation would modify the lasing thresholds for CW and CCW modes, and break the balance between the CW and CCW output power. The higher sensitivity of Q to Ω indicates the rotation-induced changes in lasing thresholds and output power can be more dramatic than the lasing frequency shift in the microdisk lasers.

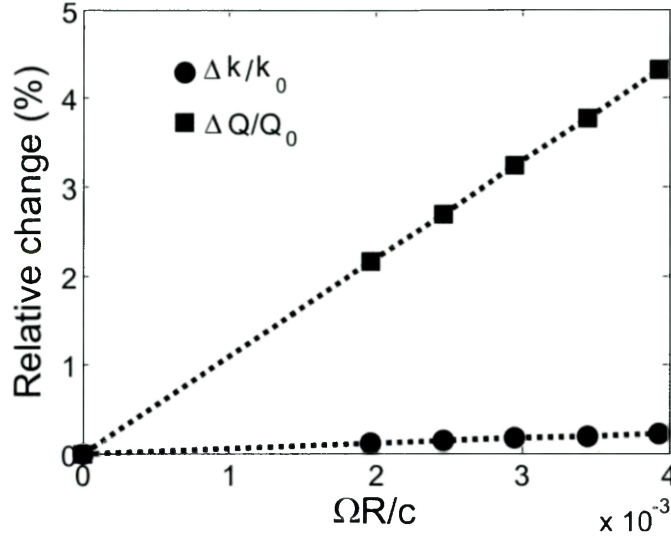


Figure 10.2: Relative change in Q factor $\frac{\Delta Q}{Q_0}$ (squares) and the normalized frequency splitting $\frac{\Delta k}{k_0}$ (circles) as a function of the normalized rotation speed $\Omega R/c$ for the WG mode of $l = 1$, $m = -7$ in the dielectric microdisk of $R = 590$ nm and $n = 3$. The dotted lines are the linear fits.

10.3 Elliptical cavities

In a stationary circular cavity, CW and CCW propagating waves do not couple and they form two degenerate resonant modes of the cavity, which are characterized by the azimuthal number m and radial number l . The superposition of these two modes can form standing waves (with sine and cosine angular dependence) that are also resonant modes of the cavity. With rotation, the CW and CCW waves experience different refractive indices and their frequencies start to split [7]. This frequency splitting is linearly proportional to the rotation velocity Ω . Since rotation makes the CW and CCW waves non-degenerate, the only resonances of a rotating circular cavity are the non-degenerate CW and CCW resonant modes.

In deformed stationary cavities, however, the CW and CCW waves may be coupled by scattering from the non-isotropic cavity boundary, and they form two quasi-degenerate resonances of frequency splitting Δk_0 . With rotation, the frequency dif-

ference between these two quasi-degenerate resonances can be written as [7]:

$$\Delta k_r(\Omega) = \left[\Delta k_0^2 + \left(\frac{g}{c} \Omega \right)^2 \right]^{\frac{1}{2}}, \quad (10.3)$$

where g is a coupling constant that is proportional to the size of the cavity. Only when the rotation velocity Ω exceeds a certain threshold value $\Omega_c = c\Delta k_0/g$, the rotation-induced frequency shift $g\Omega/c$ becomes comparable to the intrinsic splitting Δk_0 . For $\Omega < \Omega_c$, Δk_r is approximately equal to Δk_0 and is barely changed by rotation. Hence there exists a “dead zone” at low rotation speed for the Sagnac effect. Once the rotation induced frequency shift is much larger than the intrinsic splitting, Δk_r approaches its asymptote $g\Omega/c$ and increases linearly with the rotation speed.

In this section, we study a simple deformed cavity shape, the ellipse [31–36], as drawn in Fig. 10.3(a). In the Cartesian coordinates the cavity boundary is given by $(x/a)^2 + (y/b)^2 = 1$, where $2a$ and $2b$ are the lengths of the minor and major axis respectively ($a < b$). We vary the ratio a/b , while keeping the area πab constant. For the results in this section, we set $R = \sqrt{ab} = 0.54 \mu\text{m}$, and the wavelength (in vacuum) λ is around $0.72 \mu\text{m}$. The refractive index is equal to 3.0 inside the cavity, and 1.0 outside. For a/b close to 1, the high- Q modes resembles the WG modes in a circular disk, and they each can be assigned a dominant azimuthal number m and a radial number l . The coupling between CW and CCW waves in the ellipse results in a frequency splitting Δk_0 . The quasi-degenerate pair of modes have even and odd symmetry with respect to the major or minor axis, as seen in an example given in Fig. 10.3(b,c). The stronger the deformation, i.e., the smaller the ratio a/b , the larger the splitting Δk_0 .

When the ellipse rotates, the higher-frequency mode of the quasi-degenerate pair is blue shifted, and the lower-frequency one red-shifted [Fig. 10.3(d)]. We numerically

calculate the frequency splitting Δk_r in the rotating ellipse using the FDTD method. Figure 10.3(e) plots the value of Δk_r as a function of rotation speed Ω for a pair of quasi-degenerate modes with $m = 11$ and $l = 1$ in the ellipse with $a/b = 0.88$ (dashed line) and 0.92 (solid line). Their normalized frequencies are approximately the same, $kR \simeq 4.73$, where $k = 2\pi/\lambda$ and $R = \sqrt{ab}$ is the average radius of the cavity. The threshold values, expressed as $\Omega_c R/c$, are on the order of $\sim 10^{-7}$ and $\sim 10^{-9}$ for the ellipses with $a/b = 0.88$ and 0.92 respectively, below which the frequency spacing of the two resonances remains nearly unchanged from Δk_0 . Thus the larger deformation leads to a wider dead zone. For $\Omega > \Omega_c$, Δk_r increases linearly with Ω in both cavities, as it is dominated by rotation-induced frequency splitting.

The cavity shape deformation also causes a dead zone in the rotation-induced change of Q , as shown in Fig. 10.3(f). The quasi-degenerate pair of resonances have slightly different Q even at $\Omega = 0$. For $\Omega \gg \Omega_c$, the Q for one mode increases with Ω and decreases for the other. The magnitude of the change in Q due to rotation, $|\Delta Q|$, is the same for the pair (to the leading order of $R\Omega/c$ [18]). The larger the deformation (smaller a/b), the wider the dead zone for $|\Delta Q|$. Beyond the dead zone, the larger slope of $|\Delta Q|$ vs Ω for smaller value of a/b indicates the cavity with weaker deformation is more responsive to rotation.

In Fig. 10.3(g), we compare the relative changes in resonant frequency and Q factor due to rotation, i.e. $\Delta k_r/k_0$ and $\Delta Q/Q_0$, where k_0 and Q_0 are the average frequency and quality factor for the quasi-degenerate pair of modes at $\Omega = 0$. $\Delta Q/Q_0$ is more than one order of magnitude higher than $\Delta k_r/k_0$, indicating the relative change of Q by rotation is much larger than that of frequency in the wavelength-scale elliptical cavity.

Next we investigate the rotation-induced changes in the output intensity patterns of elliptical cavities with the FDTD method. As the radius of curvature varies along the cavity boundary, the strongest emission occurs at the locations of the highest

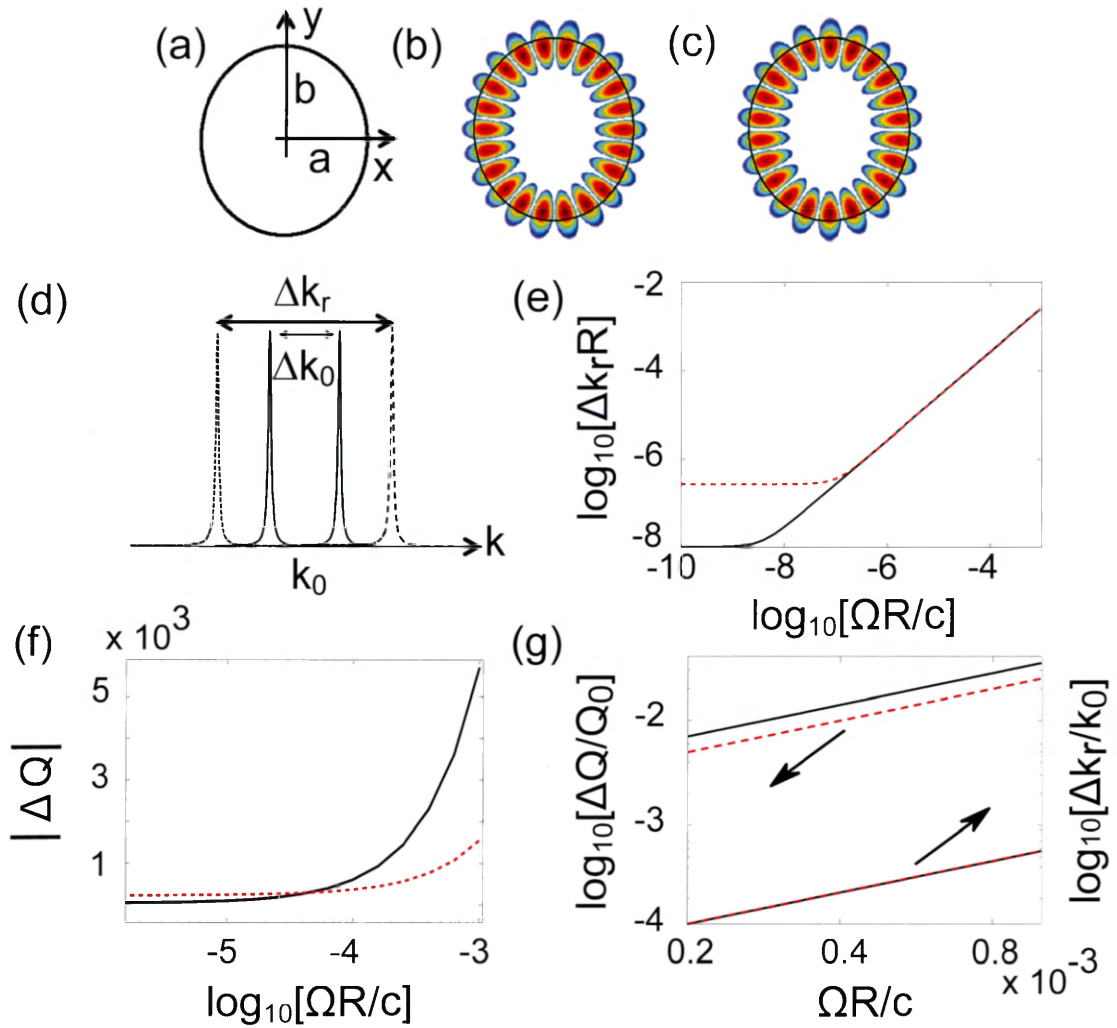


Figure 10.3: Rotation-induced changes in the resonances of elliptical cavities. (a) A 2D microcavity of elliptical shape. The length of minor (major) axis is $2a$ ($2b$). (b,c) Spatial distribution of the electric field magnitude ($|E_z|$) for a pair of quasi-degenerate modes in the elliptical cavity with $a/b = 0.88$ and refractive index $n = 3.0$. (d) A schematic showing the frequency splitting Δk_0 of a quasi-degenerate pair of modes (solid lines) in an elliptical cavity without rotation, and the frequency splitting Δk_r with rotation. The higher-frequency (lower-frequency) mode of the quasi-degenerate pair is blue (red) shifted by rotation (dashed lines). (e) Normalized frequency shift $\Delta k_r R$ as a function of the normalized rotation speed $\Omega R/c$ for a pair of quasi-degenerate modes with $m = 11$ and $l = 1$ in the ellipse with $a/b = 0.88$ (red dashed line) and 0.92 (black solid line). (f) Magnitude of rotation-induced changes in Q , $|\Delta Q|$, for the same pair of modes in (b). Black solid line and red dashed line correspond to $a/b = 0.92$ and 0.88 respectively. (g) Relative changes in the resonant frequency $\Delta k_r/k_0$ and the quality factor $\Delta Q/Q_0$ for the corresponding modes in (e,f). The vertical axis is shown in log scale to show the differences in magnitudes.

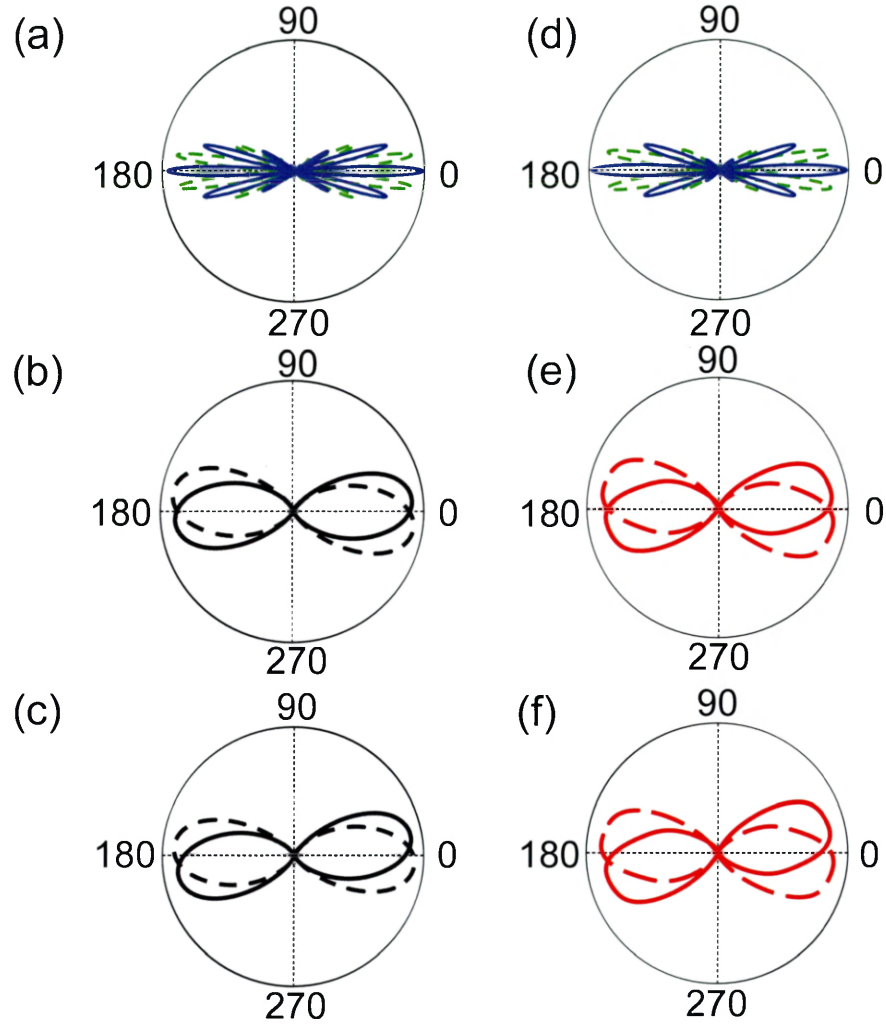


Figure 10.4: Evolution of far-field emission patterns of elliptical microcavities with rotation. The deformation of the ellipse is $a/b = 0.92$ in (a-c) and 0.88 (d-f). (a,d) Angular distribution of far-field intensity $I(\theta)$ (at $r = 50R$) of quasi-degenerate pairs of modes shown in Fig. 10.3 at $\Omega R/c = 0$. The blue solid (green dashed) curve represents the mode with even (odd) symmetry with respect to the x axis. (b,e) Angular distribution of far-field intensity for the CW and CCW wave components in the stationary resonances shown in (a,d). The solid (dashed) curve represents the CW (CCW) wave. The output directions of CW and CCW waves are symmetric with respect to the horizontal axis. (c,f) Angular distribution of far-field intensity $I(\theta)$ (at $r = 50R$) of the modes in (a,d) at $\Omega R/c = 10^{-4}$. The interference fringes in the output intensity patterns of stationary cavity (a,d) vanishes, as the modes evolve from standing wave to traveling wave with rotation. The emission patterns of the two traveling-wave modes at high rotation speed are not symmetric with respect to the horizontal axis.

curvature. The main emission directions for the elliptical cavities are therefore parallel to the minor-axis of the ellipse (x axis, $\theta = 0^\circ, 180^\circ$). As shown in Fig. 10.4(a), the far-field intensity patterns for a stationary quasi-degenerate pair of modes have even and odd parity with respect to the major and minor axes of the ellipse, and there are several lobes around $\theta = 0^\circ, 180^\circ$ as a result of the interference of the emission from CW and CCW waves in the cavity. By decomposing the field outside the cavity into CW and CCW wave components, we identify the far-field patterns for CW and CCW waves [Fig. 10.4(b)]. The CW and CCW waves in the stationary resonances do not emit exactly in the same directions, even though they are symmetrical about the major and minor axes. This difference is caused by wave effects, including the Goos-Hänchen shift and Fresnel filtering, which become significant in the wavelength-scale cavities [37–40].

With increasing rotation speed, the standing-wave modes evolve to CW and CCW traveling-wave resonances, and the interference fringes in the far-field patterns vanish in Fig. 10.4(c). Moreover, output directions for CW and CCW waves are no longer symmetric with respect to the major and minor axes, as both rotate slightly in the direction of rotation (CCW). This behavior is attributed to the rotation-induced change in the refractive index, namely, the index increases for the co-propagating wave (propagating in the same direction as the rotation) and decreases for the counter-propagating wave. In the elliptical cavity with smaller a/b , the difference between the CW and CCW output directions at $\Omega = 0$ is larger, and the rotation-induced change in the far-field pattern is smaller [Fig. 10.4(d-f)]. Above we present only the results for the higher-frequency mode of the quasi-degenerate pair; the lower-frequency mode is red-shifted by rotation and the magnitude of change is the same as that for the higher-frequency mode.

10.4 Rotating optical microcavities with broken chiral symmetry

Although the elliptical cavity is deformed, there exists a rotational or chiral symmetry in the shape i.e. the shape does not introduce any preferred sense of rotation. Optical resonators may acquire structural chirality from shape deformation or boundary scattering, which induces asymmetric coupling between the CW and CCW propagating waves in the cavity [41–43]. With open boundary, the cavity resonances are dominated by either CW or CCW waves, thus possessing a preferred sense of rotation [44–49]. Such cavities with broken chiral symmetry are called chiral cavities. In this section we investigate the interplay between openness and chirality of rotating microcavities.

It is not known what happens if a chiral cavity rotates, e.g., whether the Sagnac effect would survive in the absence of chiral symmetry, and how the intrinsic chirality is affected by rotation. In a non-rotating cavity with chiral symmetry, every resonance has balanced CW and CCW wave components, and the output intensity profile is symmetric. As shown in the previous section, rotation makes individual mode dominated by either CW or CCW wave, thus introducing asymmetry in the far-field pattern if CW and CCW waves have different output directions. In a chiral cavity, even without rotation the breaking of chiral symmetry can make the far-field pattern asymmetric; it is not clear how rotation would further modify the emission profile.

To answer these questions, in this section we investigate open microcavities with broken chiral symmetry in the rotating frame. Our calculations show that a quasi-degenerate pair of co-propagating-wave modes in the non-rotating chiral cavity evolve to counter-propagating ones at high rotation speed. The intrinsic chirality is thus removed by rotation, and the Sagnac effect is similar to that of a non-chiral cavity.

However, the flip of propagation direction for one of the quasi-degenerate modes will lead to a striking change of its far-field pattern, as long as the CW and CCW waves have distinct output directions. By tuning the cavity shape, we are able to vary the degree of chirality without spoiling the quality factor. The maximal chirality results in the largest difference in CW and CCW outputs, making the emission profile most sensitive to rotation. The surprising enhancement of rotation sensitivity of chiral microcavities may open up the possibility of on-chip rotation sensors using a new scheme for rotation sensing .

10.4.1 Simple analytical model of a rotating chiral cavity to calculate Sagnac effect

Let us first model a non-rotating chiral cavity. The asymmetric coupling between CW and CCW propagating waves can be described by an effective Hamiltonian [42, 49].

$$H_0 = \begin{pmatrix} \omega_0 & 0 \\ 0 & \omega_0 \end{pmatrix} + \begin{pmatrix} \Gamma & V \\ \eta V^* & \Gamma \end{pmatrix}, \quad (10.4)$$

where $V = |V|e^{i\gamma}$, ω_0 is the frequency of the unperturbed CCW and CW wave components. Their coupling leads to an overall frequency shift Γ , and asymmetric transition elements V and ηV^* , where the deviation of $|\eta|$ from unity represents the degree of asymmetry. Diagonalization of H_0 gives the eigenfrequencies

$$\omega_{\pm} = \omega_0 + \Gamma \pm \sqrt{\eta}|V|. \quad (10.5)$$

The frequency splitting $\Delta\omega_0 = 2\sqrt{\eta}|V|$ results from the coupling of CW and CCW waves. The normalized eigenvectors are

$$\xi = \begin{pmatrix} \xi_{\text{CCW}} \\ \xi_{\text{CW}} \end{pmatrix} = \frac{1}{\sqrt{1+|\eta|}} \begin{pmatrix} 1 \\ \pm\sqrt{\eta}e^{-2i\gamma} \end{pmatrix}. \quad (10.6)$$

The eigenvectors are composed of CW and CCW waves with relative intensity ratio $|\eta|$, thus a higher asymmetry of the coupling leads to a stronger chirality of the eigenmodes. When the cavity rotates, the Hamiltonian becomes

$$H = H_0 + \begin{pmatrix} \Delta & 0 \\ 0 & -\Delta \end{pmatrix}, \quad (10.7)$$

where $\pm\Delta$ represents the frequency shift of CCW/CW wave by rotation. We assume the rotation speed is slow enough that $|\Delta|$ is linearly proportional to the rotation frequency Ω . For simplicity, we set $\Delta = \Omega$. The eigenfrequencies are

$$\omega_{\pm} = \omega_0 + \Gamma \pm \sqrt{\eta|V|^2 + \Delta^2}. \quad (10.8)$$

The frequency splitting becomes $\Delta\omega = 2\sqrt{\eta|V|^2 + \Delta^2} = 2\sqrt{(\Delta\omega_0/2)^2 + \Omega^2}$. The normalized eigenvectors are

$$\xi = \begin{pmatrix} \xi_{\text{CCW}} \\ \xi_{\text{CW}} \end{pmatrix} = \frac{1}{\sqrt{1+|a|^2}} \begin{pmatrix} 1 \\ ae^{-2i\gamma} \end{pmatrix}, \quad (10.9)$$

where $a \equiv \pm\sqrt{\eta + \Delta^2/|V|^2} - \Delta/|V|$.

At low rotation speed, the additional frequency splitting induced by rotation (Ω) is much smaller than the original splitting ($\Delta\omega_0$), so the total splitting remains nearly constant $\Delta\omega \simeq \Delta\omega_0$. Only when Ω becomes comparable to $\Delta\omega_0$, the rotation-induced

splitting becomes significant, and $\Delta\omega$ starts to grow with Ω . Eventually at $\Omega \gg \Delta\omega_0$, $\Delta\omega \approx 2\Omega$, the linear increase of $\Delta\omega$ with Ω recovers the Sagnac effect. Hence, the frequency splitting at $\Omega = 0$ causes a “dead zone” for the Sagnac effect [7].

In a chiral cavity the dependence of $\Delta\omega$ on Ω is identical to that in a non-chiral cavity, as long as the value of $\eta|V^2|$ is kept the same [Fig. 10.5(a)]. Although without rotation both modes in the chiral cavity are dominated by CCW (CW) traveling waves for $|\eta| < 1$ ($|\eta| > 1$), one of them is transformed into a CW (CCW) traveling wave mode by rotation, and its frequency shifts in the opposite direction to the other mode, producing the same Sagnac effect as in the non-chiral cavity.

10.4.2 Resonant modes in a non-rotating chiral cavity

We choose dielectric microdisks with the shape of asymmetric limaçon, which unlike other chiral cavities have high Q factor and small frequency splitting $\Delta\omega_0$ [49]. The microdisk can be regarded as a two-dimensional (2D) cavity as the disk thickness is much smaller than the radius. In the polar coordinates, the cavity boundary is described by $r(\theta) = R[1 + \epsilon_1 \cos(\theta) + \epsilon_2 \cos(2\theta + \delta)]$, where R is the radius, ϵ_1 and ϵ_2 are the deformation parameters, and δ determines the degree of chirality. For $\delta = m\pi$ (m is an integer), the cavity has the chiral symmetry [$r(-\theta) = r(\theta)$], and the coupling from CW wave to CCW wave is equal to that from CCW to CW. As δ deviates from $m\pi$, the chiral symmetry is broken, so is the balance between CW and CCW wave coupling. Consequently, each pair of quasi-degenerate modes are dominated by either CW or CCW wave.

We consider a pair of transverse-magnetic (TM) resonant modes where normalized frequencies of the two modes are $kR \simeq 6.2$, where $k = 2\pi/\lambda$, and λ is the vacuum wavelength. Their Q factors are about 56,500. The insets in Figure 10.6(a,b) show the spatial distributions of electric field intensity for these two modes. The intra-cavity electric field (perpendicular to the cavity plane) is expanded in the cylindrical

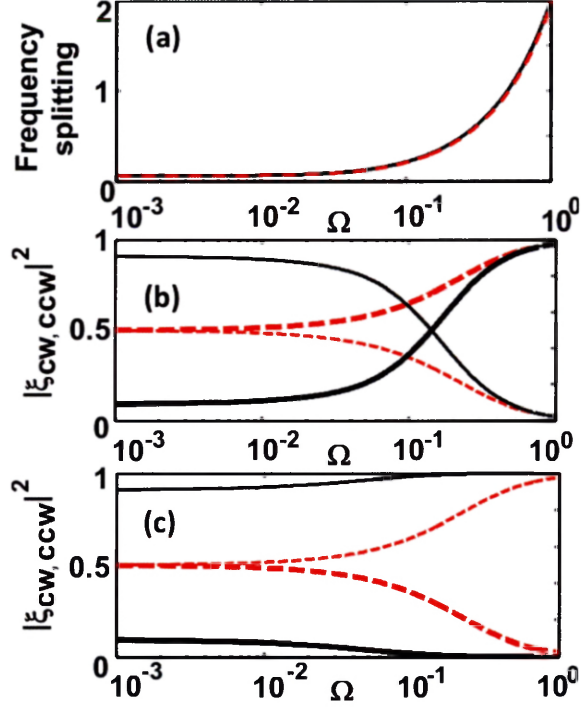


Figure 10.5: Comparison of Sagnac effect in a rotating microcavity with chiral symmetry ($\eta = 1$, dashed line) and without chiral symmetry ($\eta = 0.1$, solid line). The value of $\eta|V|^2$ is kept the same. (a) (Dimensionless) frequency splitting for a pair of quasi-degenerate modes as a function of rotation frequency Ω . (b,c) Evolution of CW (thick line) and CCW (thin line) traveling-wave components in the quasi-degenerate modes with rotation. In the symmetric cavity ($\eta = 1$), at low rotation speed the eigenmodes remain standing-wave modes with equal weights of CCW and CW components, and their frequency difference is barely changed by rotation. When the rotation speed is sufficiently high, one mode evolves to a CCW traveling-wave mode, the other one to a CW traveling-wave mode; and their frequency difference starts to grow significantly with Ω . In a chiral cavity ($\eta = 0.1$), the evolution of frequency splitting with rotation is identical to the symmetric cavity. Without rotation both modes are dominated by CCW traveling waves, but one of them (b) transforms into a CW traveling wave mode at high Ω .

harmonics, $E_z^{(in)}(r, \theta) = \sum_{-\infty}^{\infty} a_m J_m(nkr) e^{im\theta}$, where J_m is the m -th order Bessel function of the first kind. Positive (negative) values of angular momentum m correspond to CCW (CW) traveling wave components. The origin of this expansion is chosen to be $(x, y) = (\epsilon_1 R/2, 0)$. The distributions of $|a_m|^2$ in Fig. 10.6 (a,b) illustrate that both modes have more CW wave components than the CCW ones. The spatial chirality of a mode is defined as

$$\alpha \equiv 1 - \frac{\min(\sum_{-\infty}^{-1} |a_m|^2, \sum_1^{\infty} |a_m|^2)}{\max(\sum_{-\infty}^{-1} |a_m|^2, \sum_1^{\infty} |a_m|^2)}. \quad (10.10)$$

For this pair of modes, $\alpha = 0.25$.

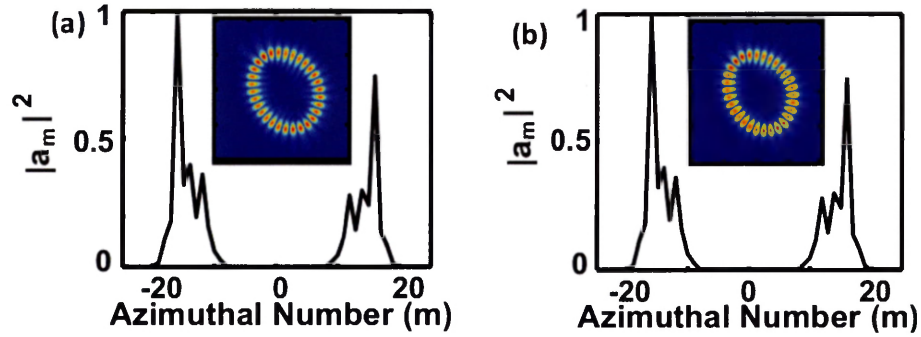


Figure 10.6: A pair of quasi-degenerate modes ($\lambda = 598$ nm) in a non-rotating dielectric disk ($n = 3.0$) of asymmetric limaçon shape ($R = 591$ nm, $\epsilon_1 = 0.1$, $\epsilon_2 = 0.075$, $\delta = 1.94$). (a,b) Spatial distributions of electric field intensity (inset) and angular momentum components (main panel) inside the cavity. Both modes have more CW wave ($m < 0$) than CCW wave ($m > 0$).

Both modes generate directional emissions, as shown in Fig. 10.7(a). To find the output directions for CW and CCW traveling waves, we decompose the electric field outside the cavity with outgoing harmonic waves, $E_z^{out}(r, \theta) = \sum_{-\infty}^{\infty} b_m H_m^{(1)}(kr) e^{im\theta}$, where $H_m^{(1)}$ is the m -th order Hankel function of the first kind. By summing only positive or negative m terms in the field expansion and taking $r \rightarrow \infty$, we obtain the far-field intensity patterns for the CW and CCW waves separately, as shown in Fig. 10.7(b). The main output direction of CW wave is $\theta \simeq 0.7$, and for the CCW wave $\theta \simeq 2.8$ [Fig. 10.7(b)]. Due to the dominant presence of CW wave in the

quasi-degenerate pair, their far-field patterns are similar to that of the CW wave.

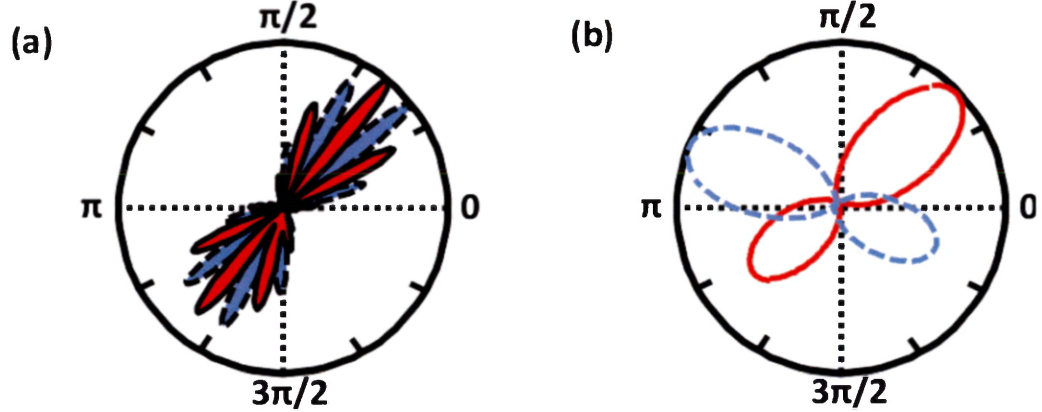


Figure 10.7: Far-field emission intensity patterns of a pair of quasi-degenerate modes ($\lambda = 598$ nm) in a non-rotating dielectric disk ($n = 3.0$) of asymmetric limaçon shape ($R = 591$ nm, $\epsilon_1 = 0.1$, $\epsilon_2 = 0.075$, $\delta = 1.94$). (a) Angular distributions of emission intensities at a distance of $r = 50R$ from the cavity center for both modes, which have similar output directions. (b) Far-field patterns of CW (red solid line) and CCW (blue dashed line) wave components in the resonances, exhibiting distinct output directions.

10.4.3 Effect of rotation on the emission patterns of chiral microcavities and comparison of its sensitivity to Sagnac effect

Next we investigate how the emission patterns of the asymmetric limaçon are modified by rotation. As shown in the previous section, without rotation, the pair of quasi-degenerate modes have similar far-field patterns, because they are both dominated by either CW or CCW traveling waves. With rotation, we expect one of them will flip the propagation direction, and its far-field pattern will change dramatically since the CW and CCW waves have distinct and different output directions. To illustrate this we simulate using FDTD an asymmetric limaçon cavity rotating with a constant angular velocity $\dot{\Omega}$ around a fixed axis perpendicular to the cavity plane. Using FDTD, we calculate the modes profiles of the resonant modes of the rotating cavity. As shown

in Fig. 10.8, one of the two modes in Fig. 10.7 switches from CW to CCW traveling-wave, while the other one remains CW. Consequently their output directions become very different.

The striking change of output direction by rotation originates from the breaking of chiral symmetry in the open microcavity. Even when the cavity is at rest, the resonances already acquire a preferred sense of rotation, as the quasi-degenerate pairs are both dominated by CW or CCW traveling waves. However, as the microcavity starts rotating, the intrinsic chirality of the resonances is removed, and every pair has one mode CW dominated and the other CCW dominated.

The direction of rotation determines which one of the quasi-degenerate pair, the higher or lower frequency mode, will flip the propagation direction and exhibit a dramatic change in the output direction. For example, the two modes in Fig. 10.7 are both dominated by CW traveling waves at rest; if the rotation is in the CCW (CW) direction, the lower (higher) frequency mode will transform to CCW, and its frequency will decrease (increase) further with rotation. Hence, by measuring the emission frequency in the main output direction of the CCW or CW wave, we can identify the direction of rotation.

In reality both of the quasi-degenerate modes are often excited simultaneously, and their relative phases depend on the excitation condition, which varies from one experimental setting to another. The interference of their output fields determine the emission pattern, which will be modified by rotation. To calculate quantitatively the change of emission pattern by rotation, we simulate a generic case. Seed pulses are launched from ten randomly chosen locations inside the cavity to excite the quasi-degenerate modes. The photodetectors are assumed to be stationary in the rotating frame and placed at a distance of $3R$ from the cavity center. After the seed pulses pass by, the photodetectors are turned on to measure the emission intensity. Figure 10.9 (a) plots the temporally-integrated intensity I_c as a function of the emission

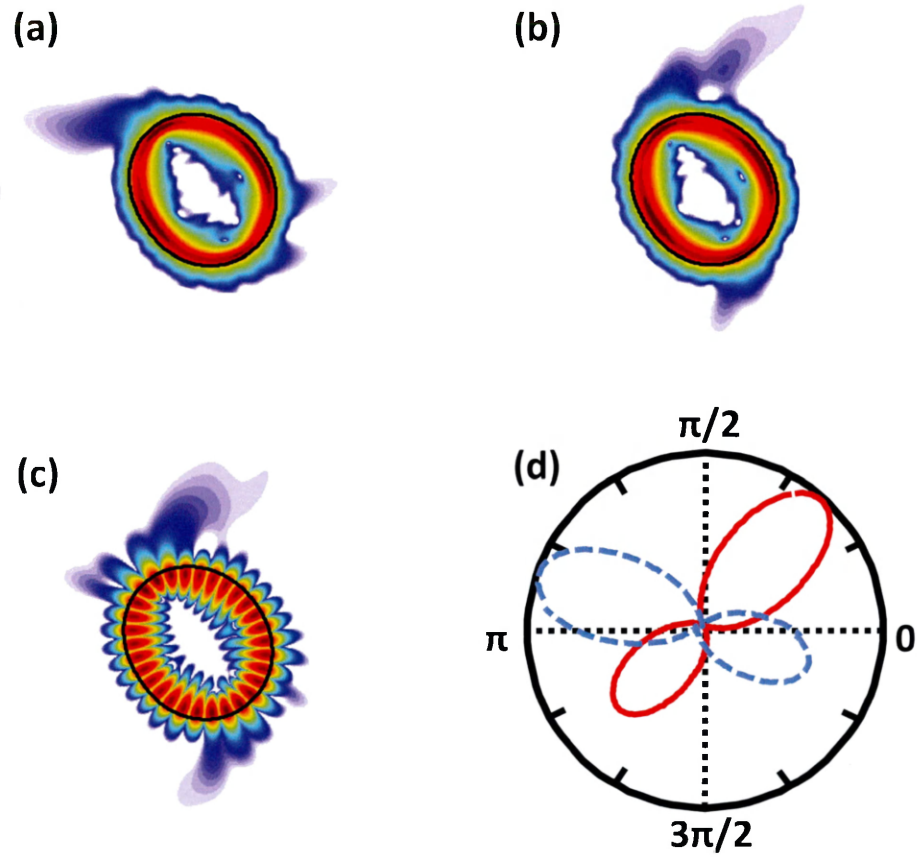


Figure 10.8: Emission from the rotating asymmetric limaçon cavity with the same parameters as the stationary one in Fig. 10.7. (a,b) Spatial distributions of field intensities for a pair of degenerate modes, which correspond to the stationary modes in Fig. 10.7, at the normalized rotation frequency $\Omega R/c = 10^{-3}$. The intensities outside the cavity are enhanced to illustrate the main output directions of the two modes are different, even though they have the same output directions without rotation [Fig. 10.7(a)]. (c) Spatial distribution of field intensity for one of the quasi-degenerate modes in the non-rotating cavity. It is dominated by CW wave. When the cavity rotates in the CCW direction, this mode switches from CW to CCW wave, and the main output direction is changed dramatically. (d) Angular distribution of far field intensity for the pair of modes shown in (a,b) in the rotating cavity.

angle θ for the quasi-degenerate pair of modes in Fig. 10.7. The irregular oscillations of I_e with θ results from the beating of the two excited modes, which depend on their initial phase difference.

The excitation condition is kept the same when the rotation speed Ω increases. With increasing Ω , some peaks of $I_e(\theta)$ increase while others decrease [Fig. 10.9(a)], as the co-propagating wave resonances evolve to counter-propagating ones. The main emission peak at $\theta \simeq 0.7$ is from the CW wave, and its intensity decreases as one of the modes is converted to CCW wave by rotation. Meanwhile, the secondary peaks at $\theta \simeq 2.8$ increases with Ω , since they are from the CCW wave. In Fig. 10.9(b), the relative changes in the main peak intensity and its ratio to the secondary peak intensity are plotted versus the normalized rotation speed $\Omega R/c$ (c is the speed of light in vacuum). The latter is about two times larger than the former.

To compare with the Sagnac effect, we calculate the frequency splitting $\Delta k = \frac{\Delta\omega}{c}$ of these two modes in a circular cavity with the same area and refractive index as the asymmetric limaçon. The normalized frequency splitting $\frac{\Delta k}{k_0}$, where $k_0 = \omega_0/c$ is the normalized resonant frequency in the non-rotating cavity, gives the relative change of the resonant frequency by rotation. A linear fit of the data in the log-log plot of Fig. 10.9(b) finds the slopes, which reflect the sensitivity to rotation. The slope for the relative change in the main emission peak intensity of the asymmetric limaçon cavity is about three orders of magnitude larger than the slope of the relative frequency shift in the circular cavity.

10.4.4 Tuning of cavity shape to maximize sensitivity

To enhance the emission sensitivity to rotation, we tune the degree of spatial chirality by varying δ of the limaçon cavity. We compute the spatial chirality α of the quasi-degenerate modes in the non-rotating cavity with varying δ . As δ increases from 0 to π , α first grows and reaches the maximum at $\delta \simeq 1.94$, then drops to zero at

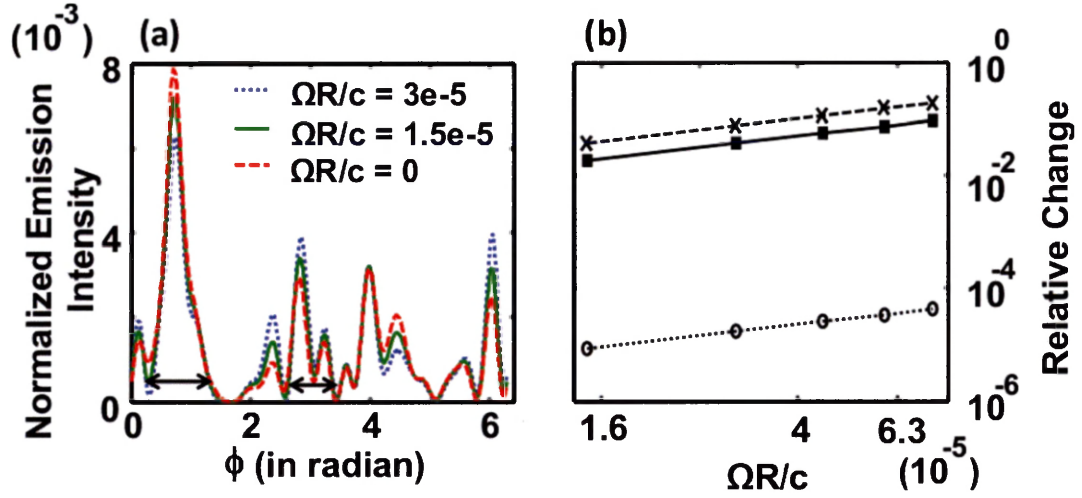


Figure 10.9: Rotation-induced change in emission pattern of the same cavity as the one in Fig. 10.8, when both quasi-degenerate modes are excited simultaneously. (a) Angular distribution of the emission intensity I_e at a distance of $r = 3R$ from the cavity center at three rotation speeds. To show the change in the emission profile, $I_e(\theta)$ is normalized ($\int_0^{2\pi} I_e(\theta)d\theta = 1$). (b) Relative changes in the main emission peak intensity (at $\theta = 0.73$) (solid squares and solid line) and in the ratio of main peak intensity over the secondary peak intensity (at $\theta = 2.79$) (crosses and dashed line) vs. the normalized rotation frequency $\Omega R/c$. Both peak intensities are integrated over a range of emission angle marked by the double-headed segments in (a). For comparison, relative changes of resonant frequencies, $\frac{\Delta k}{k_0}$, are plotted for circular cavities with the same area and refractive index (open circles and dotted line). The symbols represent the numerical data, and the straight lines are linear fit of the data in the log-log plot, which gives the slope. The values of the slope are (from top to bottom) 2.4×10^3 , 1.2×10^3 , and 5.7×10^{-1} respectively. The rotation-induced changes of output intensity are much larger than that of the resonance frequency.

$\delta = \pi$ [49]. We simulate the rotating cavities with different δ , and find that the relative change of the main emission peak intensity increases monotonically with α at a fixed rotation speed [Fig. 10.10(a)].

To interpret this result, we compare the far-field patterns for CW and CCW waves in the non-rotating cavities with different δ . The difference between CW and CCW emission patterns is quantified by $\beta = \int_0^{2\pi} |I_{CW}(\theta) - I_{CCW}(\theta)|d\theta$, which is plotted as a function of α in Fig. 10.10(a). Both $I_{CW}(\theta)$ and $I_{CCW}(\theta)$ are normalized ($\int_0^{2\pi} I_{CW,CCW}(\theta)d\theta = 1$). The monotonic increase of β with α indicates that the emission patterns for CW and CCW waves become more distinct at higher chirality, consequently the mode emission pattern changes more significantly by rotation. The maximal spatial chirality provides the highest sensitivity of microcavity output to rotation.

The tuning of the structural chirality of the asymmetric limaçon cavity to maximize the emission sensitivity to rotation does not spoil the Q factor of the cavity. To confirm, we calculate the Q values for the same resonances in the non-rotating cavities with different δ . The Q factors of the pair of modes shown in Fig. 10.6 are very close and their mean is plotted as a function of δ in Figure 10.11. As δ varies from 0 to π , the Q decreases slightly and monotonically, in agreement to the result of previous study on larger cavities [49]. Therefore, we are able to tune the spatial chirality of the resonances in the asymmetric limaçon cavity without significantly spoiling the quality factor.

10.4.5 Scaling of rotation-induced relative change in output intensity with cavity size and effect of refractive index

Due to limited computing power, we can simulate only wavelength-scale asymmetric limaçon cavities in the rotating frame. Consequently, the rotation speed must be very high to change the emission direction. The emission sensitivity will increase with the

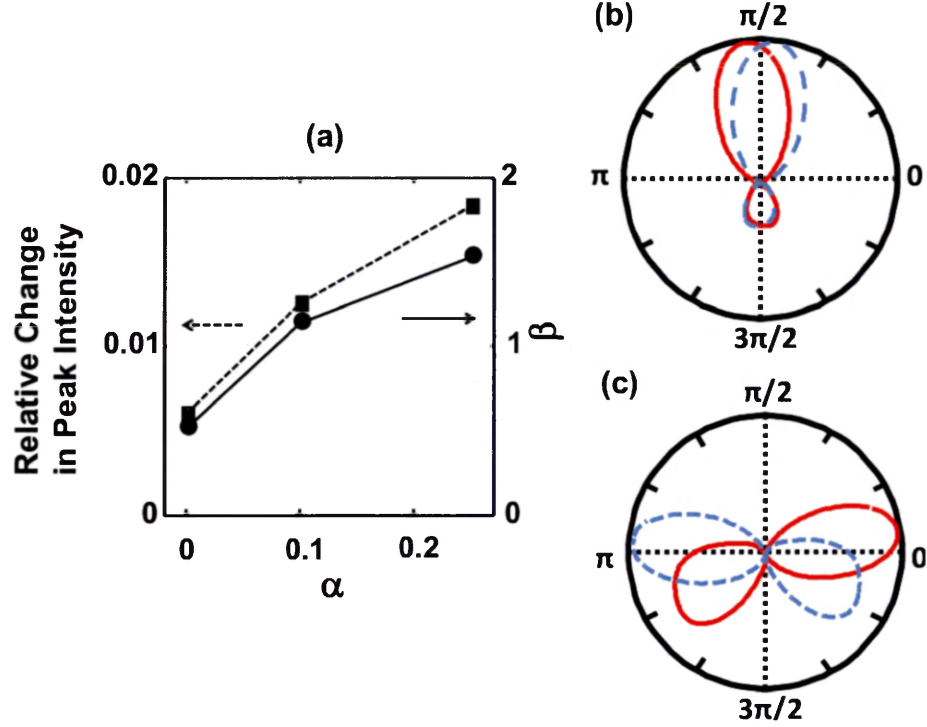


Figure 10.10: Output sensitivity to rotation for the asymmetric limaçon cavity with varying degree of spatial chirality. The cavity parameters are the same as those in Fig. 10.6 except the value of δ . (a) Relative change of the emission intensity in the main output direction (solid squares and dashed line) as a function of spatial chirality α for the quasi-degenerate modes in Fig. 10.7. The rotation frequency is fixed at $\Omega R/c \simeq 1.5 \times 10^{-5}$. The difference between the emission patterns for CW and CCW waves in the non-rotating cavity is quantified by β (solid circles and solid line), which is also plotted against α . With increasing spatial chirality α , CW and CCW outputs become more distinct, enhancing the emission sensitivity to rotation. (b,c) Far-field patterns for CW wave (red solid line) and CCW wave (blue dashed line) in two cavities with $\delta = 0$ (b), and 2.75 (c). At $\delta = 0$, both CW and CCW waves emit predominantly in the direction close to $\theta = \pi/2$ (b), and the slight difference of their emission directions is a result of wave effects in the wavelength-scale cavity. As δ increases from 0 to π , the main emission direction of the CW wave moves towards $\theta = 0$, and the CCW wave towards $\theta = \pi$; meanwhile, the secondary emission peak, which is in the opposite direction of the main peak, grows monotonically.

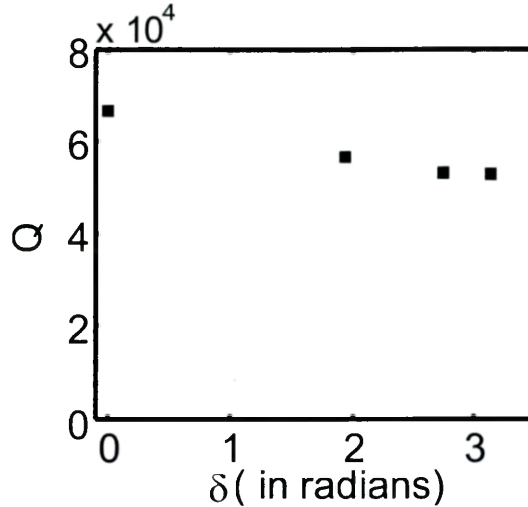


Figure 10.11: The quality (Q) factor of the non-rotating asymmetric limaçon cavity with varying δ . The refractive index of the cavity is $n = 3.0$ and the radius is $R = 591$ nm. The deformation parameters are $\epsilon_1 = 0.1$ and $\epsilon_2 = 0.075$. The Q is the mean of the quasi-degenerate pair of resonances at $\lambda \simeq 598$ nm.

cavity size R , because the spatial chirality increases with cavity size [49], along with an increase of the Q factor and a decrease of the intrinsic frequency splitting $\Delta\omega_0$. In this subsection, we present a scaling analysis using the coupled mode theory developed in the previous studies [6, 18]. The minimum rotation speed Ω_c to produce a noticeable change of the emission intensity is proportional to the size of the dead zone $\Delta\omega_0$. Our numerical simulation of non-rotating cavities reveals that $\Delta\omega_0$ reduces exponentially as kR increases, leading to an exponential drop of Ω_c with (increasing) R . Thus we can estimate Ω_c as a function of R from the numerical data of very small cavities.

For the asymmetric limaçon cavity of $R = 591$ nm [Fig. 10.9], the relative change of the main emission peak intensity is 1% at $\Omega = 4.2 \times 10^{10}$ RPM (revolution per minute). Assuming such a change can be detected experimentally, we get $\Omega_c = 4.2 \times 10^{10}$ RPM at $R = 0.59 \mu\text{m}$. If we keep the wavelength the same ($\lambda = 598$ nm) and increase R to $10 \mu\text{m}$, Ω_c reduces to 3.5×10^6 RPM; a further increase of R to $25 \mu\text{m}$ reduces Ω_c to 1.1 RPM .

The scaling of Ω_c with wavelength λ can be inferred from the above analysis, since

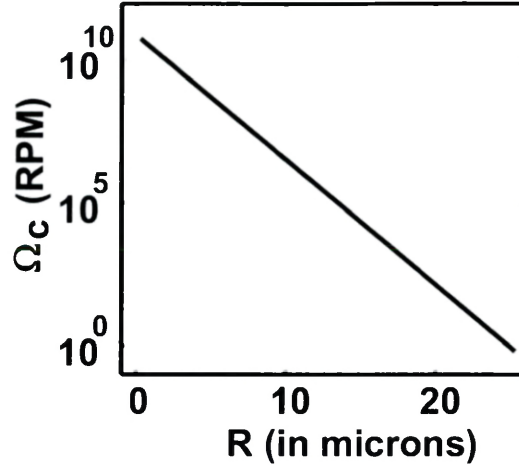


Figure 10.12: The minimum detectable rotation speed Ω_c as a function of the radius R of the asymmetric limaçon cavity. The refractive index of the cavity is $n = 3.0$, the deformation parameters are $\epsilon_1 = 0.1$ and $\epsilon_2 = 0.075$, $\delta = 1.94$. The wavelength is kept at $\lambda = 598$ nm.

Ω_c and $\Delta\omega_0$ depend on kR instead of k or R separately. Thus reducing wavelength λ in a cavity of fixed R is equivalent to increasing R while fixing λ . In a cavity of fixed R , Ω_c reduces exponentially as k increases, so the rotation-induced change of emission pattern is larger for a shorter wavelength.

The sensitivity of emission intensity will also depend on the refractive index of the microcavity. To investigate the dependence of the rotation-induced output change on the refractive index of the cavity, we repeat the numerical simulation that produces Fig. 10.9, but for different values of refractive index n . Figure 10.13 plots the relative change in the main emission peak intensity at a fixed rotation speed of $\Omega R/c \simeq 3 \times 10^{-5}$ as a function of n . As n decreases, the same rotation speed causes a larger change in the output intensity. This is because the dead zone is smaller when the refractive index of the cavity is lower. In addition, the lower refractive index will increase the output coupling efficiency due to higher radiation rate, thus further enhancing the absolute emission intensity change by rotation.

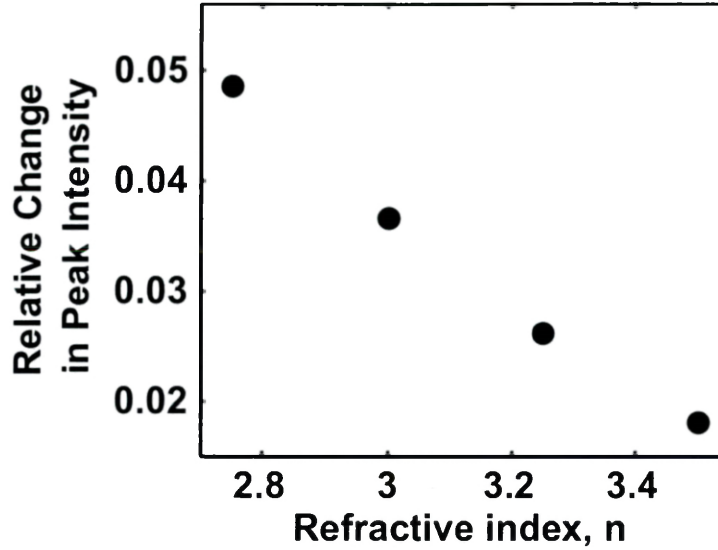


Figure 10.13: Relative changes in the main emission peak intensity as a function of refractive index n of an asymmetric limaçon cavity with $R = 591$ nm, $\epsilon_1 = 0.1$, $\epsilon_2 = 0.075$, and $\delta = 1.94$. The resonant modes in all the cases have $\lambda/n \sim 200$ nm where λ is the vacuum wavelength and n is the refractive index of the asymmetric limaçon cavity. The rotation speed is fixed at $\Omega R/c \simeq 3 \times 10^{-5}$.

10.4.6 Absolute change in output intensity by rotation

The scaling analysis in the last section is based on the relative change in the output intensity by rotation. The absolute amount of change in the output intensity, at a given input power, also depends on the output coupling efficiency of the cavity. In this final section, we analyze the absolute intensity change due to rotation, which determines the signal to noise ratio of the rotation sensing measurement [12].

We consider two dissipation channels for the input power: (i) radiation into the far field, (ii) absorption inside the cavity. The former is determined by the radiation rate γ_r , which is inversely proportional to the radiative quality factor Q_r ; and the latter is by the absorption rate γ_a which is inversely proportional to the absorptive quality factor Q_a . The total loss rate is $\gamma_t = \gamma_r + \gamma_a$, and the total quality factor is $Q_t = (1/Q_r + 1/Q_a)^{-1}$. When the input power is constant, the absolute change in

the output intensity at a fixed rotation speed Ω is

$$\Delta I_o \propto \frac{\gamma_r}{\gamma_t} \delta I_o. \quad (10.11)$$

The fraction on the right hand side is the output coupling efficiency (the percentage of the input power converted to radiation), and the second term is the relative change in the output intensity due to rotation. Both terms depend on the cavity size R . As R increases, the radiation rate decreases exponentially and eventually submerged by the absorption rate which remains constant with R .

In the wavelength-scale cavity, $\gamma_r \gg \gamma_a$, and $\gamma_t \approx \gamma_r$. The output coupling efficiency is approximately equal to unity, thus ΔI_o is determined solely by δI_o . As discussed in the previous section, the relative change in the output intensity is inversely proportional to the size of the dead zone $\Delta\omega_0$, which scales exponentially with kR at a given rotation speed, thus $\delta I_o \propto e^{fkR}$, and the exponent f depends on the cavity shape, refractive index and the type of resonance. For a small cavity whose radiation dominates over absorption, the absolute change in output intensity ΔI_o increases exponentially with R for fixed Ω and λ , i.e. $\Delta I_o \propto e^{fkR}$.

However, as R increases, γ_r decreases exponentially, $\gamma_r \propto e^{-gkR}$, where the exponent g also depends on the cavity shape, refractive index and the type of resonance. Eventually γ_r becomes much smaller than γ_a , and $\gamma_t \approx \gamma_a$ is independent of R . The output coupling efficiency then decreases exponentially with increasing R , counteracting the exponential increase of δI_o . The final scaling of ΔI_o with R depends on the values of f and g . If $f < g$, ΔI_o first increases exponentially with R and then decreases exponentially, as shown in Fig. 10.14(a). The turning point R_0 is set by $\gamma_r(R_0) = \gamma_a$. However, if $f > g$, ΔI_o keeps increasing exponentially with R , albeit the exponent decreases at $R > R_0$ [Fig. 10.14(b)]. As the absorption rate reduces, the turning point R_0 moves to a larger value, enhancing ΔI_o of large cavity [Fig.

10.14(a,b)].

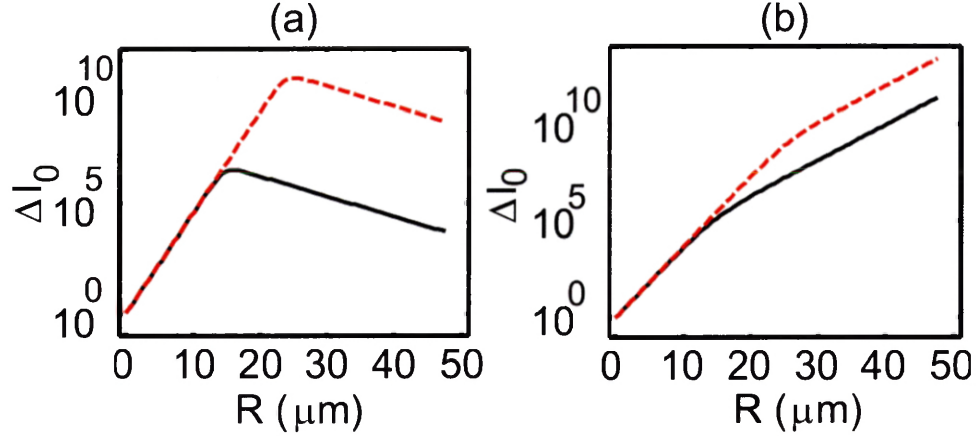


Figure 10.14: Absolute change in output intensity by rotation, ΔI_o , as a function of the cavity size R for fixed wavelength and rotation speed. The variation of ΔI_o with R depends on the values of f and g of the resonant modes. (a) When $f = 0.1$ and $g = 0.12$, ΔI_o first increases exponentially and then decreases exponentially. At the turning point R_0 , the radiation rate is equal to the absorption rate, $\gamma_r(R_0) = \gamma_a$. (b) When $f = 0.08$ and $g = 0.04$, ΔI_o keeps increasing exponentially with R , but the exponent decreases at large R . As the absorption rate reduces, the turning point R_0 moves to a larger value. In both panels, the solid line corresponds to $R_0 \sim 15\mu\text{m}$, and the dashed line to $R_0 \sim 25\mu\text{m}$.

In our numerical simulation of asymmetric limaçon cavity with $\epsilon_1 = 0.1$, $\epsilon_2 = 0.075$, $\delta = 1.94$ and refractive index $n = 3.0$, we found varying values of f and g for different high- Q resonances. Some of them have $f < g$, the others $f > g$. By optimizing the cavity shape and refractive index, we can tune the values of f and g to maximize the absolute change in output intensity. Further enhancement may be achieved by minimizing the absorption in the cavity, e.g., by fabricating the cavity with more transparent material or turning the operation wavelength farther away from the absorption band. Such optimization is beyond the scope of the work in this thesis. Such optimization will however become mandatory for designing a practical and sensitive on-chip rotation sensor.

Bibliography

- [1] R. Sarma, H. Noh, and H. Cao, *J. Opt. Soc. Am. B* **29**, 1648 (2012).
- [2] R. Sarma, L. Ge, J. Wiersig, and H. Cao, *Phys. Rev. Lett.* **114**, 053903 (2015).
- [3] R. Sarma, L. Ge, and H. Cao, *J. Opt. Soc. Am. B* **32**, 1736 (2015).
- [4] *Optical Processes in Microcavities*, edited by R. K. Chang and A. J. Campillo, Advanced Series in Applied Physics (World Scientific, Singapore, 1996).
- [5] *Optical Microcavities*, edited by K. J. Vahala, Advanced Series in Applied Physics (World Scientific, Singapore, 2004).
- [6] S. Sunada and T. Harayama, *Phys. Rev. A* **74**, 021801(R) (2006).
- [7] S. Sunada and T. Harayama, *Opt. Express* **15**, 16245 (2007).
- [8] T. Harayama, S. Sunada, and T. Miyasaka, *Phys. Rev. E* **76**, 016212 (2007).
- [9] J. Scheuer, *Opt. Express* **15**, 15053 (2007).
- [10] C. Peng, Z.B. Li, and A. S. Xu, *Appl. Opt.* **46**, 4125 (2007).
- [11] S. Sunada, S. Tamura, K. Inagaki, and T. Harayama, *Phys. Rev. A* **78**, 053822 (2008).
- [12] M. Terrel, M. J. F. Digonnet, and S. Fan, *Laser Photon. Rev.* **3**, 452 (2009).
- [13] M. A. Terrel, M. J. F. Digonnet, and S. Fan, *J. Lightwave Technol.* **27**, 47 (2009).

- [14] C. Ciminelli, F. Dell’Olio, C. E. Campanella, and M. N. Armenise, *Adv. Opt. Photon.* **2**, 370 (2010).
- [15] M. J. F. Digonnet, *J. Lightwave Technol.* **29**, 3048 (2011).
- [16] C. Sorrentino, J. R. E. Toland, and C. P. Search, *Optics Express* **20**, 354 (2012).
- [17] D. Kalantarov, and C. P. Search, *J. Opt. Soc. Am. B* **30**, 377 (2013).
- [18] Li Ge, R. Sarma, and H. Cao, *Phys. Rev. A* **90**, 013809 (2014).
- [19] Li Ge, R. Sarma, and H. Cao, *Optica* **2**, 323 (2015).
- [20] E. J. Post, *Rev. Mod. Phys.* **39**, 475 (1967).
- [21] F. Aronowitz, *The Laser Gyro*, in *Laser Applications*, edited by M. Ross (Academic, New York, 1971).
- [22] W. W. Chow, J. Gea-Banacloche, L. M. Pedrotti, V. E. Sanders, W. Schleich, and M. O. Scully, *Rev. Mod. Phys.* **57**, 61 (1985).
- [23] B. Z. Steinberg, *Phys. Rev. E* **71**, 056621 (2005).
- [24] B. Z. Steinberg, *Phys. Rev. E* **74**, 016608 (2006).
- [25] J. Scheuer and A. Yariv, *Phys. Rev. Lett.* **96**, 053901 (2006).
- [26] B. Z. Steinberg and A. Boag, *J. Opt. Soc. Am. B* **24**, 142 (2007).
- [27] C. Peng, R. Hui, X. Luo, Z. Li, and A. Xu, *Opt. Express* **16**, 5227 (2008).
- [28] D. Hah and D. Zhang, *Opt. Express* **18**, 18200 (2010).
- [29] R. Novitski, J. Scheuer, and B. Z. Steinberg, *Phys. Rev. E* **87**, 023303 (2013).
- [30] T. Shiozawa, *Proc. IEEE* **61**, 1694 (1973).

- [31] G. Hackenbroich, E. Narimanov, and A. D. Stone. *Phys. Rev. E* **57**, R5 (1998).
- [32] S. A. Backers, A. P. Heberle, J. R. A. Cleaver, and K. Kler. *Phys. Status Solidi B* **204**, 581 (1997).
- [33] H. G. L. Schwefel, N. B. Rex, H. E. Tureci, R. K. Chang, and A. D. Stone, *J. Opt. Soc. Am. B* **21**, 923 (2004).
- [34] S. Sunada, T. Harayama, and K. S. Ikeda. *Opt. Lett.* **29**, 718 (2004).
- [35] S. K. Kim, S. H. Kim, G. H. Kim, H. G. Park, D. J. Shin, and Y. H. Lee, *Appl. Phys. Lett.* **84**, 861 (2004).
- [36] J. Unterhinninghofen, J. Wiersig, and M. Hentschel. *Phys. Rev. E* **78**, 016201 (2008).
- [37] Q. H. Song, L. Ge, A. D. Stone, H. Cao, J. Wiersig, J. B. Shim, J. Unterhinninghofen, W. Fang, and G. S. Solomon, *Phys. Rev. Lett.* **105**, 103902 (2010).
- [38] B. Redding, Li Ge, Q. Song, J. Wiersig, G. S. Solomon, and H. Cao, *Phys. Rev. Lett.* **108**, 253902 (2012).
- [39] B. Redding, Li Ge, G. S. Solomon, and H. Cao. *Appl. Phys. Lett.* **100**, 061125 (2012).
- [40] Q. H. Song, Li Ge, J. Wiersig, J.B. Shim, J. Unterhinninghofen, A. Eberspacher, W. Fang, G. S. Solomon and Hui Cao, *Phys. Rev. A* **84**, 063843 (2012).
- [41] J. Wiersig, *Phys. Rev. A* **84**, 063828 (2011).
- [42] J. Wiersig, *Phys. Rev. A* **89**, 012119 (2014).
- [43] J. Yang, X. Xiao, C. Hu, W. Zhang, S. Zhou, and J. Zhang. *Nano Lett.* **14**, 704 (2014).

- [44] G. D. Chern, H. E. Tureci, A. D. Stone, R. K. Chang, M. Kneissl, and N.M. Johnson, *Appl. Phys. Lett.* **83**, 1710 (2003).
- [45] J. Wiersig, S. W Kim, and M. Hentschel, *Phys. Rev. A* **78**, 053809 (2008).
- [46] J. Wiersig, *Optics Express* **16**, 5874 (2008).
- [47] M. Hentschel and T.Y. Kwon, *Optics Lett.* **34**, 163 (2009).
- [48] M. Hentschel, T. Kwon, M. A. Belkin, R. Audet, and F. Capasso, *Optics Express* **17**, 10335 (2009).
- [49] J. Wiersig, A. Eberspächer, J. Shim, J. Ryu, S. Shinohara, M. Hentschel, and H. Schomerus, *Phys. Rev. A* **84**, 023845 (2011).

Chapter 11

Conclusions

In this thesis, we studied two types of dielectric structures. The first one is a random medium where the refractive index varies spatially in length scales comparable to the wavelength. Light inside such structures is multiply scattered and the interference of multiply scattered waves inside the medium leads to interesting mesoscopic effects. We studied and controlled experimentally some of these mesoscopic effects inside an on-chip random medium.

The first mesoscopic effect that we studied is the renormalization of the diffusion coefficient. We presented in chapter 2 of this thesis, the first direct experimental observation of position dependent diffusion which is a weak localization effect. We showed that because of interference effects, the diffusion coefficient D is no longer a constant and becomes renormalized where the amount of renormalization depends on the spatial position inside the medium. We further showed that by varying the scattering strength and absorption, the renormalization of the diffusion coefficient can be modified. In chapter 3 of this thesis, we studied another mesoscopic effect which is the long range correlation of intensity inside a random medium. We demonstrated how these correlations evolve as light propagates through the random medium. We showed that by modifying the conductance of the medium, the magnitude of these

correlations can be modified. This happens because the long range correlations arise due to crossing of the scattering paths of light and the probability of such crossings happening inside the medium is inversely proportional to the conductance. Therefore by modifying the conductance, the magnitude of such correlations can be altered.

In the second part of the thesis, we demonstrated experimentally a simple but efficient approach of using geometry to deterministically and efficiently control the above measured mesoscopic effects. In chapter 4, we showed that by varying the width in a single waveguide, the localization effects can be modified which can lead to modification of D . Using geometry, the diffusion of light inside the random media can therefore be locally modified. In chapter 5, we further demonstrated experimentally that spatial correlations can also be tailored by designing the shape of the waveguide. By fabricating photonic random waveguides with the cross section varying along their length, the functional form of the long-range correlation can be modified inside waveguides of different shapes because the crossing probability of scattering paths is affected nonuniformly in space.

The ability to control the interference effects inside a random medium besides being of fundamental importance is also important from application point of view. For example, by controlling diffusion inside the random medium, we can control the energy density inside the medium. Since the energy density dictates the light matter interactions, our ability to control the energy density also gives us the ability to control the light matter interactions inside a random medium. Similarly, the ability to control the long range correlations can also be of great significance for applications where it may be necessary to focus light in a speckle spot inside a random medium. As shown in chapter 5, by tailoring the shape of the correlation function we can tailor the contrast of focusing and the energy deposition inside the random medium.

Another fascinating interference effect in random media that has recently drawn much attention is the creation of open and closed transmission eigenchannels. The

open and closed channels not only dictate the transmission through the random medium, but also determine the spatial profile of the energy density. With recent advances in the field of adaptive wavefront shaping, it has now become possible to selectively couple input light to these eigenchannels. In chapter 6 of the thesis, we showed experimentally and numerically that by varying the geometry of a random waveguide, the spatial structure of open channels can be significantly and deterministically altered from the universal ones and that enables us to tune the energy density profiles inside the random medium. As compared to using the localization effects mentioned in chapter 2 and 4, the advantage of using geometry is that although it modifies the energy density profiles, the bimodal distribution is still maintained which implies that open channels with high transmission are still retained. In chapter 6, we also showed that by gradually increasing the waveguide cross-section, we can convert evanescent channels to propagating channels. Further, perfect reflection channels can be created in certain confined geometries, which do not exist in waveguides with uniform cross-section. Unlike high-reflection channels in uniform waveguides that exhibit shallow penetration into the disordered system, a perfect reflection channel can penetrate almost through the entire system but does not transmit any light. Such channels can be of great importance for sensing applications.

In chapter 7, we extended our work on transmission eigenchannels and implemented the adaptive wavefront shaping technique to our on-chip random nanostructures. We carefully designed our coupling waveguide to achieve complete control of the input. Using adaptive wavefront shaping techniques, we optimized our input light to selectively couple to the open and closed channels. Thanks to the complete control of the input and distinct and different spatial profiles and transmission eigenvalues of the open and closed channels, we achieved an unprecedented control of transmission and energy density inside the random nanostructures. In chapter 8, we demonstrated that such coherent control of light using wavefront shaping is also possible inside ran-

dom media with inhomogeneous scattering and loss which are common in real life for example the biological tissues.

The second type of dielectric structures that we studied in the final part of this thesis are microcavities. Dielectric microcavities, unlike random media, have a homogeneous refractive index profile and the light inside such structures is confined by total internal refraction. However, in a rotating frame, the effective refractive index of the resonant modes is no longer a constant and becomes a function of rotation speed. This leads to modification of the characteristics of the resonances in the rotating frame and such modification of the properties of the resonances can be used to detect rotation. One such example is the modification of the resonant frequency which is called as the Sagnac effect. In chapter 9, we presented a Finite Difference Time Domain simulation algorithm that we developed to study dielectric microcavities of different shapes with open boundaries in a rotating frame. In chapter 10, we used the algorithm to study rotating microcavities and along with Sagnac effect, we also studied rotation induced changes in other properties of the resonances such as the Q factor and output intensity pattern. We demonstrated that the Q factor and emission intensity can be more sensitive to rotation compared to the Sagnac effect. We further tuned the cavity shape to maximize the sensitivity of the output intensity and finally proposed an alternative scheme to detect rotation using the change in output intensity pattern.